Doctorate Dissertation

博士論文

Numerical Investigations on Explosion Mechanisms of Core-collapse Supernovae

(重力崩壊型超新星爆発メカニズムの数値的研究)

A Dissertation Submitted for Degree of Doctor of Philosophy

December 2018

平成 30 年 12 月 博士 (理学) 申請

Department of Physics, Graduate School of Science,

The University of Tokyo

東京大学大学院理学系研究科物理学専攻

Akira Harada

原田 了

Abstract

The core-collapse supernova (CCSN) is an explosive death of a massive star. The explosion mechanism of the CCSN is so complicated that the numerical simulations are required to investigate it. The main problem in the CCSN explosion mechanism is how to revive the bounce shock which is launched after the stellar core-collapse and stalls eventually. In this dissertation, the neutrino heating and the acoustic mechanisms are investigated to revive the shock. The central proto-neutron star (PNS) emits energetic neutrinos, and they provide the energy for the shock revival in the neutrino heating mechanism. Multi-dimensional effects such as turbulence are indispensable for the mechanism to work, but still some physical processes are missed to obtain explosions with observed energies. Besides, all groups employ approximate neutrino transport methods for the multi-dimensional simulations, but their accuracy is unknown. After the neutrino heating mechanism fails, intense acoustic waves are emitted from the PNS and energize the shock in the acoustic mechanism. Since this mechanism is difficult to reproduce, other groups focus on the power of the emitted acoustic waves, but the conclusion is not yet achieved.

The stellar rotation may be the missing physical process. In order to check it without the approximation mothod of the neutrino transport whose accuracy is unknown, the core-collapse of the progenitor rotating as fast as possible is simulated with the Boltzmann-radiation-hydrodynamics code which solves the Boltzmann equation directly for the neutrino transport. The evolution of the shock radii, neutrino luminosities, mean energies of neutrinos, and heating timescale imply that the model adopted here does not explode. Thus the rotation alone does not lead to the successful shock revival. Incidentally, the investigations on the momentum space distributions of neutrinos reveal that the distribution is determined by the complex combinations of the neutrino flux, reaction rates, and matter velocity. The accuracy of the M1-closure method, one of the approximation methods, is also examined. It is found that the error of this method is $\sim 20\%$.

Next, the acoustic mechanism is investigated as another possibility for the shock revival. Here, the acoustic power $\dot{E}_{\rm aco}$ required for the shock revival is examined. A steady-state flow with a stalled shock is constructed with a given mass accretion rate $\dot{M}$ and neutrino luminosity L_ν, and spherically and axially symmetric simulations with the acoustic waves injected from the PNS surface are performed. The acoustic power is estimated from the extended Myers' theory. Then the critical surface is drawn as the boundary of the parameter sets which lead the successful shock revival or not in the space spanned by $(\dot{M}, L_\nu, \dot{E}_{\rm aco})$. The spherically symmetric simulations illustrate that the shock revives when the sum of the acoustic power and neutrino heating rate exceeds a threshold value

and that not all of the acoustic power is consumed for the shock revival since the acoustic waves raise the temperature and enhance the neutrino cooling. Axisymmetric simulations show that the acoustic power found in the discovery work of the acoustic mechanism is large enough for the shock revival, and hence it is concluded that the acoustic mechanism is certainly a candidate mechanism for the shock revival.

Contents

List of Figures

List of Tables

Chapter 1

Introduction

1.1 Exploring the explosion mechanism

Core-collapse supernova (CCSN) is an explosive death of a massive star which forms an iron core. It is first proposed by Baade & Zwicky (1934). Its maximum luminosity is $\sim 10^{10} L_{\odot}$, and it shines for about a few months. Its explosion energy is $\sim 10^{51}$ erg. Origin of its energy is gravitational energy released when the stellar core collapses into a neutron star (NS), and a CCSN leaves a compact remnant. Indeed, Baade & Zwicky (1934) suggested that a CCSN is a birthplace of an NS.

The main focus of this dissertation is on explosion mechanisms of CCSN. The explosion mechanism is a long-lasting and intriguing puzzle in astrophysics. By accumulating many observational and theoretical examinations including the most crucial observation of SN1987A (the first supernova observed in 1987) in the Large Magellanic Cloud by neutrino observatories (Hirata et al., 1987; Bionta et al., 1987), an overview of the explosion mechanism as follows is obtained. The stellar iron core collapses at the end of its evolution. The gravitational collapse continues until the central density reaches the nuclear density. At that time, the infalling matter bounces due to the strong nuclear force and so-called bounce shock is launched. This process is called the core bounce. The shock wave propagates outward with losing its energy, and finally, it stalls. Then energetic neutrinos emitted from a central object called proto-neutron star (PNS) heat matter just behind the shock. If matter gets enough energy, the shock revives and starts to propagate outward again. When the shock reaches the stellar surface, a successful explosion is observed. This mechanism is called the neutrino heating mechanism. If the matter does not get enough energy, then acoustic waves are emitted from PNS and revive the shock. This mechanism for shock revival is called the acoustic mechanism. What mechanism is the most realistic is not yet concluded.

A large variety of physical processes are involved in the CCSN explosion. A CCSN produces an NS, and hence general relativistic strong gravity should be considered. Since matter is compressed to the nuclear density, the strong interaction or nuclear force should be treated appropriately, though it is difficult to model due to its self-interacting and multi-body nature. Neutrinos play a crucial role in the CCSN thus the weak interaction is indispensable to describe the CCSN. The weak interaction is described by the Weinberg-

Salam theory, but its behavior in a matter is not fully understood. All these fundamental processes combined with the hydrodynamics and neutrino transport determine how the CCSN explodes. Such an extreme environment is not realized in terrestrial experiments. Thus the CCSN is a useful probe of not-yet-understood fundamental physics in an extreme environment.

The problem of the explosion mechanism is very complicated, and hence people rely on numerical simulations in order to address it. It has been investigated for more than 50 years from early numerical works by Colgate & Johnson (1960), Colgate et al. (1961), Colgate & White (1966), and so on. In order to examine the explosion mechanism, one may think that all we have to do is to perform simulations which include all relevant physics exactly with sufficient resolution and various realistic progenitor models. So far, the limited computational resources had forced supernova modelers to rely on some approximations instead of such perfect simulations in order to model the CCSN. Much effort has been paid for the improvement of the numerical modeling including approximations. The methods and accuracy of approximations are different from group to group. Because of the lack of reference simulations, the accuracy of some approximations is still unclear.

Besides, successful shock revival which reproduces observational features like the explosion energy has not been obtained by any groups. The spherically symmetric one-dimensional (1D) simulations do not explode except for the lightest progenitor. Some of the axially symmetric two-dimensional (2D) simulations show shock revivals, but their explosion energy is not enough to explain the observations. Supernova modelers are trying to reproduce the observational results by including various physical processes called missing physics: the three-dimensional (3D) effects, rotation, progenitor asphericity, updated neutrino reactions, general relativistic gravity, and so on.

Although other supernova modelers are examining the effects of the physical processes listed above by simulations with approximate neutrino transport, I take another way: a direct simulation. Recently the development of numerical resources allows us to perform much more sophisticated code than previous codes. In this dissertation, one of the most sophisticated code is used to simulate the CCSN explosion. The most distinctive feature of the code here is to solve the Boltzmann equation for radiation transfer of neutrinos in multi-dimensions by directly discretizing the distribution function. Therefore the code is called the Boltzmann-radiation-hydrodynamics code. Using the code, the effects of rotation, one of the missing physical processes, are reported in this dissertation.

On the other hand, it should be remarked that there is a chance for the acoustic mechanism to work after the failure of the neutrino heating mechanism. Since the neutrino heating mechanism is not a unique possibility of the explosion mechanism, the acoustic mechanism should also be investigated. The Boltzmann-radiation-hydrodynamics code is, however, not appropriate to examine the acoustic mechanism since it requires enormous computational cost and cannot follow the evolution at late phase. Instead, the shock revival by the acoustic mechanism is investigated with another approach in this dissertation. In order to elucidate the explosion mechanism, investigations from several viewpoints are indispensable.

Examining the explosion mechanism of CCSN has other possible applications, though it is not the scope of this dissertation. One application is multi-messenger astronomy. The detection of neutrinos from SN1987A (Hirata et al., 1987; Bionta et al., 1987) referred to above proves the ability of the neutrino detector in the astrophysics. In 2015, the gravitational waves (GWs) from a binary black hole merger is detected (Abbott et al., 2016) and in 2017 the GWs from a binary neutron star merger is detected (Abbott et al., 2017a) and the macronova associated with the merger is observed by several telescopes (Abbott et al., 2017b). With these novel detectors, we can now use not only the electromagnetic waves but also neutrinos and GWs as messengers from astrophysical processes. Astronomy using non-electromagnetic signals is called multi-messenger astronomy.

In order to fully exploit the observational data, theoretical models are necessary. Such models for the electromagnetic signals have been made intensively so far. On the other hand, the modelings for the neutrinos and GWs are relatively poor. The CCSN is a good target for the multi-messenger observation since it emits photons, neutrinos, and GWs. The neutrinos and GWs are emitted from the core of CCSN and closely related to the explosion mechanism. Therefore investigation on the explosion mechanism also provides theoretical models for neutrinos and GWs as by-products. Offering the models facilitates the multi-messenger observations, and multi-messenger observations help us to understand the CCSN explosion mechanism.

1.2 The structure of this dissertation

This dissertation is organized as follows. In chapter 2, I review fundamentals related to the theory of the CCSNe. The results of numerical simulations of the neutrino heating mechanism is presented in chapter 3 and those of the acoustic mechanism is in chapter 4. Finally, in chapter 5, I summarize and conclude this dissertation.

I review the basic scenario, important physical processes, and problems to be addressed in chapter 2. This chapter is composed of two parts: the physical scenario during the core-collapse (section 2.1) and that after the core bounce and explosion mechanism hypotheses (section 2.2). Relevant physical processes are also included. In section 2.1.1 the gravitational stability of the stellar iron core and the onset of the core-collapse is described. Several important concepts such as neutrino trapping during the core-collapse are discussed in section 2.1.2. The section 2.1.3 explains the formation of the bounce shock and PNS. The importance and models of the nuclear equation of state (EOS) are also shown there. In section 2.2.1 the basic scenario, the current status and problems of the neutrino heating mechanism, and description of numerical code employed in chapter 3 are displayed. This includes the hydrodynamical instabilities and the neutrino reactions. Finally, those related to the acoustic mechanism are shown in section 2.2.2.

In chapter 3 a numerical simulation with the Boltzmann-radiation-hydrodynamics code in 2D is presented in order to investigate the neutrino heating mechanism. Since a simulation with non-rotating progenitor does not explode, the possibility that the rotation helps explosion is pursued in this dissertation. This goal is described at the beginning of chapter

3. The numerical modelings of progenitors and the numerical grid are explained in section 3.1. In section 3.2 the main results related to the dynamics of CCSN are presented. The shock does not revive in the simulation with rotating progenitor. Subsequently in section 3.3, I digress from the main subject to discuss the neutrino distributions in the momentum space. This is because one of the novel features of the code used here is solving the Boltzmann equation directly. Only this code can assess the momentum space distribution and hence it is worth presenting and discussing quantities related to the neutrino distributions. Finally, in section 3.4, summary and conclusions of this chapter is presented.

Since the shock does not revive even with one of the most sophisticated numerical code in chapter 3, another possibility should be pursued. The Boltzmann-radiation-hydrodynamics code employed in chapter 3 can track only several hundreds of milliseconds after the core bounce and the shock revival by the acoustic mechanism may occur after that. In order to consider this possibility, the validation of the acoustic mechanism through the critical surface is discussed in chapter 4. The critical surface is a surface drawn in a three-parameter space spanned by the mass accretion rate, neutrino luminosity, and acoustic power and divide the parameter sets into those lead to the successful explosion and not. The details are explained in chapters 2 and 4. In section 4.1 I describe the numerical modeling and method to obtain the critical surface. Although the acoustic mechanism does not work under spherical symmetry as discussed in section 2.2.2, the critical surface with spherically symmetric simulations is useful to understand the physical picture of the acoustic waves in CCSN. Therefore in section 4.2, I discuss the critical surface with spherically symmetric simulations. Then in section 4.3 the results with axisymmetric simulations are presented. This is because the acoustic mechanism is originally proposed with axisymemtric simulaions. The conclusions of this chapter are presented in section 4.4.

Finally, in chapter 5, I give the summary, conclusions, and future prospects of this dissertation.

Throughout this dissertation, I use the unit with $c = G = \hbar = 1$ in equations unless otherwise stated, with c, G, and $\hbar$ being the light speed, gravitational constant, and reduced Planck constant, respectively. The spacetime metric signature is $-+++$. Greek and Latin indices run over 0-3 (spacetime) and 1-3 (space), respectively.

Chapter 2

Explosion Mechanisms of Core-Collapse Supernovae

I first overview the basic scenario of the CCSN explosion mechanism and fundamental processes. First, I describe the physical processes and phenomena during the core collapse and bounce in section 2.1. This is relatively well understood compared with the dynamics after the core bounce and shock revival. Neutrino reactions important in this phase and some models of nuclear EOS are discussed here. The EOSs explained here are used in chapter 3 and 4. Next, the possible mechanisms and their problems are presented in section 2.2. First, the neutrino heating mechanism is discussed in section 2.2.1. The basic picture of the mechanism is reviewed first, and then the history from the first simulation in which the neutrino heating mechanism works, the problems in the mechanism, and recent effort trying to address them are explained. The critical curve, the most basic, important, and intuitive concept of the neutrino heating mechanisms, is described there. In the final part of this section, a first principle simulation of the CCSN explosion is proposed, and the current status of the code is discussed. This part describes the motivation and novel numerical technique used in chapter 3. Second, the acoustic mechanism is illustrated in section 2.2.2. The first work which proposed the acoustic mechanism, the scenario of the mechanism, and some important quantities of the work are explained. Then some works to test the validity of the acoustic mechanism and criticism to them are discussed in the following. This motivates the investigation presented in chapter 4.

2.1 Core collapse and bounce of massive stars

A massive star heavier than $8\,M_\odot$ at the zero-age-main-sequence experiences the core-collapse. The O-Ne-Mg and iron core are formed in a star of 8–$10\,M_\odot$ and in that more massive than $10\,M_\odot$, respectively, at the end of its evolution. The former starts to collapse by electron-capture reactions, while the latter begins to collapse by iron photodissociation reactions. In the following how these reactions cause the gravitational collapse is explained, and then the structure of the collapsing core and an important concept of the neutrino trapping is described.

2.1.1 The onset of the collapse

The mass of the iron and O-Ne-Mg core is close to the Chandrasekhar limit, and it is supported against the self-gravity by mainly the electron degenerate pressure and the additional thermal pressure. Therefore, the adiabatic index γ of the iron core is slightly larger than 4/3, the value for the relativistic electron degenerate pressure. If this γ becomes less than 4/3, the core starts to collapse gravitationally. This is described by the linear analysis of the gravitational stability (Shapiro & Teukolsky, 1983). In the following, the instability criterion is reviewed.

Suppose that a gas sphere is in the hydrostatic equilibrium, obeying the equations

$$\frac{\mathrm{d}P}{\mathrm{d}r} = -\rho\frac{\mathrm{d}\Phi}{\mathrm{d}r} \text{ (Euler equation)}, \tag{2.1}$$

$$\frac{1}{r^2}\frac{\mathrm{d}}{\mathrm{d}r}\left(r^2\frac{\mathrm{d}\Phi}{\mathrm{d}r}\right) = 4\pi G\rho \text{ (Poisson equation)}, \tag{2.2}$$

where r is the radial coordinate and P, ρ, Φ, and G are the pressure, density, gravitational potential, and gravitational constant, respectively. Then, fluid elements are perturbed in a spherically symmetric mannar. By letting ξ the displacement by perturbation, the radial coordinate of the element is changed from r to $r' = r + \xi$. Since the perturbation depends on both the time and radius, perturbed Euler and Poisson equations are satisfied,

$$\frac{\partial\rho\Delta v}{\partial t} + \frac{\partial\Delta P}{\partial r} + \rho\frac{\partial\Delta\Phi}{\partial r} + \Delta\rho\frac{\partial\Phi}{\partial\rho} = 0, \tag{2.3}$$

$$\frac{1}{r^2}\frac{\partial}{\partial r}\left(r^2\frac{\partial\delta\Phi}{\partial r}\right) = 4\pi G\delta\rho, \tag{2.4}$$

where t and v are the time and fluid velocity, respectively. Here Δ and δ indicate the Lagrangian and Eulerian perturbations,

$$\Delta X(r) = X'(r') - X(r) = X'(r+\xi) - X(r) \tag{2.5}$$

$$\delta X(r) = X'(r) - X(r), \tag{2.6}$$

where X and X' are an arbitrary physical quantity as a function of the radius and its perturbed counterpart, respectively. These two ways of perturbation are related by a formula

$$\Delta X = \delta X + \xi\frac{\partial X}{\partial r}. \tag{2.7}$$

The perturbed density is expressed by the divergence of the displacement,

$$\Delta\rho = -\rho\frac{1}{r^2}\frac{\partial}{\partial r}(r^2\xi), \tag{2.8}$$

and the perturbed velocity is the time differentiation of the displacement,

$$\Delta v = \frac{\partial\xi}{\partial t}. \tag{2.9}$$

By integrating equation (2.4) from 0 to some radius r,

$$\frac{\partial \delta\Phi}{\partial r} = \frac{4\pi G}{r^2}\int_0^r \delta\rho(r')r'^2 \mathrm{d}r. \tag{2.10}$$

By using equations (2.7) and (2.8), this equation is cast into

$$\frac{\partial \delta\Phi}{\partial r} = -4\pi G\rho\xi. \tag{2.11}$$

Next, equation (2.3) is cast into

$$\rho\frac{\partial^2\xi}{\partial t^2} + \frac{\partial \Delta P}{\partial r} + \frac{4\xi}{r}\frac{\partial P}{\partial r} = 0, \tag{2.12}$$

by using equations (2.1–2.2), (2.7–2.9), and (2.11). By introducing the adiabatic index

$$\gamma = \left.\frac{\partial \ln P}{\partial \ln \rho}\right|_s, \tag{2.13}$$

the perturbed pressure is expressed as

$$\Delta P = \frac{\gamma P}{\rho}\Delta\rho = -\frac{\gamma P}{r^2}\frac{\partial}{\partial r}(r^2\xi) \tag{2.14}$$

with equation (2.8). Then the equation finally takes the form

$$\rho\frac{\partial^2\xi}{\partial t^2} - \frac{\partial}{\partial r}\left(\frac{\gamma P}{r^2}\frac{\partial}{\partial r}(r^2\xi)\right) + \frac{4\xi}{r}\frac{\partial P}{\partial r} = 0. \tag{2.15}$$

By focusing on a single mode of the Fourier modes in time, the displacement ξ is proportional to $\exp(i\omega t)$ where ω is the eigenmode frequency. Then the governing equation is

$$\frac{\mathrm{d}}{\mathrm{d}r}\left(\gamma P\frac{1}{r^2}\frac{\mathrm{d}}{\mathrm{d}r}(r^2\xi)\right) - \frac{4}{r}\frac{\mathrm{d}P}{\mathrm{d}r}\xi + \omega^2\rho\xi = 0. \tag{2.16}$$

This equation is cast into the following form:

$$\omega^2 = \frac{\int_0^R \mathrm{d}r\left\{\gamma P\frac{1}{r^2}\left[\frac{\mathrm{d}}{\mathrm{d}r}(r^2\xi)\right]^2 + 4r\xi^2\frac{\mathrm{d}P}{\mathrm{d}r}\right\}}{\int_0^R \mathrm{d}r\rho\xi^2 r^2} = \frac{|W|}{I}\left(3\bar{\gamma} - 4\widetilde{\left(\frac{\xi}{r}\right)^2}\Big/\overline{\left(\frac{\xi}{r}\right)^2}\right). \tag{2.17}$$

The definitions of the symbols are as follows:

$$\begin{aligned} I &:= \int_0^M r^2\mathrm{d}m, \quad \overline{\left(\frac{\xi}{r}\right)^2} := \frac{1}{I}\int_0^M \xi^2\mathrm{d}m, \quad \widetilde{\left(\frac{\xi}{r}\right)^2} := \frac{1}{|W|}\int_0^M \left(\frac{\xi}{r}\right)^2\frac{Gm}{r}\mathrm{d}m \\ |W| &:= \int_0^M \frac{Gm}{r}\mathrm{d}m, \qquad \bar{\gamma} := \frac{\overline{(\nabla\cdot\xi)^2\gamma}}{\overline{(\xi/r)^2}}, \qquad \overline{(\nabla\cdot\xi)^2\gamma} := \frac{\int_0^R (\nabla\cdot\xi)^2\gamma P 4\pi r^2\mathrm{d}r}{\int_0^R P 4\pi r^2\mathrm{d}r}. \end{aligned} \tag{2.18}$$

Here $\bar{\gamma}$ is the pressure-weighted average of γ. When $\gamma \to 4/3$, the squared eigenfrequency approaches to the form of

$$\omega^2 \simeq \frac{|W|}{I}(3\bar{\gamma} - 4), \tag{2.19}$$

therefore if $\bar{\gamma} < 4/3$, the eigenfrequency is purely imaginary, and the perturbation develops exponentially.

As discussed above, γ is slightly larger than $4/3$ for the stellar core. As the core evolves, electron capture and iron-photodissociation process reduce γ below the critical value. In the stellar core, the pressure consists of the degenerate pressure of the relativistic electrons $P_{\rm e}$, the radiation pressure of the photons P_γ, and the thermal pressure of the nuclei P_A:

$$P = P_{\rm e} + P_\gamma + P_A = \frac{1}{3}\left(\frac{3}{8\pi}\frac{\rho Y_{\rm e}}{m_{\rm u}}\right)^{4/3} + \frac{1}{3}aT^4 + \frac{3}{2}\frac{\rho}{Am_{\rm u}}k_{\rm B}T, \tag{2.20}$$

where $Y_{\rm e} := n_{\rm e}/n_{\rm b}$, $n_{\rm e}$, $n_{\rm b}$, $m_{\rm u}$, a, T, A, and $k_{\rm B}$ are the electron fraction, electron number density, baryon number density, atomic mass unit, radiation constant, temperature, (mean) mass number of nuclei, and Boltzmann constant, respectively. Here, $P_{\rm e} \gg P_\gamma$, P_A, thus the adiabatic index is dominated by $P_{\rm e}$.

If the density is high enough, the electron capture process occurs. Since the iron core is mainly composed of iron nuclei, the electron capture reaction is, for example,

$$^{56}{\rm Fe} + {\rm e}^- \to {}^{56}{\rm Mn} + \nu_{\rm e}. \tag{2.21}$$

The mass of manganese is larger than that of iron. In order to enable the electron capture on nuclei, there should be electrons whose energy is larger than the mass difference of these nuclei, several MeV typically. The electron degeneracy realizes such high energy electrons: if the electrons are relativistic and completely degenerate with zero temperature, the Fermi energy of electrons is

$$\mu_{\rm e} \simeq 11\,{\rm MeV}\left(\frac{\rho Y_{\rm e}}{10^{10}\,{\rm g\,cm^{-3}}}\right)^{1/3}. \tag{2.22}$$

At the center of the iron core of a massive star at the onset of the collapse, the density is $\sim 10^{10}\,{\rm g\,cm^{-3}}$, and the temperature is $\leq 1\,{\rm MeV}$. Therefore the assumption of relativistic and complete degeneracy is valid, and the electrons have enough energy to be captured by iron nuclei. When the electron fraction does not change with the density, the adiabatic index for the electron degenerate pressure is $4/3$ as seen in equation (2.20). On the other hand, when the electron capture reduces the electron fraction with increasing density, the pressure does not rise as high as the case without electron captures, and hence the adiabatic index effectively becomes smaller than $4/3$.

For the low-temperature environment, the iron nuclei, whose binding energy is the lowest, tend to be formed since the free energy $F = U - TS$ is dominated by the internal energy U, with S being the entropy. As the core contracts, the temperature gets higher, and the influence of the second term of the free energy increases, and the matter tends to increase the entropy by breaking up iron nuclei into nucleons. In this reaction, high energy photons produced by the high-temperature environment dissociate iron nuclei. These reactions are endothermic:

$$^{56}{\rm Fe} \leftrightarrow 13\,{}^4{\rm He} + 4{\rm n} - 125\,{\rm MeV}, \tag{2.23}$$

$$^4{\rm He} \leftrightarrow 2{\rm p} + 2{\rm n} - 28.3\,{\rm MeV}. \tag{2.24}$$

This energy loss reduces the temperature with the increasing density, and hence the thermal pressure decreases. Although the contribution to γ from the degenerate pressure alone is 4/3, this reduction of the thermal pressure further contribute to γ, and by this effect, γ gets smaller than 4/3.

2.1.2 The physical processes in the collapsing core

Once the stellar core becomes unstable, the gravitational collapse begins. The collapse is adiabatic (Bethe et al., 1979), and hence the equation of state is expressed as $P = \kappa\rho^{\gamma}$. Since the dimensional quantities present in the system are only κ and G, the gravitational constant, the system is self-similar. The self-similar solution of the collapse is developed by Yahil (1983) and well describes the result of numerical simulations. That solution revealed that the collapsing core is divided into two parts: a subsonically and homologously collapsing inner core and a supersonically and freely falling outer core. Moreover, Yahil (1983) found that the mass of the inner core approximately coincides with the Chandrasekhar mass. Note that the Chandrasekhar mass in this argument is defined by the mass coordinate in which the total energy is zero. If $\gamma = 4/3$, the Chandrasekhar mass of this definition coincides with that of the usual definition.

The collapse continues until the adiabatic index of the inner core becomes $\gamma > 4/3$. This occurs when the central density reaches the nuclear density and the strong interaction between nucleons dominates the pressure. However, some physical processes may increase the adiabatic index before the density reaches the nuclear density, and hence enough gravitational energy may not be released. Although these processes are actually suppressed, it is worth mentioning what processes have such possibilities.

During the collapse, as the density increase, the Fermi energy of the electrons increases, and hence the electron capture reactions continue, and neutrinos are emitted not only in the O-Ne-Mg core but also in the iron core. The electron capture reactions produce neutrons and entropy since this is an irreversible process going to the β-equilibrium. If the entropy in the core is high, not only heavy nuclei such as iron but also free nucleons exist as a consequence of the thermal equilibrium. The free nucleons are heavy enough to behave as non-relativistic gas, whose adiabatic index is 5/3. Thus, these free nucleons can stop the collapse before the central density reaches nuclear density. However, the entropy produced by the electron capture reaction is taken away by the escaping neutrinos, and hence the entropy of the core keeps low value during the collapse (Bethe, 1990). Therefore, such free nucleons are not produced actually.

The produced neutrons can also affect the collapse. The electron capture considered here is the capture on a heavy nucleus, thus after the reaction neutron number increases. By repeating the capture, the nucleus becomes neutron-rich (neutronization). Although the neutron number of stable heavy nuclei is slightly larger than the proton number because of the Coulomb energy, nuclei with too many neutrons are unstable due to the symmetry energy. As a consequence, neutrons escape from the nuclei. This phenomenon is called the "neutron drip." If the neutron drip occurred, again free neutrons would increase the adiabatic index.

If the electron capture process continues, the neutron drip would stop the collapse. However, the neutrino trapping prevents it. As the density increases, the neutrinos produced by the electron capture scatter off nuclei via coherent scattering process (Freedman, 1974). For the coherent scattering, the scattering cross section is proportional to the square of the mass number of the nuclei. This is understood as follows: Consider the wave function of a neutrino. If a single nucleon scatters the neutrino, a scattered wave function is generated. On the other hand, if several nucleons gather narrower than the wavelength of the neutrino like a nucleus, the waves scattered by each nucleon are superimposed coherently, then the total amplitude of the scattered wave is enhanced. Actually, superimposing occurs each pair of nucleons, and hence the total amplitude is proportional to the number of pairs of the nucleon, approximately the squared mass number of the nucleus.

The neutrino trapping proposed by Sato (1975) occurs when the diffusion timescale of the neutrinos exceeds the dynamical timescale of the collapse. First, the diffusion timescale is evaluated as follows. The cross section of the coherent scattering is

$$\frac{\mathrm{d}\sigma}{\mathrm{d}\Omega} = \frac{\sigma_0}{64\pi}\left(\frac{\epsilon}{m_\mathrm{e}}\right)^2 A^2 \left\{1 - \frac{2Z}{A}(1 - 2\sin^2\theta_\mathrm{W})\right\}^2 C_\mathrm{FF}^2(1+\cos\theta), \tag{2.25}$$

where

$$\sigma_0 := \frac{4G_\mathrm{F}^2 m_\mathrm{e}^2}{\pi} \simeq 1.7\times10^{-44}\,\mathrm{cm}^2, \tag{2.26}$$

G_F, m_e, ϵ, Z, θ_W, and C_FF are the Fermi coupling constant, mass of the electron, energy of the neutrinos, atomic number, Weinberg angle, and form factor of the nucleus. Since the neutrinos are mainly produced by the capture of degenerate electrons and the recoil of the nuclei is negligible due to the large mass compared to the electron energy, the energy of the neutrinos is approximately equal to the Fermi energy of the electrons:

$$\epsilon \simeq \left(3\pi^2 \frac{\rho Y_\mathrm{e}}{m_\mathrm{u}}\right)^{1/3}. \tag{2.27}$$

Thus the mean free path is

$$\ell_\mathrm{mfp} := \frac{1}{\sigma_A n_A} \simeq 5\times10^7\,\mathrm{cm}\left(\frac{\rho}{10^{10}\,\mathrm{g\,cm^{-3}}}\right)^{-5/3}\left(\frac{Y_\mathrm{e}}{26/56}\right)^{-2/3}\left(\frac{A}{56}\right)^{-1}, \tag{2.28}$$

where σ_A is the total cross section of the coherent scattering and $n_A = \rho/(m_\mathrm{u}A)$ is the number density of nuclei. For the above estimation, I approximate that $A \simeq 2Z$. Since the core mass is approximately the Chandrasekhar mass

$$M_\mathrm{core} \simeq 1.26\,M_\odot\left(\frac{Y_\mathrm{e}}{26/56}\right)^2, \tag{2.29}$$

the size of the core is

$$R_\mathrm{core} = \left(\frac{3M_\mathrm{core}}{4\pi\rho}\right)^{1/3} \sim 10^7\,\mathrm{cm}\left(\frac{\rho}{10^{10}\mathrm{g\,cm^{-3}}}\right)^{-1/3}\left(\frac{Y_\mathrm{e}}{26/56}\right)^{2/3}. \tag{2.30}$$

Therefore the neutrinos start to be scattered when the density exceeds $\sim 10^{10}\,\mathrm{g\,cm^{-3}}$. By using the mean free path, the diffusion timescale is

$$t_{\mathrm{diff}} := \frac{3R_{\mathrm{core}}^2}{\ell_{\mathrm{mfp}}c} \simeq 30\,\mathrm{ms}\left(\frac{\rho}{10^{11}\,\mathrm{g\,cm^{-3}}}\right)\left(\frac{Y_{\mathrm{e}}}{26/56}\right)^2\left(\frac{A}{56}\right). \tag{2.31}$$

On the other hand, the dynamical timescale of the collapse is

$$t_{\mathrm{dyn}} := \sqrt{\frac{1}{G\rho}} \simeq 10\,\mathrm{ms}\left(\frac{\rho}{10^{11}\,\mathrm{g\,cm^{-3}}}\right)^{-1/2}, \tag{2.32}$$

thus when the density exceeds $10^{11}\,\mathrm{g\,cm^{-3}}$, the diffusion timescale exceeds the dynamical timescale and the neutrinos no longer diffuse out from the core. Once the neutrinos are trapped, the Pauli blocking prevents the further production of neutrinos, and hence the neutronization is also stopped.

The neutrino trapping has two positive feedback processes (Sato, 1975). The trapped neutrinos achieve the β-equilibrium with matter and degenerate. As the density increases, the Fermi energy of the neutrinos rises. Then the cross section of the coherent scattering also increase as $\propto \epsilon^2$, and the neutrino opacity rises further. Due to the higher opacity, the more strongly the neutrinos are trapped. Not only the increase of the cross section but also the suppression of the neutronization plays a role in another feedback process. The suppression of the neutron drip also suppresses the melting of nuclei due to the neutron drip. This process makes the coherent scattering efficient since the cross section $\propto A^2$. Thanks to these feedback processes, the neutrino trapping proceeds automatically.

The surface of the region where neutrinos are trapped is called the "neutrinosphere", which is an analogy of the photosphere for photons. For practical definition, the neutrinosphere is defined sometimes as the isodensity surface of $\rho = 10^{11}\,\mathrm{g\,cm^{-3}}$ or at other times the surface where the optical depth for neutrinos is 2/3. The neutrinosphere is formed in the outer core, i.e., the part of the collapsing stellar core whose velocity is supersonic.

2.1.3 The core bounce

Formation of the bounce shock, proto-neutron star, and neutronization burst

When the central part of the core reaches the nuclear density, the strong interaction between nucleons rapidly increases the pressure, the adiabatic index, and hence the collapse stops. The information of the braking is communicated only inside the subsonic inner core, while the supersonic outer core does not know that inner core is braking. Therefore, at the interface of the inner and outer cores, the shock wave is formed. This shock is called the bounce shock, and the formation of the bounce shock is called the core bounce.

After the core bounce, the central part of the shocked core settles down to be in the hydrostatic equilibrium. This object is called the proto-neutron star (PNS). The PNS still has a lot of protons ($Y_{\mathrm{e}} \sim 0.3$) and high temperature and evolves to be the neutron star by losing the internal energy and leptons via the neutrino emission.

At the bounce, the shock lies inside the neutrinosphere. The entropy between the central PNS and the shock is high due to the shock heating, and hence the heavy nuclei are

dissolved. Since the coherent scattering is not efficient, the mean free path is large there. However, the matter between the shock and the neutrinosphere is composed of heavy nuclei and opaque enough to confine the neutrinos. After a while, the shock propagates and crosses the neutrinosphere. At that time, heavy nuclei that contribute to the large opacity are disintegrated by the shock, and hence the neutrinosphere rapidly shrinks to the surface of the PNS. Therefore, a large part of the matter instantaneously becomes optically thin and the neutrinos trapped until the crossing time are liberated promptly. As a consequence, many neutrinos are emitted from the stellar core. Note that the neutrinos confined in the neutrinosphere are mainly the electron-type neutrinos since during the collapse the electrons are degenerate and there are little positrons, and hence the electron capture reactions, which produces the electron-type neutrinos, are dominant. Besides, inside the shock, the heavy nuclei are dissociated into nucleons whose electron capture rate is large, thus again the electron-type neutrinos are mainly produced. Since the many electron-type neutrinos are emitted, the electron fraction of the remnant core rapidly decrease, and hence this is called the "neutronization burst".

The energy released by the bounce is evaluated as

$$E_{\rm bounce} = \left(-G\frac{M_{\rm IC}^2}{R_{\rm ini}}\right) - \left(-G\frac{M_{\rm IC}^2}{R_{\rm fin}}\right) \simeq 1.3 \times 10^{53}\,{\rm erg}, \tag{2.33}$$

where $R_{\rm ini} = 1000\,{\rm km}$, $R_{\rm fin} = 10\,{\rm km}$, and $M_{\rm IC} = 0.7\,M_\odot$ are the initial and final core radius and the inner core mass, respectively. The hydrostatic object, which is nothing but the PNS, is formed at the center, and hence the virial theorem

$$|W| = 3(\gamma - 1)U, \tag{2.34}$$

where W and U are the gravitational energy and the internal energy, respectively, can be applied. Since $\gamma \simeq 4/3$ averagely,[*1] the internal energy of the core is almost the same as the released gravitational energy, and the energy of the shock is $\sim 10^{51}\,{\rm erg}$, only a few per cent of W (Brown et al., 1982). The energy released at the bounce depends on the electron fraction $Y_{\rm e}$ through the inner core mass $M_{\rm IC}$ and the details of the nuclear EOS through the final core radius $R_{\rm fin}$.

Nuclear equations of state

The energy of the bounce shock and the postbounce dynamics depend on the nuclear EOS. However, the knowledge about the nuclear force is limited, since the dense nuclear matter such as that in the CCSN cannot be realized on the Earth. Therefore, in order to simulate the dense and hot celestial phenomena such as CCSNe, several model nuclear EOSs are proposed. Here, I introduce two often-used EOS models: the Lattimer-Swesty (LS) EOS (Lattimer & Swesty, 1991) and the Shen (Shen-Toki-Oyamatsu-Sumiyoshi: STOS) EOS (Shen et al., 1998). Subsequently, an extension of the STOS EOS is introduced.

[*1] Although the adiabatic index of the central part of the core is $\simeq 2$ due to the nuclear force, the other part of the core is supported by the relativistic particles and photons, and hence the adiabatic index there is 4/3. As a result, the average adiabatic index is similar to 4/3.

symbol	$n_{\rm s}$	B	K	$S_{\rm v}$
meaning	saturation density	binding energy	incompressibility	symmetry energy
value	$0.155\,{\rm fm}^{-3}$	16.0 MeV	375, 220, 180 MeV	29.3 MeV

Table 2.1. Experimental parameters to determine the model parameters in equation (2.35).

The LS EOS is based on the liquid-drop model of the nuclei. Consider that the heavy nuclei exist in the atmosphere of the nucleons, leptons, and photons. Lattimer & Swesty (1991) estimated the free energy by modeling the bulk and surface energy and so on. Then the configuration is determined to minimize the free energy, and the thermodynamic quantities are calculated.

The bulk energy proposed in Lattimer & Swesty (1991) is

$$E_{\rm bulk,LS} = \sum_t \frac{\tau_t}{2m_t^*} + \{a + 4bY_{\rm e}(1-Y_{\rm e})\}n^2 + cn^{1+\delta} - Y_{\rm e}n\Delta, \tag{2.35}$$

where t is the isospin of the nucleon. The first term is the kinetic energy density, where m_t^* is the effective mass of the nucleon t; the second term is the two-body potential, which contributes to the attractive force, where a and b are the model parameters and n is the number density of the nucleon; the third term is the three- or many-body potential, which contributes to the repulsive force, where c and δ are the model parameters; the fourth term is the symmetric energy, where $\Delta = m_{\rm n} - m_{\rm p}$ is the mass difference between the neutron and proton. In this expression, by using the electrical charge neutrality, the proton fraction is replaced by $Y_{\rm e}$. The model parameters a, b, c, and δ are determined to match several experimental parameters indicated in table 2.1. These experimental parameters are defined as the expansion coefficients of the bulk energy around the saturation density and the symmetric matter:

$$E_{\rm bulk} \simeq -B - Y_{\rm e}\Delta + \frac{1}{18}K\left(1 - \frac{n}{n_{\rm s}}\right)^2 + S_{\rm v}(1-2Y_{\rm e})^2 + \cdots, \tag{2.36}$$

again the proton fraction is replaced by $Y_{\rm e}$.

For the high-density matter, the heavy nuclei suspended in the nucleon atmosphere forms so-called nuclear pasta, where the nuclei deformed into rods, sheets, bubbles, and so on. This nuclear pasta phase contributes to the surface and Coulomb energy. In Lattimer & Swesty (1991), only drop phase (the nuclei is spheres) and bubble phase (the atmosphere of nucleons is confined in spherical regions). Other phases of the nuclear pasta are expressed by interpolating these two phases.

On the other hand, the STOS EOS is based on the relativistic mean field (RMF) theory.

The Lagrangian of the nuclear matter is expressed as

$$\mathcal{L}_{\rm RMF} = \bar{\psi}[i\gamma^\mu\partial_\mu - M - g_\sigma\sigma - g_\omega\gamma^\mu\omega_\mu - g_\rho\gamma^\mu\tau_a\rho^a_\mu]\psi \tag{2.37}$$

$$+\frac{1}{2}\partial_\mu\sigma\partial^\mu\sigma - \frac{1}{2}m_\sigma^2\sigma^2 - \frac{1}{3}g_2\sigma^3 - \frac{1}{4}g_3\sigma^4 \tag{2.38}$$

$$-\frac{1}{4}W_{\mu\nu}W^{\mu\nu} + \frac{1}{2}m_\omega^2\omega_\mu\omega^\mu + \frac{1}{4}c_3(\omega_\mu\omega^\mu)^2 \tag{2.39}$$

$$-\frac{1}{4}R^a_{\mu\nu}R^{a\mu\nu} + \frac{1}{2}m_\rho^2\rho^a_\mu\rho^{a\mu}, \tag{2.40}$$

$$W_{\mu\nu} := \partial_\mu\omega_\nu - \partial_\nu\omega_\mu, \tag{2.41}$$

$$R^a_{\mu\nu} := \partial_\mu\rho^a_\nu - \partial_\nu\rho^a_\mu + g_\rho\epsilon^{abc}\rho^b_\mu\rho^c_\nu, \tag{2.42}$$

where ψ is the spinor of the nucleon doublet; σ, ω, and ρ are meson fields which mimic the nuclear force whose spin and isospin is (0, 0), (1, 0), and (1, 1), respectively; W and R are the field strength of ω and ρ, respectively; g_σ, g_ω, g_ρ, g_2, g_3, and c_3, are coupling constants, and M, m_σ, m_ω, and m_ρ are the masses of each field; γ^μ and τ_a are Dirac's gamma matrices and the isospin operator, respectively. The coupling constants and the masses are determined according to the TM1 parameter set (Sugahara & Toki, 1994). In the RMF theory, the equations of motion are derived from the Lagrangian, and the meson fields are regarded as the steady and homogeneous classical mean fields. Let us denote the mean field values with subscript 0. Finally, the bulk energy in the RMF theory is calculated as

$$E_{\rm bulk,RMF} = \sum_t \frac{1}{\pi^2}\int_0^\infty {\rm d}pp^2\sqrt{p^2+(M^*)^2}f_t(p) + g_\omega\omega_0(n_{\rm p}+n_{\rm n}) + g_\rho\rho_0(n_{\rm p}-n_{\rm n})$$
$$+(\text{masses and self energies of meson fields}), \tag{2.43}$$

where

$$f_t(p) = \frac{1}{1+\exp[(\sqrt{p^2+(M^*)^2}-\nu_t)/k_{\rm B}T]} \tag{2.44}$$

is the distribution functions of nucleon and $M^* := M + g_\sigma\sigma_0$ and $\nu_t := \mu_t - g_\omega\omega_0 - g_\rho\tau_3\rho_0$ are the effective mass of the nucleon and the effective chemical potential of the nucleon with μ_t being the chemical potential, respectively.

In addition to the bulk energy, we should consider the surface and the Coulomb energies when the nuclei exist. In the STOS EOS, the nucleon number density distribution inside and outside the nucleus is analytically modeled, and the total energy is evaluated by the Thomas-Fermi approximation, i.e., the local energy density is determined via equation (2.43) with local number densities of nucleons.

Lattimer & Swesty (1991) provides subroutines which calculate the EOS. They offer three kinds of EOSs whose incompressibility parameter K is 375, 220, and 180 MeV as shown in table 2.1. The $K = 375$ MeV is referred to as unrealistically high in their paper, but they consider the value for comparison with older papers. They proposed that $K =$ 220, 180 MeV EOSs are more realistic. However, the EOS with $K = 220$ MeV is mainly used these days since the EOS with $K = 180$ MeV cannot support the most massive, i.e., $\sim 2\,M_\odot$ neutron star discovered by Demorest et al. (2010). Table 2.2 shows the maximum

EOS	LS			STOS
K [MeV]	375	220	180	281
The maximum NS mass [$M_\odot$]	2.72	2.04	1.83	2.24

Table 2.2. The maximum gravitational mass of the neutron star supported by each EOS calculated in O'Connor & Ott (2011).

gravitational mass of the neutron star supported by each EOS, above which the neutron star collapse to the black hole. Except for unrealistic LS EOS with $K = 375\,\mathrm{MeV}$, the table indicates that the STOS EOS is stiffer than the LS EOS.

There are a lot of nuclear species in the sub-nuclear matter phase. However, a single nuclear species represents such an ensemble of nuclei in both the LS and STOS EOSs. This treatment is called the single nuclear approximation. Recently, instead of the single nuclear approximation, EOSs based on the multi-nuclear species with the nuclear statistical equilibrium (NSE) are constructed. In this dissertation, an EOS proposed by Furusawa et al. (2011, 2013) is considered as an example of such an NSE EOS. This EOS is based on STOS EOS and called Furusawa-Shen (FS) EOS.

In the context of CCSNe, a soft EOS leads to more compact PNS. The compact PNS has high temperature and emits high energy neutrinos. Since the neutrino reaction rates are proportional to the squared energy, the neutrino opacity and the heating rate are large for high energy neutrinos. Therefore, it is said that the models with soft EOSs are easier to explode than those with stiff EOSs. The comparison between LS and FS EOSs is discussed in Nagakura et al. (2018) and will be briefly reviewed in section 3.

2.2 Mechanisms for shock revival

After the core bounce, the launched shock propagates the still-collapsing outer core. If the shock propagates further to reach the surface of the star, the successful explosion is observed, and this scenario is called the prompt shock mechanism. However, the prompt shock mechanism does not work well. When the heavy nuclei pass the shock wave, the photodissociation of nuclei consumes the energy of the shock (see the discussion in section 2.1.1). The iron nuclei, which is the main component of the iron core, requires 8.8 MeV per a nucleon to dissociate. There is a shock radius in which all the iron nuclei are dissociated into the nucleons. This radius is called the dissociation radius R_{diss} (Janka, 2012). When the shock radius is R, the kinetic energy of the infalling matter at just upstream of the shock is $GM_{\mathrm{PNS}}m_{\mathrm{u}}/R$ per a nucleon. The kinetic energy of the infalling matter is converted into the internal energy at the downstream of the shock, and hence $GM_{\mathrm{PNS}}m_{\mathrm{u}}/R \geq 8.8\,\mathrm{MeV}$ is satisfied for the photodissociation to occur. The dissociation radius is derived by equating both sides of this inequality. By setting the PNS mass as $1.5\,M_\odot$, the dissociation radius is $\sim 240\,\mathrm{km}$. Therefore when the shock is smaller than this radius, all the nuclei are dissolved into the nucleons and consume the shock energy.

Although the photodissociation of the nuclei is the primary source of the energy loss of

the shock (Mazurek, 1982), neutrino emission additionally loses the energy. The electron capture rate of the nucleon inside the shock is larger than that of the nuclei outside of the shock, and hence many electrons are converted to neutrinos and escape out.

By these processes, the bounce shock stalls finally. This shock is called the stalled shock, or sometimes the standing accretion shock (SAS). The central question of the CCSNe mechanism is how to revive the stalled shock. So far, several mechanisms to explain the shock revival is proposed, and in this dissertation I discuss two of these mechanisms: the neutrino heating mechanism and the acoustic mechanism.

In the following, I describe these mechanisms. Section 2.2.1 presents the outline of the neutrino heating mechanism, brief history of numerical simulations for the mechanism, current status of this research field, and numerical techniques used in chapter 3. Some useful concept to understand the mechanism is also explained. In section 2.2.2 the proposition of the acoustic mechanism and some criticisms to the mechanism are discussed.

2.2.1 The neutrino heating mechanism

The basic scenario of the neutrino heating mechanism

As discussed in section 2.1.3, only a few portions of the released gravitational energy ($\sim 10^{53}\,\mathrm{erg}$ in total) is imparted to the shock, and the left energy is contained in the PNS as the internal energy. The PNS evolves to be the neutron star by losing its energy and the electron number, which equals the proton number, via the neutrino emission. The neutrinos diffuse out from the PNS with the timescale of

$$t_{\mathrm{diff}} = \frac{3R_{\mathrm{PNS}}^2}{\ell_{\mathrm{mfp}}c} = 4\,\mathrm{s}\left(\frac{R_{\mathrm{PNS}}}{10\,\mathrm{km}}\right)^2\left(\frac{\rho}{10^{14}\,\mathrm{g\,cm^{-3}}}\right)\left(\frac{\epsilon}{10\,\mathrm{MeV}}\right)^2, \tag{2.45}$$

where R_{PNS} is the radius of the PNS and assumed to be 10 km. Since the internal energy of the PNS is lost by the emission of the six species of the neutrinos with this timescale, the neutrino luminosity of each species is $\sim 10^{52}\,\mathrm{erg\,s^{-1}}$. Note that this timescale and the luminosity are consistent with the duration and the flux of the neutrino burst from SN1987A (Hirata et al., 1987; Bionta et al., 1987).

Since the explosion energy observed is $\sim 10^{51}\,\mathrm{erg}$, if only $\sim 1\%$ of the energy in the PNS is absorbed by the shock, it is enough for successful shock revival. The mechanism in which the neutrinos emitted from the PNS heat and revive the shock is called the neutrino heating mechanism. Since the shock revival occurs after the shock stagnation in this mechanism, the mechanism is also called the delayed shock mechanism. Wilson (1985) first argued that his spherically symmetric simulation of the stellar collapse shows successful shock revival by this mechanism. Since his work, much effort is paid for this mechanism, and it is revealed that his simulation itself assumes some artificial, unrealistic processes and may not be robust. However, at the same time, the potential success of this mechanism is also widely accepted, and the neutrino heating mechanism is the leading hypothesis for the shock revival these days.

In the neutrino heating mechanism, the most important processes are the neutrino

absorption/emission by the free nucleon:

$$\nu_{\rm e} + {\rm n} \leftrightarrow {\rm p} + {\rm e}^-, \tag{2.46}$$

$$\bar{\nu_{\rm e}} + {\rm p} \leftrightarrow {\rm n} + {\rm e}^+. \tag{2.47}$$

The cross sections for the absorption reactions of the electron-type neutrinos and the electron-type anti-neutrinos are

$$\sigma_{\nu_{\rm e}{\rm n}} = \sigma_0 \left(\frac{1+3g_{\rm A}^2}{4}\right)\left(\frac{\epsilon+\Delta}{m_{\rm e}}\right)^2 \sqrt{1-\frac{m_{\rm e}^2}{(\epsilon+\Delta)^2}}, \tag{2.48}$$

$$\sigma_{\bar{\nu_{\rm e}}{\rm p}} = \sigma_0 \left(\frac{1+3g_{\rm A}^2}{4}\right)\left(\frac{\epsilon-\Delta}{m_{\rm e}}\right)^2 \sqrt{1-\frac{m_{\rm e}^2}{(\epsilon-\Delta)^2}}\Theta(\epsilon-\Delta-m_{\rm e}), \tag{2.49}$$

respectively (Bruenn, 1985). Here, again $\Delta = m_{\rm n} - m_{\rm p}$ is the mass difference between nucleons, Θ is the Heaviside's step function, and $g_{\rm A} \simeq -1.26$ is the axial vector coupling constant. Since the energy scale of the CCSNe ($\sim 10\,{\rm MeV}$) is much smaller than the mass of weak bosons ($\sim 100\,{\rm GeV}$), the effective Lagrangian with Fermi-type four-point interaction is used to derive the formulae. In addition, the weak magnetism and the recoil of the nucleon are neglected. Among all neutrino reactions, these two kinds of charged current reactions have the largest cross sections per nucleon. The neutrino absorption via this reaction mainly heats the shock in the mechanism.

The gain radius in the stalled shock phase

A useful concept in the neutrino heating mechanism is the gain radius. Let us consider the structure of the CCSNe in order to define the gain radius based on the discussion in Janka (2001). The temperature of the post-shock region is so high that electrons are relativistic, thus the adiabatic index of the post-shock gas is 4/3: $P = k\rho^{4/3}$ where k is some constant. In the stalled shock phase, the structure of the gas is determined by the hydrostatic equilibrium. Assuming that the gravity is dominated by the point-mass gravity of the PNS,

$$\frac{{\rm d}P}{{\rm d}r} = -\frac{GM_{\rm PNS}\rho}{r^2}. \tag{2.50}$$

Since the gas is relativistic, this equation leads to $\rho \propto r^{-3}$. On the other hand, the pressure is dominated by the relativistic particles, i.e., photons and electrons:

$$P = P_\gamma + P_{\rm e^\pm} = \frac{1}{3}aT^4 + \frac{7}{12}aT^4 = \frac{11}{12}aT^4. \tag{2.51}$$

These expressions for the pressure imply $\rho^{4/3} \propto T^4$. Combining with $\rho \propto r^{-3}$, the temperature structure of the post-shock gas is that $T \propto r^{-1}$.

Now consider that the neutrino heating and cooling. The neutrino heating rate is determined by the local neutrino flux. Since the central PNS is the primary source of the neutrino emission, the flux is proportional to r^{-2} similarly to the light from a light-bulb. On the other hand, the neutrino cooling rate is determined by the local temperature,

proportional to T^6. This is understood as follows: the cooling rate Q^- is calculated as

$$Q^- = \int \mathrm{d}p^3 \sigma_{\nu_\mathrm{e}\mathrm{n}/\bar{\nu_\mathrm{e}}\mathrm{p}} \epsilon (n_\mathrm{p} f_{\mathrm{e}^-} + n_\mathrm{n} f_{\mathrm{e}^+}), \tag{2.52}$$

where, $n_{\mathrm{p/n}}$ and $f_{\mathrm{e}^\pm}$ are the number densities of the protons/neutrons and the distribution function of the electrons/positrons. The cross section is presented in equation (2.48–2.49). The distribution functions are $f_{\mathrm{e}^\pm} = 1/(1 + \exp((\epsilon - \mu_{\mathrm{e}^\pm})/T))$. By performing the momentum integral, equation (2.52) is revealed to be $\propto T^6$. Combining the temperature structure discussed in the previous paragraph, the neutrino cooling rate is $\propto r^{-6}$. Therefore, the neutrino cooling rate drops faster than the neutrino heating rate as going out, and there is a point where the neutrino heating and cooling balance. This point is the gain radius, outside and inside which the neutrino heating and cooling dominate, respectively. The region where the neutrino heating dominates is called the gain region or the gain layer, and the region where cooling dominates is the cooling layer.

The critical condition for the shock revival

Another useful concept is the critical curve suggested by Burrows & Goshy (1993), which provides a basic picture of the neutrino heating mechanism. The (quasi-)hydrostatic equilibrium is established in the stalled shock phase. Burrows & Goshy (1993) numerically modeled this phase as the steady-state solution of hydrodynamic equations with the mass accretion and neutrino heating.

The detailed construction is as follows. Although Burrows & Goshy (1993) are the first people to construct the steady-state solution to model the stalled shock in the CCSN, some other groups also utilize the steady-state solution in order to investigate the properties of the stalled shock (Yamasaki & Yamada, 2007; Ohnishi et al., 2006; Fernández, 2012; Pejcha & Thompson, 2012). Here, the more modern prescription adopted in chapter 4 is presented. Basic equations are the time-independent hydrodynamic equations under spherical symmetry with the point-mass gravity:

$$\frac{1}{r^2}\frac{\mathrm{d}}{\mathrm{d}r}(r^2 \rho v) = 0, \tag{2.53}$$

$$\frac{1}{r^2}\frac{\mathrm{d}}{\mathrm{d}r}(r^2 \rho v^2) + \frac{\mathrm{d}P}{\mathrm{d}r} = -\rho \frac{\mathrm{d}\Phi}{\mathrm{d}r}, \tag{2.54}$$

$$\frac{1}{r^2}\frac{\mathrm{d}}{\mathrm{d}r}\left\{ r^2 \rho v \left(e + \frac{1}{2}v^2 + \frac{P}{\rho} \right) \right\} = -\rho v \frac{\mathrm{d}\Phi}{\mathrm{d}r} + Q, \tag{2.55}$$

$$\frac{1}{r^2}\frac{\mathrm{d}}{\mathrm{d}r}(r^2 \rho v Y_\mathrm{e}) = \rho \Gamma, \tag{2.56}$$

$$\Phi = -\frac{GM_\mathrm{PNS}}{r}, \tag{2.57}$$

where e, Q, Γ, G, and M_PNS are the specific internal energy, net neutrino heating rate per unit volume, change rate in the electron fraction, gravitational constant, and the PNS mass, respectively. The outer boundary is set to the sufficiently distant radius from the PNS center, and the mass accretion rate through the outer boundary is set by hand. The central PNS is excised, and the region from the PNS surface to the outer boundary is considered. How to determine the PNS radius is described later.

The neutrino reactions Q and Γ are treated with so-called light-bulb method, in which the neutrino heating and cooling rates are calculated locally with given neutrino luminosity and temperature. Here, I employ the light-bulb method described in Ohnishi et al. (2006). For simplicity, let me call Γ the reaction rate. Only the reactions of absorption and emission by free nucleons, $\nu_{\rm e}+{\rm n} \leftrightarrow {\rm e}^-+{\rm p}$ and $\bar{\nu}_{\rm e}+{\rm p} \leftrightarrow {\rm e}^++{\rm n}$, are considered. Considering the Pauli blocking of neutrinos, the neutrino heating rate Q_i and reaction rate Γ_i of each reaction ($i=\nu_{\rm e}$ for the former reaction and $i=\bar{\nu_{\rm e}}$ for the latter reaction) are calculated as

$$Q_i = -\frac{4\pi}{(2\pi)^3}\int_0^\infty {\rm d}\epsilon\epsilon^3\{(1-f_i(r,\epsilon))j_i(\epsilon)-\kappa_i(\epsilon)f_i(r,\epsilon)\} \tag{2.58}$$

and

$$\Gamma_i = s\frac{m_{\rm u}}{\rho}\frac{4\pi}{(2\pi)^3}\int_0^\infty {\rm d}\epsilon\epsilon^2\{(1-f_i(r,\epsilon))j_i(\epsilon)-\kappa_i(\epsilon)f_i(r,\epsilon)\}, \tag{2.59}$$

respectively, where

$$s = \begin{cases} -1 & (\text{for } \nu_{\rm e}) \\ 1 & (\text{for } \bar{\nu_{\rm e}}) \end{cases}. \tag{2.60}$$

With these heating and reaction rates, $Q=Q_{\nu_{\rm e}}+Q_{\bar{\nu_{\rm e}}}$ and $\Gamma=\Gamma_{\nu_{\rm e}}+\Gamma_{\bar{\nu_{\rm e}}}$. The neutrino absorptivity κ_i and emissivity j_i are defined by

$$\kappa_{\nu_{\rm e}}(\epsilon) = \sigma_{\nu_{\rm e},{\rm n}}[1-F_{\rm e}^-(\epsilon+\Delta)]\times 2\int\frac{{\rm d}^3p}{(2\pi)^3}F_{\rm n}(\epsilon)[1-F_{\rm p}(\epsilon)], \tag{2.61}$$

$$j_{\nu_{\rm e}}(\epsilon) = \exp\left\{-\frac{\epsilon-(\mu_{\rm p}-\mu_{\rm n}+\mu_{\rm e})}{T}\right\}\kappa_{\nu_{\rm e}}(\epsilon), \tag{2.62}$$

$$\kappa_{\bar{\nu_{\rm e}}}(\epsilon) = \sigma_{\bar{\nu_{\rm e}},{\rm p}}[1-F_{\rm e^+}(\epsilon-\Delta)]\times 2\int\frac{{\rm d}^3p}{(2\pi)^3}F_{\rm p}(\epsilon)[1-F_{\rm n}(\epsilon)], \tag{2.63}$$

and

$$j_{\bar{\nu_{\rm e}}}(\epsilon) = \exp\left\{-\frac{\epsilon-(\mu_{\rm n}-\mu_{\rm p}-\mu_{\rm e})}{T}\right\}\kappa_{\bar{\nu_{\rm e}}}(\epsilon), \tag{2.64}$$

respectively, where F_j and μ_j are the Fermi-Dirac distribution function and chemical potential of particle j, respectively, $\sigma_{\nu_{\rm e},{\rm n}}$ and $\sigma_{\bar{\nu_{\rm e}},{\rm p}}$ are the cross sections of reactions defined in equations (2.48) and (2.49), respectively, Δ is the mass difference between the neutron and proton. The Pauli blocking of nucleons, electrons, and protons are considered contrary to equation (2.52). The distribution function of $\nu_{\rm e}$ and $\bar{\nu_{\rm e}}$ is defined as

$$f_{\nu_{\rm e}/\bar{\nu_{\rm e}}} = \frac{1}{1+\exp(\epsilon/T_{\nu_{\rm e}/\bar{\nu_{\rm e}}})}\frac{1-\sqrt{1-(r_{\nu_{\rm e}/\bar{\nu_{\rm e}}}/r)^2}}{2}, \tag{2.65}$$

the black body radiation from the neutrinosphere. The temperatures of neutrinos from neutrinosphere are set to be $T_{\nu_{\rm e}}=4\,{\rm MeV}$ for $\nu_{\rm e}$ and $T_{\bar{\nu_{\rm e}}}=5\,{\rm MeV}$ for $\bar{\nu}_{\rm e}$, respectively. The neutrinospheric radius r_ν is determined by the condition $L_{\nu_{\rm e}/\bar{\nu_{\rm e}}}=\frac{7}{16}\pi r^2_{\nu_{\rm e}/\bar{\nu_{\rm e}}}\sigma T^4_{\nu_{\rm e}/\bar{\nu_{\rm e}}}$, and then the radius of the PNS surface is set to r_ν.

With this preparation, now let me describe the construction of the steady-state solution. First, the stalled shock radius $r_{\rm s}$ is assumed. Since the upstream matter freely infalls, its velocity is given by the free-fall velocity at the shock $v=\sqrt{GM_{\rm PNS}/r_{\rm s}}$. With

the given mass accretion rate, the density is determined through $\dot{M} = 4\pi r_{\rm s}^2 \rho v$. Other thermodynamical quantities such as the specific entropy and electron fraction are also assumed appropriately. These conditions give the upstream values, and downstream values are determined by the Rankine-Hugoniot condition. Equations (2.53—2.56) is solved from just downstream of the shock to the PNS surface, i.e., the neutrinospheric radius r_ν. In general, this procedure leads inconsistency at the neutrinosphere: the density other than $10^{11}\,{\rm g\,cm^{-3}}$. Then, this procedure is repeated by changing the stalled shock radius $r_{\rm s}$, until the density at the neutrinosphere becomes $10^{11}\,{\rm g\,cm^{-3}}$. Finally, the steady-state solution is obtained.

What Burrows & Goshy (1993) found is that the steady-state solution cannot be constructed for large neutrino luminosity. They interpreted it as the shock revival since the large neutrino luminosity is the key in the absence of the steady-state. Moreover, for a given mass accretion rate, there is a critical value of the neutrino luminosity above which the steady-state solution does not exist. The critical curve is the curve drawn in a parameter plane spanned by the mass accretion rate and neutrino luminosity and connects the critical neutrino luminosities of each mass accretion rate. This critical curve separates the models which succeed in the shock revival or not. Their results provide us a useful insight that whether the neutrino heating mechanism works or not is determined by the balance between the ram pressure of the accretion flow, which suppresses the shock, and the thermal pressure of the post-shock matter heated by the neutrinos, which pushes the shock.

The diagnostics for the shock revival

There are several diagnostics to predict the shock revival. The timescale ratio is one of the useful diagnostics for the shock revival and first pointed out by Thompson et al. (2005). It is defined by the advection timescale of the gain layer divided by the heating timescale of the gain layer. Although there are some definitions of the advection and heating timescales, they are essentially defined by

$$\tau_{\rm adv} := \frac{M_{\rm gain}}{\dot{M}} \tag{2.66}$$

and

$$\tau_{\rm heat} := \frac{E_{\rm gain}}{Q}, \tag{2.67}$$

respectively, where $\dot{M}$, $E_{\rm gain}$, and Q are the mass accretion rate, the total energy including the gravitational binding energy, and the heating rate by the neutrino absorption, respectively. Therefore the timescale ratio is

$$\frac{\tau_{\rm adv}}{\tau_{\rm heat}} = \frac{M_{\rm gain} Q}{E_{\rm gain} \dot{M}}. \tag{2.68}$$

If this ratio exceeds unity, the fluid element gets enough amount of energy to be unbound from the gravitational potential well before going through the gain layer completely to sink into the cooling layer and hence the shock revives.

Another useful diagnostic is the antesonic condition suggested by Pejcha & Thompson (2012). The antesonic factor is defined by them as $a^2/v_{\rm esc}^2$, where a and $v_{\rm esc}$ are the sound speed and escape velocity, respectively. From the spherically symmetric isothermal accretion flow and the steady flow with the stalled shock and neutrino heating, they found that when the maximum value of the antesonic factor with respect to the radius exceeds a certain value, the steady-state solution no longer exists. For the flows with the neutrino heating, the critical value is ~ 0.2. This is called the antesonic condition.

Numerical simulations in multi-dimensions

The discussion about the gain radius and the critical curve is understood by rather simple models, but whether this mechanism works successfully or not is only accessible by numerical simulations. However, the numerical simulations of CCSNe are very tough works. One reason is that the computational cost of the neutrino transfer is very expensive. Since the neutrinos interact with matter only via the weak force, they are in equilibrium with matter only deep inside the PNS. For the post-shock region, where the heating by the neutrinos is crucially important for the mechanism, the matter is neither optically thick nor thin for the neutrinos. For such semi-transparent neutrinos, we should consider the behavior of the neutrinos in the six-dimensional (6D) phase space (three in the configuration and three in the momentum), that is, we should solve the Boltzmann equation for the neutrinos. Since solving this 6D equation requires very high computational cost, even the most sophisticated supercomputers in the world cannot fully treat this problem. Another reason for the difficulty in the CCSNe simulations is the treatment of gravity. The PNS is a compact object whose Schwarzschild radius is a few–ten percent of the PNS radius. Therefore, the general relativistic effects are non-negligible. However, the general relativistic simulation is complicated, and only a few works consider it.

Although Wilson (1985) discovered successful explosion under spherical symmetry, the failure of the CCSNe under spherical symmetry is the consensus of recent CCSNe researchers. After Wilson (1985), many supernova modelers tried to reproduce the shock revival in their simulations. All of them except for Kitaura et al. (2006) failed. Kitaura et al. (2006) found a successful shock revival under the spherical symmetry, but the progenitor of their simulation is the almost light end of massive stars whose fate is the core-collapse. Therefore, for the main population of the CCSNe progenitors, the explosion fails in 1D. The deterministic simulations under spherical symmetry are performed by Liebendörfer et al. (2001); Sumiyoshi et al. (2005). Contrary to other works, they included the Boltzmann neutrino transport and the general relativistic gravity to their spherically symmetric code. Since these full Boltzmann simulations show the failure of the shock revival, it is known that the spherically symmetric CCSNe do not explode except for the light progenitors.

After the consensus that the CCSN does not explode in 1D is obtained, multi-dimensional CCSNe simulations have been performed. From the early 1990s, a lot of 2D axisymmetric simulations have been reported (Herant et al., 1994; Burrows et al., 1995; Buras et al., 2003b, 2006; Marek & Janka, 2009; Müller et al., 2012; Bruenn et al.,

2013; Dolence et al., 2015; Summa et al., 2016; Bruenn et al., 2016; O'Connor & Couch, 2018). Thanks to these simulations, it is realized that the multi-dimensional effect such as fluid instability is crucial for the neutrino heating mechanism to work. Indeed, some simulations obtain successful shock revivals with the help of the multi-dimensional effect. There are two classes of fluid instability: the convection and the standing accretion shock instability (SASI).

According to the Schwarzschild's criterion, the convection occurs when the negative entropy gradient emerges. This is easily achieved in CCSNe: since the accreting matter flows inward with being heated by neutrinos, the matter at the more inner part is heated for a longer time and has higher entropy. Thus it may seem natural for the convection to occur, but sometimes it fails due to the advection. Qualitatively speaking, if the timescale of the advection, which is defined by the timescale for the matter to flow across the gain layer, is smaller than the growth timescale of the convection, the convection does not grow before the matter is swallowed by the cooling layer, where the entropy gradient is positive. This is investigated by Foglizzo et al. (2006) in the linear regime of the perturbation. In their paper, the ratio of the advection timescale to the convection timescale is denoted by χ and called (Foglizzo's) χ parameter. Quantitatively, when this χ parameter exceeds three, the convective instability develops.

In addition to the neutrino-driven convection, there exists convection at an earlier stage of the CCSNe. Soon after the bounce, the bounce shock propagates with losing its energy as discussed at the beginning of section 2.2. Since the strength of the shock is also weakened with the propagation, the negative entropy gradient is formed, and the matter is unstable to the convection. This convection is called the prompt convection because it immediately follows the core bounce (e.g., Bruenn & Mezzacappa, 1994). Note that this convection finally settles down due to the absence of the energy source to persist the instability, but in turn, it serves as a perturbation seed for the neutrino-driven convection at the later stage.

As for convection, there is another criterion, called Ledoux's criterion. In this criterion, not only the entropy gradient but also the composition gradient is also considered. Of course, this criterion is a generalization of the Schwarzschild's criterion. In the situations discussed above, the composition gradient plays a minor role compared to the entropy gradient. However, inside the PNS, the convection originated from this criterion develops, called the PNS convection (Keil et al., 1996). The concrete form of the Ledoux's criterion is that when

$$\left(\frac{\partial\rho}{\partial s}\right)_{P,Y_\mathrm{e}}\left(\frac{\mathrm{d}s}{\mathrm{d}r}\right)+\left(\frac{\partial\rho}{\partial Y_\mathrm{e}}\right)_{P,s}\left(\frac{\mathrm{d}Y_\mathrm{e}}{\mathrm{d}r}\right)>0, \tag{2.69}$$

the matter is unstable for the convection. Usually, the derivatives with respect to the thermodynamic variables are

$$\left(\frac{\partial\rho}{\partial s}\right)_{P,Y_\mathrm{e}}<0, \quad \left(\frac{\partial\rho}{\partial Y_\mathrm{e}}\right)_{P,s}<0. \tag{2.70}$$

On the surface of the PNS, the entropy gradient is positive, but the composition gradient is negative. The positive entropy gradient is formed at the core bounce. The negative

composition gradient is originated from the neutrino diffusion. Since inside the PNS the matter is optically thick to neutrinos, the neutrinos escape only from the surface of the PNS. When the neutrinos escape, the Pauli blocking of the electron capture process is relaxed, and the electrons are converted to the neutrinos. As a consequence, the electron fraction at the surface of the PNS is less than that inside the PNS. This forms the negative composition gradient, and thanks to this, the PNS is convectively unstable. The PNS convection dredges up the neutrino-rich matter inside the PNS and enhances the neutrino luminosity. Therefore, the PNS convection has a positive role for the neutrino heating mechanism.

When the χ parameter is less than three, the convection does not develop. Instead, another class of fluid instability, SASI, develops. The SASI is the large-scale oscillatory or rotational deformation of the shock. It is characterized by the oscillation in the expansion coefficient $a_{\ell m}(t)$ of the angle-dependent shock radius $r_{\rm sh}(t,\theta,\phi)$ by the spherical harmonics $Y_{\ell m}$ with $\ell = 1$–2: $r_{\rm sh}(t,\theta,\phi) = \sum_{\ell,m} a_{\ell m}(t) Y_{\ell m}(\theta,\phi)$. When all three coefficients of $\ell = 1$ spherical harmonics with different m oscillate in phase, the shock presents just a back-and-forth motion called the sloshing mode; when the coefficients oscillate out of phase, the shock shows rotation-like motion called the spiral mode. The SASI itself is found in the context of the black hole accretion by Foglizzo (2002), and then Blondin et al. (2003) suggested that the SASI occurs in the context of CCSNe. The mechanism of the SASI is not fully understood, but the leading hypothesis is the advective-acoustic cycle (Foglizzo et al., 2007). If the spherical shock is deformed slightly, the radially accreting shock is refracted, and then the vorticity is produced. This vortex advects to the PNS surface, where the background density and so on sharply change, and is dissipated there. At that time, the acoustic wave is launched from there to the shock. When this acoustic wave reaches the shock, the shock is deformed further.

Whichever fluid instability develops, it eventually grows to the turbulence. At the first stage of the fluid instability the perturbations are in the linear regime. After that the perturbations become non-linear and complex turbulence. It is this turbulence that plays the vital role for the neutrino heating mechanism. There are several ways for the turbulence to help the mechanism: the turbulent mixing, turbulent pressure, and extension of the gain layer.

First, the turbulence induces the large-scale mixing. For a similar reason to the formation of the negative entropy gradient which drives the neutrino-driven convection, the deeper matter is hotter. The turbulent mixing dredges up the hot deep matter to the region just behind the shock. Therefore the internal energy and hence the pressure just behind the shock gets higher, which results in further expansion of the shock (Yamasaki & Yamada, 2006).

Second, the turbulence itself has a kind of pressure called the Reynolds stress (Murphy & Meakin, 2011; Murphy et al., 2013). The turbulent flow is analyzed by the Reynolds decomposition. Noting that the turbulence can be regarded as a collection of eddies, the Reynolds averaging is defined by the averaging of a fluid quantity over the eddy spatial scale and the eddy turnover timescale. Then, a fluid quantity q with turbulence can be

decomposed into $q = q_0 + q'$, where $q_0 = \langle q \rangle$ with $\langle \cdot \rangle$ being the Reynolds average of the quantity $\cdot$. The quantity with the prime symbol is the fluctuation whose Reynolds average is zero. With this decomposition in mind, the Reynolds stress tensor is defined by the tensor product of the two velocity fluctuations, $\overleftrightarrow{R} = \overrightarrow{v'} \otimes \overrightarrow{v'}$. The shock radius can be estimated from the Rankine-Hugoniot condition and the extrapolations of the fluid profiles. For the angle averaged shock radius, Murphy et al. (2013) found that the estimated shock radius without the Reynolds stress is smaller than the actual shock radius, but by including the Reynolds stress, the estimated shock radius expands and successfully reproduces the actual shock radius. This result indicates that the turbulent pressure pushes the shock outward and helps the shock revival.

Finally, as Takiwaki et al. (2012) visually indicated, the lateral motion induced by the turbulence increases the dwell time in the gain region. Due to this increase, the total amount of the neutrino heating per fluid element before sinking into the cooling layer is enhanced, helping the shock revival by the neutrino heating mechanism. From the viewpoint of the diagnostic, the advantageous effect of this lateral motion is realized in the timescale ratio discussed above. The dwell time is related to the mass in the gain layer (gain mass) $M_{\rm gain}$, which emerges in the timescale ratio (equation (2.68)). The increase of the dwell time results in the increase of the gain mass and hence the increase in the timescale ratio, which leads to the successful explosion.

In addition to the turbulent effect discussed above, multi-dimensionality has another positive role for the shock revival. Not only the internal energy which the PNS gets at the core bounce but also the accretion of the matter into the PNS during the stalled shock phase is the energy source of the neutrinos. If the spherical symmetry is imposed, once the shock starts to expand, the accretion luminosity, i.e., the energy released with the matter accretion per unit time becomes zero since no matter accretes to the PNS. Therefore the neutrino luminosity drops significantly, and the shock is no longer heated. On the other hand in multi-dimensional flow, both shock expansion to one direction and the matter accretion from the other direction are simultaneously realized, and hence the expanding shock can be heated further by the continual neutrino luminosity.

Supernova modelers report not only 2D but also 3D simulations recently (Fryer & Warren, 2002; Takiwaki et al., 2012; Hanke et al., 2013; Takiwaki et al., 2014; Tamborra et al., 2014; Lentz et al., 2015; Melson et al., 2015; Müller, 2015; Kuroda et al., 2016b; Ott et al., 2017; Vartanyan et al., 2019). Nature is, of course, 3D and there are several qualitative differences between 2D and 3D. First, the scale of the turbulence is different. In 3D turbulence, energy cascade from large to small scales is realized according to Kolmogorov's theory Kolmogorov (1941a,b). On the other hand, inverse energy cascade from small to large scales occurs instead in 2D (Kraichnan, 1967). As a consequence, small-scale eddies are dominant in 3D whereas large-scale eddies are dominant in 2D. Second, only the sloshing mode of SASI activity arises in 2D flow due to the presence of symmetry axis, while both sloshing and spiral modes emerge in 3D. How the difference between 2D and 3D affects the explosion properties, for example, shock evolution and explosion energy is not concluded yet.

Although some of the multi-dimensional simulations show shock revival, there still are some puzzles. First, there are simulations whose progenitor model is the same but whether the shock revives or not is different. Second, even though the model successfully explodes, the explosion energy is only $\sim 10\%$ of the observed energy (10^{51} erg). Bruenn et al. (2013, 2016) suggested that by performing the long-term simulations exceeding 1 s, the explosion energy increase to reach the observed explosion energy. Since almost all of these multi-dimensional simulations are truncated at several hundreds of millisecond, they all may reproduce enough energy if the simulation time is extended. On the other hand, recently Suwa et al. (2017) suggested that not enough amount of ^{56}Ni, which illuminate the supernova itself by radioactive decay, for the observed photon luminosity is produced with the multi-dimensional CCSNe simulations. Therefore it is now considered that the current CCSNe simulations lack other important physical processes. It is often called the missing physics.

Current status and updates in simulations

One possible missing physics is the stellar rotation. Observations imply that massive stars are rotating (Maeder & Meynet, 2012, for a review). Many NSs are observed as pulsars. The origin of pulsar spin is mainly the rotation of progenitor core. Thus it is natural to consider the collapse of rotating stellar core. Although progenitor models of rotating stars are proposed, a common way to consider rotating CCSNe is to impose rotational velocity artificially on non-rotating progenitor models at the onset of collapse. The rotational law is taken from Eriguchi & Müller (1984); Zwerger & Mueller (1997); Ott et al. (2004): it is a cylindrical rotation profile

$$\Omega = \frac{\Omega_0}{1 + (r \sin\theta / r_0)^2}, \tag{2.71}$$

where Ω_0 is the rotational velocity at center and r_0 is the radius of the rigidly rotating core, and r and θ are the coordinates of spherical coordinates. On the other hand, some supernova modelers employ shellular profile

$$\Omega = \frac{\Omega_0}{1 + (r / r_0)^2}, \tag{2.72}$$

which is resulted from turbulence. The size of the rigid core r_0 can be freely chosen but is commonly set to $r_0 = 1000$ km. The central rotational velocity Ω_0 is also free to choose, but according to Heger et al. (2000), it is $\mathcal{O}(1)\,\mathrm{rad\,s^{-1}}$ at most. In addition, if the stellar magnetic field is considered (Heger et al., 2005), the rotational velocity is much smaller ($\mathcal{O}(10^{-1}$–$10^{-2})\,\mathrm{rad\,s^{-1}}$).

Stellar rotation affects the dynamics of CCSN in both positive and negative ways. Ram pressure along the equatorial plane is reduced due to centrifugal force, and hence the critical neutrino luminosity is also reduced (Yamasaki & Yamada, 2005; Iwakami et al., 2014). Again due to centrifugal force, the released gravitational energy is reduced, and the explosion becomes difficult (Yamada & Sato, 1994). PNS is extended due to centrifugal force. The neutrino energy is hence reduced, and the heating rate is reduced (Summa

reaction name	reaction formula
electron capture on nucleon	$\nu_{\rm e} + {\rm n} \leftrightarrow {\rm e}^- + {\rm p}$
anti-electron capture on nucleon	$\bar{\nu_{\rm e}} + {\rm p} \leftrightarrow {\rm e}^+ + {\rm n}$
electron capture on nuclei	$\nu_{\rm e} + A \leftrightarrow {\rm e}^- + A'$
nucleon scattering	$\nu + N \leftrightarrow \nu + N$
coherent scattering	$\nu + A \leftrightarrow \nu + A$
electron scattering	$\nu + {\rm e}^- \leftrightarrow \nu + {\rm e}^-$
pair annihilation	$\nu + \bar{\nu} \leftrightarrow {\rm e}^- + {\rm e}^+$

Table 2.3. The standard set in Bruenn (1985). Symbols A, A', N, ν, and $\bar{\nu}$ are a nucleus, another kind of nucleus, nucleon, some type of neutrinos, and some type of anti-neutrinos, respectively. For the three scattering reactions, the symbol ν includes both neutrinos and anti-neutrinos, while for the pair annihilation ν and $\bar{\nu}$ only represent neutrinos and anti-neutrinos, respectively.

et al., 2018). Centrifugal force makes PNS oblate, and the temperature on the equator is lower than that of the north/south-poles. This results in anisotropic neutrino heating: neutrino heating rate is lower on the equatorial plane because of lower temperature on the equator of PNS and smaller solid angle of oblate PNS (Kotake et al., 2003). This anisotropic heating leads to a jet-like explosion. On the other hand, Walder et al. (2005) suggested that the anisotropy of neutrino heating is less prominent since the collection of neutrinos originating from various points reduces anisotropy. In 3D, a bar-like mode instability called "low-$T/|W|$ instability" (Shibata et al., 2002, 2003) develops to help neutrino heating and transfer the energy from deep inside (Takiwaki et al., 2016). Since centrifugal force both enhances and suppresses shock revival, how rotation affects CCSN should be investigated further.

Another possible missing physics is the progenitor asphericity. The standard assumption of the stellar evolution model is that the star is quasi-static: the hydrostatic equilibrium is achieved at a given time. The convection sometimes occurs due to the large energy production by the nuclear reactions in the stellar evolution. Since the convection is a dynamical process, hydrostatic equilibrium is broken, but by exploiting the so-called mixing length theory (MLT), the dynamical transfer of the matter is treated in the framework of the quasi-static evolution. However, for the last stage of the stellar evolution, the violent convection emerges, and the MLT does not work well. Such violent convection imprints an aspherical fluctuation on the stellar core (Arnett & Meakin, 2011). If the core with such fluctuation collapses, the fluctuation works as the perturbation seed for the turbulence (Couch & Ott, 2015; Müller & Janka, 2015). In short, by considering the violent convection at the last phase of the stellar evolution, the turbulence in the shock may be enhanced.

Microphysics like neutrino reactions is also one of possible missing physics. Modifications to the neutrino reaction rates may play crucial roles for the neutrino heating mechanism. So far, the so-called standard set of neutrino reactions are mainly consid-

ered. The standard set is the neutrino reaction sets considered in Bruenn (1985). The list of reactions is presented in table 2.3. In addition, several reaction processes are considered; the nucleon-nucleon bremsstrahlung (Friman & Maxwell, 1979; Maxwell, 1987): $N + N \leftrightarrow N + N + \nu + \bar{\nu}$; the neutrino pair-annihilation into another neutrino pair (Buras et al., 2003a): $\nu_{\rm e} + \bar{\nu_{\rm e}} \leftrightarrow \nu_{\mu/\tau} + \bar{\nu_{\mu/\tau}}$; and the neutrino scattering (Buras et al., 2003a): $\nu_{\rm e}(\bar{\nu_{\rm e}}) + \nu_{\mu/\tau} \leftrightarrow \nu_{\rm e}(\bar{\nu_{\rm e}}) + \nu_{\mu/\tau}$.

Besides, the reaction rates in Bruenn (1985) utilize some approximations. The electron capture rate on a nucleus is only considered for limited kinds of nuclei. Langanke & Martínez-Pinedo (2000); Langanke et al. (2003); Juodagalvis et al. (2010) updated the capture rate on a broader range of nuclei. For the electron/anti-electron capture on the nucleon, the nucleon is assumed to be heavy enough, and its recoil is neglected. Horowitz (2002) included the recoil into the reaction rate. They also incorporated the weak magnetism contribution to the reaction. Finally, Bruenn (1985) only considered the reaction of the free neutrinos and the free particles, while in the real situations the nucleons are interacting with other particles. Such in-medium effects are also considered partially so far: Martínez-Pinedo et al. (2012) included the mean field potential of the nucleons, which results in the enhancement in the $\nu_{\rm e}$ absorption and the suppression in the $\bar{\nu_{\rm e}}$ absorption; Fischer et al. (2016) suggested that the axial coupling constant is changed due to interaction with other particles; Horowitz et al. (2016) considered the many-body correction with which the spin-flip reaction is suppressed due to the formation of spin-triplet of nucleons. The reactions discussed above does not distinguish the reactions of the μ-type neutrinos and the τ-type neutrinos because the temperature in CCSNe is thought to be too low to produce the μ particles. However, the high energy tail of the thermal distributions may produce the μ particles as discussed in Bollig et al. (2017). By considering the μ particle production, the EOS effectively gets softer since the thermal energy is consumed by the particle production. When the μ particle production is considered, the reaction rates around μ-type neutrinos should be individually considered.

These modifications to the neutrino reaction rates are minor. For example, Kotake et al. (2018) considered almost all of the modifications discussed above (not all and a few reactions which are not discussed above is also included) and performed spherically symmetric simulations. It results in the enhancement of the heating rate by several tens of percent. The enhancement may change the failed model into the successful model if the failed model is about to explode, e.g., according to the timescale ratio. However, this enhancement may not resolve the puzzle around the ^{56}Ni.

The general relativistic (GR) gravity is another important physics for the CCSNe. The numerical simulation of the spacetime metric is called the numerical relativity. The numerical relativity is developed and widely utilized (Shibata & Nakamura, 1995; Baumgarte & Shapiro, 1999), producing amazing results especially of the binary compact star merger (Shibata & Taniguchi, 2006, for example). The numerical relativity widely used is based on the $3 + 1$ decomposition of the spacetime, in which the spacetime is described as the collection of 3D hypersurface with different times. The $3+1$ decomposed metric is written

as

$$\mathrm{d}s^2 = -\alpha^2 \mathrm{d}t^2 + \gamma_{ij}(\mathrm{d}x^i + \beta^i \mathrm{d}t)(\mathrm{d}x^j + \beta^j \mathrm{d}t), \tag{2.73}$$

where α, β^i, and γ_{ij} are the lapse function, the shift vector, and the spatial metric, respectively. The lapse function describes the interval of adjacent hypersurfaces. The shift vector indicates the drift of spatial coordinates. A timelike unit normal vector n^α perpendicular to a hypersurface is written as

$$n^\alpha = \left(\frac{1}{\alpha}, \frac{\beta^i}{\alpha}\right). \tag{2.74}$$

The spatial metric measures the distance on a hypersurface. In numerical relativity, these quantities are evolved with given gauge conditions.

Although the fully GR simulation is desirable for the CCSNe simulations, the difficulty in the numerical relativity technique prevents the supernova modelers from exploiting them. In addition, roughly speaking, the CCSNe are spherical systems, and hence the spherical coordinate is suitable for the CCSNe simulations. However, the spherical coordinate has the coordinate singularities at the center and along the polar axis. These singularities are harmful to the numerical relativity. In order to avoid them, only the Japan-Basel group developed a fully GR CCSNe code in the Cartesian coordinates (Kuroda et al., 2012, 2014, 2016a,b).

Recently Baumgarte et al. (2013) suggested a scheme of numerical relativity in the spherical coordinates. The coordinate singularity arises from the difference between the coordinate bases and local orthonormal bases. Consider a spherical coordinate in a flat spacetime. Then, the coordinate bases are ∂_r, ∂_θ, and ∂_ϕ and the orthonormal bases are $e_r = \partial_r$, $e_\theta = \partial_\theta / r$, and $e_\phi = \partial_\phi / r \sin\theta$. Then if a tensor component of a physical quantity is regular with respect to the orthonormal basis, the component with respect to the coordinate basis is not necessarily regular. This is the origin of the coordinate singularity. In Baumgarte et al. (2013), dependent variables to be solved is expressed with the orthonormal basis. With this treatment, the singular factors $1/r$ and $1/r\sin\theta$ are explicitly present in equations, and they are analytically treated. Thanks to this analytical differentiation, Singular behavior is suppressed, and numerical relativity in spherical coordinates successfully works. Although this scheme is developing gradually (Montero et al., 2014; Baumgarte et al., 2015; Ruchlin et al., 2018; Mewes et al., 2018), CCSN simulations with this scheme have not been performed yet.

Instead of the full GR approach, several approximate methods are suggested. The simplest and widely-used one is to replace the monopole component of the Newtonian gravity by the solution of the Tolman-Oppenheimer-Volkoff equation (Case A in Marek et al., 2006). More complicated but realistic one is the conformal flat approximation (Wilson et al., 1996; Isenberg, 2008), where the spatial part of the metric tensor is proportional to the flat space metric. The biquadratic root of the proportionality coefficient is called the conformal factor. The application to the CCSNe simulation is developed by Dimmelmeier et al. (2005); Müller et al. (2010).

One of the reasons why simulation results are different from group to group is possibly they use different approximation method in their codes. The most significant difference

is in the neutrino transport. Neutrinos rarely interact with matter and hence not in the equilibrium state. It is required to solve neutrino transport with the Boltzmann equation. The Boltzmann equation for neutrinos written in the covariant form in 4D spacetime is (Lindquist, 1966)

$$\frac{\mathrm{d}x^\alpha}{\mathrm{d}\tau}\frac{\partial f}{\partial x^\alpha}\bigg|_{p^i} + \frac{\mathrm{d}p^i}{\mathrm{d}\tau}\frac{\partial f}{\partial p^i}\bigg|_{x^\alpha} = (-p^\alpha \hat{u}_\alpha) S_{\mathrm{rad}}, \tag{2.75}$$

where $x^\alpha = (t, x^i)$, p^i, τ, f, $\hat{u}^\alpha$, and S_{rad} are coordinates in the spacetime, those in the momentum space, affine parameter of neutrino, distribution function of neutrinos, a time-like vector (e.g., the four-velocity of matter or normal vector to the spatial hypersurface of $3+1$ decomposed spacetime), and collision term. A numerical scheme in which the Boltzmann equation is directly discretized is called the S_N scheme. This seven-dimensional equation requires a significant amount of computational cost. Due to limited computing resources, supernova modelers approximate the Boltzmann equation. There are two classes of approximation: one is related to the momentum space distribution, and the other is related to the configuration space distribution.

For the approximation of the momentum space distribution, a common way is to solve the moment equations. By taking the angular moments of the Boltzmann equation, the equations for the energy density, energy flux, and stress tensor (Eddington tensor), and so on are obtained. By assuming some closure relations, these moment equations are solved. A scheme to solve only first order moment equation with closure relation between the energy density and flux is called flux-limited diffusion scheme (e.g., Burrows et al., 2006, 2007b). A scheme to evolve both the energy density and flux by solving up to first order moment equations with analytic closure relation among the Eddington tensor and energy density and flux is often called M1-closure scheme (e.g., Kuroda et al., 2012; Just et al., 2015). Some researchers use a simplified Boltzmann equation to obtain the numerical closure relation for the Eddington factor. This scheme is called variable Eddington factor scheme (e.g., Rampp & Janka, 2002). Another way to approximate the Boltzmann equation is isotropic diffusion source approximation (IDSA; Liebendörfer et al., 2009). In this approximation, the distribution function is decomposed into the free-streaming part and matter-trapped part. They are evolved individually, and exchange of neutrinos between two parts are described by diffusion source term.

Since I pay particular attention to the M1-closure method in chapter 3, I describe the M1-closure method in detail here. The M1-closure method is first proposed by Levermore (1984), and he employs two assumptions. The first assumption is that the neutrino distributions are axisymmetric with respect to the flux direction. The second assumption is related to the Eddington factor. The Eddington factor is defined as the largest eigenvalue of the second angular moment of the distribution function called the Eddington tensor, but it is assumed to be given by an approximate formula in the M1-closure method. Although approximation formulae with these assumptions are derived in Levermore (1984), the modern prescription presented in Shibata et al. (2011) is reviewed in the following. The latter is represented in the $3+1$ decomposed spacetime discussed above. Especially, how the Eddington tensor is determined is the focus of the following discussion.

The Eddington tensor is defined by

$$k^{ij}(\epsilon) := \frac{P^{ij}(\epsilon)}{E(\epsilon)}, \tag{2.76}$$

where

$$P^{ij}(\epsilon) := \gamma^i{}_\sigma \gamma^j{}_\rho M^{\sigma\rho}(\epsilon), \tag{2.77}$$

$$E(\epsilon) := n_\sigma n_\rho M^{\sigma\rho}(\epsilon). \tag{2.78}$$

Here, $\gamma^i{}_\sigma$ is the projection tensor onto the spatial hypersurface in the $3+1$ decomposed spacetime, and $M^{\sigma\rho}(\epsilon)$ is the second angular moment of the distribution function,

$$M^{\sigma\rho}(\epsilon) := \int f \delta\left(\epsilon - \epsilon'\right) p'^\sigma p'^\rho \epsilon' \mathrm{d}\epsilon' \mathrm{d}\Omega'_p. \tag{2.79}$$

In this definition, Ω'_p is the solid angle in the momentum space measured in the fluid-rest frame and $\epsilon' \mathrm{d}\epsilon' \mathrm{d}\Omega'_p = \mathrm{d}V'_p$ is the volume element in the momentum space. Note that the neutrino energy ϵ is measured in the fluid-rest frame.

On the other hand, the Eddington tensor in the M1-closure method

$$k^{ij}_{\mathrm{M1}}(\epsilon) := \frac{P^{ij}_{\mathrm{M1}}(\epsilon)}{E(\epsilon)} \tag{2.80}$$

is calculated by using the formula

$$P^{ij}_{\mathrm{M1}} := \frac{3\zeta(\epsilon) - 1}{2} P^{ij}_{\mathrm{thin}}(\epsilon) + \frac{3(1-\zeta(\epsilon))}{2} P^{ij}_{\mathrm{thick}}(\epsilon). \tag{2.81}$$

Here, $\zeta(\epsilon)$ is the Eddington factor and approximated by Levermore (1984) as

$$\zeta(\epsilon) = \frac{3 + 4\bar{F}(\epsilon)^2}{5 + 2\sqrt{4 - 3\bar{F}(\epsilon)^2}}, \tag{2.82}$$

where $\bar{F}(\epsilon)$ is the flux factor. The flux factor is defined in the fluid-rest frame by

$$\bar{F}(\epsilon) = \sqrt{\frac{h_{\sigma\rho} H^\sigma(\epsilon) H^\rho(\epsilon)}{J(\epsilon)^2}}, \tag{2.83}$$

where

$$h_{\sigma\rho} := g_{\sigma\rho} + u_\sigma u_\rho, \tag{2.84}$$

$$J(\epsilon) := u_\sigma u_\rho M^{\sigma\rho}(\epsilon), \tag{2.85}$$

and

$$H^\sigma(\epsilon) := -h^\sigma{}_\rho u_\lambda M^{\sigma\lambda}(\epsilon) \tag{2.86}$$

are the spatial metric projected onto the fluid-rest frame, the energy density in the fluid-rest frame, and the energy flux in the fluid rest frame, respectively, with u^σ being the 4-velocity of the matter. In the M1-closure method, the optically thin limit value P^{ij}_{thin}

and thick limit $P^{ij}_{\rm thick}$ are smoothly connected as in equation (2.81). The thin and thick limits are defined by

$$P^{ij}_{\rm thin}(\epsilon) = E(\epsilon)\frac{F^i(\epsilon)F^j(\epsilon)}{F(\epsilon)^2}, \tag{2.87}$$

and

$$P^{ij}_{\rm thick}(\epsilon) = J(\epsilon)\frac{\gamma^{ij} + 4V^iV^j}{3} + H^i(\epsilon)V^j + V^iH^j(\epsilon), \tag{2.88}$$

respectively, where

$$F^i(\epsilon) := -\gamma^i{}_\sigma n_\rho M^{\sigma\rho}(\epsilon), \tag{2.89}$$

and $V^i := u^i/u^t$ are the energy flux in the laboratory frame and the 3D vector of the fluid velocity, respectively. Note that in equation (2.88), some correction terms whose order with respect to the local mean free path is higher than zero-th are neglected. In this dissertation, the k^{ij} and $k^{ij}_{\rm M1}$ are called "the Boltzmann-Eddington tensor" and "the M1-Eddington tensor", respectively.

In the above discussion, the approximation of the momentum space distribution is presented, while there is another class of approximation related to the configuration space distribution. The ray-by-ray(-plus) (RbR(+)) approximation (Buras et al., 2006) is often used in multi-dimensional simulations. In RbR approximation, neutrino transport under spherical symmetry is solved along each radial ray (Rampp & Janka, 2002). In RbR+, the advection of neutrinos due to the neutrino trapping phenomena at high densities is also incorporated (Buras et al., 2006).

Although these approximations are widely used, the accuracy of them is not well understood. The problem in explosion energy may result from inaccuracy of the approximation. To estimate the accuracy is hence one of the essential issues in CCSN explosion mechanism. In order to assess the accuracy, some groups start a collaboration to compare their numerical codes (O'Connor et al., 2018; Cabezón et al., 2018; Pan et al., 2019; Just et al., 2018; Glas et al., 2018). They compared the results of different neutrino transport scheme, the effect of RbR+, in 1D, 2D, and 3D. Although the differences among the codes are presented, the accuracy of each code is not yet obtained. A reference code which utilizes the S_N method without RbR+ in multi-dimension is required. Ott et al. (2008) developed a code with the S_N method. They solved, however, the Boltzmann equation only outside the PNS and applied the flux-limited diffusion scheme inside the PNS, and it is not satisfactory.

First principle simulations of CCSN

So far, recent progress in CCSN code is discussed. It is summarized in figure 2.1. By simulations with the full-Boltzmann neutrino transport (the S_N scheme) and full GR gravity, it is concluded that the shock revival fails under spherical symmetry (the upper left panel of figure 2.1). Next, supernova modelers moved on 2D, axisymmetric simulations. At that time some groups use Newtonian gravity, and some use approximate GR gravity such as Case A in Marek & Janka (2009) and conformal flat approximation (the upper right panel). After that, supernova modelers moved on 3D simulations without spatial

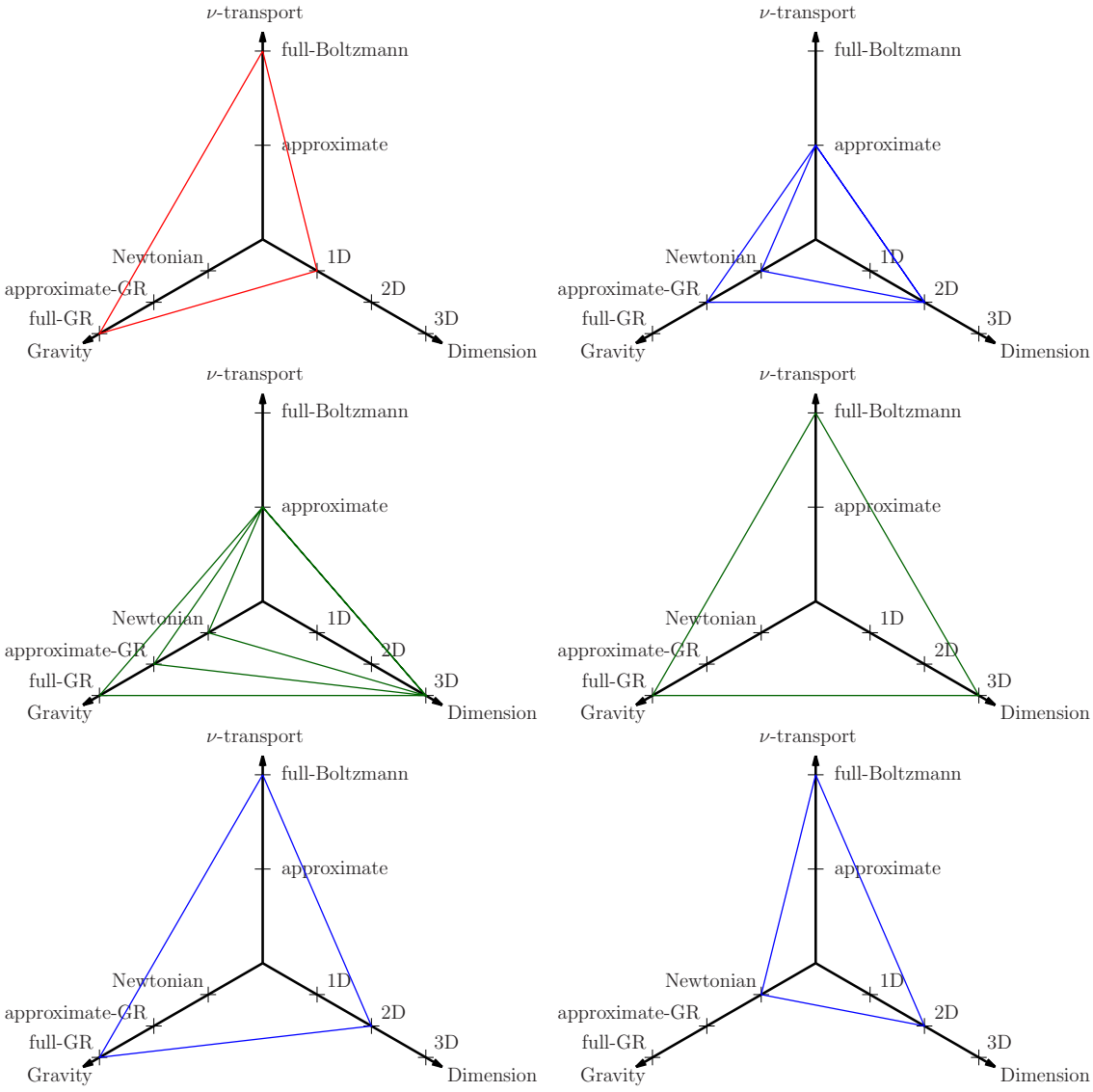

Figure 2.1. Recent progress in CCSN simulations. Each arrow shows how sophisticated physical processes are in CCSN simulations. Processes whose improvement is nontrivial are not shown here. The upper left panel indicates the most sophisticated 1D simulations. The upper right and middle left panels show recent 2D and 3D simulations, respectively. The middle right panel displays the first principle simulation, which is as sophisticated as possible. The lower left panel shows the first principle simulation in 2D and lower right indicates the current status of such 2D simulation.

symmetry. In this stage treatments of gravity ranges from Newtonian to full GR (the middle left panel). All of 2D and 3D simulations employ approximate neutrino transport. Ultimately, a code with sophisticated microphysics, general relativistic gravity, and the S_N method neutrino transport for 3D simulations is ideal (the middle right panel). In this dissertation let us call it the first principle code. Recent computational resources allows the first principle simulation in 2D to run, and it has been developed (the lower left panel).

Updating microphysics requires a deep understanding of nuclear force, and hence it is now underway. Currently, the best way is to collect the simulation results with various models of microphysics and to consider that the common results are robust. Contrary to microphysics, how to improve gravity and neutrino transport is clear since the basic equations are already well known. Indeed, the development of the first principle code has started with improving neutrino transport. Since the developing version of this code is used in this dissertation (the lower right panel), I review the code in detail.

First Sumiyoshi & Yamada (2012) developed a solver of multi-dimensional Boltzmann equation. They adopted spherical coordinates in order to impose spatial symmetry easily. They considered the flat spacetime with the fixed origin, and hence the Boltzmann equation (2.91) takes the form

$$\frac{\partial f}{\partial t} + \frac{1}{r^2}\frac{\partial}{\partial r}(r^2 \cos\theta_\nu f) + \frac{1}{r\sin\theta}\frac{\partial}{\partial \theta}(\sin\theta \sin\theta_\nu \cos\phi_\nu f) + \frac{1}{r\sin\theta}\frac{\partial}{\partial \phi}(\sin\theta_\nu \sin\phi_\nu f) - \frac{1}{r\sin\theta_\nu}\frac{\partial}{\partial \theta_\nu}(\sin^2\theta_\nu f) - \frac{\partial}{\partial \phi_\nu}\left(\frac{\cos\theta}{r\sin\theta}\sin\theta_\nu \sin\phi_\nu f\right) = S_{\rm rad}, \tag{2.90}$$

where θ_ν and ϕ_ν are the angles of the flight direction of the neutrino, in the laboratory frame. If axisymmetry is imposed, the fourth term in equation (2.90) automatically vanishes. If spherical symmetry is imposed, the third and sixth terms in the equation cancel. In order to guarantee this cancellation, the Boltzmann equation is carefully discretized. The differential terms are discretized by interpolation of the central and upwind differencing according to the local mean free path of neutrinos. Integration in time is performed implicitly, by using the Bi-CGSTAB method (Saad, 2003) with the point-Jacobi-preconditioner is used for the matrix inversion.

Second Nagakura et al. (2014) included special relativistic (SR) effect. This is indispensable to treat the neutrino trapping correctly. Consider neutrinos trapped by moving matter. In the fluid-rest frame, the neutrinos interact with matter frequently and are isotropically distributed. On the other hand in the laboratory frame, the neutrinos comove with matter and the distribution is not isotropic but peaked into the direction of matter motion. This is realized by relativistic aberration or beaming effect. The CCSN codes except for this code included the SR effect up to only first order in fluid velocity. This is because they solve the neutrino transport in the fluid-rest frame in order to simplify the collision terms. Since the expression of the advection terms (the left-hand side of equation (2.90)) in the fluid-rest frame is too complicated to implement, they truncated the velocity dependent terms higher than the first-order. Nagakura et al. (2014) included the effect up to full order by exploiting two-grid approach. They used a uniform grid in

the laboratory frame to evaluate the advection terms, whereas an essentially uniform grid in the fluid-rest frame to evaluate the collision terms.

Finally, Nagakura et al. (2017) implemented the moving-mesh technique. It is observed that some NSs have large proper motions. When the CCSNe explode anisotropically, NSs left should be kicked out due to momentum conservation. This is called the NS kick (e.g., Bray & Eldridge, 2016). Since the shock revival itself occurs anisotropically, the proper motion arises from the PNS phase. Since it is numerically difficult to treat PNS whose center deviates from the origin of the spherical coordinates, PNS center is artificially fixed on the coordinate center in almost all simulations (Marek & Janka, 2009). In the code reported in Nagakura et al. (2017), however, such artificial fixing is avoided. Instead, not an inertial frame but an acceleration frame is utilized to track the proper motion of PNS. Inertial force terms are added to hydrodynamics equations. The Boltzmann equation is, on the other hand, expressed in general spacetime and then drifting coordinates in the flat spacetime is employed.

The Boltzmann equation in general spacetime is equation (2.75). For numerical simulations, the conservative form of the equation is appropriate and it in $3+1$ decomposed spacetime is proposed by Shibata et al. (2014):

$$\frac{1}{\sqrt{-g}}\frac{\partial}{\partial x^\alpha}\bigg|_{q_i}\left[\left(e^\alpha_{(0)}+\sum_{i=1}^{3}\ell_{(i)}e^\alpha_i\right)\sqrt{-g}f\right]-\frac{1}{\epsilon^2}\frac{\partial}{\partial\epsilon}(\epsilon^3 f\omega_{(0)}) \\ +\frac{1}{\sin\theta_\nu}\frac{\partial}{\partial\theta_\nu}(\sin\theta_\nu f\omega_{(\theta_\nu)})+\frac{1}{\sin^2\theta_\nu}\frac{\partial}{\partial\phi_\nu}(f\omega_{(\phi_\nu)})=S_{\rm rad}, \tag{2.91}$$

where x^α, ϵ, θ_ν and ϕ_ν are the coordinates of the spacetime and momentum space, respectively, and g, $e^\alpha_{(\mu)}$ ($\mu=0,\,1,\,2,\,3$), and $\ell_{(i)}$ are the determinant of the spacetime metric, a set of the tetrad bases for a local orthonormal frame, and directional cosines for the neutrino-propagation-direction with respect to $e^\alpha_{(i)}$, respectively. The directional cosines are expressed as $\ell_{(1)}=\cos\theta_\nu$, $\ell_{(2)}=\sin\theta_\nu\cos\phi_\nu$, and $\ell_{(3)}=\sin\theta_\nu\sin\phi_\nu$. By using the tetrad bases, the neutrino energy is expressed as $\epsilon:=-p_\alpha e^\alpha_{(0)}$ with the four-momentum of the neutrino p^α. There is some degree of freedom to choose the tetrad bases, and the normal vector of the spatial hypersurface n^α (see equation (2.74)) is chosen as $e^\alpha_{(0)}$ in the code. Other spatial tetrad bases are set to be

$$e^\alpha_{(1)}=\gamma_{rr}^{-1/2}\partial_r, \tag{2.92}$$

$$e^\alpha_{(2)}=-\frac{\gamma_{r\theta}}{\sqrt{\gamma_{rr}(\gamma_{rr}\gamma_{\theta\theta}-\gamma_{r\theta}^2)}}\partial_r+\sqrt{\frac{\gamma_{rr}}{\gamma_{rr}\gamma_{\theta\theta}-\gamma_{r\theta}^2}}\partial_\theta, \tag{2.93}$$

$$e^\alpha_{(3)}=\frac{\gamma^{r\phi}}{\sqrt{\gamma^{\phi\phi}}}\partial_r+\frac{\gamma^{\theta\phi}}{\sqrt{\gamma^{\phi\phi}}}\partial_\theta+\sqrt{\gamma^{\phi\phi}}\partial_\phi, \tag{2.94}$$

where γ_{ij} is the spatial metric in the $3+1$ decomposition of the spacetime (see equation (2.73)). The polar coordinate (r,θ,ϕ) is adopted for space. The coordinate bases ∂_r, ∂_θ, and ∂_ϕ are expressed as usual. In this code, neutrinos are assumed to be massless. The

factors $\omega_{(0)}$, $\omega_{(\theta_\nu)}$, and $\omega_{(\phi_\nu)}$ are given as

$$\omega_{(0)} := \epsilon^{-2} p^\alpha p_\beta \nabla_\alpha e^\beta_{(0)}, \tag{2.95}$$

$$\omega_{(\theta_\nu)} := \sum_{i=1}^{3} \omega_i \frac{\partial \ell_{(i)}}{\partial \theta_\nu}, \tag{2.96}$$

$$\omega_{(\phi_\nu)} := \sum_{i=2}^{3} \omega_i \frac{\partial \ell_{(i)}}{\partial \phi_\nu}, \tag{2.97}$$

with

$$\omega_i := \epsilon^{-2} p^\alpha p_\beta \nabla_\alpha e^\beta_{(i)}. \tag{2.98}$$

If the coordinates are spherical coordinates in an inertial frame with flat spacetime, equation (2.90) is recovered. Although this general relativistic expression for the Boltzmann equation is used, the spatial hypersurface is assumed to be flat, i.e., $\gamma_{ij} = \mathrm{diag}(1, r^2, r^2 \sin^2\theta)$. The lapse function α is set to be unity, and the shift vector coincides with the velocity of the PNS center. These gauge conditions affect the equation through $e^\alpha_{(0)} = n^\alpha$. This is referred to as the moving-mesh. Note that in this condition $\sqrt{-g} = r^2 \sin\theta$.

In order to utilize the special discretization for the possible symmetry, equation (2.91) is cast into the form

$$\begin{aligned} &V \left\{ \frac{\partial}{\partial t}(K^t f) + \frac{1}{r^2}\frac{\partial}{\partial r}(K^r r^2 \cos\theta_\nu f) + \frac{1}{r\sin\theta}\frac{\partial}{\partial\theta}(K^\theta \sin\theta_\nu \cos\phi_\nu \sin\theta f) \right. \\ &\left. + \frac{1}{r\sin\theta}\frac{\partial}{\partial\phi}(K^\phi \sin\theta_\nu \sin\phi_\nu f) \right\} - \frac{1}{r\sin\theta_\nu}\frac{\partial}{\partial\theta_\nu}(\sin^2\theta_\nu f) - \frac{\partial}{\partial\phi_\nu}\left(\frac{\cos\theta}{r\sin\theta}\sin\theta_\nu \sin\phi_\nu f\right) \\ &- \frac{1}{\epsilon^2}\frac{\partial}{\partial\epsilon}(\epsilon^3 f \omega_{(0)}) + \frac{1}{\sin\theta_\nu}\frac{\partial}{\partial\theta_\nu}(\sin\theta_\nu f \Delta\omega_{(\theta_\nu)}) + \frac{1}{\sin^2\theta_\nu}\frac{\partial}{\partial\phi_\nu}(f\Delta\omega_{(\phi_\nu)}) = S_{\mathrm{rad}}. \end{aligned} \tag{2.99}$$

Several GR corrections are presented in the equation:

$$V := \frac{r^2 \sin\theta}{\sqrt{-g}}, \tag{2.100}$$

$$K^t := \frac{\sqrt{-g}}{r^2\sin\theta}\left(e^t_{(0)} + \sum_{i=1}^{3}\ell_i e^t_{(i)}\right), \tag{2.101}$$

$$K^r := \frac{\sqrt{-g}}{r^2\sin\theta\cos\theta_\nu}\left(e^r_{(0)} + \sum_{i=1}^{3}\ell_i e^r_{(i)}\right), \tag{2.102}$$

$$K^\theta := \frac{\sqrt{-g}}{r\sin\theta\sin\theta_\nu\cos\phi_\nu}\left(e^\theta_{(0)} + \sum_{i=1}^{3}\ell_i e^\theta_{(i)}\right), \tag{2.103}$$

$$K^\phi := \frac{\sqrt{-g}}{r\sin\theta_\nu\sin\phi_\nu}\left(e^\phi_{(0)} + \sum_{i=1}^{3}\ell_i e^\phi_{(i)}\right), \tag{2.104}$$

$$\Delta\omega_{(\theta_\nu)} := \omega_{(\theta_\nu)} + \frac{\sin\theta_\nu}{r}, \tag{2.105}$$

$$\Delta\omega_{(\phi_\nu)} := \omega_{(\phi_\nu)} + \frac{\cos\theta}{r\sin\theta}\sin^3\theta_\nu \sin\phi_\nu. \tag{2.106}$$

Note that V, $K^\alpha\,(\alpha = 0,1,2,3)$ are unity and $\Delta\omega_{(\psi)}\,(\psi = \theta_\nu, \phi_\nu)$ are zero in the flat spacetime with fixed spherical coordinate.

Implementing general relativistic gravity is currently underway. Instead, Newtonian limit hydrodynamics and gravity in the spherical coordinates are employed in the code. For the hydrodynamics, the basic equations are

$$\partial_t(\sqrt{-g}\rho) + \partial_i(\sqrt{-g}\rho v^i) = 0, \tag{2.107}$$

$$\begin{aligned}\partial_t(\sqrt{-g}\rho v_r) + \partial_i\left(\sqrt{-g}(\rho v_r v^i + p\delta^i_r)\right) = \\ \sqrt{-g}\rho\left(-\partial_r\Phi + r(v^\theta)^2 + r\sin^2\theta(v^\phi)^2 + \frac{2p}{r\rho}\right) - \sqrt{-g}G_r + \sqrt{-g}\rho\dot{\beta}_r,\end{aligned} \tag{2.108}$$

$$\begin{aligned}\partial_t(\sqrt{-g}\rho v_\theta) + \partial_i\left(\sqrt{-g}(\rho v_\theta v^i + p\delta^i_\theta)\right) = \\ \sqrt{-g}\rho\left(-r^2\partial_\theta\Phi + \sin\theta\cos\theta(v^\phi)^2 + \frac{p\cos\theta}{\rho\sin\theta}\right) - \sqrt{-g}G_\theta + \sqrt{-g}\rho\dot{\beta}_\theta,\end{aligned} \tag{2.109}$$

$$\partial_t(\sqrt{-g}\rho v_\phi) + \partial_i\left(\sqrt{-g}(\rho v_\phi v^i + p\delta^i_\phi)\right) = -\sqrt{-g}\rho\partial_\phi\Phi - \sqrt{-g}G_\phi + \sqrt{-g}\rho\dot{\beta}_\phi, \tag{2.110}$$

$$\partial_t\left(\sqrt{-g}(e + \frac{1}{2}\rho v^2)\right) + \partial_i\left(\sqrt{-g}(e + p + \frac{1}{2}\rho v^2)v^i\right) = -\sqrt{-g}\rho v^j\partial_j\Phi - \sqrt{-g}G_t + \sqrt{-g}\rho v^j\dot{\beta}_j, \tag{2.111}$$

and

$$\partial_t(\sqrt{-g}\rho Y_{\rm e}) + \partial_i(\sqrt{-g}\rho Y_{\rm e}v^i) = -\sqrt{-g}(\Gamma_{\nu_{\rm e}} - \Gamma_{\bar{\nu_{\rm e}}}). \tag{2.112}$$

Here, ρ, v^i, p, e, $Y_{\rm e}$, Φ, and β_i are the density, the velocity, the pressure, the internal energy, the electron fraction, the gravitational potential, and the shift vector, respectively. The dotted symbols represent the time derivatives of non-dotted quantities. The energy-momentum transfer between neutrinos and the matter is defined by

$$G^\mu = \int p^\mu \nu S_{\rm rad}{\rm d}V_p, \tag{2.113}$$

where ${\rm d}V_p$ is the invariant volume element in the momentum space. The neutrino reaction rate for neutrino species i ($i = \nu_{\rm e}$ for electron-type neutrinos and $i = \bar{\nu_{\rm e}}$ for anti-electron-type neutrinos) is

$$\Gamma_i = m_{\rm u}\int \nu S_{{\rm rad},i}{\rm d}V_p, \tag{2.114}$$

with $m_{\rm u}$ and $S_{{\rm rad},i}$ being the atomic mass unit and the collision term for neutrino species i, respectively. The numerical flux is calculated by the Harten-Lax-van Leer scheme (Harten et al., 1983) with piecewise-parabolic interpolation (Colella & Woodward, 1984), and the time integration is performed by the second-order Runge-Kutta method. For the gravitational potential Φ, the Poisson equation

$$\Delta\Phi = 4\pi\rho \tag{2.115}$$

is solved by the MICCG method (Nagakura et al., 2011).[*2]

This code is one of the most sophisticated simulation code in the field. In section 3, I present the simulation result by using this code. The validation of the code is summarized in Appendix A.

2.2.2 The acoustic mechanism

In the neutrino heating mechanism, the energy stored in the PNS is transferred to the shock by the neutrinos. It is possible that another energy transfer process is responsible to the shock revival. By Burrows et al. (2006, 2007a,b), the shock revival whose energy transfer is mediated by the acoustic waves is discovered. This explosion mechanism is called the acoustic mechanism.

The details of the acoustic mechanism are as follows: until the stalled shock phase, the scenario is the same as the neutrino heating mechanism discussed in section 2.2.1. At the stalled shock phase, the neutrino luminosity is not large enough for the shock to revive, and hence the matter accretion and the turbulence continues. In their simulations, the class of the developed fluid instability is the SASI. Then the turbulence beats the central PNS. As a consequence, the PNS starts to oscillate with $\ell = 1 - 2$ mode. The oscillation mode is the so-called g-mode, whose restoring force is the buoyancy. In Burrows et al. (2006, 2007a,b), the oscillation energy is estimated as 10^{50}–10^{51} erg and the period of the most pronounced mode is ~ 3 ms. Then, the oscillating PNS starts to emit the acoustic waves outward. Since the power of acoustic waves increases while the neutrino luminosity decreases, the acoustic power dominates the heating rate after ~ 400 ms after the core bounce. Finally, the shock starts to expand at around 500 ms after the core bounce. An important feature is that the shock expansion is unipolar, i.e., the shock only expands in the northern direction. In the southern direction, the matter still accretes and beats the PNS, feeding the energy for the oscillation.

Burrows et al. (2006, 2007a,b) suggested that the acoustic mechanism is a self-regulating mechanism for the following reason. The matter accretion continues until the shock revival to any direction is achieved. It is probable that the ominidirectional shock expansion is achieved when enough gravitational energy is released by the accretion flow. Therefore soon after enough energy is released, the energy supply by the accretion is terminated and the explosion energy tends to be uniform independent of the progenitor. This is consistent with the fact that the explosion energies of CCSNe are very similar, $\sim 10^{51}$ erg. Another merit of the acoustic mechanism is that the acoustic waves do not escape from the shock, and thus whole energy released by the accretion is eventually used for the shock revival. It means that the efficiency of the energy transfer is much higher compared to the neutrino heating mechanism.

Unfortunately, only Burrows et al. (2006, 2007a,b) found the acoustic mechanism explosion and other groups do not reproduce it (Marek & Janka, 2009, for example). It

[*2] In the real calculation, an inverse matrix of the discretized Laplacian is first generated by the MICCG method, and it is directly multiplied to the right-hand side during the time evolution.

may be because the acoustic mechanism works only after the neutrino heating mechanism fails. Therefore, it requires a long time simulation exceeding $\sim 1\,\mathrm{s}$ after the core bounce to reproduce the explosion by the acoustic mechanism. Since other groups obtain the shock revival by the neutrino heating mechanism or terminate the simulations before the acoustic mechanism works, the explosion by the acoustic mechanism has not been reproduced.

Since the acoustic mechanism is difficult to reproduce in self-consistent simulations as discussed above, other approaches than the fully self-consistent CCSNe simulations are desirable. So far for such a phenomenological approach, whether the PNS oscillation can store and emit such large energy or not is questioned. In order to examine that, Yoshida et al. (2007) applied the linear perturbation analysis to the PNS oscillation. They considered the forced oscillations of PNS by the pressure fluctuations which mimics the beating by the accreting matter. Since Burrows et al. (2006, 2007a,b) found the turbulence originated from the SASI, Yoshida et al. (2007) also tried to include the SASI fluctuation by imposing the numerical model of the SASI by Ohnishi et al. (2006), who simulated the behavior of the SASI itself, to the boundary condition on the PNS surface. As a result, they found that the energies of the excited g-modes are $\lesssim 10^{50}\,\mathrm{erg}$ and estimated that the emitted acoustic power is $\sim 10^{51}\,\mathrm{erg\,s^{-1}}$, which is comparable with the results in Burrows et al. (2006).

On the other hand, Weinberg & Quataert (2008) utilized the nonlinear three-mode couplings among g-modes to investigate the energy of each mode of the PNS oscillations. Due to the three-mode couplings, the "mother" mode decays into two "daughter" modes with lower frequencies and the energy is transferred from higher frequencies to lower frequencies. If the daughter mode has low enough frequency, the energy contained in the mode is dissipated to the heat and converted into the neutrinos. If this mechanism works, the PNS should have little energy in the form of oscillations. According to their calculations, the $\ell = 1$ mode, which is the dominant mode in Burrows et al. (2006), has only $\sim 10^{47\text{–}48}\,\mathrm{erg}$ with steady energy injection of $10^{50\text{–}51}\,\mathrm{erg}$. Note that the energy injection from the turbulent beating is impulsive, but Weinberg & Quataert (2008) approximate that the averaged energy injection is steadily fed. By assuming that the damping rate is $10\,\mathrm{Hz}$, the emitted acoustic power is $\sim 10^{48\text{–}49}\,\mathrm{erg\,s^{-1}}$, which is much smaller than that in Burrows et al. (2006).

Weinberg & Quataert (2008) claimed that the reason why Burrows et al. (2006) have very intense oscillations is that their numerical simulation does not have enough resolution to capture the small-scale daughter modes of relevance. Since Yoshida et al. (2007) considers the linear perturbation and hence neglects the mode couplings, it is likely that the energy in Yoshida et al. (2007) is larger than that in Weinberg & Quataert (2008). However, whether the assumptions used in Weinberg & Quataert (2008) are valid or not is also unknown, and hence further investigation in the PNS oscillation energy or another approach is needed to verify the acoustic mechanism.

Chapter 3

The Neutrino Heating Mechanisms with Boltzmann Neutrino Transport

In the last subsection of section 2.2.1, the Boltzmann-radiation-hydrodynamics code is described. Since it is the most sophisticated in neutrino transport, whether the inaccuracy of the approximations in neutrino transport is the cause of the failure in reproducing the explosion energy or not may be judged by performing simulations with the Boltzmann-radiation-hydrodynamics code. The simulation requires substantial computational cost, but K-computer in Institute of Physical and Chemical Research (RIKEN) in Japan can provide sufficient resources.

Nagakura et al. (2018) presented simulation results using the Boltzmann-radiation-hydrodynamics code. They conducted two simulations with different EOSs: LS EOS and FS EOS introduced in section 2.1.3. They found that the simulation with LS EOS seemed to explode, while that with FS EOS failed. Although the maximum shock radius in LS model is quite large and increasing at the end of the simulation, its mean shock radius is not so large, and it is uncertain that whether the shock will recede or not finally. The larger shock radius in the LS model compared to the FS model is ultimately originated from the difference in nuclear composition. Since single nuclear approximation utilized in LS EOS is the unphysical approximation, the apparent shock revival in the LS model itself may be unphysical. Since FS EOS is more realistic, despite its stiff nature of nuclear force may be an artifact of modeling, explosion of non-rotating progenitor may not be obtained.

Then, in this chapter, whether rotation plays a vital role in the explosion or not is investigated. In section 2.2.1, it is discussed that the rotation may be a missing physics, and subsequently the effects of rotation on CCSN are also discussed. Since all of them are performed in approximate neutrino transport, how rotation affects on CCSN with Boltzmann transport is the focus here.

This chapter is organized as follows: In section 3.1, I describe the numerical setup. Next, in section 3.2, the simulation results are presented, and the effects of rotation on

the post-bounce dynamics are discussed. Since exploiting the Boltzmann solver is one of the novel features of the code, I show some features related to the momentum space of neutrino distributions next in section 3.3. Finally, in section 3.4, I summarize and conclude this chapter.

3.1 Numerical Modeling

The progenitor model employed in this chapter is the non-rotating $11.2\,M_\odot$ model taken from Woosley et al. (2002). This is the same progenitor with those in Nagakura et al. (2018). Employing the prescription described in section 2.2.1, I added the rotational velocity artificially at the onset of the collapse. The functional form of the rotational velocity is the shellular rotation profile (equation (2.72)). The central angular velocity is $\Omega_0 = 1\,\mathrm{rad/s}$ and the size of the rigid core is $r_0 = 10^3\,\mathrm{km}$. Note that this is almost the fastest end according to the current stellar evolution theory (Heger et al., 2000).

The Boltzmann-radiation-hydrodynamics code described at the end of section 2.2.1 is used for the simulation. This is validated in Appendix A. FS EOS discussed in section 2.1.3, which is based on the RMF theory and NSE, is employed. The neutrino reactions are based on Bruenn (1985) (see table 2.3) and the non-elastic electron scattering, the updated electron capture on heavy nuclei (Juodagalvis et al., 2010; Langanke & Martínez-Pinedo, 2000; Langanke et al., 2003), and the nucleon-nucleon bremsstrahlung (Friman & Maxwell, 1979; Maxwell, 1987) are also included. Since the neutrino reactions involving ν_μ, $\bar{\nu_\mu}$, ν_τ, and $\bar{\nu_\tau}$ are almost the same (but see Bollig et al., 2017), these heavy-lepton-type neutrinos are treated together and denoted as ν_x. Therefore, three neutrino species of ν_e, $\bar{\nu_\mathrm{e}}$, and ν_x are evolved in the simulation.

I run the 2D axisymmetric simulation from the onset of collapse. The radial coordinate is set from center to outer 5000 km and divided into 384 bins. The θ-coordinate is spanned from 0 to π and initially divided into 64 bins. When the negative entropy gradient starts to develop after the core bounce, the θ-grid number increases to 128, and the radial velocity is perturbed randomly by 0.1% in $30 \leq r \leq 50\,\mathrm{km}$ artificially as the seeds of fluid instabilities. The way to perturb is the same as in Nagakura et al. (2018). For the momentum space, the neutrino energy ϵ is considered up to 300 MeV and divided into 20 bins. The angular coordinates in the momentum space cover the full solid angle of 4π. The zenith θ_ν and the azimuthal ϕ_ν angles are divided into 10 and 6, respectively.

3.2 The Time Evolution

In this section, I discuss the dynamics of simulated CCSN and several key diagnostics regarding the pre- and post-bounce dynamics. First, I show a $T/|W|$ parameter from the onset of collapse to a time slightly after core bounce in figure 3.1. The $T/|W|$ parameter measures how rapidly the stellar core rotates. Here,

$$T := \int \frac{1}{2}\rho(r\sin\theta v^\phi)^2 \mathrm{d}V_x, \tag{3.1}$$

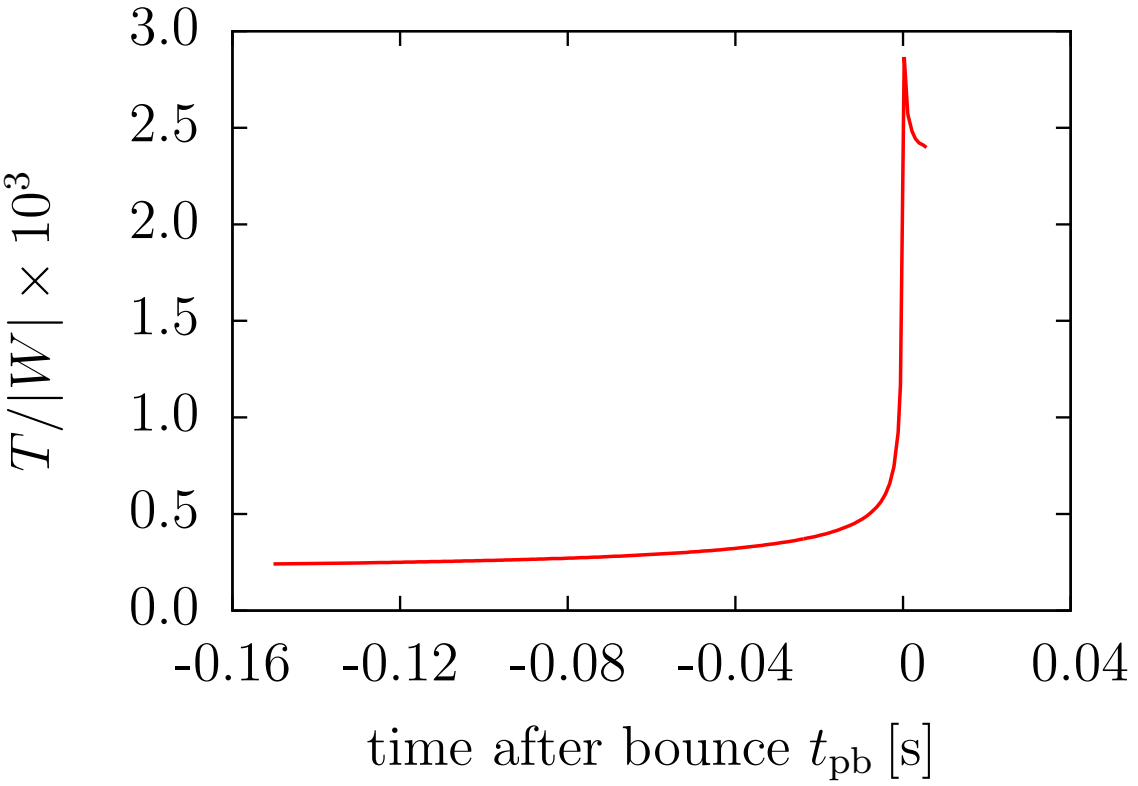

Figure 3.1. The time evolution of the $T/|W|$ parameter from the onset of collapse to a time slightly after the core bounce.

where $\mathrm{d}V_x$ is the invariant volume element in the configuration space, is the rotational kinetic energy (note that the v^ϕ is the ϕ-component of the velocity with respect to the coordinate basis), and

$$W := -\frac{1}{2}\int \frac{\rho(\boldsymbol{r})\rho(\boldsymbol{r}')}{|\boldsymbol{r}-\boldsymbol{r}'|}\mathrm{d}V_x\mathrm{d}V_x' \tag{3.2}$$

is the gravitational energy. The $T/|W|$ is $\sim 2.5\times10^{-4}$ at the onset of collapse and $\sim 3\times10^{-3}$ at the core bounce, and after the bounce it reduces. This behavior is qualitatively similar to other groups (Ott et al., 2008; Kuroda et al., 2014; Abdikamalov et al., 2014). Although the adopted rotational velocity is very high, the $T/|W|$ is rather low. It is much smaller than the value required to cause instabilities (Shibata et al., 2002, 2003).

Since the moving mesh method illustrated in section 2.2.1 is employed in the code, the trajectory of the center of PNS can be followed. The laboratory frame, or center-of-mass frame, is distinguished from the acceleration frame, or PNS-rest frame. In order to measure how different these two frames are, I show in figure 3.2 the proper motion of PNS for both the rotating model calculated here and the non-rotating counterpart presented in Nagakura et al. (2018). The kick velocities read from the figure is very small (at most $v/c \sim 10^{-4}$), and hence the difference between the laboratory frame and the acceleration frame is small. Therefore, hereafter in this chapter, the difference is neglected and only the term "the laboratory frame" is used even for the acceleration frame.

Before discussing the difference of proper motions of PNSs between the rotating and

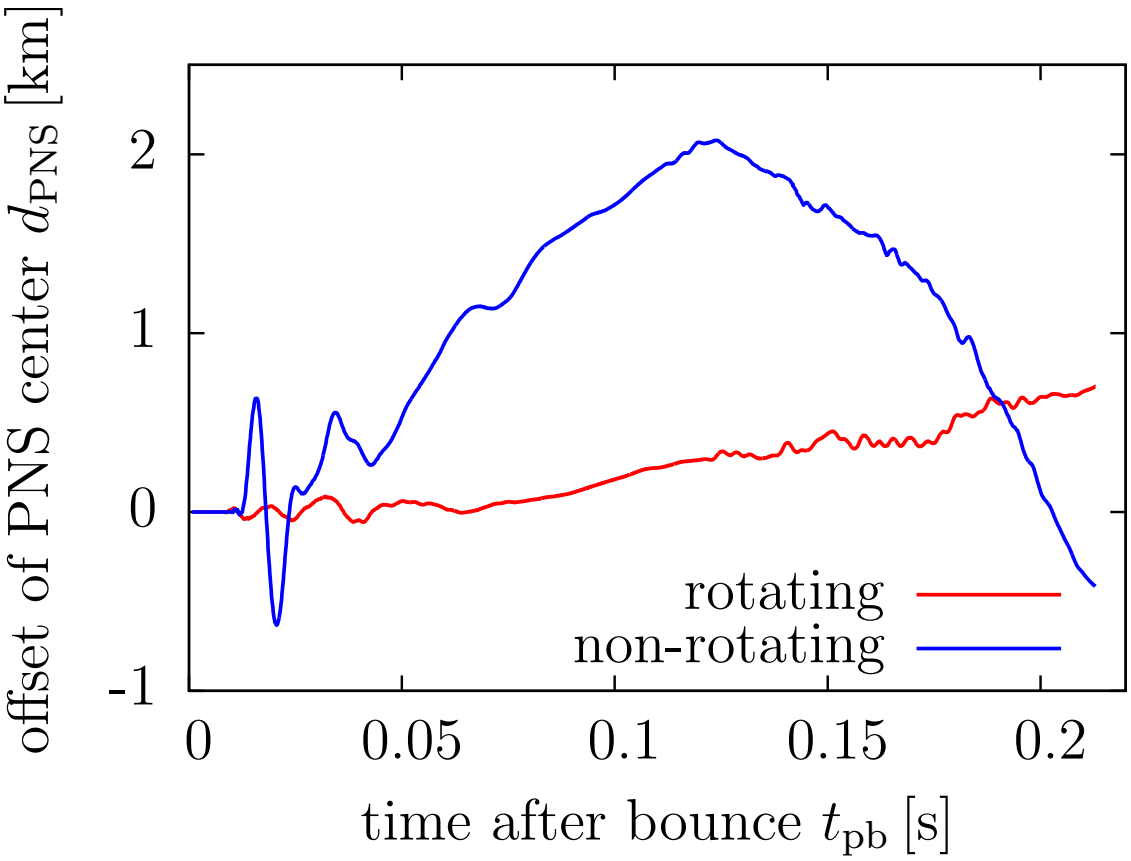

Figure 3.2. The comparison of proper motions of PNSs between the rotating (the red line) and non-rotating (the blue line) models. The offset is measured in the laboratory frame.

non-rotating models, let me focus on the dynamics of the post-bounce flow. This is because it describes the origin of the difference.

I show the snapshots of the entropy distributions in figure 3.3. Immediately after the core bounce, the shock expands to take an oblate form (the upper left panel) by the centrifugal force. Accretion flow is directed to the center and hence refracted by the oblate shock to the northern and southern poles. Then the refracted flow converges at both poles due to the imposed axisymmetry. Next, the flow pushes the shock at both poles, and hence the shock takes a prolate form (the lower left panel). At that time the radial accretion flow is refracted to the equator by the prolate shock and converges there. Then the shock takes the oblate form again. The shock increases its average radius with repeating this oblate-prolate oscillation (the upper and lower middle panels, respectively), and finally, it stalls. During the stalled-shock phase, developed convective bubbles break this oscillation. The scale of these bubbles is so large that only two bubbles develop (the upper right panel). Finally, these bubbles are mixed, torn up, and complex turbulent pattern arises (the lower right panel).

The difference shown in figure 3.2 is now explained. Figure 3.3 shows symmetric distributions of the entropy with respect to the equator until the stalled shock phase. The

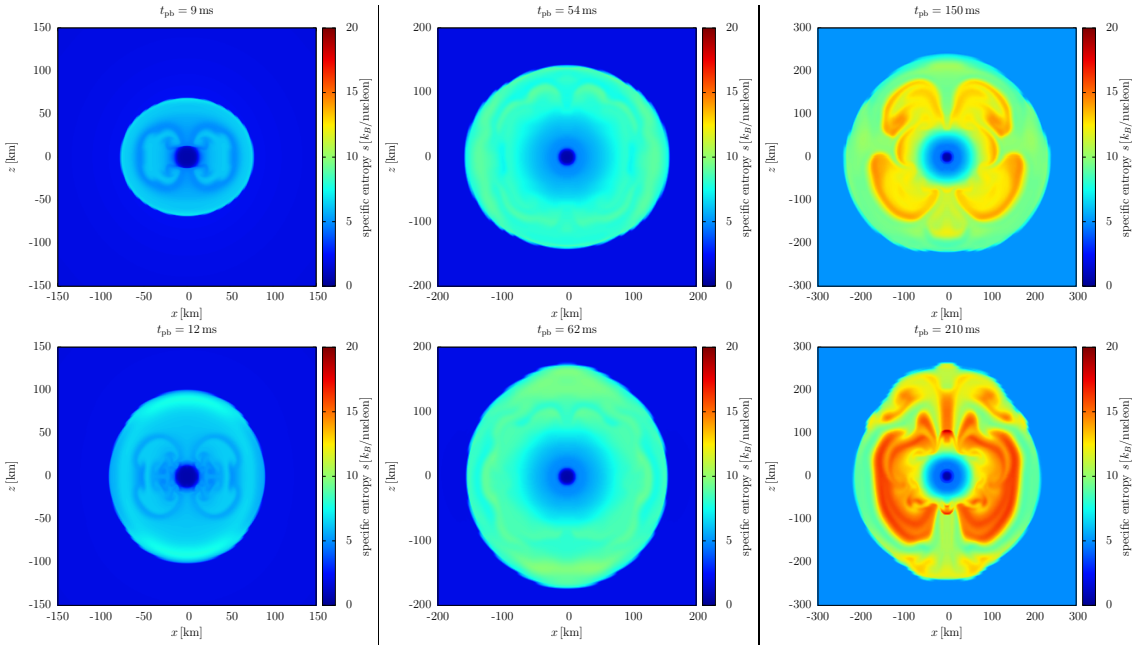

Figure 3.3. The color maps of specific entropy distributions in the meridional section at the post-bounce times of $t_{\rm pb} = 9$ (upper left), 12 (lower left), 54 (upper middle), 62 (lower middle), 150 (upper right), and 210 (lower right) ms. The color scale of the entropy is displayed on the right of each panel. The position of the shock is the boundary of the cold and warm colors. Since the shock expands, the range of x and z coordinates are different as presented in each figure.

kick motion of the PNS is determined by the force balance between the matter in the northern and southern halves. Since the matter distribution is symmetric in the rotating model, the force is almost balanced and little kick is achieved. However, this symmetry is a result of the centrifugal force and does not exist in the non-rotating model. Thus in the non-rotating model, the force imbalance between the north and south leads to the strong PNS kick.

Next, evolutions of several important quantities related to the explosion dynamics are compared between the rotating and non-rotating models in figure 3.4. The displayed quantities are the shock radii $r_{\rm shock}$, the PNS radii $r_{\rm PNS}$, the neutrino luminosities L_ν, and the mean energy of the neutrinos E_ν. Here, the shock radius is defined by the outermost radius where the velocity is slower than 30% of the free-fall velocity. The PNS radius is chosen as the radius where the angle-averaged density is $10^{11}\,{\rm g\,cm^{-3}}$. The neutrino luminosities and the mean energies are measured at the 500 km from the center.

Although the morphology of the shock in the rotating model is affected by the centrifugal force as in figure 3.3, the evolution of the average shock radius resembles that in the non-rotating model. The neutrino luminosities and the mean energies of neutrinos also show very similar evolutions. The $\nu_{\rm e}$ luminosities and $\nu_{\rm e}$ and $\bar{\nu_{\rm e}}$ mean energies in the rotating model are slightly smaller than those in the non-rotating model. This trend is consistent

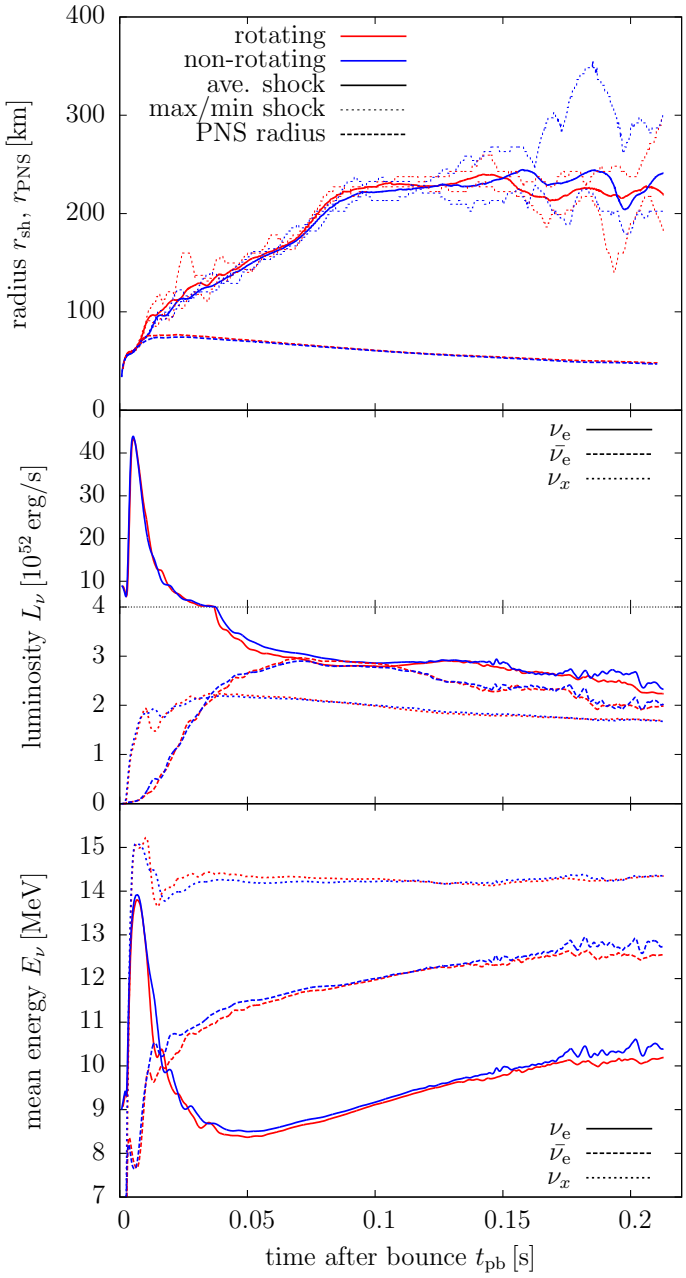

Figure 3.4. The evolutions of some radii and neutrino quantities. For all panels, red and blue lines represent the rotating and non-rotating model, respectively. (Top panel: the shock radii and the PNS radii) The thick solid and thin dotted lines show the average and maximum (minimum) shock radii, respectively. The thick dashed lines indicate the PNS radii whose angular averaged density is $10^{11}\,{\rm g\,cm^{-3}}$. The running average over 5 ms smoothes the evolution of the PNS radii. (Middle panel: the neutrino luminosities) The solid, dashed, and dotted lines correspond to the luminosities of $\nu_{\rm e}$, $\bar{\nu}_{\rm e}$, and ν_x, respectively. In order to indicate the peak luminosities at the neutronization bursts and to compare the luminosities of each species at later times, the vertical scales of the upper and lower halves of the panel are different. (Bottom panel: the mean energies of neutrinos) The line types are the same for those in the middle panel.

with Summa et al. (2018). Remembering that the non-rotating model with FS EOS in Nagakura et al. (2018) fails to revive the shock within $\sim 300\,\mathrm{ms}$ after the core bounce, the rotating model also seems to be unsuccessful. Thus, I terminated the simulation at $\sim 200\,\mathrm{ms}$ after the core bounce.

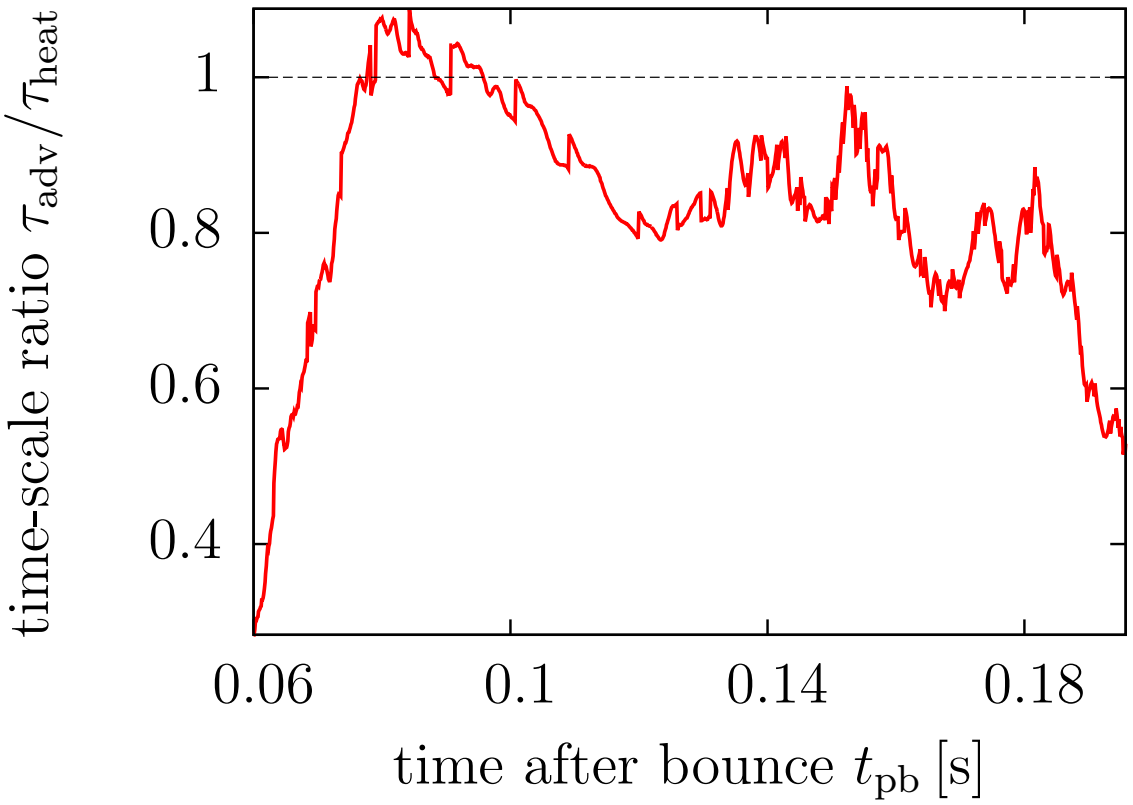

Figure 3.5. The time evolution of the time-scale ratio $\tau_{\rm adv}/\tau_{\rm heat}$.

The failure is also indicated by the time-scale ratio. Figure 3.5 shows the time-scale ratio $\tau_{\rm adv}/\tau_{\rm heat}$ discussed in equation (2.68). The energy in the gain layer $E_{\rm gain}$ here is defined as

$$E_{\rm gain} = \int_{r_{\rm gain}}^{r_{\rm shock}} \left(e_{\rm th} + \frac{1}{2}\rho v^2 + \rho\Phi \right) {\rm d}V, \tag{3.3}$$

where $e_{\rm th}$ and Φ are thermal energy and gravitational potential, respectively. According to appendix A in Bruenn et al. (2016), thermal energy should be defined by

$$e_{\rm th} = \frac{3}{2}\frac{\rho}{\bar{A}m_{\rm u}}kT + aT^4 + \left(e_{\rm e^{\mp}} - Y_{\rm e}m_{\rm e}c^2\frac{\rho}{m_{\rm u}} \right), \tag{3.4}$$

where $e_{\rm e^{\mp}}$, $\bar{A}$, and a are the internal energy density of the electron-positron gas, the mean mass number, and the radiation constant, respectively. From figure 3.5, the ratio of our model exceeds unity only limited period and has decreasing trends, indicating the failure of shock revival.

The similarities in neutrino luminosities and mean energies between the rotating and non-rotating models are originated from the PNS radius in the top panel of figure 3.4. If

the centrifugal force were strong enough, the PNS radius could be extended, but actually, the model here has too weak rotation to have such large force and shows the similar evolution of the PNS radius as that in the non-rotating model. By weak centrifugal force in the model, the radius along the equator is only $\sim 5\%$ larger than that along the pole. It is too small to influence the shock evolution.

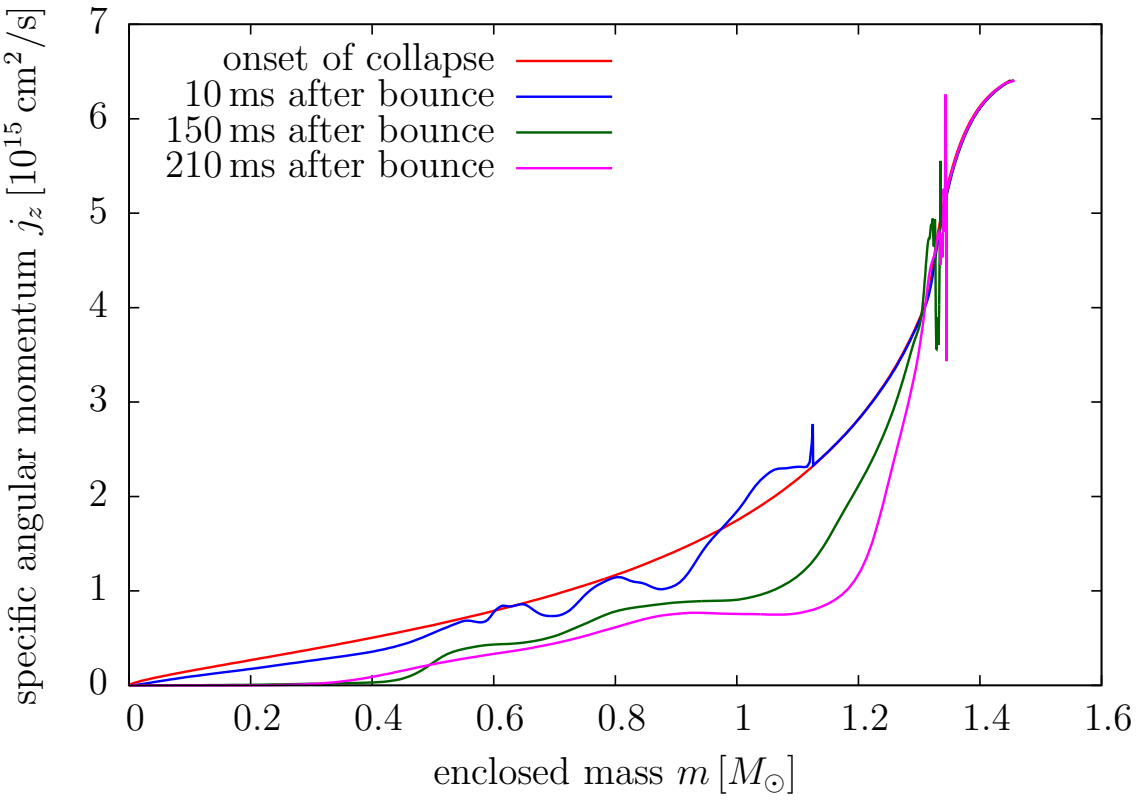

Figure 3.6. The specific angular momentum of each mass shell as a function of the enclose mass. Different colors represent the specific angular momentum profiles at different times: at the onset of the collapse (red) and ~ 10 ms (blue), ~ 150 ms (green), and ~ 210 ms (magenta) after the core bounce. The spikes in the profiles correspond to the positions of the shock at each time.

Figure 3.6 shows the evolution of the specific angular momentum

$$j_z := \frac{\int_{\rm shell} \rho r^2 \sin^2\theta v^\phi {\rm d}V_x}{\int_{\rm shell} \rho {\rm d}V_x} \tag{3.5}$$

on each mass shell, where the integration is carried out over each radial bins. Note that the specific angular momentum inside the shock decreases with time. This is because neutrinos carry the angular momentum out (for a detailed discussion, see section 3.3). In the outer part the angular momentum conserves, since the neutrino reactions rarely occur. Summa et al. (2018) computed two models with different rotational velocities. Although the rotational velocity itself in our model is faster than those of both model in Summa et al. (2018), the specific angular momentum of our model lies between their two models ($\sim 10^{14}$ cm^2 s^{-1} for the slower model named "rot" and $\sim 10^{16}$ cm^2 s^{-1} for the faster model

named "artrot") because of the different progenitor model. Considering that their "rot" model has no effect on the PNS radius and "artrot" model extends it, the border in the angular momentum which divides whether rotation extends the PNS radius or not might lie between $10^{15}\,\mathrm{cm^2\,s^{-1}}$ and $10^{16}\,\mathrm{cm^2\,s^{-1}}$.

The discussion above indicates that the rotation imposed in this chapter is not fast enough to change the non-exploding model into exploding model. Considering that the rotation of $1\,\mathrm{rad\,s^{-1}}$ at the center is almost the fastest end of the range indicated by the stellar evolution theory, another physical ingredient such as microphysics or another mechanism such as the acoustic mechanism should be considered.

3.3 Neutrino distribution

Investigations on hydrodynamic features and explosion diagnostics in the previous section shows the failure of the shock revival. On the other hand, the neutrino distributions in the phase space are worth examining since one of the novel aspects of the code is to treat the distribution functions of the neutrinos directly. In the following sections, I provide detailed analyses of the neutrino distributions though this is a digression from the explodability (the capability of the explosion) itself. The contents of sections 3.3.1, 3.3.2, 3.3.3, and 3.3.4 are the Y_e prescription in the rotating core-collapse, the angular distributions of neutrinos in the momentum space, the rotational component of the neutrino flux, and the Eddington tensor of the neutrinos, respectively.

3.3.1 Y_e Prescription

First, let me focus on the pre-collapse phase. Since I solve the Boltzmann equation directly, the lepton distribution during the collapsing phase can be correctly followed. Liebendörfer (2005) performed 1D general relativistic Boltzmann-radiation-hydrodynamics simulation and suggested the distribution of the electron fraction Y_e as a function of density, whose functional form is fitted from the simulation. However, only 1D results are presented in his work and the effect of rotation on this "Y_e prescription" has not been examined, which can be examined by the Boltzmann solver here. Figure 3.7 shows the comparison between the rotating model and the non-rotating model. Note that contrary to Liebendörfer (2005), the electron fraction cannot be fitted by a function of the density only. This is not unexpected since the updated electron capture rate and the Newtonian gravity are used. There is almost no difference between the two models in the figure. The more rapid rotation might have some influence, but it is not in the scope of this dissertation since such a rapid rotation may not be realized as a result of the stellar evolution.

3.3.2 Angular Distribution

Figures 3.8, 3.9, and 3.10 show the angular distributions in the momentum space of ν_e for several neutrino energies at 12 ms after the core bounce in the laboratory frame. They are distributions at the points in the optically thick region (figure 3.8), semi-transparent

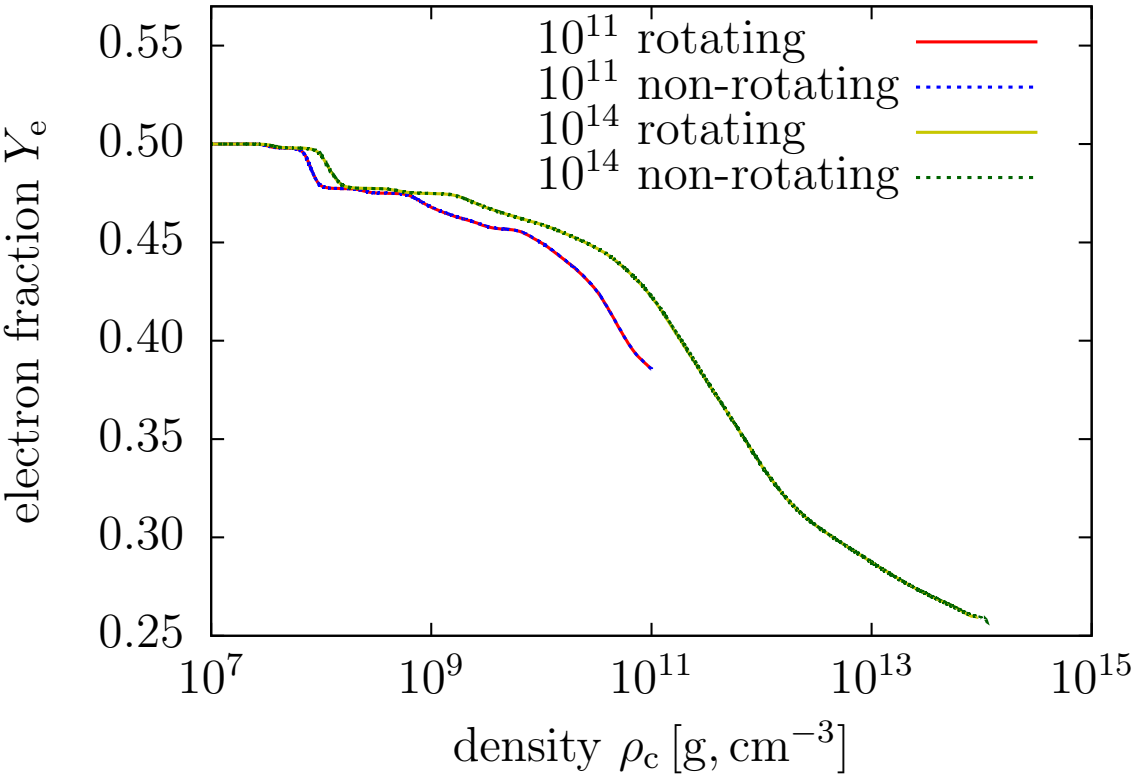

Figure 3.7. The electron fractions as functions of the density. Distributions at the time when the central density is $10^{11}\,\mathrm{g\,cm^{-3}}$ (red and blue lines) and $10^{14}\,\mathrm{g\,cm^{-3}}$ (yellow and green lines) are shown. The solid and dotted lines represent the rotating and non-rotating models, respectively.

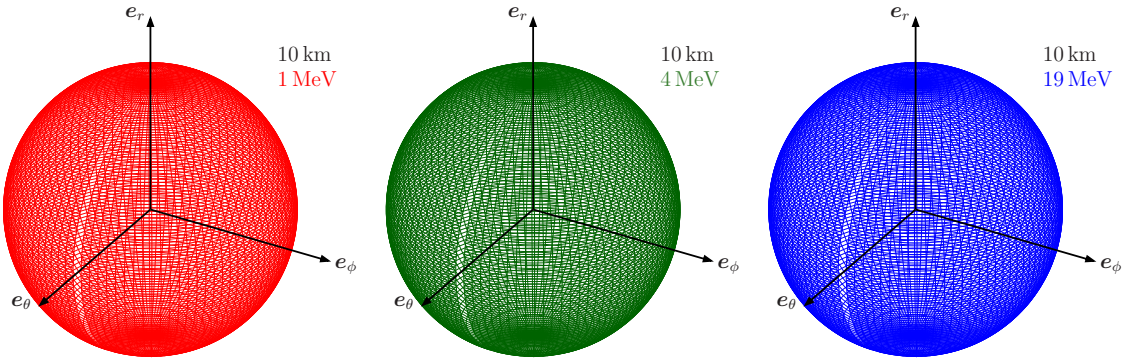

Figure 3.8. Angular distributions in the momentum space of ν_e at 12 ms after the core bounce in the laboratory frame. The spatial point is $r = 10\,\mathrm{km}$ (the optically thick region) on the equator. Surfaces with different colors represent the angular distributions of different neutrino energies measured in the laboratory frame: red–1 MeV, green–4 MeV, blue–19 MeV. Arrows with $\boldsymbol{e}_r$, $\boldsymbol{e}_\theta$, and $\boldsymbol{e}_\phi$ represent the spatial part of the tetrad bases (equations (2.92–2.94)). All distributions are normalized so that the maximum value is the same. In order to obtain the smooth surface, angular interpolation is applied in this and the following figures.

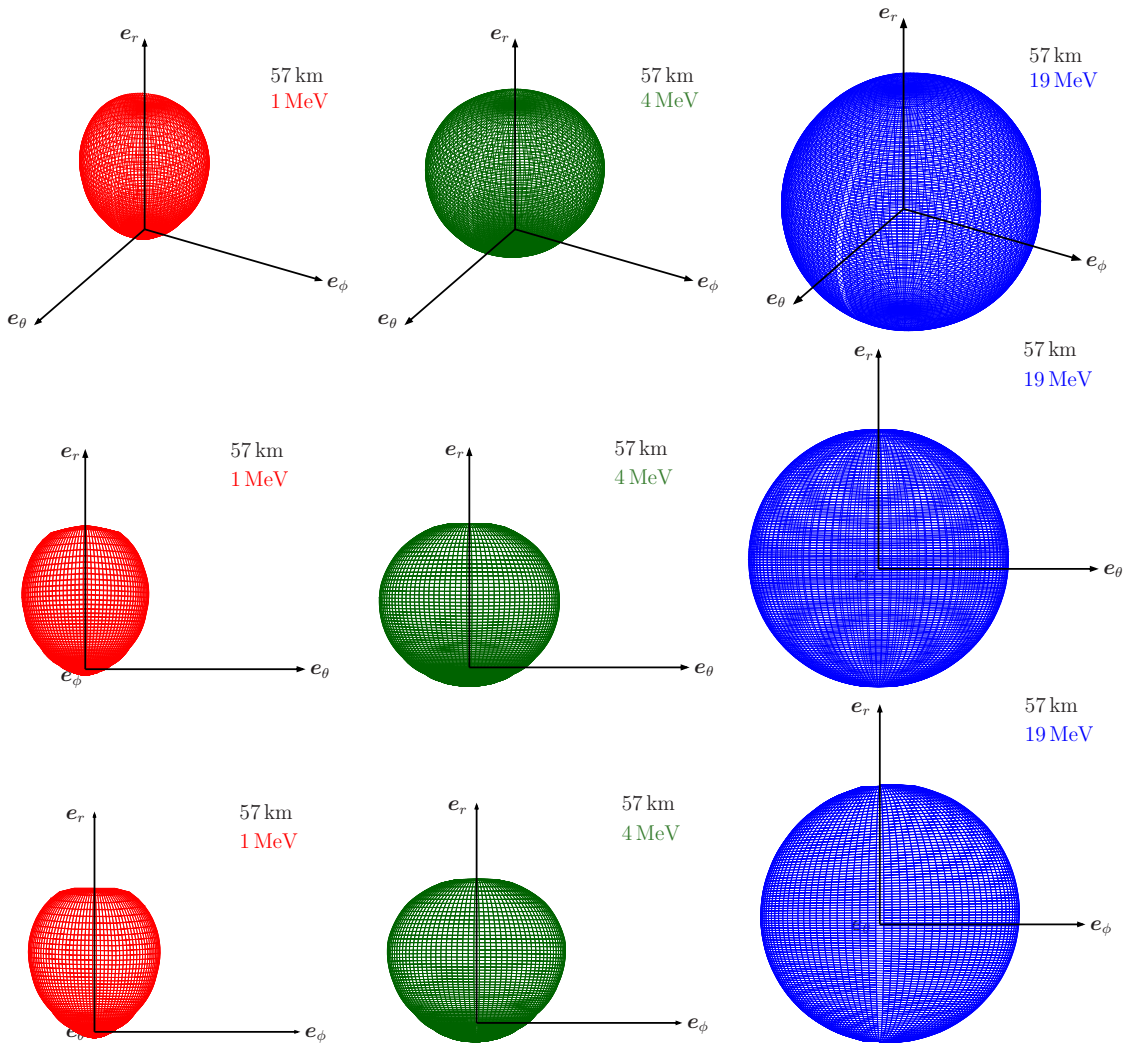

Figure 3.9. The same as figure 3.8, except that the spatial point is $r = 57\,\mathrm{km}$ (the semi-transparent region). The middle and bottom rows of figures are the distributions seen from different angles, projected to $\boldsymbol{e}_r$–$\boldsymbol{e}_\theta$ and $\boldsymbol{e}_r$–$\boldsymbol{e}_\phi$ planes, respectively.

region (figure 3.9), and the optically-thin region (figure 3.10), and all points are on the equator ($\theta = \pi/2$).

The neutrinos and matter are in equilibrium in the optically thick region, and hence the neutrinos are isotropically distributed in the fluid-rest frame. Since the velocity at the point is negligible ($v/c \sim 2 \times 10^{-2}$), the angular distributions shown in figure 3.8 are almost isotropic independent of the neutrino energy, even though the figure is shown in the laboratory frame.

On the other hand, the distributions in the semi-transparent region (figure 3.9) are not isotropic and are different among the energies. The lowest energy neutrinos are forward-peaked, and middle energy neutrinos are blunter than the lowest energy. For the highest energy neutrinos, the distribution is more or less isotropic but slightly dragged to the

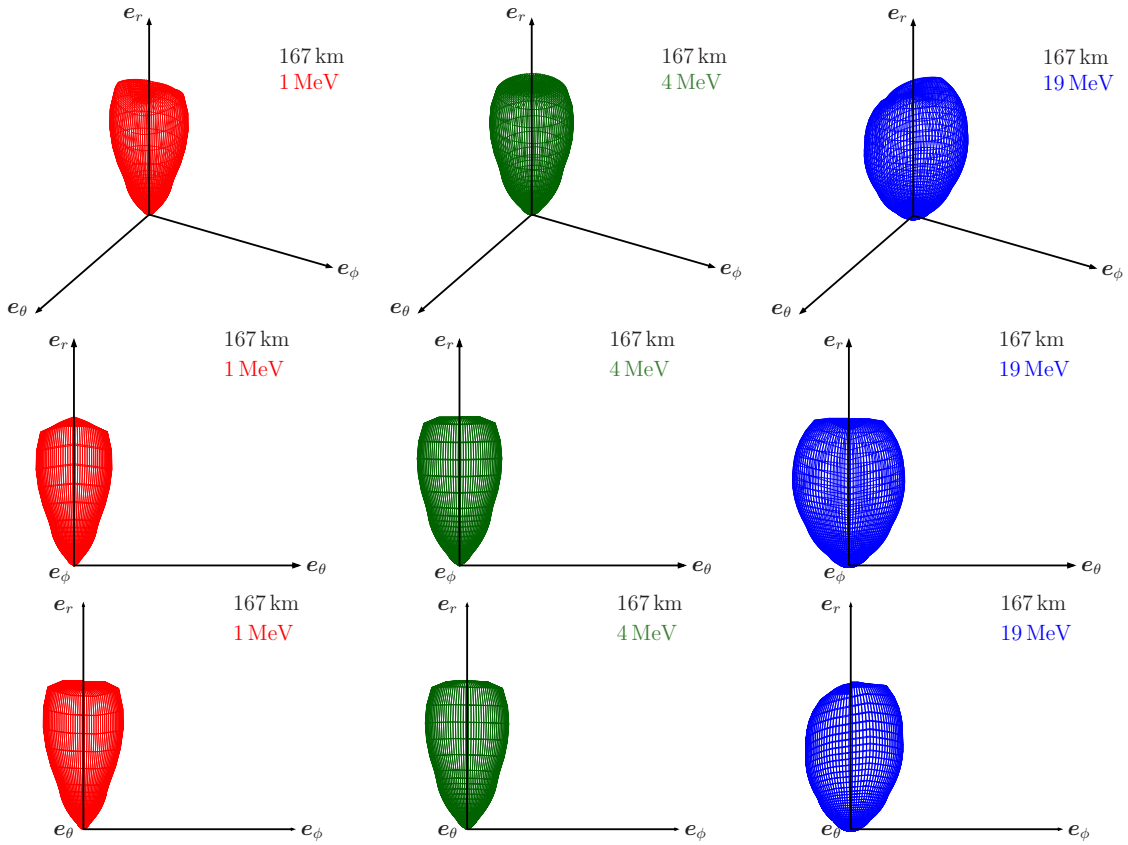

Figure 3.10. The same as figures 3.8 and 3.9, except that the spatial point is $r = 167\,\mathrm{km}$ (the optically thin region).

ϕ-direction because of the Lorentz transformation, or the relativistic beaming. The lower the neutrino energy is, the smaller the reaction rates are. Thus lower energy neutrinos couple with the matter more loosely compared to higher energy neutrinos. Therefore, the lower the neutrino energy is, the more the distribution gets forward-peaked.

Then in the optically thin region (figure 3.10), neutrinos with all energies show the forward-peaked distributions. This is because all neutrinos are decoupled from the matter and streaming freely. Although such behavior is common for all energies, the streaming directions are slightly different. The lowest and middle energy neutrinos direct along the radial direction ($\boldsymbol{e}_r$), while for the highest energy neutrinos, the distribution gets slightly tilted to the rotational direction ($\boldsymbol{e}_\phi$). This is again due to the dependence of the reaction rates on the neutrino energies.

The situation is illustrated in figure 3.11. During the neutrinos are trapped by matter, the neutrino distributions are dragged by matter via the relativistic beaming as shown by the blue surface in figure 3.9. This dragging is imprinted even when the neutrinos are decoupled from matter, thus the free-streaming direction is not exactly radial but slightly tilted to the ϕ-direction like the dashed lines in figure 3.11. Once the neutrinos start to stream freely and go far away, the angle between the radial and the propagation directions $\bar{\theta}$ gets smaller and smaller as $\sin\bar{\theta} = b/r$, where b is the impact parameter of the neutrino

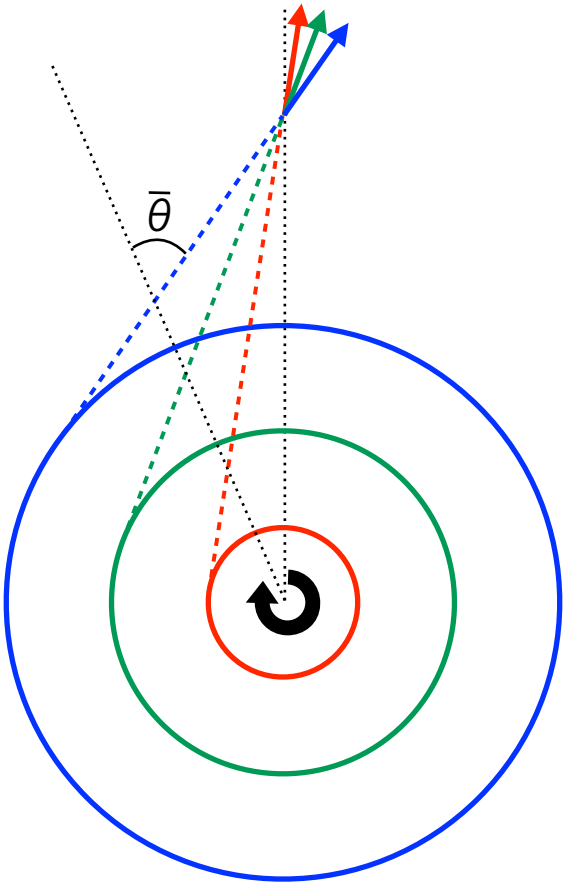

Figure 3.11. A schematic picture for the neutrino distributions in figure 3.10. The colored circles represent the neutrinospheres of each energy of neutrinos on the equator. The colors correspond to those of figure 3.10. The black circular arrow at the center indicates the rotation of the PNS. The dashed lines and solid arrows are the trajectory of neutrinos and propagating directions, respectively, of each energy. The black dotted lines are radial lines. The angle $\bar{\theta}$ defined in the text is also indicated as the angle between the dashed and dotted lines.

with respect to the center. Since the neutrinosphere for the higher energy neutrinos (blue circle in figure 3.11) are larger than that for the lower energy neutrinos (red circle in figure 3.11) as discussed by Kotake et al. (2006), the impact parameter is larger for the higher energy neutrinos. As a consequence, the higher the neutrino energies are, the more the distributions are tilted to the ϕ-direction like the straight arrows in figure 3.11.

3.3.3 Rotational Flux

Since rotation makes the neutrino distributions asymmetric with respect to the plane spanned by $\boldsymbol{e}_r$ and $\boldsymbol{e}_\theta$, the ϕ-component of the neutrino flux is non-zero in general. The "rotational" component of the electron-type neutrino number flux at 100 ms after the core

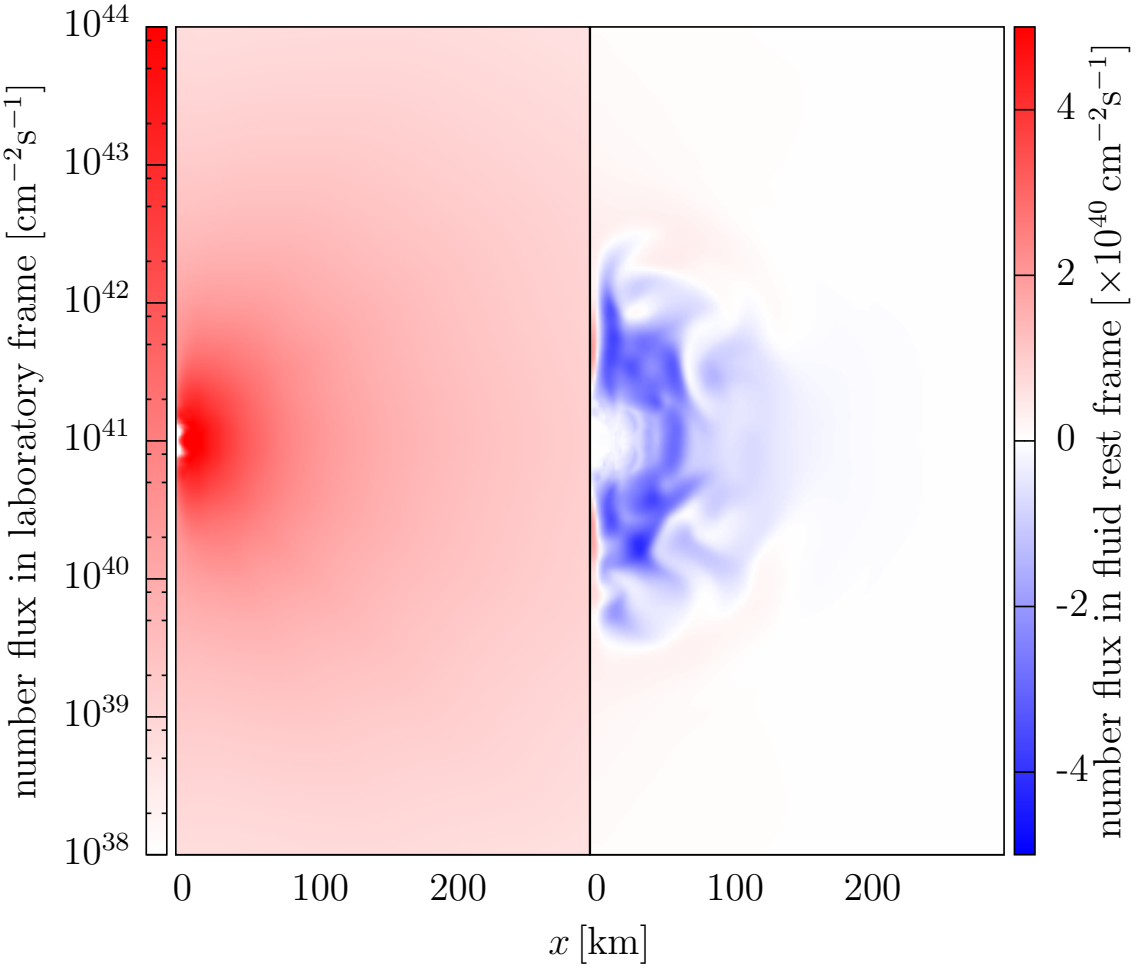

Figure 3.12. The rotational component of the number flux of ν_e at 100 ms after the core bounce. The left panel shows the ϕ-component measured in the laboratory frame. The color bar is shown with the log-scale. The right panel displays the flux measured in the fluid-rest frame. The color bar is shown with the linear scale.

bounce is illustrated in figure 3.12. The rotational component measured in the laboratory frame is shown in the left panel. Since the ϕ-component is positive (the same direction with the rotation) everywhere, the color bar is shown with the log-scale. This figure indicates that the ϕ-component decreases rapidly with the radius. This tendency is consistent with the above discussion on $\bar{\theta}$.

The ϕ-component of the flux in the fluid-rest frame is shown in the right panel. Contrary to the left panel, the color bar is indicated with the linear scale, and the flux is not necessarily positive. Now let me define the "rotational velocity" of the neutrinos by the number flux divided by the number density of neutrinos. The rotational velocity of the neutrinos in the laboratory frame is slower than that of matter after the neutrinos decouple with the matter. This fact is described in figure 3.13. The radial profiles of the rotational component of the number flux and the rotational velocities of matter and neutrinos along the equatorial direction are shown in the figure. The rotational components in the fluid-

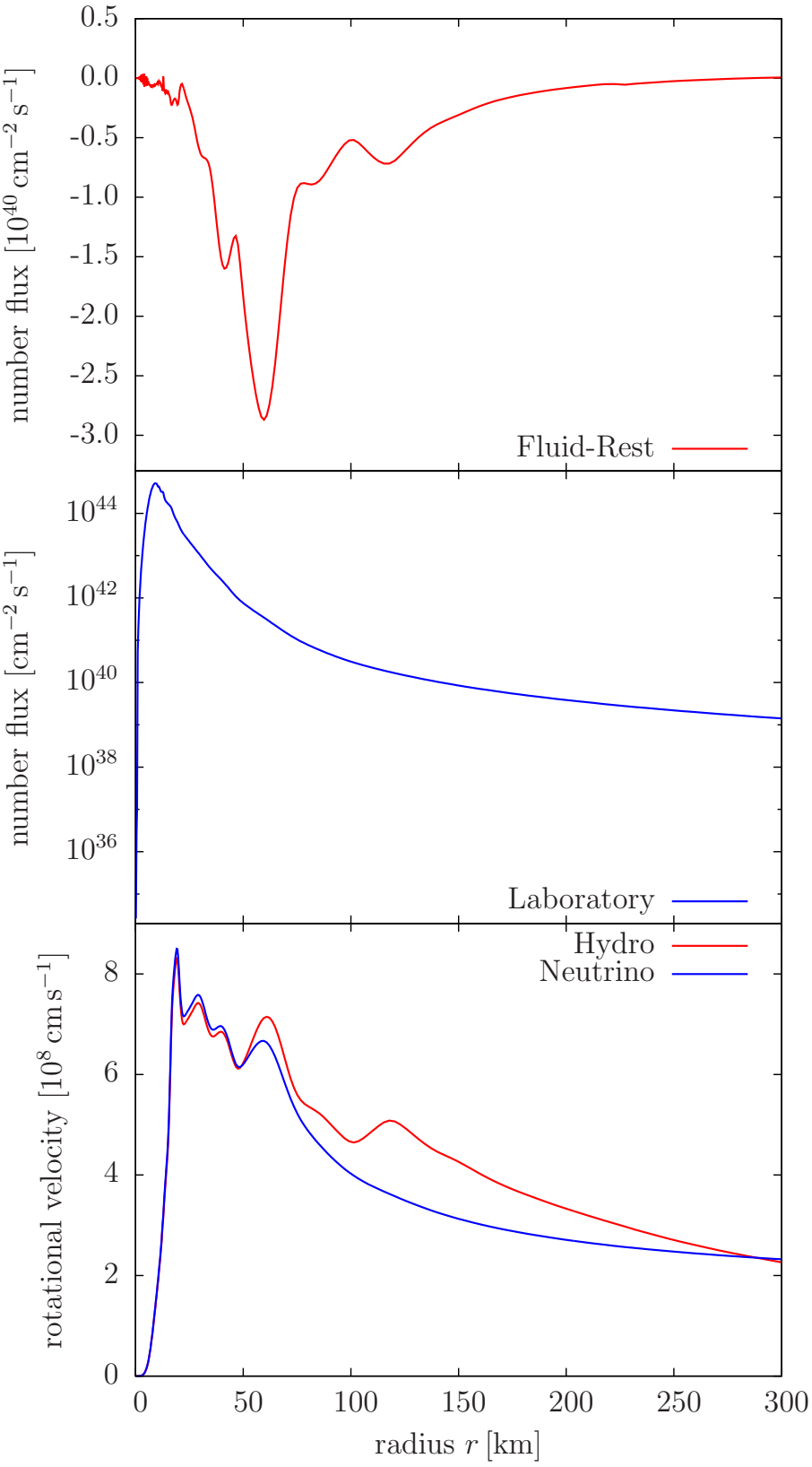

Figure 3.13. The radial profile of the ϕ-component of the neutrino number flux for the electron-type neutrinos in the fluid-rest frame, that in the laboratory frame, and the rotational velocities of both matter and neutrinos in the laboratory frame are shown in the top, middle, and bottom panels, respectively. In the bottom panel, the matter and neutrino velocities are drawn with red and blue lines, respectively. Only the middle panel is displayed with the log-scale.

rest frame and laboratory frame are negative and positive, respectively. The ϕ-components of the velocity of matter and neutrinos in the laboratory frame are almost the same at $r < 50\,\mathrm{km}$ and the matter velocity exceeds the neutrino velocity at larger radii. Since the matter overtakes neutrinos, the ϕ-component of the neutrino flux in the fluid-rest frame is negative. This neutrino trapping and the overtaking show that the simulation successfully captures the neutrino transport on the moving matter.

3.3.4 Eddington Tensor

Recall that the spherically symmetric neutrino transport is solved in the RbR(+) approximation (Buras et al., 2006) discussed in section 2.2.1, and hence the neutrino distributions are assumed to be axisymmetric with respect to the radial direction. Therefore, the lateral component of the flux discussed in the previous section is artificially set to zero with RbR(+). On the other hand, if RbR(+) is not employed, one can treat the non-radially directed flux. Among the non-RbR(+) approximate schemes, the M1-closure method without RbR(+) (Levermore (1984); Shibata et al. (2011), and for example of the application to the CCSNe, see Kuroda et al. (2012); Just et al. (2015)) is the most sophisticated currently. As discussed in section 2.2.1, two assumptions are employed in the M1-closure method: the axisymmetric distribution of neutrinos and the formula for the Eddington factor. Since the Boltzmann solver employed in this chapter does not impose such assumptions, the validity of these assumptions can be evaluated quantitatively.

In order to evaluate the accuracy of the M1-closure method, I compare the Boltzmann- and M1-Eddington tensors defined in section 2.2.1. First, the second angular moment $M^{\sigma\rho}(\epsilon)$ is calculated from equation (2.79). Then, the Boltzmann-Eddington tensor $k^{ij}(\epsilon)$ is evaluated by using equation (2.76) with spatial-spatial (equation (2.77)) and time-time (equation (2.78)) projections of $M^{\sigma\rho}(\epsilon)$[*1]. For the M1-Eddington tensor $k^{ij}_{\mathrm{M1}}(\epsilon)$, however, the energy fluxes and energy densities are obtained from equations (2.78), (2.85), (2.86), and (2.89), and then equation (2.80) is evaluated from equations (2.81), (2.82), (2.83), (2.87), and (2.88). Although one can think the energy-integrated version of the Eddington tensor, the energy-dependent version of the Eddington tensor is adopted in this chapter. The neutrino energy is always chosen as the mean energies at each spatial point.

The M1-closure prescription described in section 2.2.1 is the same as Kuroda et al. (2016b) except that they employ the Eddington factor formula different from equation (2.82). Variations of the Eddington factor formulae are presented in Just et al. (2015), and they use the Eddington tensor defined in the fluid-rest frame.

[*1] Actually a modified version of equation (2.79) where the argument of the delta function $\epsilon - \epsilon'$ is replaced by $\epsilon^3/3 - \epsilon'^3/3$ is employed. Since the original version of Shibata et al. (2011) considers the neutrino-radiation field in an intensity-like way, the independent variables are the energy and flight direction. On the other hand, the neutrino-radiation field in this chapter is considered as an ensemble of particles, and hence the independent variables are three components of momentum. Thus the energy ϵ itself is a natural choice in Shibata et al. (2011) while the volume element in the momentum space $\epsilon^3/3$ is natural here. This difference results in an extra factor of ϵ^2, but have no effects on the discussions below, since the extra factors are canceled in the calculation of the Eddington tensors.

Physical Interpretation of the Eddington Tensor

In figure 3.14, I compare the spatial distributions of each component of the Boltzmann- and M1-Eddington tensors at the 12 ms in the laboratory frame. They are the Eddington tensors of electron-type neutrinos with mean energies. The oval shapes seen in each figure roughly correspond to the shock (see the lower left panel of figure 3.3). For diagonal components, the central value is 1/3 both for the Boltzmann- and M1-Eddington tensors. This is consistent with the optically thick limit. Then, the rr-components increase ($\theta\theta$- and $\phi\phi$-components decrease) with the radius to the optically thin limit. The transition from the optically thick to thin limits occurs in the vicinity of the shock for both Eddington factors, but it occurs at the slightly smaller radius for the M1-Eddington tensor as illustrated in the left panels of top two and middle left figures.

The off-diagonal components are $\sim$ 10–100 times smaller than the diagonal components, but their presence indicates that the principal axes of the Eddington tensor differ from r-, θ-, and ϕ-directions. The off-diagonal components are determined by complex interplays of the matter velocities and neutrino reactions. In order to see the physical origin of the pattern of the off-diagonal component, radial profiles of several quantities along selected direction are shown in figures 3.15, 3.16, and 3.17. Here, I focus on the $r\theta$-component $k^{r\theta}$ since the difference between $k^{r\theta}$ and $k^{r\theta}_{\rm M1}$ is even qualitative level and discussed later.

The Eddington tensor is the second angular moment of the distribution functions, that is, the $\ell = 2$ mode amplitudes in the words of spherical harmonics expansion. On the other hand, the flux is the first angular moment and $\ell = 1$ mode amplitudes. In principle, the $\ell = 2$ modes and $\ell = 1$ modes are independent. However, for example, if a bunch of neutrinos flies toward a single direction, the signs of the Eddington tensor itself and the product of the components of flux is the same. Consider that the neutrinos fly toward the direction where both r- and θ-components are positive, then the $r\theta$-component of the Eddington tensor is also positive. If several bunches of neutrinos fly, on the other hand, the sings are not necessarily the same. Keep this fact in mind, let me show the details of these figures.

In the optically thick region, the neutrinos move with the fluid elements due to neutrino trapping. The relativistic beaming distorts the neutrino distributions toward the fluid velocity, then the neutrino flux and the matter velocity have the same direction. The signs of the neutrino flux and the matter velocity is the same in the optically thick (optical depth, say, $\tau \gtrsim 50$) regions as indicated by the second and fourth (r-component), and the third and fifth (θ-component) panels. Since the sign of the $k^{r\theta}$ and the product of $v^r v^\theta$ or $F^r F^\theta$ are the same there, the Eddington tensor is entirely determined by the fluid motion via the relativistic aberration in the optically thick region.

In the semi-transparent (optical depth $50 \gtrsim \tau \gtrsim 2/3$) region, the sign of the tensor component $k^{r\theta}$ and the product $F^r F^\theta$ are still the same. Thus it is implied that the Eddington tensor is determined by a bunch of neutrinos. The signs of r-components of the neutrino flux and the fluid velocity are opposite since the neutrinos are escaping from the optically thick regions. On the other hand, the θ-components of them are the

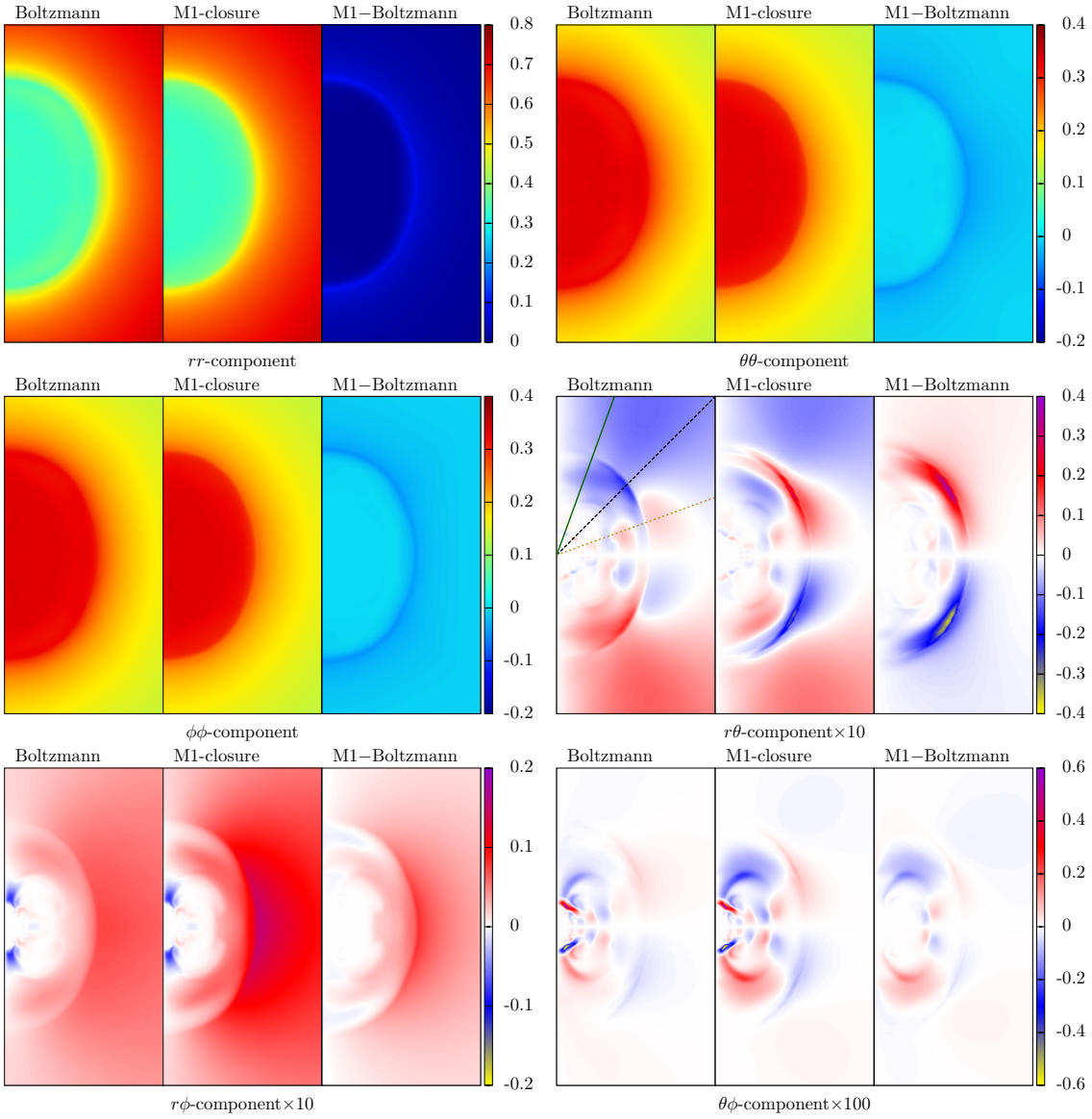

Figure 3.14. The comparison of each component of the Boltzmann- and M1-Eddington tensors at 12 ms in the laboratory frame. The neutrino species is the electron-type and the energy is chosen to be mean energies. The range of $0\,\mathrm{km} \leq x \leq 150\,\mathrm{km}$ and $-150\,\mathrm{km} \leq z \leq 150\,\mathrm{km}$ is displayed. Each panel represents each component of the Eddington tensors (rr: top left, $\theta\theta$: top right, $\phi\phi$: middle left, $r\theta$: middle right, $r\phi$: bottom left, $\theta\phi$: bottom right). In each figure, the left and middle parts show the Boltzmann- and M1-Eddington tensors, respectively. The right parts are the difference of the M1- and Boltzmann-Eddington tensors, $k^{ij}_{\mathrm{M1}} - k^{ij}$. For off-diagonal components, the indicated values are multiplied by 10 or 100 as written in the bottom of each figures, in order to show them in similar color scales. However, note that the color scales itself are different among figures.

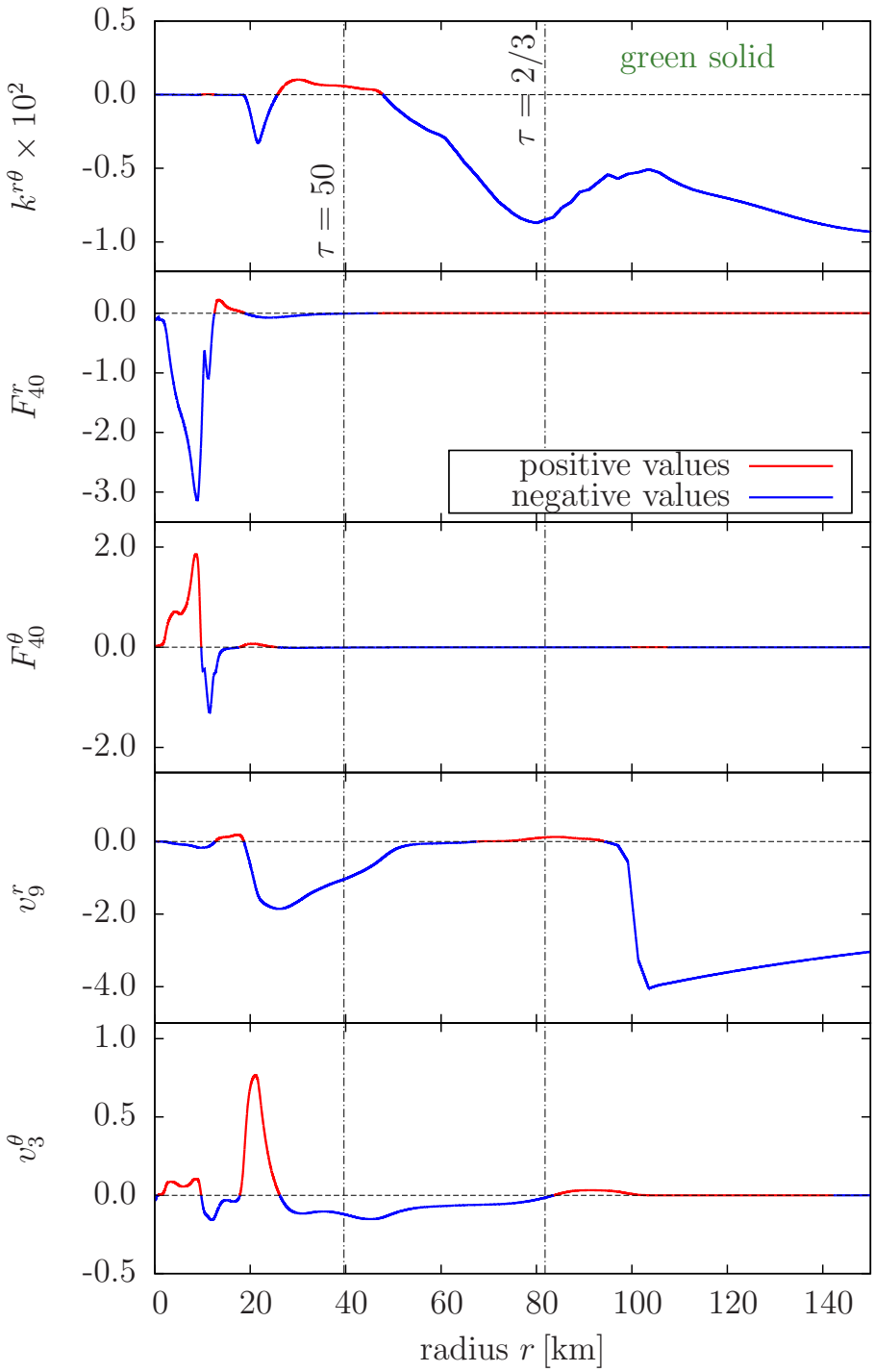

Figure 3.15. Radial profiles of several quantities related to the $r\theta$-component of the Eddington tensor $k^{r\theta}$ along the green solid line in the middle right panel of figure 3.14. From top to bottom, the r-component $F^r_{40} := (F^r/10^{40}\,\mathrm{erg\,cm^{-2}\,s^{-1}})$, θ-component $F^\theta_{41} := (F^\theta/10^{41}\,\mathrm{erg\,cm^{-2}\,s^{-1}})$ of the energy flux of ν_e , r-component $v^r_9 := (v^r/10^9\,\mathrm{cm\,s^{-1}})$ and θ-component $v^\theta_3 := (v^\theta/10^3\,\mathrm{rad\,s^{-1}})$ of the matter velocity are displayed. For each panel, parts of lines whose values are positive are colored red, while those negative is blue. The vertical dash-dotted lines correspond to the radii where the optical depths τ along the radial ray are 50 and 2/3 as indicated near the lines.

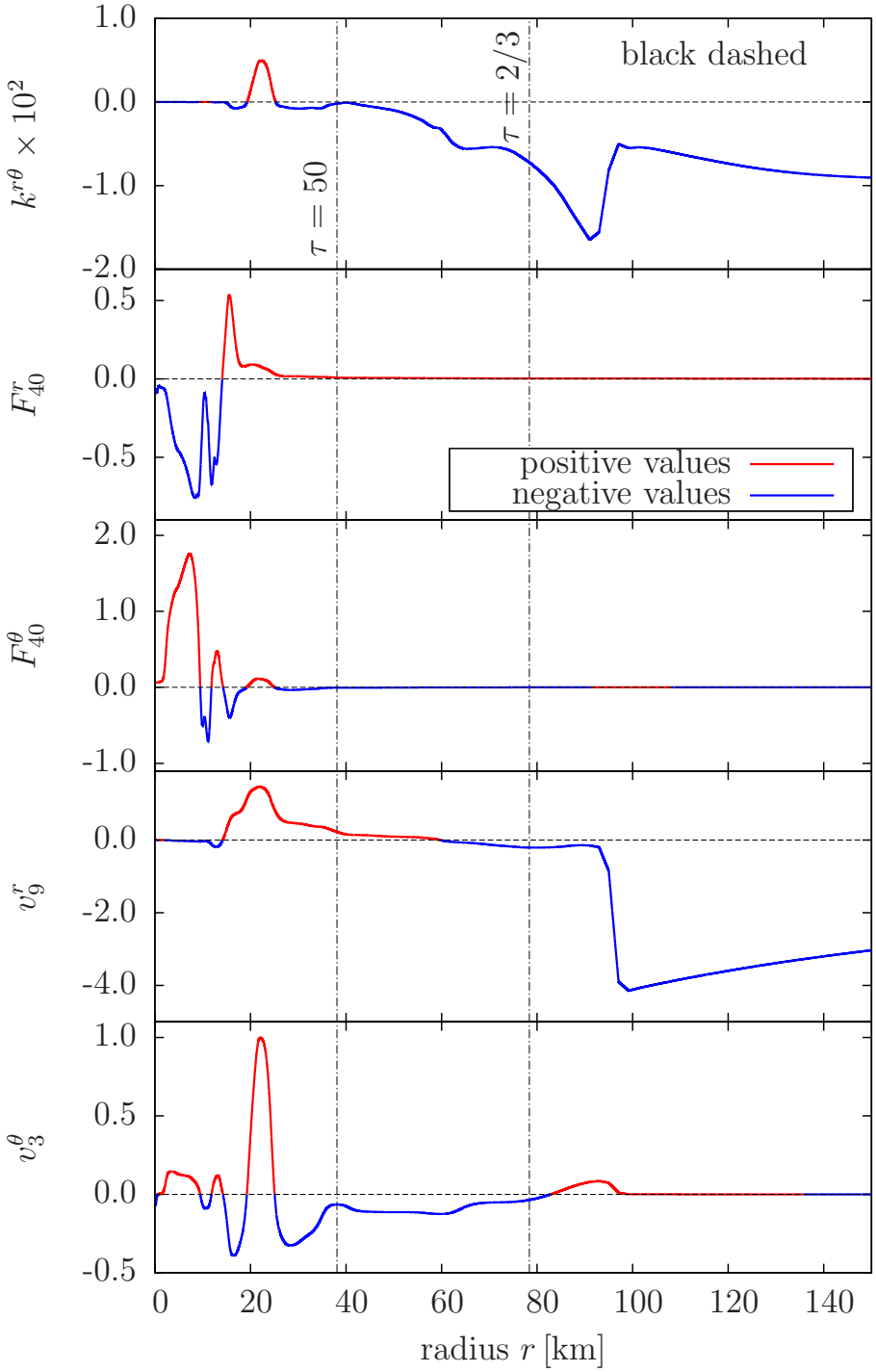

Figure 3.16. The same as figure 3.15 but along with the black dashed line.

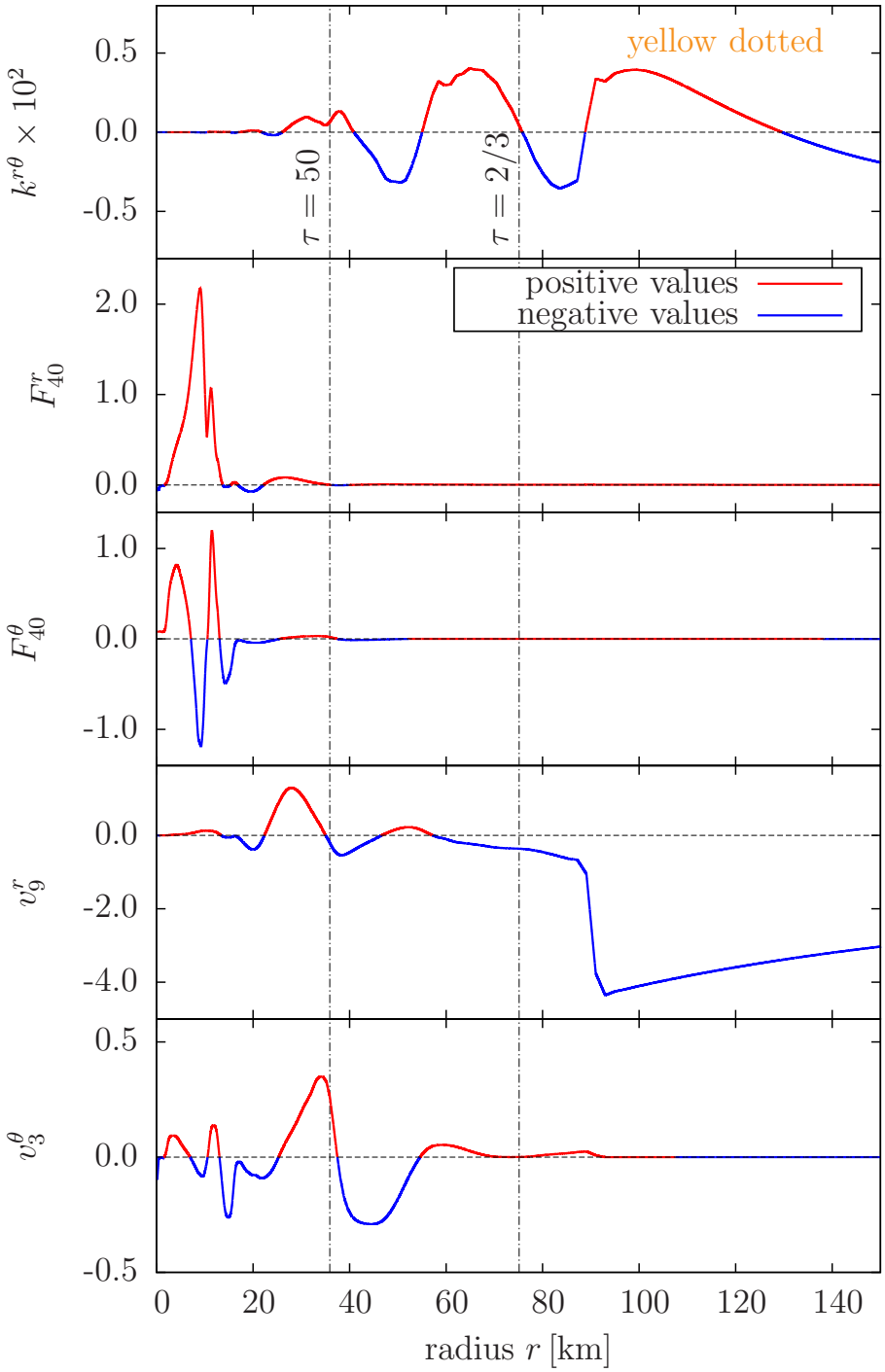

Figure 3.17. The same as figure 3.15 but along with the yellow dotted line.

same. This is because, in the semi-transparent regions, interactions between neutrinos and matter are so weak that the matter cannot reverse the radial flow of neutrinos, but strong enough to bend the direction of neutrinos.

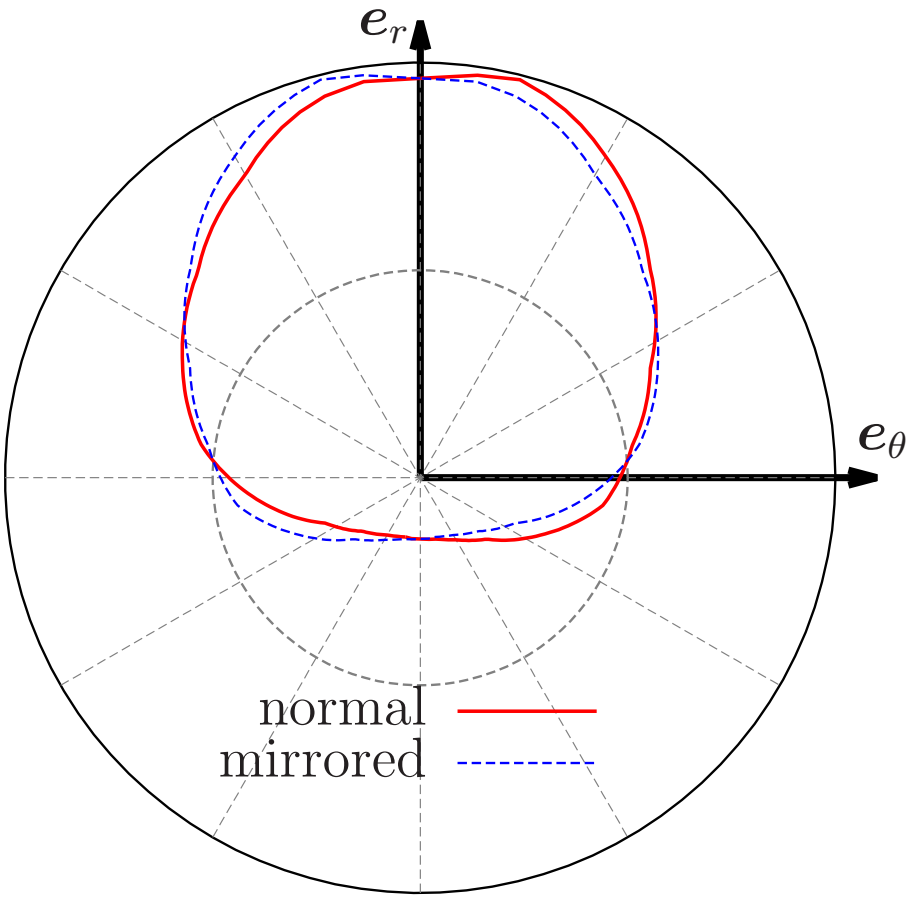

Figure 3.18. The solid red curve shows a section of the angular distribution function of the electron-type neutrinos spanned by $\boldsymbol{e}_r$-$\boldsymbol{e}_\theta$. The spatial point is $r = 82\,\mathrm{km}$ along the yellow dotted line in figure 3.14, and the neutrino energy is the mean energy ($\sim 11\,\mathrm{MeV}$) there. The blue dashed curve is a mirror image of the red curve with respect to the $\boldsymbol{e}_r$ axis.

In the optically thin (optical depth $\tau \lesssim 2/3$) region, the flux and the Eddington tensor does not necessarily correlate. For the three rays in figures 3.15, 3.16, and 3.17, there are regions where the signs of the $k^{r\theta}$ and the product $F^r F^\theta$ are different. This implies that there are multiple bunches of neutrinos. The angular distribution of ν_e at a point in the optically thick region ($r = 82\,\mathrm{km}$ on the yellow dotted line in figure 3.14) shown in figure 3.18 describes the situation. Not only the angular distribution itself but also the mirror image of it are displayed, in order to emphasize the distortion of the distribution.

It is indicated that the neutrinos mainly fly toward the upper right direction of the figure. Besides, some neutrinos are flying toward the lower right direction. The upper right component is neutrinos coming from the PNS, bent by the matter in the semi-transparent regions. On the other hand, the lower right component is originated from the

neighborhood: the matter inside the shock is dense and hot enough to emit neutrinos even at just downstream of the shock, and the neutrinos emitted from there is beamed by the matter velocity. At the spatial point considered in figure 3.18, the fluid velocity directs lower right: figure 3.17 implies $v^r < 0$ and $v^\theta > 0$ at $r = 82\,\mathrm{km}$. Thus the neutrinos emitted from the neighborhood matter contributes to the lower right component of the distribution. Hereafter the upper right and lower right components are called the PNS and neighborhood components, respectively.

The Eddington tensor in the optically thin region is determined by the competition of the PNS and neighborhood components. Along the yellow line, the neighborhood component determines the $k^{r\theta}$. The sign of the $k^{r\theta}$ changes from the semi-transparent region in the vicinity of the shock due to the neighborhood contribution, and the sign recovers outside the shock. On the other hand, on the green line, the sign of $k^{r\theta}$ is determined by the PNS component. Although the neighborhood component has a positive contribution to $k^{r\theta}$ (the fluid velocity in the optically thin region is $v^r > 0$ and $v^\theta > 0$ as seen in figure 3.15), the $k^{r\theta}$ is negative, indicating that the PNS component dominates it. Along the black dashed line, another case is observed. Both the PNS and neighborhood components have negative contributions on the $k^{r\theta}$, although the product of $F^r F^\theta$ is positive. In detail, the PNS component has large positive and small negative contributions to F^r and F^θ, respectively, while the local component has small negative and large positive contributions to F^r and F^θ, respectively. Therefore the $k^{r\theta} < 0$ and $F^r F^\theta > 0$ are realized simultaneously.

Comparison Between Boltzmann- and M1-Eddington Tensors

Here, let me move on the comparison between the Boltzmann- and M1-Eddington tensors. Between the off-diagonal components of Boltzmann- and M1-Eddington tensors, the similarity in both optically thick and thin limits is seen. This is because only one bunch of neutrinos (trapped by and moving with the matter in the optically thick limit and streaming freely in the optically thin limit) determines both the flux and Eddington tensor. On the other hand, the behaviors are different in the semi-transparent regions. Even the signature is different in the vicinity of the shock for the $r\theta$-component, while the values of the M1-Eddington tensor are twice as large as that of the Boltzmann-Eddington tensor there for the $r\phi$- and $\theta\phi$-components.

In order to see the qualitative difference in the $r\theta$-components of the Eddington tensors, the radial profiles of the Eddington tensors are shown in figure 3.19: the Boltzmann-Eddington tensor $k^{r\theta}$ (equation (2.77)), the M1-Eddington tensor $k^{r\theta}_{\mathrm{M1}}$ (equation (2.81)), the optically thin Eddington tensor $k^{r\theta}_{\mathrm{thin}} := P^{r\theta}_{\mathrm{thin}}/E$ (equation (2.87)), and the optically thick Eddington tensor $k^{r\theta}_{\mathrm{thick}} := P^{r\theta}_{\mathrm{thick}}/E$ (equation (2.88)). The $k^{r\theta}_{\mathrm{M1}}$ and $k^{r\theta}_{\mathrm{thick}}$ are positive at $r \gtrsim 85\,\mathrm{km}$, while the $k^{r\theta}_{\mathrm{thin}}$ is positive at $r \gtrsim 87\,\mathrm{km}$. As indicated in figure 3.16, F^r is always positive in $80\,\mathrm{km} \leq r \leq 100\,\mathrm{km}$, and F^θ is negative at $r \gtrsim 87\,\mathrm{km}$. Thus the optically thin Eddington tensor mistakenly takes positive values at $r \gtrsim 87\,\mathrm{km}$. Besides, although the $k^{r\theta}_{\mathrm{thin}}$ is negative at $r \lesssim 87\,\mathrm{km}$, the $k^{r\theta}_{\mathrm{thick}}$, which determines the $k^{r\theta}_{\mathrm{M1}}$, takes positive values. This is because the terms $H^r V^\theta + V^r H^\theta$ in equation (2.88) take positive

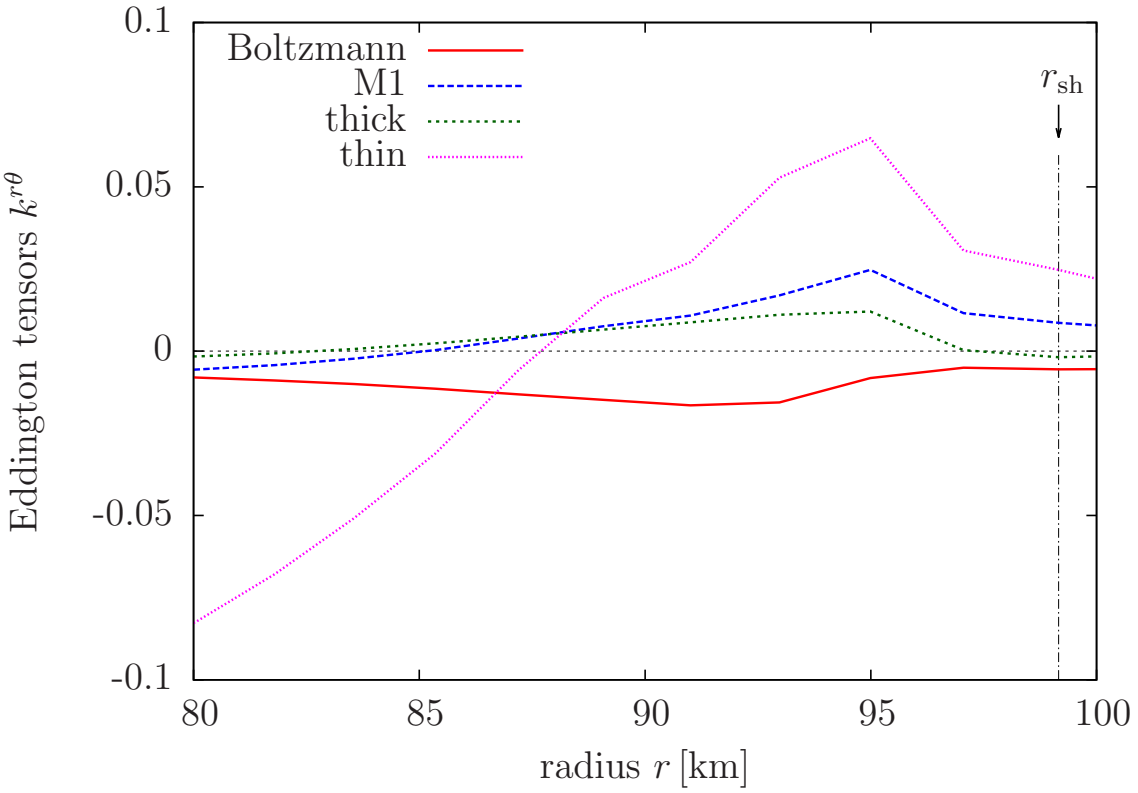

Figure 3.19. Radial profiles of the $r\theta$-components the Eddington tensors $k^{r\theta}(\epsilon)$, $k^{r\theta}_{\rm M1}(\epsilon)$, $k^{r\theta}_{\rm thin}(\epsilon)$, and $k^{r\theta}_{\rm thick}(\epsilon)$ along the black dashed line in figure 3.14. The neutrino energy ϵ is chosen as the mean energy. The vertical dash-dotted line indicates the position of the shock.

values. These terms are the higher than zero-th order terms with respect to the mean free path. Since some correction terms higher than zero-th order are neglected in equation (2.88) as discussed in section 2.2.1, such corrections may be required. Instead, the M1-closure method tries to correct by interpolating the optically thick and thin limits. The figure describes that such correction fails. The differences in the off-diagonal components of the Eddington tensors may have non-negligible effects on the lateral component of the neutrino flux as discussed in Nagakura et al. (2018).

The Eddington tensor can be diagonalized thanks to its symmetric property, and its eigenvalues illustrate the shape of the angular distribution of neutrinos. The largest eigenvalue is called the Eddington factor, and it represents how sharp the distribution in one direction is. Other two eigenvalues describe the flatness of the angular distribution along the perpendicular directions. The eigenvalues of the Boltzmann- and M1-Eddington tensors are shown in figure 3.20. Again, the figure implies that the Eddington factor takes optically thick limit values of 1/3 deep inside the shock, starts to increase in the vicinity of the shock, and reaches the free-streaming value outside. Two eigenvalues, which are named "lateral 1, 2", other than the Eddington factor decrease with the radius since the sum of three eigenvalues is unity (c.f. equation (14) in Levermore (1984)).

As discussed in section 2.2.1, the axisymmetric distribution with respect to the flux

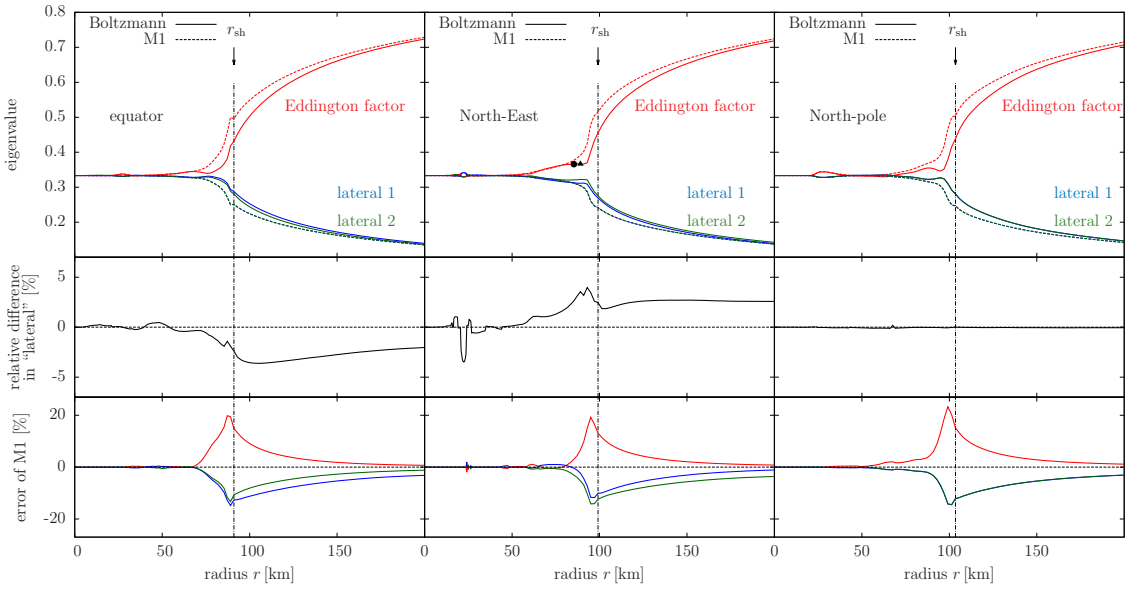

Figure 3.20. The radial profiles of eigenvalues of the Boltzmann- and M1-Eddington tensors for ν_e with the mean energies along three radial rays. They are measured at 12 ms after the core bounce in the laboratory frame. The red, blue, and green lines indicate the largest eigenvalue (the Eddington factor), other two eigenvalues named "lateral 1", and "lateral 2", respectively. The solid and dashed lines correspond to the eigenvalues of the Boltzmann- and M1-Eddington tensors, respectively. The chosen rays are on the equatorial direction (the left panels), the north-east direction (the middle panels), and the north-pole direction (the right panels). The vertical dash-dotted lines indicate the shock radii in each direction. From top to bottom rows, the eigenvalues, the relative difference between lateral 1 and 2, and the fractional errors of the M1-Eddington tensor are illustrated. The black small circle and triangle in the top middle panel are the points where the angular distributions are compared (see the discussion about figure 3.21).

direction is assumed in the M1-closure method. As a consequence, lateral 1 and lateral 2 for the M1-Eddington tensor are degenerate in figure 3.20. On the other hand, the lateral eigenvalues of the Boltzmann-Eddington tensor are slightly different, since no artificial symmetry in the distributions is imposed. However, the relative difference between lateral 1 and 2 is only a few percents as shown in the middle panels of figure 3.20. Here, the lateral difference is defined as $(\kappa_{\rm lat2} - \kappa_{\rm lat1})/\kappa_{\rm lat1}$, where $\kappa_{\rm lat1}$ and $\kappa_{\rm lat2}$ are the eigenvalues of lateral 1, 2, respectively. The small difference implies that the almost axisymmetric distribution with respect to the flux direction is nearly achieved as a consequence of the evolution. It may seem that the assumption of the symmetry in the M1-closure method is accurate up to a few percents, but such a small deviation from the axisymmetry leads to the complicated relationships among the Eddington tensor, the flux, and the matter velocity.

The M1-closure method is not so accurate to estimate the Eddington factor. In order

to discuss the accuracy, let me define the fractional errors between the eigenvalues of the Boltzmann- and M1-Eddington tensors as $(\kappa_{\rm M} - \kappa_{\rm B})/\kappa_{\rm B}$ where $\kappa_{\rm B}$ and $\kappa_{\rm M}$ are some eigenvalues of the Boltzmann- and M1-Eddington tensors, respectively. The fractional errors are shown in the bottom panels of figure 3.20 and reach $\sim 20\%$ at most in the vicinity of the shock. There are other choices than equation (2.82) to determine the Eddington factor analytically (e.g., Just et al., 2015), though they also have at least $\sim 10\%$ errors.

Consider two points indicated by the black circle and triangle in the top middle panel of figure 3.20. The M1-Eddington factor is larger for the point with the black triangle than that with the black circle, while the Boltzmann-Eddington factor is almost the same. For the left and right panels, the Boltzmann-Eddington factors even decrease with radius in some regions close to the shock. According to equation (2.82), the Eddington factor is a monotonically increasing function of the flux factor. Therefore, in these regions, the flux factors increase while the Eddington factors do not. This different behavior is again illustrated by examining the shape of the distribution function.

In figure 3.21, two angular distributions of $\nu_{\rm e}$ are shown. These two distributions are taken from the points with the small black circle and triangle in the top middle panel of figure 3.20. Let me define the "flux direction" as the direction where the distribution function is the maximum, although this definition might not coincide with the direction of the flux F^i. This is because the latter is determined by the angular average of the unit vector. Figure 3.21 shows the flux direction by the green arrow in the middle panel. From the figure, the distribution function in the opposite side of the flux direction is smaller for the point of the triangle. Roughly speaking, the flux factor is the average value $\langle \cos\tilde{\theta} \rangle$ and the Eddington factor is $\langle \cos^2\tilde{\theta} \rangle$, where $\tilde{\theta}$ is the angle measured from the flux direction and $\langle \cdot \rangle := \int f \cdot {\rm d}V_p / \int f {\rm d}V_p$ is the angle average with respect to the distribution function. Therefore, when the distribution around $\cos\tilde{\theta} \sim -1$, i.e., the opposite side of the flux direction, reduces with the radius, the flux factor increases while the Eddington factor decreases. Note that the reduction of the distribution in the opposite side leads to a decrease in the denominator of the angle average defined above and hence to an increase in the average value. In summary, the reduction of the distribution around $\cos\tilde{\theta} \sim -1$ necessarily leads to an increase in the flux factor, but the Eddington factor is not changed so much due to the decrease in both the numerator and denominator. This is what happens in the vicinity of the shock.

From the viewpoint of the physical situation, the reduction discussed above means that the backward propagating neutrinos decrease with getting closer to the shock. Since the shocked matter is hot and dense, it emits neutrinos not only outward, but also inward. As getting closer to the shock, the region of such inwardly neutrino-emitting matter gets smaller. The code here can treat this situation appropriately since the forward and backward propagating neutrinos are treated individually. The M1-closure method, however, only treat the energy density and the flux, and cannot distinguish the increase in outward propagating neutrinos and the decrease in backward propagating neutrinos. As discussed above, the physical situation is relatively clear. If information from the neighborhood

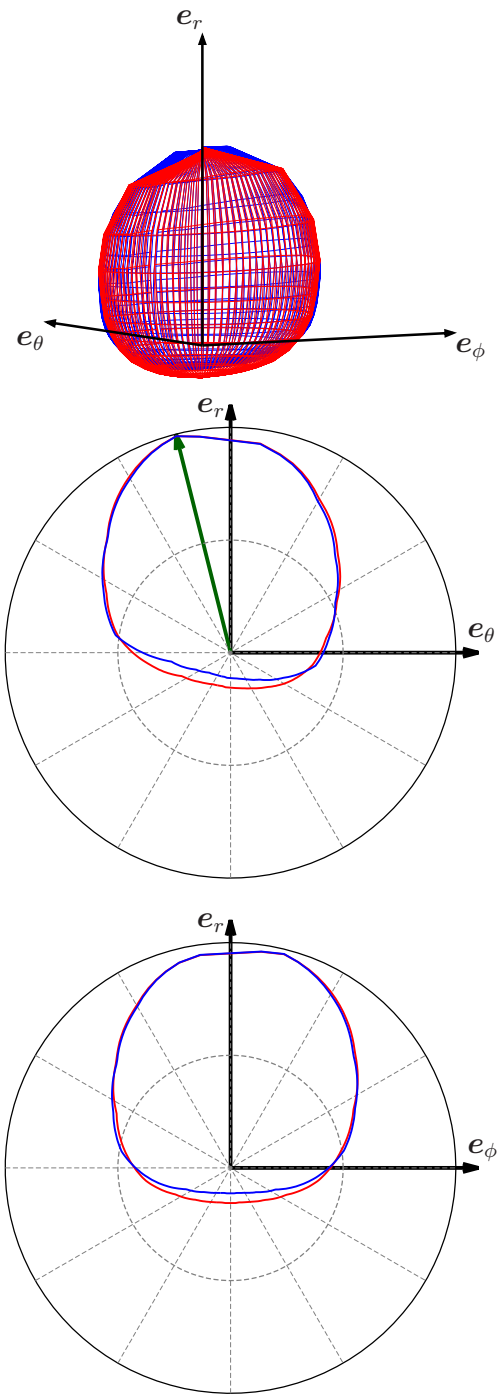

Figure 3.21. Angular distributions of ν_e in the laboratory frame at the two points shown as the black circle and triangle in the top middle panel of figure 3.20. The neutrino energy is again the mean energy at each point. The distributions are normalized so that the maximum values are the same. Red surface and lines show the angular distribution at the small black circle in figure 3.20, while blue surface and lines represent that at the small black triangle. The top panel shows the full angular distribution, whereas the middle and bottom panels indicate the sections spanned by $\boldsymbol{e}_r$-$\boldsymbol{e}_\theta$ and $\boldsymbol{e}_r$-$\boldsymbol{e}_\phi$ planes, respectively. The green arrow in the middle panel shows the flux direction.

is considered, the approximate formula like equation (2.82) may be calibrated, and the M1-closure method may be improved, while this is beyond the scope of this dissertation.

Resolution

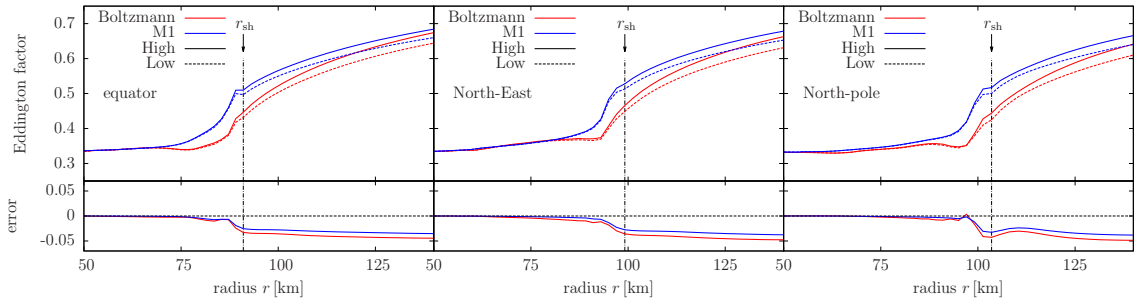

Figure 3.22. The comparison of the Boltzmann- (red) and M1- (blue) Eddington factors for electron-type neutrinos with the high- (solid) and low- (dashed) resolutions. The neutrino energies are the mean energies at individual points. Shown in the lower panel is the fractional error between high- and low-resolution results.

The angular grid number in the momentum space is not large because of the limited computational resources. For the detailed investigations on the resolution and convergence, see Richers et al. (2017). The neutrino distributions are almost isotropic in the optically thick region, and hence the grid number employed in this chapter is enough to resolve them. The forward-peaked distribution of neutrinos in the optically-thin region, on the other hand, requires higher resolution than that employed in the code here. Therefore one may think that the differences shown in figure 3.20 are artifacts of low resolutions.

In order to check the effects of numerical resolutions on the errors indicated in figure 3.20, I run additional simulations with low and high resolutions. In these simulations, the steady-state solutions of the Boltzmann equation with the background matter fixed at 12 ms after the core bounce are constructed. The computational domain is limited from ~ 40 km to ~ 300 km in order to reduce the computational cost. The angular grid numbers in momentum space are $(\theta_\nu, \phi_\nu) = (10, 6)$ for low resolution and (14, 10) for high resolution.

Results of the high- and low-resolution simulations are shown in figure 3.22. I plot the Boltzmann- and M1-Eddington factors of high- and low-resolution simulations and the error between the high- and low-resolutions in the figure. Note that contrary to figure 3.20, the error between the Boltzmann- and M1-Eddington factors are not presented. In the figure, the errors of both the Boltzmann- and M1-Eddington tensors are small in the optically thick region, especially where the Boltzmann-Eddington factor itself is ≤ 0.4. The errors are, however, $\sim 5\%$ in the semi-transparent and optically thin regions. Therefore the numerical convergence is achieved only in the inner, optically thick region in the low-resolution simulation. Note that this is compatible with the results in Richers et al. (2017). Since the large error shown in figure 3.20 can also be seen as the difference of red and blue lines in figure 3.22, the error between the Boltzmann- and M1-Eddington

factors is not an artifact due to the limited resolution employed in this chapter.

3.3.5 Angular Momentum Transport

At the end of this section, I discuss the angular momentum transport by neutrinos. The neutrinos carry the angular momentum of matter away as shown in figure 3.6. The angular momentum loss is evaluated from the distribution function directly. The energy-momentum tensor of the neutrinos is defined as

$$T^{\sigma\rho}_{(\nu)} := \int f p^\sigma p^\rho \mathrm{d}V_p. \tag{3.6}$$

From this definition and the Boltzmann equation, the energy-momentum conservation with matter interactions is derived (Cercignani & Kremer, 2002)

$$\nabla_\sigma T^{\sigma\rho}_{(\nu)} = G^\rho, \tag{3.7}$$

where G^ρ is the same term defined in equation (2.113). The energy-momentum tensor is calculated by using the second angular moment tensor (equation (2.79)) as $T^{\sigma\rho}_{(\nu)} = \int M^{\sigma\rho}(\epsilon)\mathrm{d}(\epsilon^3/3)$. Considering that there exists the Killing vector $\xi = \partial_\phi$ under axisymmetry, the angular momentum 4-current is defined by $j^\rho := \xi_\sigma T^{\sigma\rho}$, which obeys

$$\nabla_\rho j^\rho = \xi_\rho G^\rho, \tag{3.8}$$

according to equation (3.7). By defining the total angular momentum of neutrinos enclosed by the sphere of radius r as $J_{(\nu)}(r) := \int_0^r j^t \mathrm{d}V_x$, the conservation law is rewritten in the integral form,

$$\dot{J_{(\nu)}}(r) + \int_{S(r)} j^r \mathrm{d}s = \int \xi_\rho G^\rho \mathrm{d}V_x, \tag{3.9}$$

where $\mathrm{d}s$ and $S(r)$ are the surface element and sphere of radius r, respectively. The angular momentum exchange between the neutrinos and matter is described by the right-hand side. Assuming that the angular momentum transport of the matter by advection is negligible, the angular momentum of the matter is transferred to the neutrinos via the term $\int \xi_\rho G^\rho \mathrm{d}V_x$, and lost by neutrino emission via the term $\int j^r \mathrm{d}s$. Therefore this angular momentum loss by neutrinos is

$$\begin{aligned}\dot{J}(r) &:= -\int_{S(r)} j^r \mathrm{d}s = -\int_{S(r)} r^2 \sin^2\theta T^{\phi r}_{(\nu)} \mathrm{d}s \\ &= -\int \mathrm{d}s \int \mathrm{d}V_p r^2 \sin^2\theta f p^\phi p^r.\end{aligned} \tag{3.10}$$

The surface of the integral $S(r)$ can be chosen freely, and I chose it with $r = 100\,\mathrm{km}$ in the discussions below. This is because this radius is the largest radius where the numerical convergence is achieved by the resolution test in section 3.3.4. Besides, a sum over all neutrino flavors should be taken.

On the other hand, an analytic estimation of the angular momentum loss is proposed in Epstein (1978). In his paper but in terms of the natural unit, the angular momentum

loss by neutrinos $\dot{J}$ is evaluated as

$$\dot{J} = -\int \left(\frac{L_\nu}{4\pi r^2} \right) \omega r_\perp^2 \, \mathrm{d}s, \tag{3.11}$$

where L_ν and $r_\perp$ are the neutrino luminosity and the distance from the rotational axis, respectively, and the surface of the integral is the "stellar surface" where neutrinos are emitted. In the context of the CCSN, it is the neutrinosphere. In the derivation, he assumes the isotropic neutrino distributions in the fluid-rest frame, and hence its angular momentum in the laboratory frame is achieved by the relativistic beaming by the matter rotation. In order to exploit this equation, the neutrino luminosity is also needed. For simplicity, I adopt the black body formula,

$$L_\nu = 4\pi r^2 \times \frac{7}{16} \sigma_{\mathrm{SB}} T^4, \tag{3.12}$$

for each neutrino flavor at the neutrinosphere, where σ_{SB} and T are the Stefan-Boltzmann constant and the matter temperature at the neutrinosphere, respectively. Here the neutrinosphere is defined at the radius where the density is $\rho = 10^{11}\,\mathrm{g\,cm^{-3}}$. The expression is finally multiplied by six, in order to account for the six neutrino flavors.

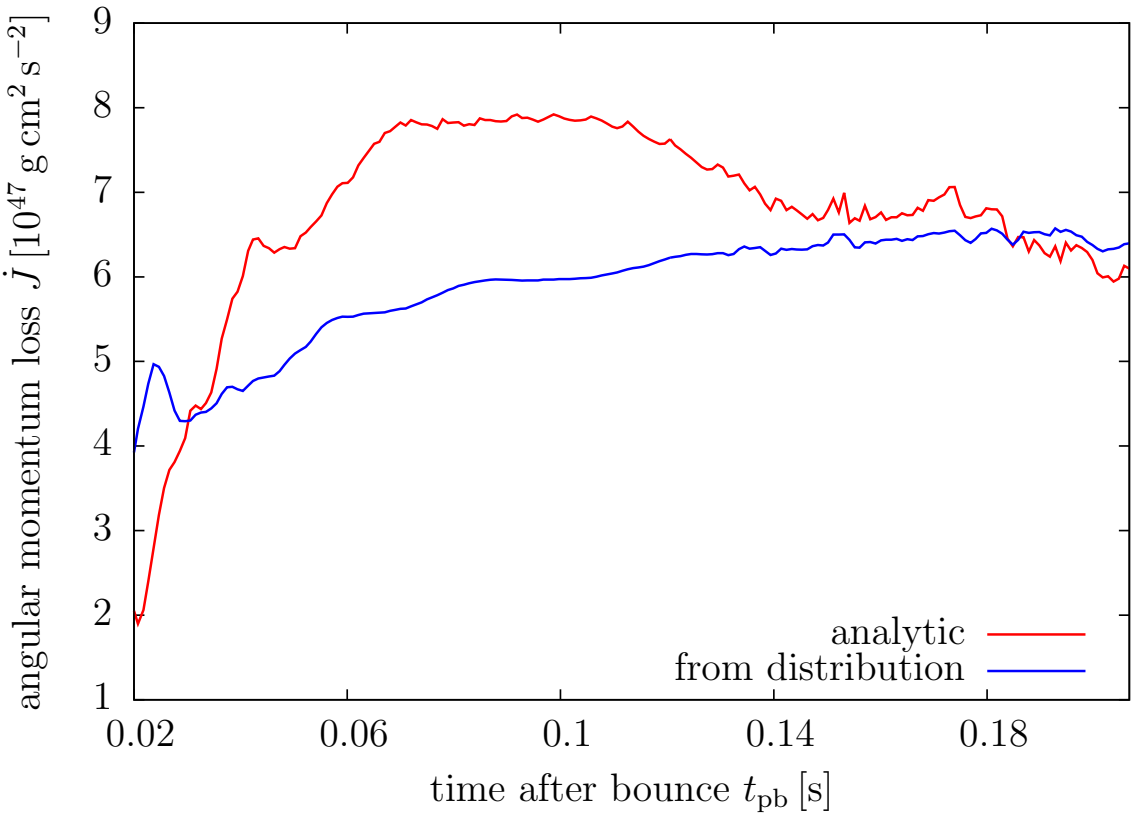

Figure 3.23. The time evolution of the angular momentum loss by the neutrino emission. The red and blue lines show the evaluation from equations (3.11) and (3.10), respectively.

In figure 3.23, I compare the angular momentum losses estimated from equations (3.11) and (3.10). Since equation (3.10) is evaluated at $r = 100\,\mathrm{km}$, I only plot the time when

the minimum shock radius exceeds that radius. Although the evaluation by equation (3.10) shows a gradual increase, the analytic evaluation (equation (3.11) shows a steep rise and a gradual decrease. The errors between them are $\sim 30\%$ around 100 ms after the core bounce. Although the analytic estimation (equation (3.11)) is simple, this is accurate enough to know the order of magnitude of the angular momentum loss. Therefore Epstein (1978) correctly described the basic picture of the angular momentum loss by neutrino emission.

3.4 Summary and discussion

In order to examine the effects of rotation on the CCSN, the core-collapse simulation with the rotating progenitor is performed with the Boltzmann-radiation-hydrodynamics code. Although the morphology of the shock is different from the non-rotating and non-exploding model in Nagakura et al. (2018), the average shock radii, the neutrino luminosities, and the neutrino mean energies are similar. Besides, the time-scale ratio diagnostic is less than unity except for only a limited period. These facts indicate that the rotating model employed in this chapter can not revive the shock successfully. Recalling that the rotation velocity adopted here is almost the fastest end according to the stellar evolution theory, other physical processes than rotation is required for the successful explosion.

Although the failure in the shock revival is observed in the simulation, yet other interesting features related to the momentum space distributions of neutrinos are worth investigating since the Boltzmann equation is solved directly. In this chapter, the angular distributions of neutrinos, rotational component of the neutrino flux, and the Eddington tensor are discussed. Neutrinos are dragged by matter via the relativistic beaming and hence have rotational velocities. This is indicated from the angular distributions and the rotational flux. Then, it is demonstrated that the Eddington tensor is determined by the complicated interactions among the matter velocity, neutrino reactions, and neutrino flux. The accuracy of the M1-closure method is discussed. The off-diagonal components of the M1-Eddington tensor are quantitatively and even qualitatively different from that of the Boltzmann-Eddington tensor. The error of M1-Eddington tensor is $\sim 20\%$ at most. The reason is that the flux factor solely determines the Eddington factor. Finally, the angular momentum loss by neutrinos is evaluated from the distribution function and compared with the analytic formula by Epstein (1978). The latter can evaluate the order of magnitude of the angular momentum loss.

The stellar rotation of $1\,\mathrm{rad\,s^{-1}}$ at the center is too slow for shock to revive under axisymmetry. On the other hand, Takiwaki et al. (2016) reported that the low-$T/|W|$ instability helps the neutrino heating to revive the shock as discussed in section 2.2.1. Such instability may develop if 3D simulations with the Boltzmann-radiation-hydrodynamics code is performed, and the results may change qualitatively. The $T/|W|$ parameter obtained in section 3.2 may be too small to develop the low-$T/|W|$ instability. Even faster rotation of, say, $\Omega_0 = 2\,\mathrm{rad\,s^{-1}}$, however, can develop the instability according to Takiwaki et al. (2016). Although the rotation employed in this chapter is almost the fastest end, the

rotation of $2\,\mathrm{rad\,s^{-1}}$ is still possible. Once after the 3D version of the code is completed and enough computational resources are acquired, I will perform the 3D simulations.

In order to revive the shock, one of the possible physical processes to consider is the emission of acoustic waves. This acoustic mechanism, however, works with a longer timescale $\sim 1\,\mathrm{s}$ after the core bounce. The Boltzmann-radiation-hydrodynamics code employed in this chapter requires significant computational cost and hence can not follow such a long timescale. Therefore an approach with a simplified model is adopted in the next chapter.

Chapter 4

The Critical Condition for the Shock Revival by the Acoustic Mechanism

In chapter 3, I performed the rotating stellar collapse simulation with the Boltzmann-radiation-hydrodynamics code. Since the explosion failed in the simulation, other physical processes are required. Among a large number of possibilities discussed in section 2.2, I resort to the emission of acoustic waves. This is because the acoustic mechanism is less understood compared with the neutrino heating mechanism, and hence the more investigations are required.

In order to investigate the acoustic mechanism, I ask how large acoustic power is needed to revive the stalled shock. The reason is as follows. The later phase than several hundreds of milliseconds after the core bounce, when the acoustic mechanism works, cannot be examined by the Boltzmann-radiation-hydrodynamics code in chapter 3. Instead of performing such self-consistent simulations, modeling approaches are useful. As discussed in section 2.2.2, the emission of the acoustic waves is examined, but the conclusion is not yet achieved. Therefore I change the point of view from the acoustic emission to the acoustic heating.

In this chapter, I extend the concept of the critical curve theory described in section 2.2.1. Although only the two-dimensional parameter plane (the neutrino luminosity and the mass accretion rate) is considered in the original theory, I add another dimension and discuss the critical "surface". Such attempts have been made in the context of the neutrino heating mechanism: Murphy & Dolence (2017) investigated the dependence of the critical curve on the parameters (e.g., the mass of the central PNS) which are fixed in Burrows & Goshy (1993), and Iwakami et al. (2014) introduced the rotation. In this section, the new axis I add is the intensity of the acoustic waves. The critical surface discussed here will allow us to assess how intense acoustic waves are required for the CCSNe to explode and estimate the robustness of the acoustic mechanism explosions by realistic simulations. Note that in this approach the acoustic power and neutrino heating are treated equally, though Burrows et al. (2006) originally proposed that the acoustic

power is dominant over the neutrino heating. From this viewpoint, the model considered in this chapter may be called the "hybrid model".

In addition, I perform simulations in 1D spherical symmetry and 2D axisymmetry. The acoustic mechanism only works in multi-dimension since the g-modes are excited, and hence 1D simulations are not realistic. The 1D flow, however, is much simpler than the 2D flow. I can analyze and capture the essential features of the acoustic waves of the 1D flow deeper than those in the 2D flow. Thus, analysis of the 1D flow helps to understand the 2D flow.

This chapter is organized as follows: In section 4.1, the numerical methods are described. Subsequently, simulation results are shown. First, I show simulations of spherically symmetric 1D results in order to get some insight into the acoustic mechanism in section 4.2. Second, axially symmetric 2D results are shown in section 4.3. In section 4.4, I give some discussions and conclusions.

4.1 Numerical modelings

In this chapter, the steady accretion flow with constant mass accretion rate $\dot{M}$ and constant neutrino luminosity L_ν is disturbed by acoustic waves emitted from the central PNS. For models with various $\dot{M}$ and L_ν, critical amplitudes of acoustic waves are investigated. Here, the critical amplitude is defined as the minimum amplitude needed for the shock to revive, i.e., for the minimum shock radius to reach 500 km within 500 ms from the time when the acoustic waves emission starts. By collecting the critical amplitudes, the critical surface is drawn in the parameter space spanned by $\dot{M}$, L_ν, and critical acoustic amplitudes.

Basic equations in this chapter are the inviscid hydrodynamics equations with the neutrino heating by the light-bulb prescription and Newtonian point-mass gravity:

$$\frac{\partial \rho}{\partial t} + \boldsymbol{\nabla}\cdot(\rho \boldsymbol{v}) = 0, \tag{4.1}$$

$$\frac{\partial \rho \boldsymbol{v}}{\partial t} + \boldsymbol{\nabla}\cdot(\rho \boldsymbol{v}\boldsymbol{v} + P\boldsymbol{I}) = -\rho \boldsymbol{\nabla}\Phi, \tag{4.2}$$

$$\begin{aligned}\frac{\partial \rho(e + \frac{1}{2}\boldsymbol{v}^2)}{\partial t} + \boldsymbol{\nabla}\cdot\left\{\rho \boldsymbol{v}\left(e + \frac{1}{2}\boldsymbol{v}^2 + \frac{P}{\rho}\right)\right\} \\ = -\rho \boldsymbol{v}\cdot\boldsymbol{\nabla}\Phi + Q,\end{aligned} \tag{4.3}$$

$$\frac{\partial \rho Y_\mathrm{e}}{\partial t} + \boldsymbol{\nabla}\cdot(\rho \boldsymbol{v} Y_\mathrm{e}) = \rho\Gamma, \tag{4.4}$$

$$\Phi = -\frac{GM_\mathrm{PNS}}{r}, \tag{4.5}$$

where ρ, $\boldsymbol{v}$, e, P, Q, Y_e, Γ, Φ, G, M_PNS, and r are the density, velocity, specific internal energy, pressure, net neutrino heating rate, electron fraction, neutrino reaction rate, gravitational potential by the PNS, gravitational constant, mass of the PNS, and distance from the central object. The net neutrino heating rate Q and reaction rate Γ are the sums of equations (2.58) and (2.59) over $i = \nu_\mathrm{e}$ and $\bar{\nu_\mathrm{e}}$, respectively. Here, the light-bulb method for the neutrino heating and reaction rates are utilized, and it is validated in Appendix

A.3. In order to express in vector-invariant form, the unit tensor $\boldsymbol{I}$ and dyadic tensor $\boldsymbol{vv}$ are used. In this chapter, the PNS mass is fixed to $M_{\rm PNS} = 1.4\,M_\odot$. The equation of state (EOS) is the STOS EOS (Shen et al., 1998) introduced in section 2.1.3 for simplicity.

The spherical coordinates are employed, and the 1D spherical symmetry and 2D axisymmetry are imposed. The width of the radial mesh Δr_i at the i-th radial grid point r_i is set to $\Delta r_i = 0.01 r_i$. The inner boundary r_0 is fixed to the neutrinosphere r_ν. In this chapter, the neutrinosphere is defined as the radius where the density is $10^{11}\,{\rm g\,cm^{-3}}$. The number of the radial grid is basically 256, but if the outermost radius is smaller than 500 km, the radial grid number is increased to 320. For 2D models, the cell centers and widths of the zenith angle θ mesh are set to the Gaussian quadrature points and weights, respectively, in the same way as Sumiyoshi & Yamada (2012). The number of the θ-grid is 128.

Initial condition is the steady-state solution of equations (4.1)–(4.5) with the stalled shock. The mass accretion rate and the neutrino luminosity are constant with respect to the time and model parameters. The construction of the steady-state is described in section 2.2.1. I further give the quantities at the upstream of the standing shock: the specific entropy $s = 3$ in units of the Boltzmann constant $k_{\rm B}$ per nucleon, electron fraction $Y_{\rm e} = 0.5$, and radial velocity $v_r = \sqrt{GM_{\rm PNS}/r}$.

The hydrodynamical code adopted in this chapter is basically the same one described in section 2.2.1, but there are several differences: not the self-gravity but the point-mass gravity is adopted; the acceleration $\dot{\beta}^i$ and the momentum transfer from neutrinos G_i are neglected; the central part of the computational domain is excised.

The values at the outer boundary are fixed to the steady-state values. In order to inject acoustic waves from the PNS surface, the time-dependent inner boundary conditions are imposed. The sinusoidal oscillation around the steady-state value is imposed on the density as $\rho = \rho_0(1 + \delta \mathcal{P}_\ell(\mu)\sin(\omega t - kr)$, where ρ_0, δ, $\mathcal{P}_\ell(\mu)$, ω, and k are the steady-state density at the inner boundary, the normalized dimensionless amplitude, the Legendre polynomial of ℓ-th order with $\mu = \cos\theta$, the frequency, and the wave number of the acoustic wave, respectively. Note that the ω and k are given later. Although the g-mode oscillations observed in Burrows et al. (2006) are non-spherical, the spherical $\ell = 0$ mode is considered in the 1D simulations in order to understand the acoustic energy transport in CCSNe. On the other hand, the $\ell = 1$ mode, which is the most dominant mode in Burrows et al. (2006), is adopted in 2D simulations. The specific entropy and the electron fraction at the inner boundary are fixed at the steady-state values since the perturbations by the acoustic waves are adiabatic. The EOS determines other thermodynamic quantities such as temperature and pressure. The velocity at the inner boundary is set to $v_r = v_0 + a\mathcal{P}_\ell\delta\sin(\omega t - kr)$, where v_0 and $a = \sqrt{(\partial P/\partial\rho)_{s,Y_{\rm e}}}$ are the steady-state velocity at the inner boundary and the sound speed there, respectively. By setting $k = \omega/(v_0 + a)$, the boundary condition for the velocity is consistent with the outgoing sound waves. The frequency ω is set so that the oscillation period is 3 ms, which is the period of the most prominent g-mode oscillation in Burrows et al. (2006).

For given parameters of $\dot{M}$, L_ν, and δ, simulations are performed 500 ms. If the mean

shock radius goes to larger radii than 500 km within 500 ms, the shock is interpreted as revived. The criterion of 500 km is the same as that employed in Iwakami et al. (2014) and slightly larger than that of Nordhaus et al. (2010) and Hanke et al. (2012), who adopted 400 km. The shock radius in this chapter is defined as the radius where not the velocity is a particular value but the specific entropy is $s = 6$, twice as large as the pre-shock value. The critical δ for the shock revival is determined as a function of $\dot{M}$ and L_ν, and then the critical surface is drawn. For 1D and 2D simulations, the critical values are searched with intervals of 0.005 and 0.01, respectively.

Before going to the results, let me discuss the robustness of the critical surface. Especially I measured how much the numerical resolution and initial phase of acoustic waves affect the critical amplitudes. First, in order to check the effects of the resolution, I performed additional high-resolution simulations with $\Delta r = 0.005r$ at any grid points. The mass accretion rate and the neutrino luminosity are $\dot{M} = 0.6\,M_\odot\,\mathrm{s}^{-1}$ and $L_\nu = 4.0 \times 10^{52}\,\mathrm{erg\,s}^{-1}$. It results in the rise of the critical amplitude by 0.01–0.015. Second, the effects of the initial phase are examined. I performed four additional simulations. Their numerical resolutions are the same as original simulations, but the initial phases of the acoustic waves are 0, $\pi/2$, π, and $3\pi/2$. The critical amplitude is shifted by 0.005. These two results demonstrated that the critical surface with 1D simulations is determined fairly robustly. I also checked the resolution and initial phase dependence of 2D simulations. With the doubled number of the radial (angular) grid points, the critical amplitude is lowered by ~ 0.02 (~ 0.01) at $\dot{M} = 1.0\,M_\odot\,\mathrm{s}^{-1}$ and $L_\nu = 4.5 \times 10^{52}\,\mathrm{erg\,s}^{-1}$. By changing the initial phase in the same way as 1D, the critical amplitude for 2D simulation is shifted by ~ 0.01. Therefore the 2D critical surface is also well determined.

4.2 1D result

4.2.1 critical surface

The critical surface for the 1D simulations is shown in figure 4.1. The models with parameters on or above the critical surface successfully explode, while those below the surface fail. For visualization, the sections of the surface by planes with constant $\dot{M}$ are also shown in the lower panel of the figure. In the following of this section, an overview of a typical simulation is presented, and then the properties of the models on the critical surface are examined in detail.

Shown in figure 4.2 is the time evolution of the radial velocities of the model with $\dot{M} = 0.6\,M_\odot\,\mathrm{s}^{-1}$, $L_\nu = 4.0 \times 10^{52}\,\mathrm{erg\,s}^{-1}$, and $\delta = 0.105$ as an example of the successful 1D simulation on the critical surface. The acoustic waves are emitted into the computational domain from the PNS surface. If the amplitude is large enough, the waves become the secondary shock waves. Although these secondary shocks are weak (typical Mach number is ~ 1.3), the velocity jumps by them are seen as the boundaries between the light and dark orange colors going to upper right for every 3 ms in the top panel of figure 4.2, which is a zoom-in of the lower panel. The primary shock (the outermost shock) indicated by

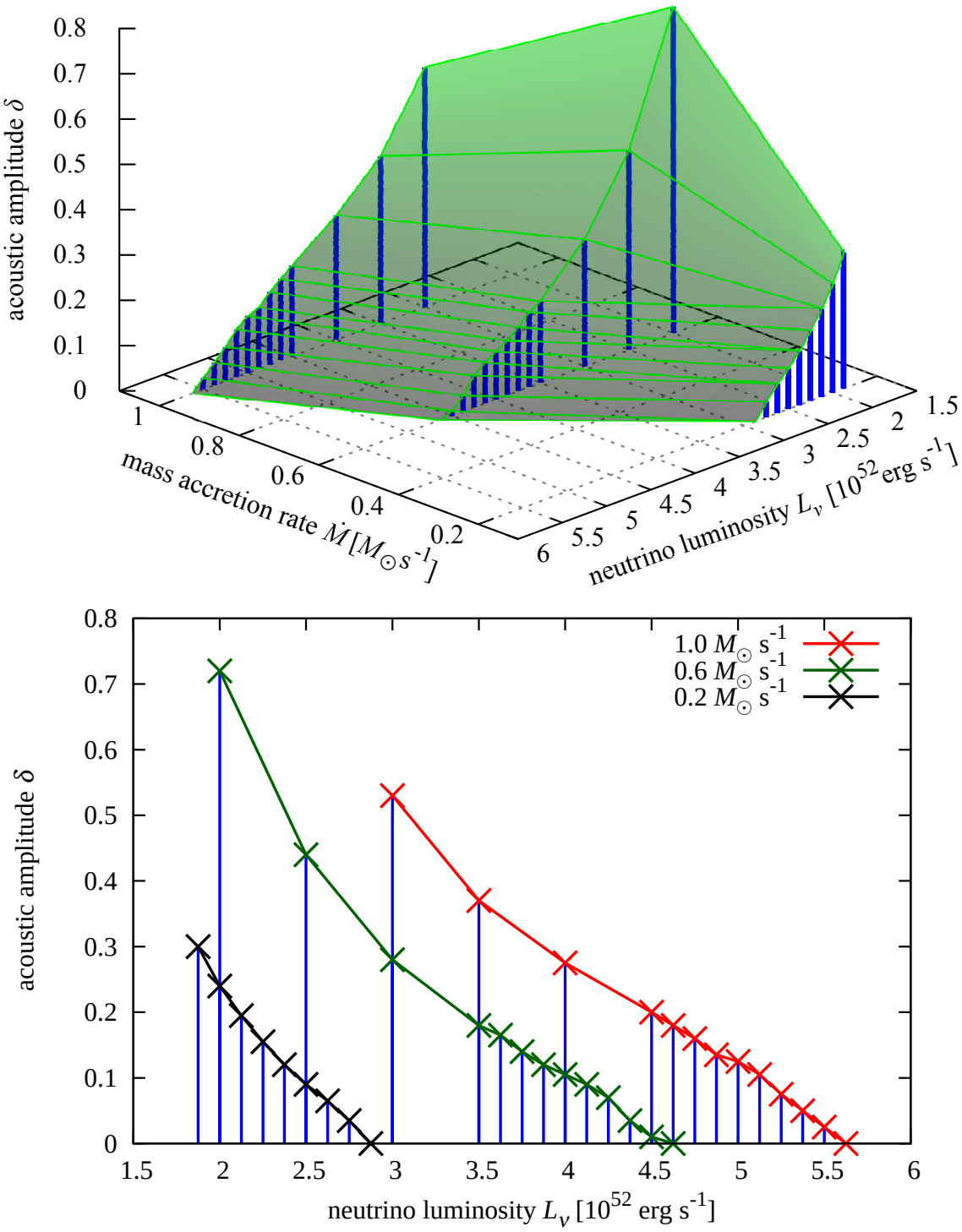

Figure 4.1. The critical surface for the 1D simulations (upper panel) and the sections of the surface by planes of constant mass accretion rates (lower panel). The blue lines dropped from the surface to the bottom plane in the upper panel indicate the $\dot{M}$ and L_ν of the models. The red, green, and black lines correspond to the sections by the plane with $\dot{M} = 1.0\,M_\odot\,\mathrm{s}^{-1}$, $0.6\,M_\odot\,\mathrm{s}^{-1}$, and $0.2\,M_\odot\,\mathrm{s}^{-1}$, respectively. The blue lines in the lower panel are the same as those in the upper panel. This figure is reproduced from Harada et al. (2017) by permission of the AAS.

the boundary of the violet and orange colors in the figure shows tremble motion caused by the repeating collision of the primary and the secondary shock waves.

The primary shock shows not only the tremble motions apparent in the top panel of figure 4.2 but also an oscillatory motion with the longer timescale and the growing amplitude illustrated in the bottom panel of the figure. The period of the latter oscillation is $\sim 70\,\mathrm{ms}$, and the timescale of the advection from the shock to the maximum cooling point is $\sim 24\,\mathrm{ms}$. Since the latter is between 1/4–1/2 of the former as discussed in Fernández (2012), the oscillatory motion with growing amplitude observed in the figure is originated from the oscillatory instability found by Fernández (2012).

The oscillatory instability commonly develops in the 1D simulations. Figure 4.3 shows the comparison of the trajectory of the primary shocks with different δ. The mass accretion rate and the neutrino luminosity are $\dot{M} = 0.6\,M_\odot\,\mathrm{s}^{-1}$ and $L_\nu = 4.0 \times 10^{52}\,\mathrm{erg\,s}^{-1}$, respectively. The oscillatory instability of the primary shock is seen for all models presented in the figure, with the tremble motions caused by the secondary shocks shown in the inset. The oscillatory motions finally change into runaway shock revivals. This transition occurs later for the model with smaller δ, and for sufficiently small δ the transition no longer occurs until 500 ms. This behavior demonstrates that there is a threshold value of δ for the shock revival. Therefore by collecting the critical δ with different $\dot{M}$ and L_ν, the critical surface shown in figure 4.1 is drawn.

Although the acoustic amplitude is employed in figure 4.1, the acoustic power $\dot{E}_{\mathrm{aco}}$, the heating rate of the matter by the acoustic waves, is more useful in interpreting the physical picture and comparing with the previous works (Burrows et al., 2006; Yoshida et al., 2007; Weinberg & Quataert, 2008). Since the acoustic waves are confined within the primary shock, all of the energy is probably used to revive the shock and the acoustic power $\dot{E}_{\mathrm{aco}}$ should coincide with the acoustic luminosity L_{aco} at the inner boundary. Here, the acoustic luminosity is defined as the angle-integrated acoustic energy flux. One may think that the acoustic energy flux is easily calculated from the squared amplitude. Such a formula is derived with the assumption that the amplitude is small enough for third and higher order terms to be neglected. The amplitude considered in this chapter, however, is not necessarily small, and hence the formula for the small amplitudes is inappropriate. In order to estimate the energy flux of the large-amplitude acoustic waves, I utilized an extended version of Myers' theory (Myers, 1986, 1991).

Myers (1986) derived the corollary of the energy conservation theorem for the perturbations in the flow with uniform entropies, i.e., acoustic waves, and then Myers (1991) derived that in the flow with non-uniform entropies. While he considered the continuity, Euler, and the entropy equations to derive the corollary, the basic equations in this chapter also include another one, the electron fraction equation (4.4). Here, I extend the discussion of Myers (1991) in order to derive the corollary that reflects the change of the electron fraction. The detailed derivations and discussions are presented in appendix B. According to appendix B, the extension of Myers' corollary is

$$\frac{\partial E_{\mathrm{dis}}}{\partial t} + \boldsymbol{\nabla}\cdot\boldsymbol{F}_{\mathrm{dis}} = -D_{\mathrm{dis}}, \tag{4.6}$$

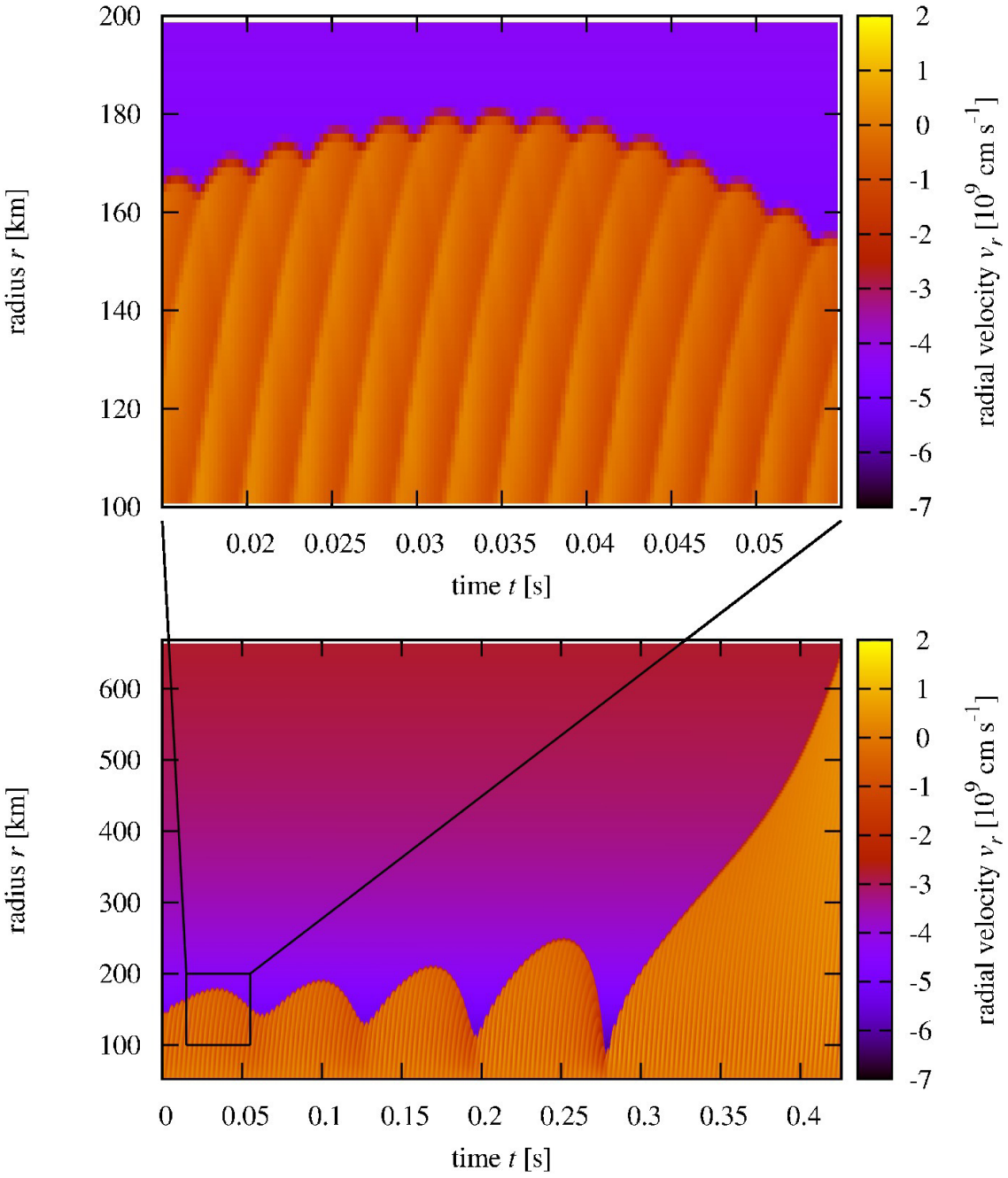

Figure 4.2. The time evolution of the radial velocity profiles. The model with $\dot{M} = 0.6\,M_\odot\,\mathrm{s}^{-1}$, $L_\nu = 4.0 \times 10^{52}\,\mathrm{erg\,s}^{-1}$, and $\delta = 0.105$, on the critical surface, is presented. The boundaries of colors show shock waves. The upper panel is a zoom-in figure of the region enclosed by the black rectangle in the lower panel. The lower panel shows the entire distributions of the velocity profiles. The lower boundary of the figure is the PNS surface. This figure is reproduced from Harada et al. (2017) by permission of the AAS.

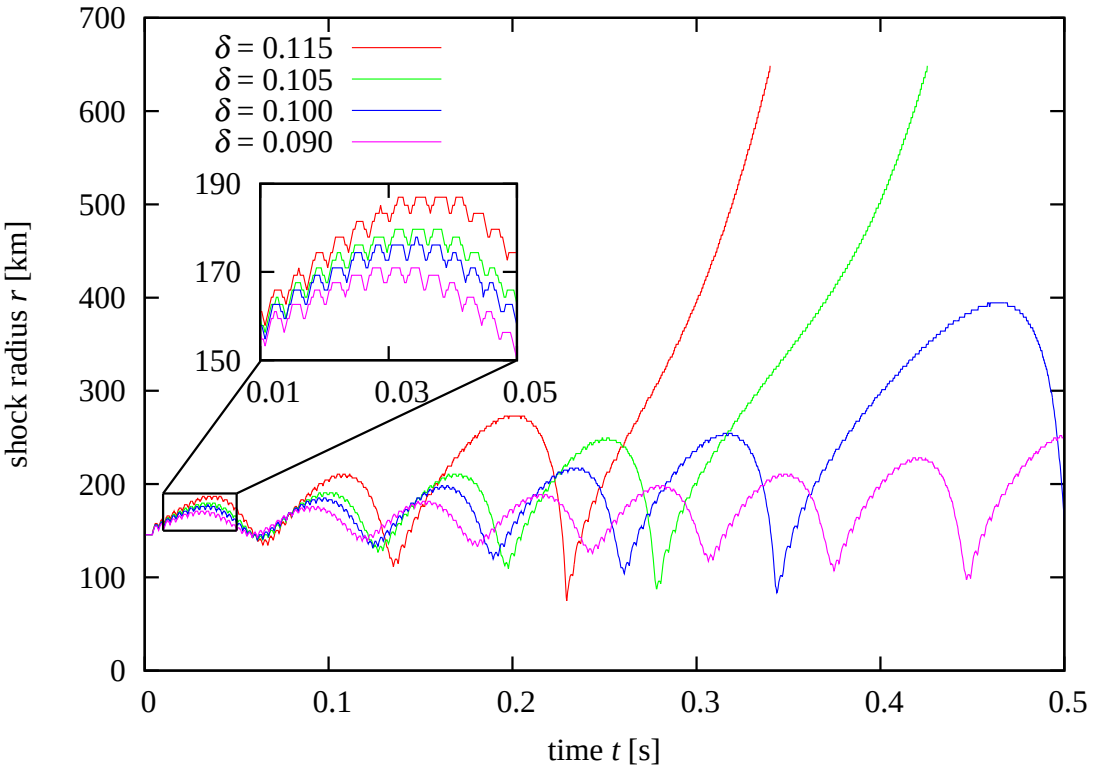

Figure 4.3. The evolutions of the primary shock radii of models with $\dot{M} = 0.6\,M_\odot/\mathrm{s}$, $L_\nu = 4.0\times10^{52}\,\mathrm{erg/s}$, and different δ indicated in the legend. Both successful (red and green) and failed (blue and magenta) models are shown. The model with $\delta = 0.105$ is on the critical surface, and the model with $\delta = 0.100$ is just below the surface. Note that lines for the successful models are truncated when the shock reaches the outer boundary. The inset is the zoom-in figure of the region enclosed by the black rectangle. This figure is reproduced from Harada et al. (2017) by permission of the AAS.

where

$$E_{\rm dis} := \rho\left(H - H_0 - T_0(s-s_0) - \frac{\mu_0}{m_{\rm u}}(Y_{\rm e}-Y_{\rm e0})\right) - \boldsymbol{m}_0\cdot(\boldsymbol{u}-\boldsymbol{u}_0) - (P-P_0) \tag{4.7}$$

$$\boldsymbol{F}_{\rm dis} := (\boldsymbol{m}-\boldsymbol{m}_0)\left(H - H_0 - T_0(s-s_0) - \frac{\mu_0}{m_{\rm u}}(Y_{\rm e}-Y_{\rm e0})\right) + \boldsymbol{m}_0\left((T-T_0)(s-s_0) + \frac{\mu-\mu_0}{m_{\rm u}}(Y_{\rm e}-Y_{\rm e0})\right) \tag{4.8}$$

$$D_{\rm dis} := -(s-s_0)\boldsymbol{m}_0\cdot\boldsymbol{\nabla}(T-T_0) - (Y_{\rm e}-Y_{\rm e0})\boldsymbol{m}_0\cdot\boldsymbol{\nabla}\frac{\mu-\mu_0}{m_{\rm u}} + (\boldsymbol{m}-\boldsymbol{m}_0)\cdot\left(\boldsymbol{\zeta}-\boldsymbol{\zeta}_0 + (s-s_0)\boldsymbol{\nabla}T_0 + (Y_{\rm e}-Y_{\rm e0})\boldsymbol{\nabla}\frac{\mu_0}{m_{\rm u}}\right) - (T-T_0)\left(\frac{Q}{T}-\frac{Q_0}{T_0}\right) + \frac{\mu\mu_0}{m_{\rm u}}\left(\frac{T}{\mu}-\frac{T_0}{\mu_0}\right)\left(\frac{\rho\Gamma}{T}-\frac{\rho_0\Gamma_0}{T_0}\right). \tag{4.9}$$

Here, $m_{\rm u}$, $H := e + P/\rho + \frac{1}{2}\boldsymbol{v}^2$, $\boldsymbol{m} := \rho\boldsymbol{v}$, T, and s are the atomic mass unit, specific stagnation enthalpy (the Bernoulli function), mass flux, temperature, and specific entropy, respectively. By using the chemical potentials of electrons, protons, and neutrons, $\mu_{\rm e,p,n}$, μ is the chemical potential of the electron-type neutrinos defined by $\mu = \mu_{\rm e} + \mu_{\rm p} - \mu_{\rm n}$. The symbol $\boldsymbol{\zeta}$ is defined as $\boldsymbol{\zeta} := \boldsymbol{\omega} \times \boldsymbol{v}$ with $\boldsymbol{\omega} := \boldsymbol{\nabla} \times \boldsymbol{v}$ being the vorticity. The quantities with and without subscript 0 stand for the unperturbed and perturbed quantities of the flow, respectively. If s, T, $Y_{\rm e}$, and μ is the same as those with subscript 0, or equivalently the neutrino reaction is neglected, and taking the limit of disturbance is weak, we can reproduce the well-known acoustic energy that is proportional to the squared amplitude from above expression. Although these expressions are complicated, $E_{\rm dis}$, $\boldsymbol{F}_{\rm dis}$, and $D_{\rm dis}$ are interpreted as the energy density, the energy flux, and the dissipation, respectively. This is because the corollary is written in a conservative form with these quantities, and these quantities reduce to the well-known formulae for the energy density, flux, and dissipation, in an appropriate limit. For more detailed justification, see appendix B.

Figure 4.4 shows the radial profiles of the acoustic luminosities defined as $L_{\rm aco}(r) = 4\pi r^2 F_{{\rm aco},r}(r)$ for models on the critical surface. In this figure, acoustic luminosities are averaged over the first 3 ms from the time when the perturbations from the inner boundary reach a given radius. Although $\dot{E}_{\rm aco}$ should coincide with $L_{\rm aco}$ at the inner boundary, peculiar behavior is seen on the first two points from the inner boundary in figure 4.4. This is because the injected acoustic waves are partially reflected in the vicinity of the inner boundary. Therefore, I choose the acoustic luminosity at the third grid point from the inner boundary as the acoustic power $\dot{E}_{\rm aco}$ in order to exclude the energy flux of the reflected waves. Fernández (2012) also observed a similar transient and concluded that the influence at the third grid point is small. Note that the acoustic luminosities $L_{\rm aco}$ decrease with radius. This reduction is more significant for larger δ. This is because the dissipation term $D_{\rm dis}$ is positive.

Let me estimate the order-of-magnitude of the acoustic power here. Since the 1D simulations are considered in this section, only the radial components of vectors are considered. The typical values of relevant quantities at $r \simeq 50\,{\rm km}$ are listed as follows: the temperature $k_{\rm B}T_0 \sim {\rm MeV}$; the specific entropy $s_0 \sim 10\,k_{\rm B}\,{\rm nucleon}^{-1}$; the electron fraction $Y_{\rm e0} \sim 0.1$; the chemical potential $\mu_0 \sim {\rm MeV}$; the specific stagnation enthalpy $H_0 \sim 10^{19}\,{\rm erg\,g^{-1}}$; the mass flux $m_{0r} \sim -10^{18\text{–}19}\,{\rm g\,cm^{-2}}$. The typical amplitudes are $\sim 10\%$ of the unperturbed quantities, except that the mass flux is $m_r - m_{0r} \sim (1\text{–}10) \times |m_{0r}|$. Note that m_{0r} is negative since the unperturbed flow is the accretion flow, and the perturbed flow sometimes go outward. From these values,

$$(m_r - m_{0r})(H - H_0) \sim 10^{36\text{–}38}\,{\rm erg\,cm^{-2}\,s^{-1}}, \tag{4.10}$$

$$(m_r - m_{0r})T_0(s - s_0) \sim 10^{36\text{–}38}\,{\rm erg\,cm^{-2}\,s^{-1}}, \tag{4.11}$$

$$m_{0r}(T - T_0)(s - s_0) \sim 10^{35\text{–}36}\,{\rm erg\,cm^{-2}\,s^{-1}}, \tag{4.12}$$

$$(m_r - m_{0r})\frac{\mu_0}{m_{\rm u}}(Y_{\rm e} - Y_{\rm e0}) \sim 10^{34\text{–}36}\,{\rm erg\,cm^{-2}\,s^{-1}}, \tag{4.13}$$

$$m_{0r}\frac{\mu - \mu_0}{m_{\rm u}}(Y_{\rm e} - Y_{\rm e0}) \sim 10^{33\text{–}34}\,{\rm erg\,cm^{-2}\,s^{-1}}. \tag{4.14}$$

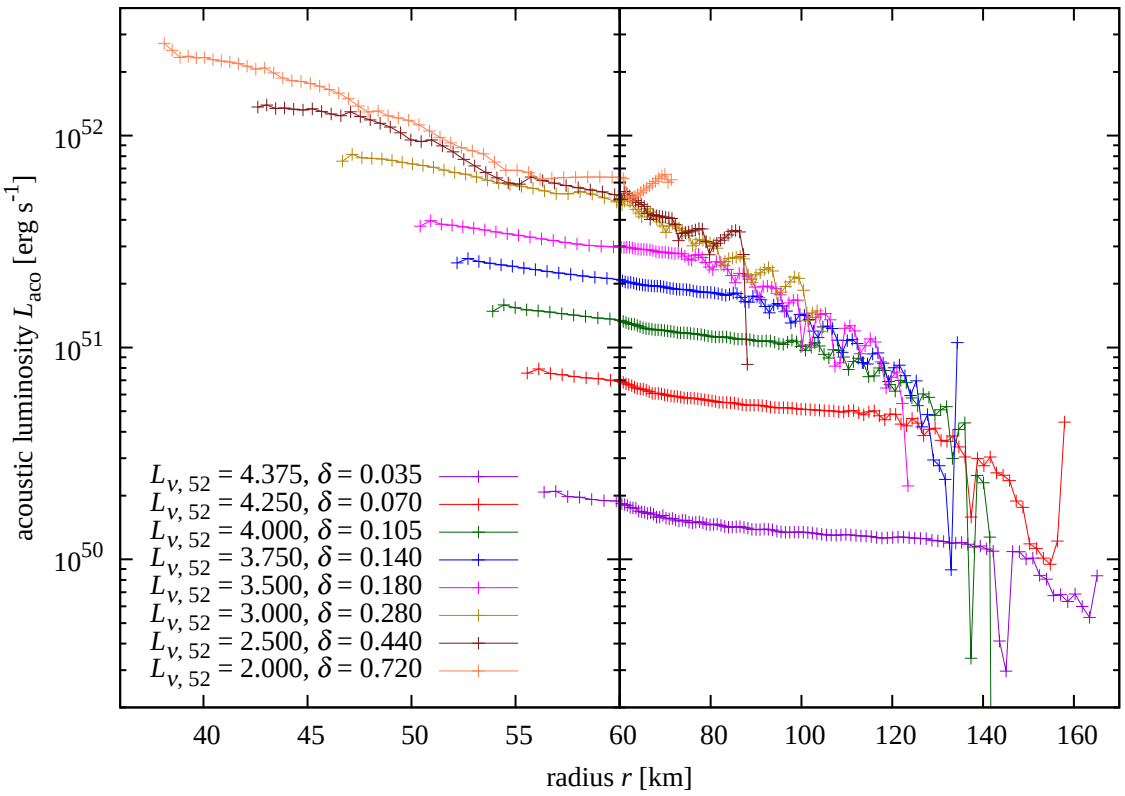

Figure 4.4. The radial profiles of the acoustic luminosity $L_{\rm aco}$. The model parameters are on the critical surface, and the mass accretion rate is commonly chosen as $\dot{M} = 0.6\,M_\odot\,{\rm s}^{-1}$. The luminosities are averaged over 3 ms from the time of the arrival of the acoustic waves from the PNS surface. The "+" symbols represent the on-grid values. The neutrino luminosity $L_{\nu,\,52} = L_\nu/(10^{52}\,{\rm erg\,s^{-1}})$ and amplitude δ are indicated in the legend. Note that since the models on the critical surface are employed, different amplitudes correspond to different neutrino luminosities. This figure is reproduced from Harada et al. (2017) by permission of the AAS.

Combining them,

$$F_{{\rm dis},r} \sim 10^{36-38}\,{\rm erg\,cm^{-2}\,s^{-1}} \tag{4.15}$$

is obtained. With $4\pi r^2 \sim 10^{14}\,{\rm cm}^2$ being multiplied, the estimated acoustic power is

$$\dot{E}_{\rm aco} \sim 10^{50-52}\,{\rm erg\,s^{-1}}. \tag{4.16}$$

By measuring the acoustic power $\dot{E}_{\rm aco}$ from the acoustic luminosity $L_{\rm aco}$, the critical surface in the parameter space spanned by $\dot{M}$, L_ν, and $\dot{E}_{\rm aco}$ is drawn in figure 4.5. In the lower panel of the figure, again the sections of the critical surface are shown. The lower the neutrino luminosity L_ν is, the higher the required acoustic power is. This is consistent with the picture that acoustic power injection causes the explosion.

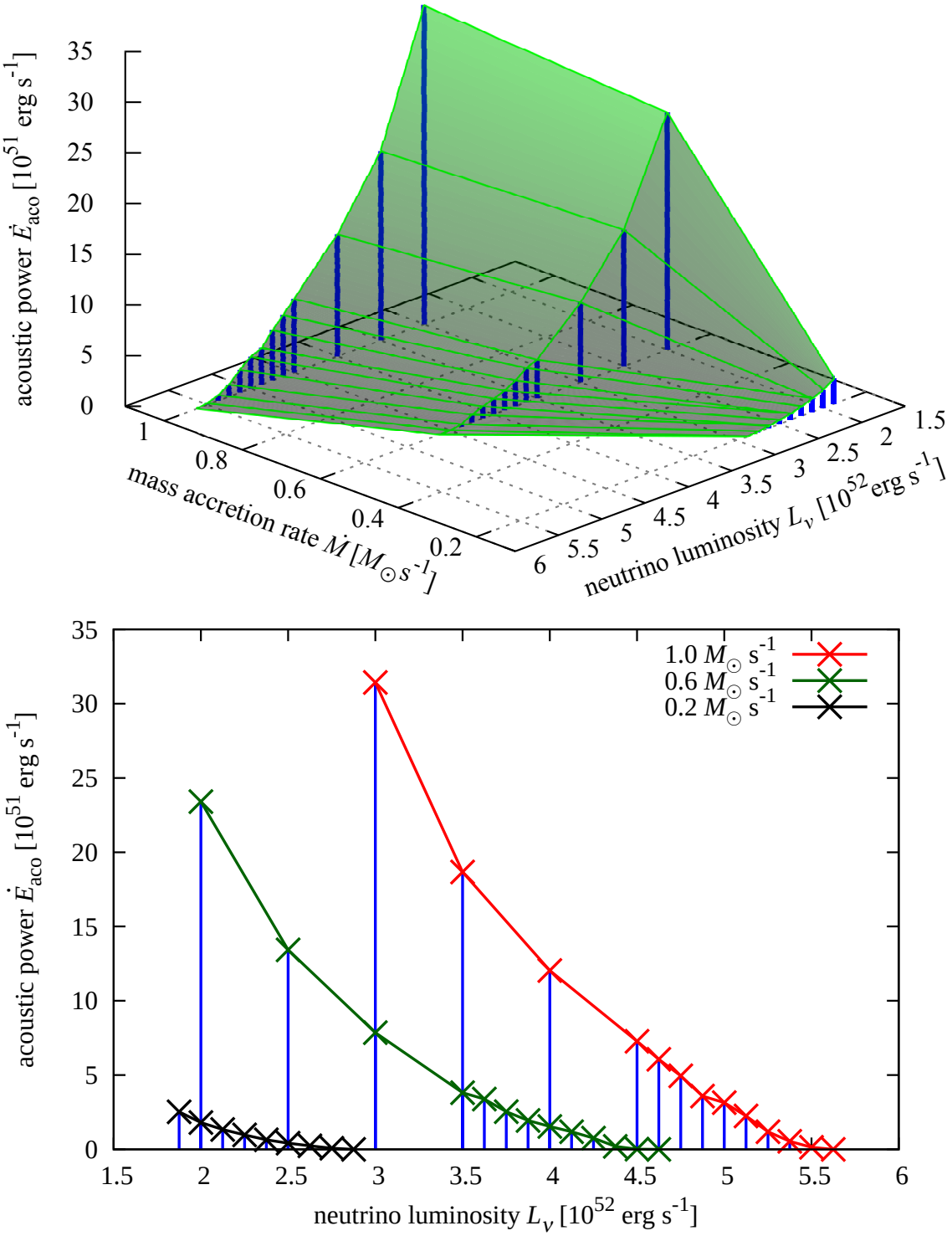

Figure 4.5. The same as figure 4.1 except that the vertical axes measures the acoustic power. This figure is reproduced from Harada et al. (2017) by permission of the AAS.

4.2.2 energetics

In order to understand the physical picture, the energetics is investigated deeply in this section. The acoustic power, the net neutrino heating rate, and the sum of these two (total heating rate) of the models on the critical surface are displayed in figure 4.6. The net neutrino heating rate is defined by the integrated Q in equation (4.3), the sum of the heating and cooling rates, of the initial steady-state over the gain region. For models in which the neutrino heating rate exceeds the acoustic power, the total heating rate is almost constant. This is because the decreased net neutrino heating rate is almost compensated for by the increased acoustic power. This consideration implies that the shock revives when the total heating rate exceeds a certain threshold value. Since the values of the total heating rates are different among models with different $\dot{M}$, the threshold may depend on the mass accretion rate. On the other hand, for the models with the acoustic powers larger than the net neutrino heating rate, the total heating rates not are constant but increase with the acoustic powers. Since the required total heating rates are larger than the threshold value for these models, the heating efficiency of the acoustic waves with large power may be low.

A candidate origin of the inefficiency is the neutrino cooling. The secondary shock raises the temperature as indicated in figures 4.7 and 4.9. The higher the temperature is, the larger the neutrino cooling is, since the neutrino cooling rate is proportional to T^6 where T is the temperature. This neutrino cooling reduces the efficiency of the acoustic heating. Indeed, $-(T-T_0)(Q/T-Q_0/T_0)$ in $D_{\rm dis}$ (equation (4.9)) illustrates the energy loss of the acoustic waves by the neutrino emissions as discussed in appendix B. The larger the acoustic power is, the less efficient the acoustic power is, since the stronger secondary shock makes the post-shock temperature higher and the neutrino cooling rate larger.

In figures 4.7, 4.8, and 4.9, the radial profiles of the velocity, temperature, and entropy at different times are indicated in order to illustrate this effect. The cooling and heating layers are painted with bluish and reddish colors, respectively. The cooling region initially resides in the vicinity of the inner boundary. This is because the temperature is high there at the beginning of the simulations as shown in panels (a) of figures 4.7. As indicated in panel (b) of figure 4.7, the cooling layer follows the propagating secondary shock. The reason is that the temperature of the shocked matter rises, and hence the neutrino cooling rate is enhanced. This enhancement in cooling reduces the efficiency of the acoustic heating. One of the merits of the acoustic mechanism proposed in Burrows et al. (2006) is that the acoustic heating is much more efficient than the neutrino heating since all the energy is confined in the primary shock. It does not mean, however, that all of them are not necessarily used for the shock revival, according to the results presented here.

The cooling layer is sometimes detached from that in the vicinity of the inner boundary, and the gap becomes the heating layer as shown in panels (b) of figures 4.7 and 4.8, and in figure 4.9. This "gap heating layer" is located at the troughs in the temperature. The compressed matter by the secondary shock is then rarefied subsequently, and hence the temperature is lowered. This results in the suppression of the cooling and the emergence

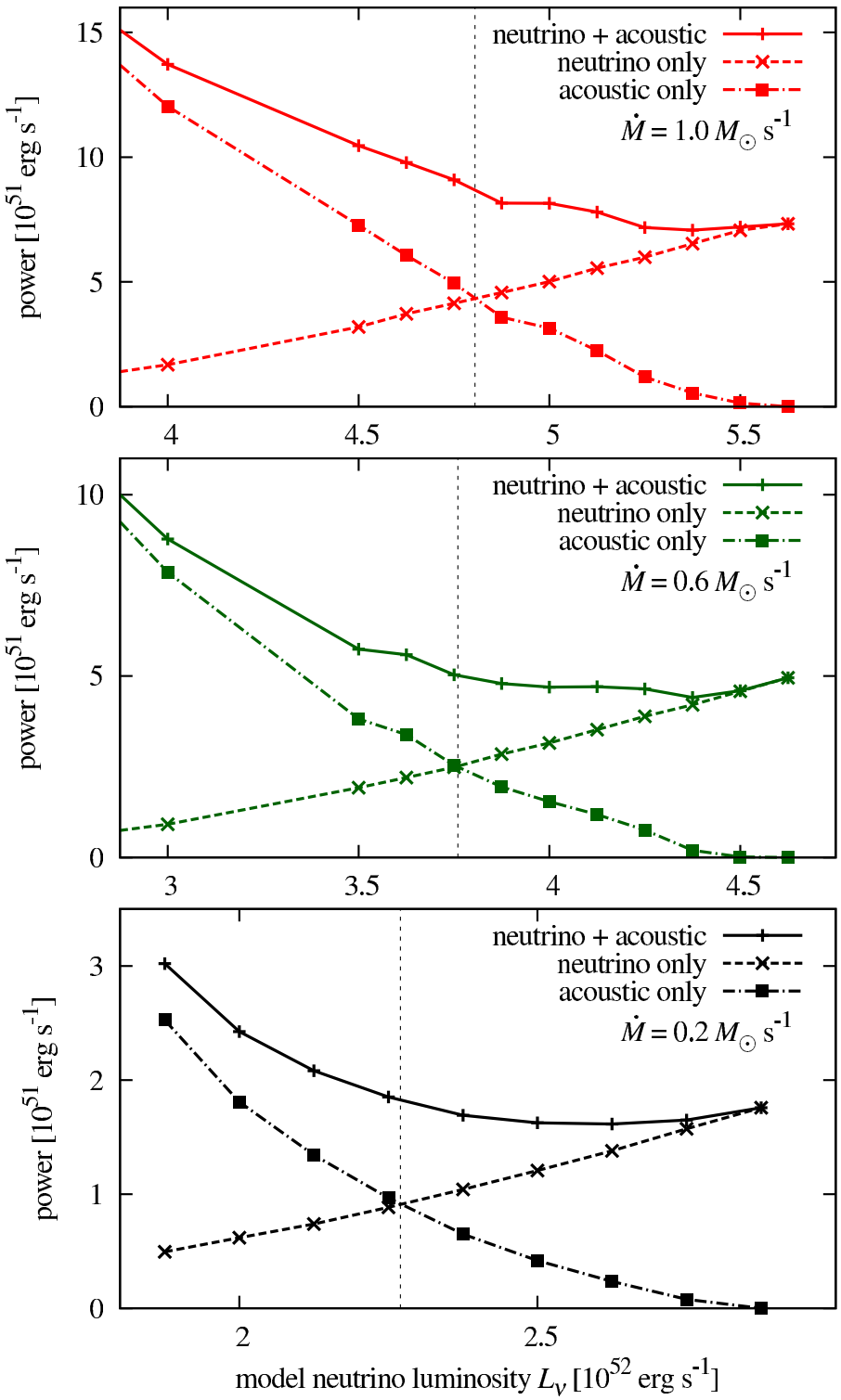

Figure 4.6. The acoustic power (dash-dotted lines), the net neutrino heating rate (dashed lines), and the total heating rate (solid lines) of the models on the critical surface. The top, middle, and bottom panels show the models with $\dot{M} = 1.0\,M_\odot\,\mathrm{s}^{-1}$, $0.6\,M_\odot\,\mathrm{s}^{-1}$, and $0.2\,M_\odot\,\mathrm{s}^{-1}$, respectively. The dotted vertical lines indicate the points where the acoustic powers and the net neutrino heating rates are the same. This figure is reproduced from Harada et al. (2017) by permission of the AAS.

of the gap heating layer. The heating in this gap is small, however, and the secondary shock enhances the cooling as a whole.

Although the acoustic heating enhances the neutrino cooling, not all the heating is consumed by the cooling, either. Figure 4.8 indicates the entropy distributions at the initial time and the time when the secondary shock collides with the primary shock. This time of collision is slightly later than the time indicated in panel (b) of figure 4.7. The entropy production by the merging shocks is seen as a spike in panel (b) of figure 4.8. Although the entropy production raises the temperature, it is not enough to convert the heating layer into the cooling layer. This is because the primary shock is far from the gain radius and the temperature there is initially low. Therefore the deposited energy is not entirely consumed by the neutrino emission.

If the primary shock advances to the large radii, the cooling layer no longer catches up with the secondary shock before the primary and secondary shocks collide as illustrated in figure 4.9. This is because the temperature gets lower with larger radii and the rise of the temperature by the secondary shock is not enough for the neutrino cooling to dominate over the heating. Although some of the energy provided by the secondary shock is lost via neutrino emissions, most of them are still available for the explosion.

Not only the neutrino cooling discussed above but also the reflection of the secondary shocks may make the acoustic heating inefficient. When the secondary shock collides with the primary shock, the rarefaction wave or reverse shock is formed according to the shock tube theory. In the models discussed here, only the rarefaction wave is observed. An example of the rarefaction wave is seen at $r \sim 100\,\mathrm{km}$ in panel (b) of figure 4.8. Due to the reflection, the primary shock does not get all the power of the secondary shock, and hence the efficiency of the acoustic heating is lowered. Note that the reflection may not reduce the efficiency in the realistic simulations where the Dirichlet-type inner boundary is not imposed unlike the simulations in this chapter since the reflected waves may collide with the PNS and be re-emitted, and finally the whole power may be provided to the primary shock.

4.2.3 explosion diagnostics

In section 2.2.1, the timescale ratio and the antesonic condition are described as the diagnostics to predict the shock revival. Although they are suggested in the context of the neutrino heating mechanism, they may be applicable since the model examined in this chapter can be seen as the hybrid mechanism as discussed at the beginning of this chapter.

As discussed in sections 2.2.1 and 3.2, the shock successfully revives when the timescale ratio exceeds unity. Instead of the ratio used in section 3.2, the advection and the heating timescales are evaluated as

$$\tau_{\mathrm{adv}} := \int_{r_{\mathrm{g}}}^{r_{\mathrm{s}}} \frac{\mathrm{d}r}{|v_r|} \tag{4.17}$$

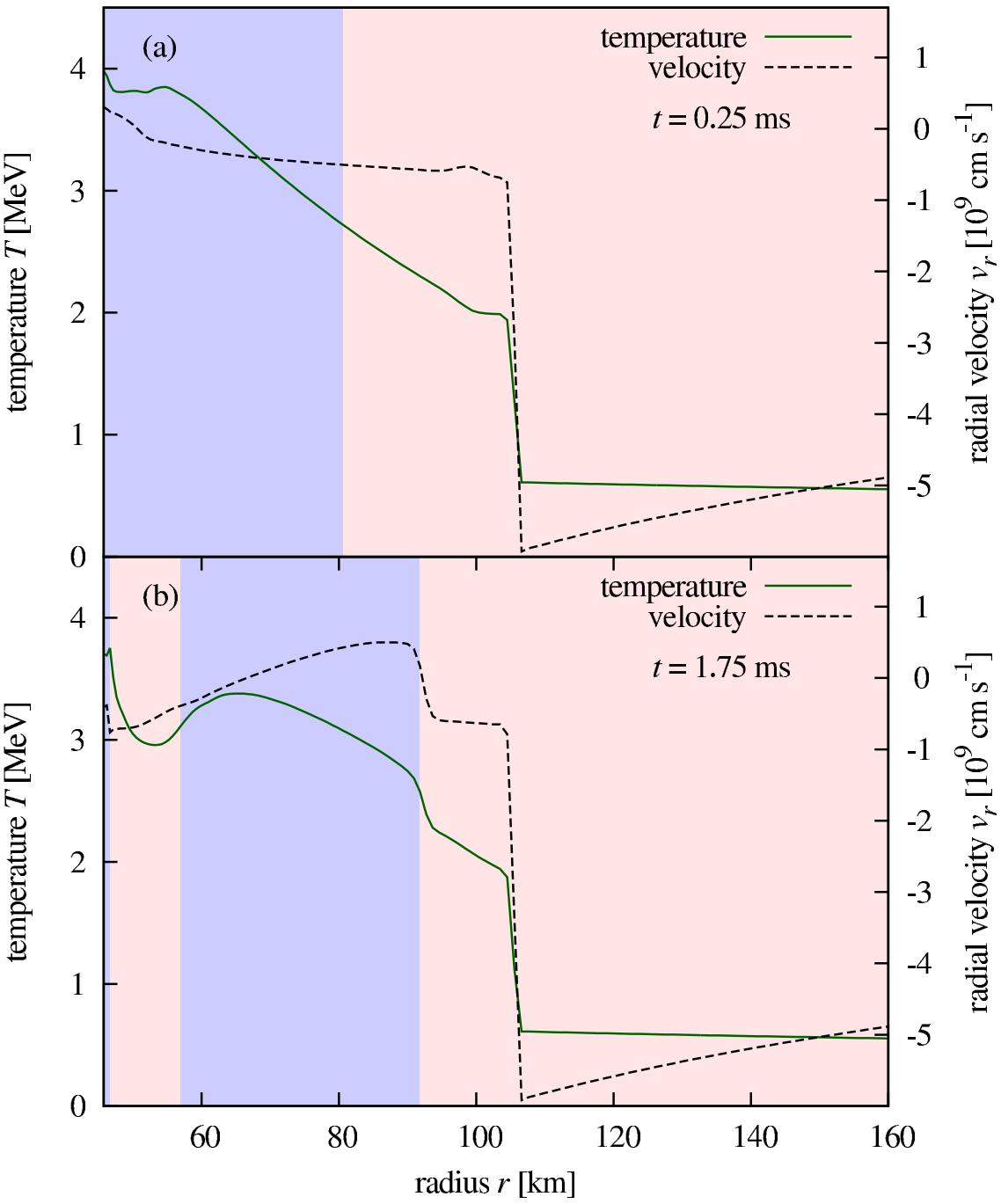

Figure 4.7. The radial profiles of the temperature (green solid line) and the velocity (black dashed line) at $t = 0.25$ ms (panel (a), shortly after the onset of the simulation) and 1.75 ms (panel (b), the time when the secondary shock slightly propagate outward). Note that the secondary shock in panel (b) is seen as the jump in the radial velocity at $r \sim 90$ km. The reddish and bluish regions are the gain and cooling layers, respectively. The adopted model is on the critical surface and the parameters are $\dot{M} = 0.6\,M_\odot\,\mathrm{s}^{-1}$, $L_\nu = 3.0 \times 10^{52}\,\mathrm{erg\,s}^{-1}$, and $\delta = 0.280$. This figure is reproduced from Harada et al. (2017) by permission of the AAS.

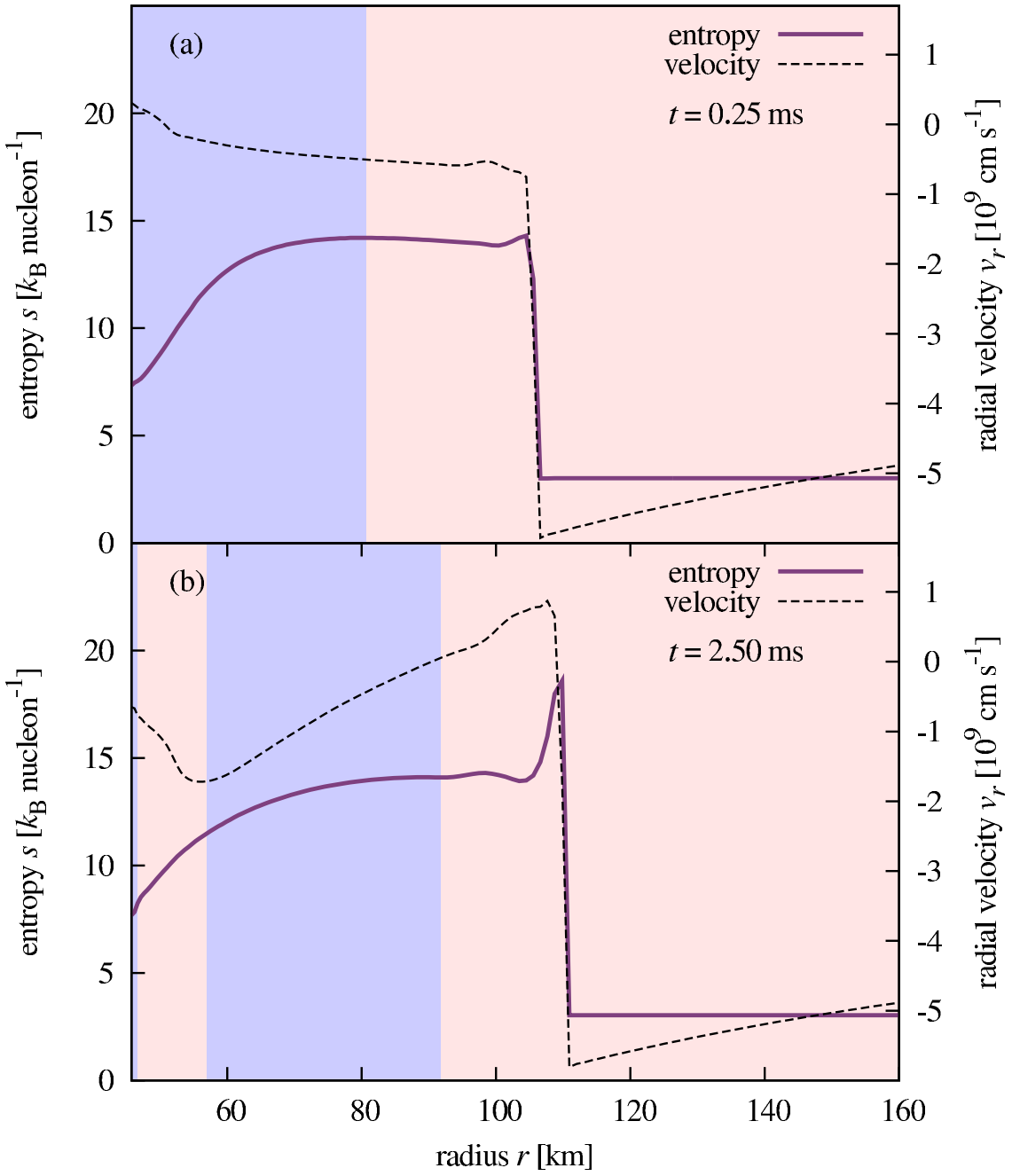

Figure 4.8. The same as figure 4.7, except that the entropy profiles instead of the temperature profiles are shown with violet solid lines, and $t = 2.50$ ms, when the secondary shock collides with the primary shock, is employed for panel (b). This figure is reproduced from Harada et al. (2017) by permission of the AAS.

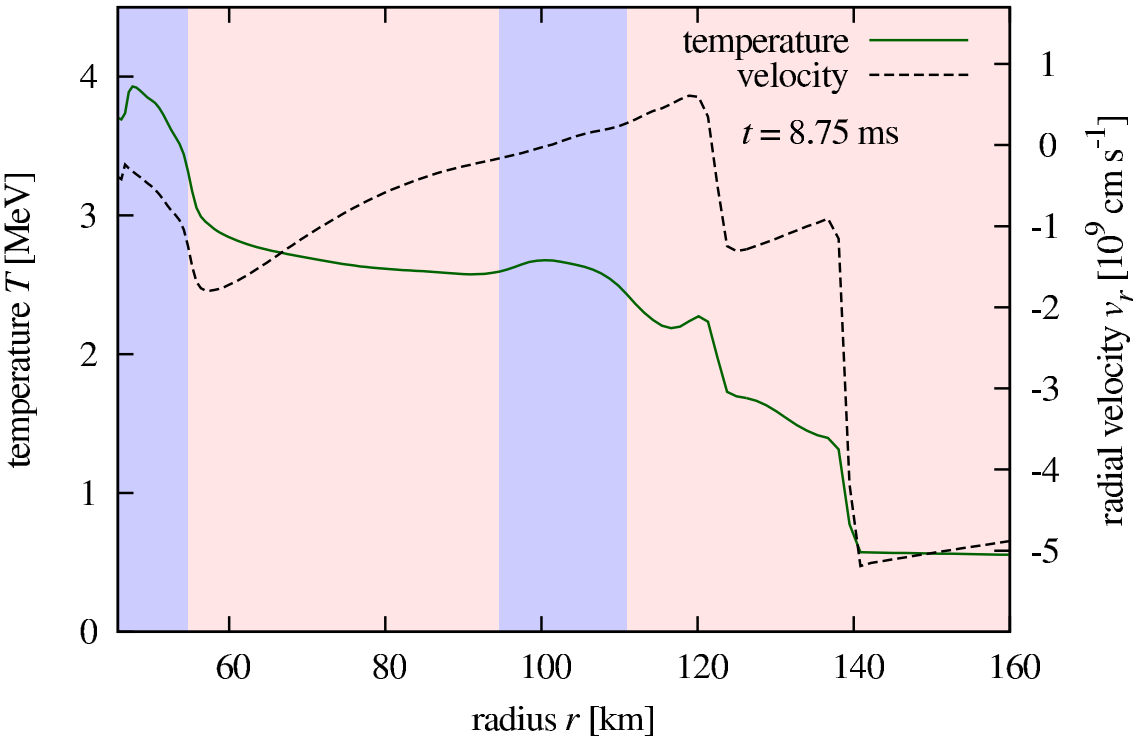

Figure 4.9. Identical to Figure 4.7 except that the time is much later, $t = 8.75$ ms. This figure is reproduced from Harada et al. (2017) by permission of the AAS.

and

$$\tau_{\rm heat} := \frac{\int_{r_{\rm g}}^{r_{\rm s}} {\rm d}V \rho |\Phi|}{\int {\rm d}V Q}, \tag{4.18}$$

respectively, where $r_{\rm g}$, $r_{\rm s}$, and ${\rm d}V$ are the gain radius, the shock radius, and the volume element, respectively. Shown in figure 4.10 is the timescale ratios with models on and below the critical surface, i.e., the successful and failed models, respectively. The differences between the successful and failed models are small. Even the ratio in failed models exceeds unity at some time, and the shock revival of successful model does not necessarily occur soon after the ratio exceeds unity. Therefore, this diagnostic is not sensitive enough to distinguish the explosion or failure.

According to the antesonic condition discussed in section 2.2.1, an explosion occurs when the maximum antesonic factor $\max(a^2/v_{\rm esc}^2)$ exceeds the critical value, ~ 0.2. Figure 4.11 shows the maximum antesonic factor of models just on (successful models) and below (failed models) the critical surface. In this section, I searched the maximum value of the antesonic factor in a space-time domain below the shock and before the explosion. The beginning of the explosion is identified with the time when the shock radius reaches its minimum because the shock radius undergoes rapid expansion just after its minimum is achieved as shown in figure 4.3. For the failed models, the maximum antesonic factor is searched until 500 ms.

Contrary to the original discussion in Pejcha & Thompson (2012), almost all of the successful models have smaller $\max(a^2/v_{\rm esc}^2)$ compared to the failed models. Although

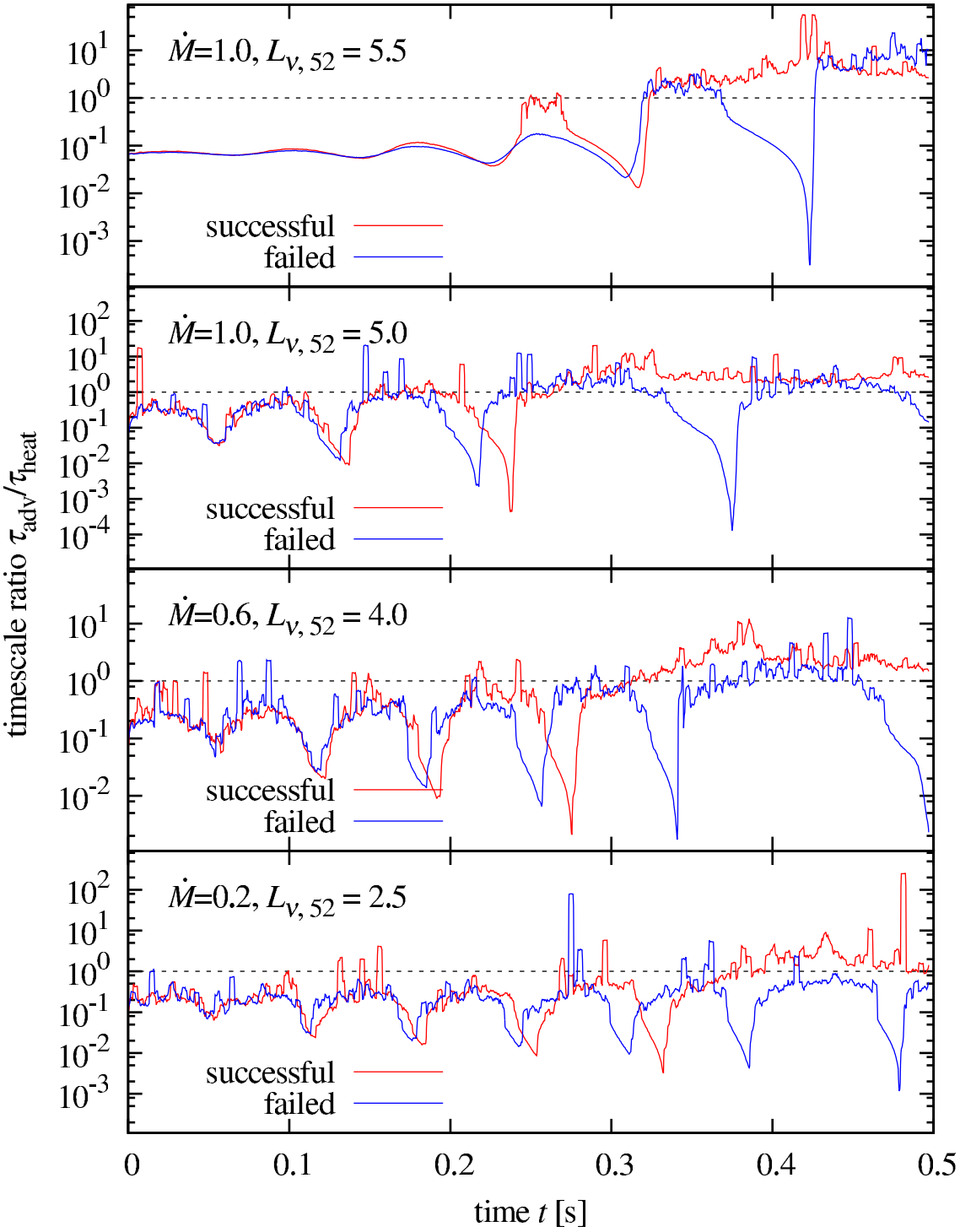

Figure 4.10. Timescale ratios of selected models on and below the critical surface. Red and blue lines show the ratios of successful and failed models, respectively. Different panels show the models with different $\dot{M}$ and $L_{\nu,52}$ as shown at the top left of each panel in units of $M_\odot\,\mathrm{s}^{-1}$ and $10^{52}\,\mathrm{erg\,s}^{-1}$, respectively. Note that the timescales τ_{adv} and τ_{heat} are averaged over 3 ms before taking the ratio. This figure is reproduced from Harada et al. (2017) by permission of the AAS.

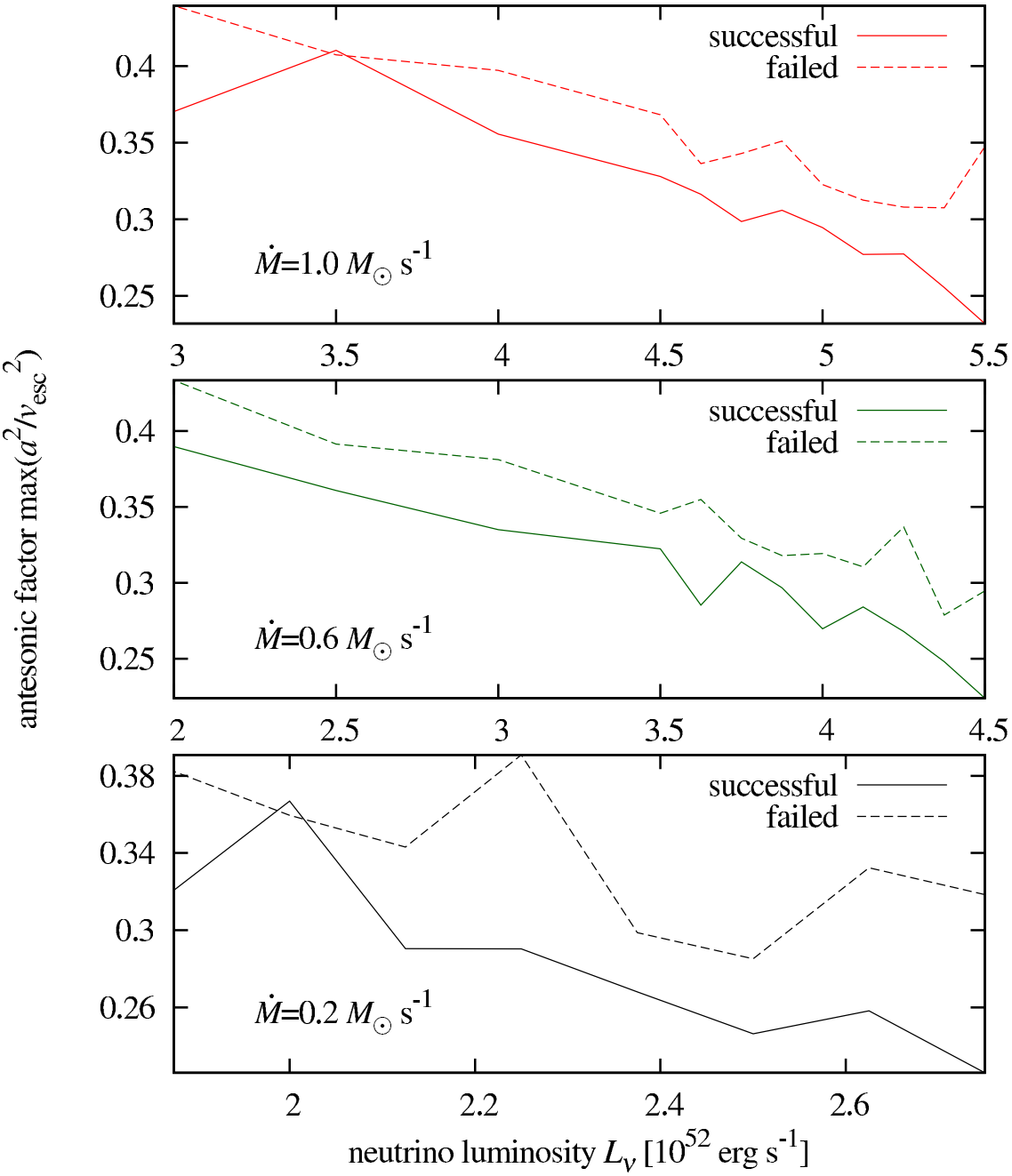

Figure 4.11. The maximum antesonic factors $\max(a^2/v_{\rm esc}^2)$ for different neutrino luminosities and mass accretion rates. Solid lines stand for the successful models on the critical surface, while dashed lines are the failed models just below the critical surface. The top, middle, and bottom panels show the models with $\dot{M} = 1.0\,M_\odot\,{\rm s}^{-1}$, $0.6\,M_\odot\,{\rm s}^{-1}$, and $0.2\,M_\odot\,{\rm s}^{-1}$, respectively. This figure is reproduced from Harada et al. (2017) by permission of the AAS.

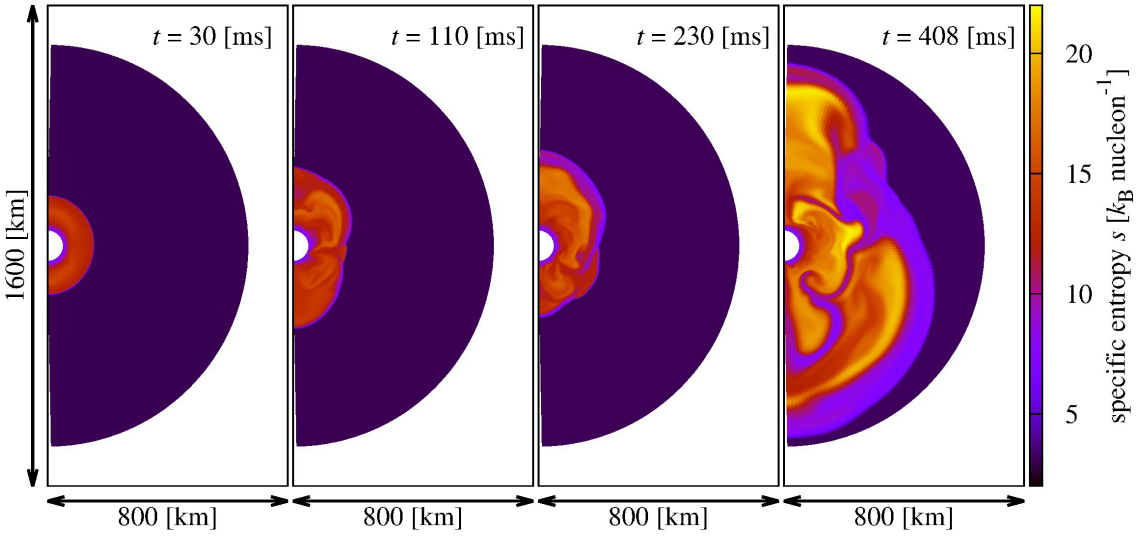

Figure 4.12. Entropy distributions for the 2D model with $\dot{M} = 0.6\,M_\odot/\mathrm{s}$, $L_\nu = 4.0 \times 10^{52}\,\mathrm{erg/s}$, and $\delta = 0.07$, on the critical surface. Each panel corresponds to the different time from the onset of the injection of the acoustic waves as indicated in the panels. The horizontal and vertical lengths are also displayed in the figure with arrows. The central white regions are PNSs and excised from the computational domain. The symmetry axis is the left end of each panel. This figure is reproduced from Harada et al. (2017) by permission of the AAS.

the antesonic condition is interpreted as the condition for the shock revival, it originally means the condition for the non-existence of the steady-state solution. Therefore it is not surprising that the antesonic condition cannot distinguish the successful and failed models in which the dynamical processes play crucial roles.

Conditions discussed above are suggested in the context of the neutrino heating mechanism. With this in mind, it is natural that these conditions cannot explain the explosions by the acoustic models. Conversely, if a model fails to explode by the neutrino heating mechanism and does not satisfy these conditions, one cannot conclude that the model also does not explode by the acoustic (or hybrid) mechanism.

4.3 2D result

Although the 1D simulations are simple enough to understand the relevant physical processes, the acoustic mechanism works in multi-dimensions intrinsically since the g-mode which is the origin of the acoustic waves are non-spherical mode. In this section, the 2D simulation results are presented. Numerical settings are already explained in section 4.1.

Before going to the critical surface, let me illustrate the typical evolution of the 2D models. Shown in figure 4.12 is the entropy distributions in the meridional section at the chosen times indicated in each panel. The model parameters are $\dot{M} = 0.6\,M_\odot\,\mathrm{s}^{-1}$, $L_\nu = 4.0 \times 10^{52}\,\mathrm{erg\,s}^{-1}$, and $\delta = 0.07$. This model is on the critical surface, and hence the

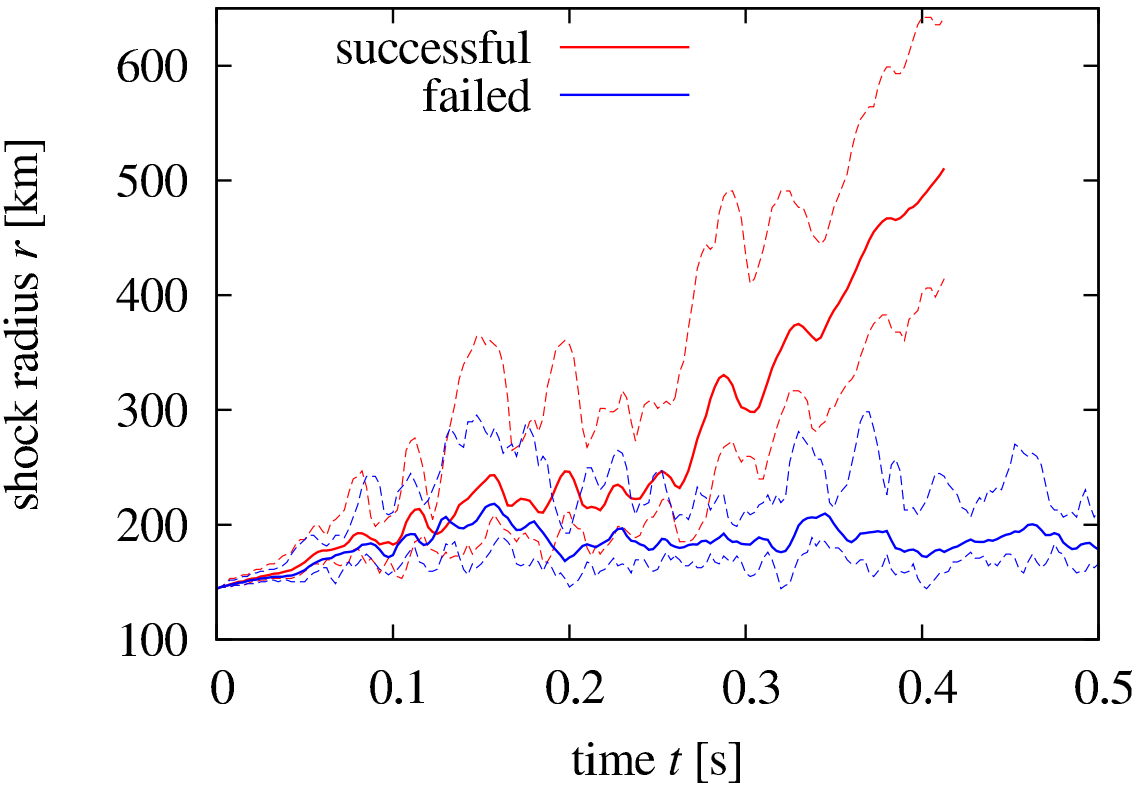

Figure 4.13. The trajectory of the primary shock for the successful (failed) model on (just below) the critical surface indicated with red (blue) lines. The mass accretion rate and the neutrino luminosities are $0.6\,M_\odot\,\mathrm{s}^{-1}$ and $4.0\times10^{52}\,\mathrm{erg\,s}^{-1}$, respectively. The solid lines represent the mean shock radii, and the dashed lines indicate the maximum and minimum shock radii. The red lines are truncated at the time when the maximum shock radius reaches the outer boundary. This figure is reproduced from Harada et al. (2017) by permission of the AAS.

shock successfully revives. The shock is almost spherical initially ($t = 30\,\mathrm{ms}$), then takes prolate shape by large bubbles which are created by the dipolar acoustic waves emitted from the PNS surface, which oscillates in $\ell = 1$ angular mode ($t = 110,\ 230\,\mathrm{ms}$). The shape of the shock changes with time and the shock revives finally ($t = 408\,\mathrm{ms}$).

Figure 4.13 shows the time evolution of the primary shock for both successful and failed models. In the early phases, the shock evolutions are similar. Both shocks expand for the first $\sim 100\,\mathrm{ms}$ and are stalled for the next $\sim 100\,\mathrm{ms}$. The differences appear in the late phase. For the failed model, the mean shock radius is almost constant until 500 ms. For the successful model, on the other hand, the mean shock radius rapidly expands and reaches 500 km at $\sim 410\,\mathrm{ms}$. The difference in δ between these models is only 0.01.

By collecting the successful models like that indicated in figures 4.12 and 4.13, the critical surface for the 2D models is drawn in figure 4.14. It is in the space spanned by $\dot{M}$, L_ν, and δ. It should be noted that the critical surface for 2D models has some ambiguity contrary to the 1D models. Table 4.1 describes the success or failure of the shock

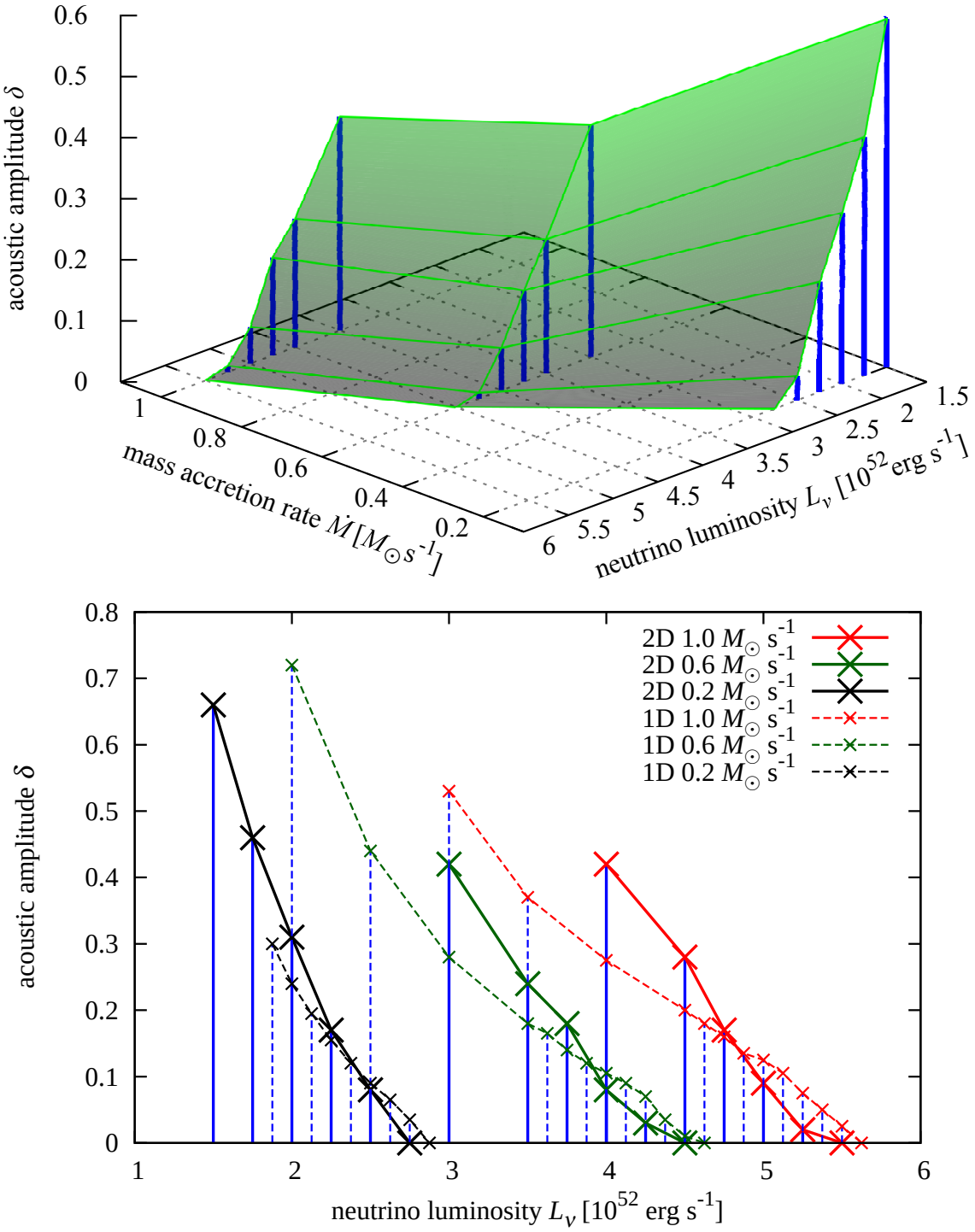

Figure 4.14. The same as figure 4.1 except that they are for the 2D models and the 1D counterparts are also illustrated in the lower panel. This figure is reproduced from Harada et al. (2017) by permission of the AAS.

Table 4.1. Success/Failure Score-sheet of the acoustic mechanism for the 2D models. This table is reproduced from Harada et al. (2017) by permission of the AAS.

$\dot{M} = 1.0\,M_\odot\,\mathrm{s}^{-1}$			
$L_\nu = 4.5 \times 10^{52}\,\mathrm{erg\,s}^{-1}$		$L_\nu = 4.0 \times 10^{52}\,\mathrm{erg\,s}^{-1}$	
$\delta = 0.40$	successful	$\delta = 0.24$	successful
$\delta = 0.39$	successful	$\delta = 0.23$	successful
$\delta = 0.38$	failed	$\delta = 0.22$	failed
$\delta = 0.37$	successful	$\delta = 0.21$	successful
$\delta = 0.36$	failed	$\delta = 0.20$	failed
$\delta = 0.35$	successful	$\delta = 0.19$	failed
$\delta = 0.34$	failed		
$\delta = 0.33$	failed		

revival for models with $\dot{M} = 1.0\,M_\odot\,\mathrm{s}^{-1}$, $L_\nu = 4.5 \times 10^{52}\,\mathrm{erg\,s}^{-1}$ and $4.0 \times 10^{52}\,\mathrm{erg\,s}^{-1}$, and several δ's. As δ for models with both L_ν's increases from some low value, a successful model appears. Above that model, failed models appear again. If δ increases further, only successful models appear finally. Since the turbulence develops in the 2D models due to the convection and/or SASI, its stochastic nature affects whether the shock revives or not. Taking the ambiguity into account, the definition of the critical surface can be either the surface below which all models fail or that above which all models succeed: the points $(\dot{M},\ L_\nu,\ \delta) = (1.0\,M_\odot\,\mathrm{s}^{-1},\ 4.5 \times 10^{52}\,\mathrm{erg\,s}^{-1},\ 0.35)$ and $(1.0\,M_\odot\,\mathrm{s}^{-1},\ 4.0 \times 10^{52}\,\mathrm{erg\,s}^{-1},\ 0.21)$ are on the critical surface with the former definition, while the points $(\dot{M},\ L_\nu,\ \delta) = (1.0\,M_\odot\,\mathrm{s}^{-1},\ 4.5 \times 10^{52}\,\mathrm{erg\,s}^{-1},\ 0.39)$ and $(1.0\,M_\odot\,\mathrm{s}^{-1},\ 4.0 \times 10^{52}\,\mathrm{erg\,s}^{-1},\ 0.23)$ are on the surface with the latter definition. In this chapter, the former definition is employed.

For the comparison between the critical surfaces for different dimensional models, the sections of the critical surfaces for both 1D and 2D models by planes with constant $\dot{M}$ are shown in the lower panel of figure 4.14. The critical amplitudes for both the 1D and 2D models are similar, but those for the 2D models with large L_ν are smaller than those for the 1D models, and vice versa for models with small L_ν. This similarity is not essential, however, since the $\ell = 0$ mode amplitude for the 1D models and the $\ell = 1$ mode amplitude for the 2D models are compared. For the comparison between the 1D and 2D models, not the amplitude but the acoustic power is the appropriate quantity.

In order to estimate the acoustic power, the Myers' flux is again utilized. The radial component of Myers' flux is shown in figure 4.15. The lateral component is not shown since it is negligible compared with the radial component. The outer black semi-circles in each panel are the shock radii of the initial condition. As seen from the figure, the radial component of the Myers' flux is positive for almost whole regions inside the shock, indicating that the outward directed acoustic waves indeed transfer the energy outward. The Myers' flux is intense in the vicinity of the symmetry axis and weak on the equator since the acoustic waves are emitted in a dipolar way. Note that the negative Myers' flux

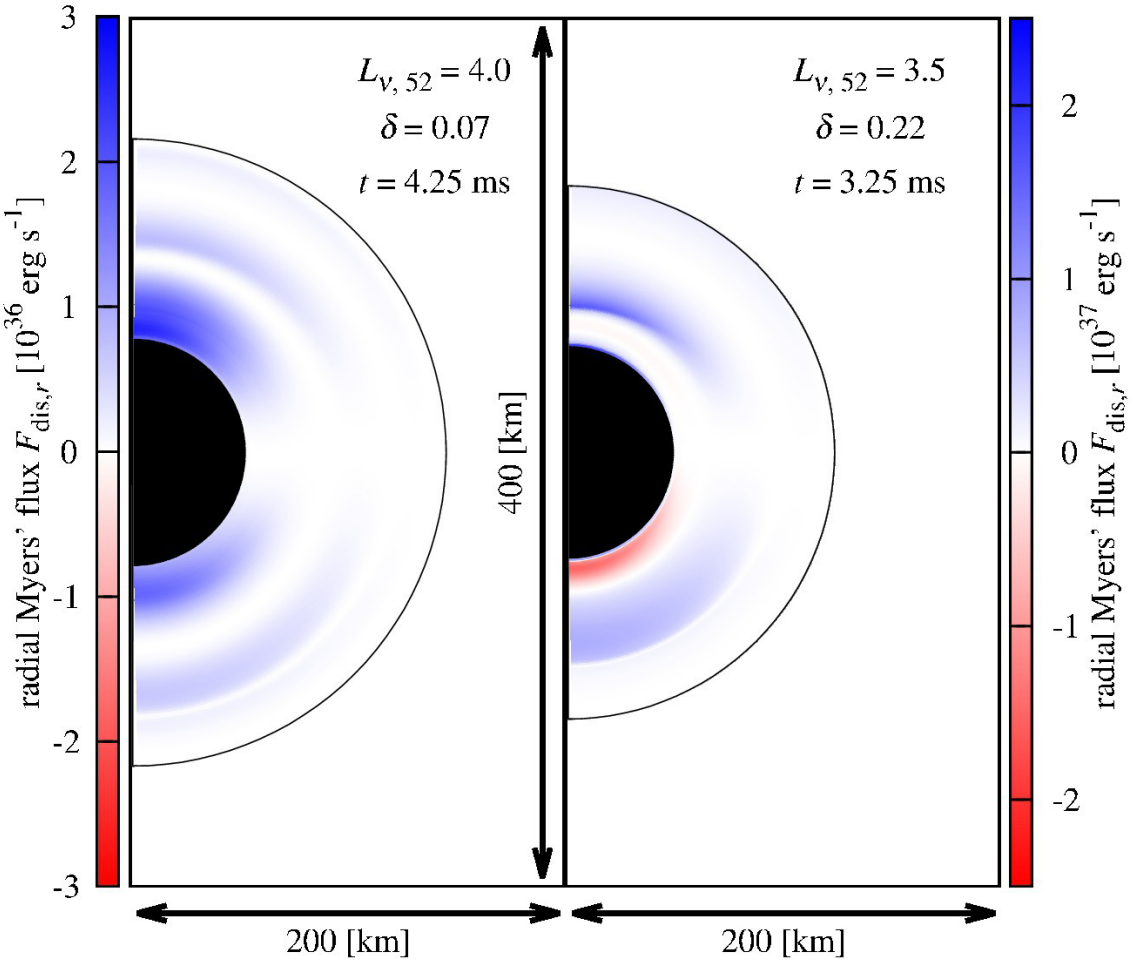

Figure 4.15. The distributions of the radial component of the Myers' flux. Two models on the critical surface are adopted: left panel–$L_{\nu,\,52} = L_\nu/(10^{52}\,\mathrm{erg\,s^{-1}}) = 4.0$, $\delta = 0.07$ and right–$L_{\nu,52} = 3.5$, $\delta = 0.22$. Blue colors indicate the positive radial flux, while red colors are the negative one. The central black regions are the PNSs and excised from the simulation. The outer black thin circles are the positions of the initial shock radii. Note that the Myers' flux outside the black thin circle is not shown. This is because the unperturbed flows are quite different from the perturbed flow after the passage of the primary shock, and hence Myers' flux does not purely describe the energy transport by the acoustic waves to the primary shock. This figure is reproduced from Harada et al. (2017) by permission of the AAS.

appears in the southern region close to the PNS in the right panel. Since the background density gradient is steep in the vicinity of the PNS surface, the acoustic waves are reflected inward there.

Since the Myers' flux is positive almost everywhere, the acoustic luminosity can be estimated by the surface integral and employed as the acoustic power. In figure 4.16, the acoustic luminosities for several models are shown. The acoustic luminosity at a radius r is defined by the 3 ms average of the angular integrated Myers' flux from the instant when

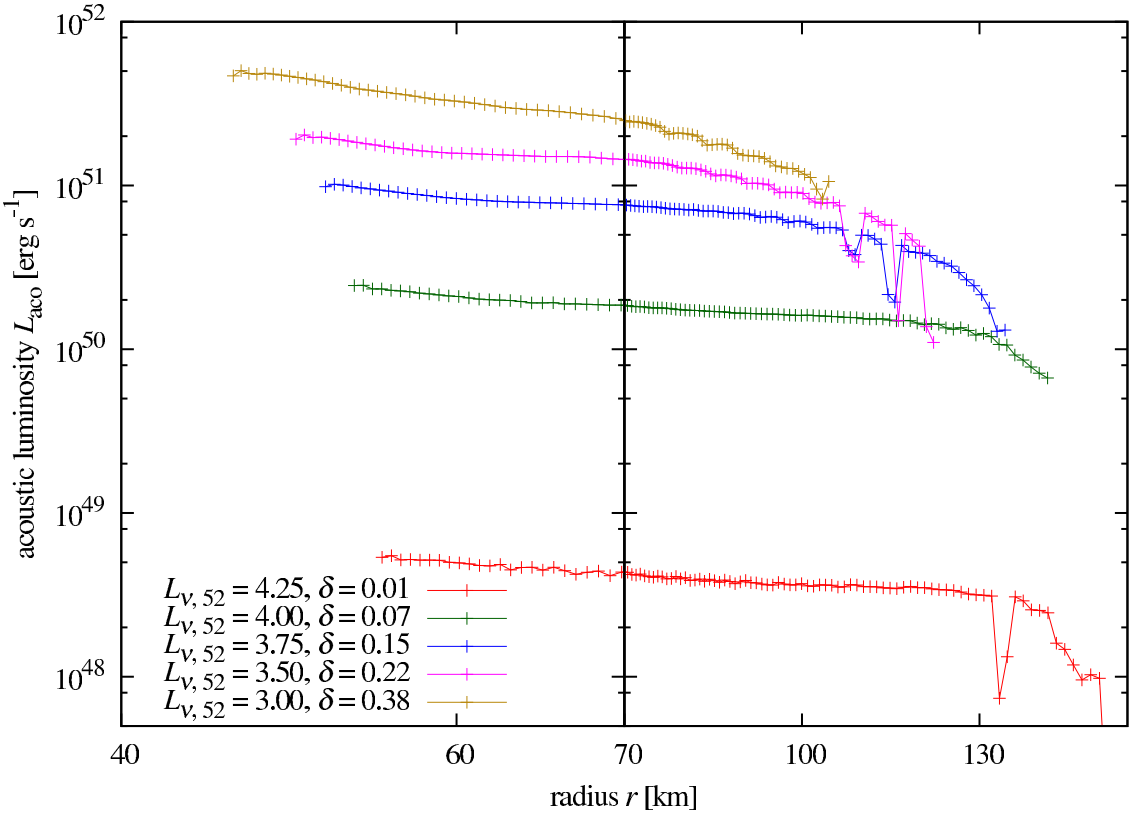

Figure 4.16. The radial profiles of the periodic averaged acoustic luminosities for the 2D models with $\dot{M} = 0.6\,M_\odot/\mathrm{s}$. Line colors and legends are the same as in figure 4.4. The "+" symbols are again the on-grid values. This figure is reproduced from Harada et al. (2017) by permission of the AAS.

the mean radius of the front of the acoustic waves reaches the radius r. This is a similar procedure to the 1D case once after the Myers' flux is surface-integrated. The peculiar behaviors on the first two grid points are also seen like those in figure 4.4, and hence the values at the third grid points are employed as the acoustic power.

The critical surface using the acoustic power explained above is shown in figure 4.17. The acoustic-power-critical-surface for the 2D models is systematically below the surface for the 1D models, although the amplitude-critical surface is similar as shown in figure 4.14. This is because the amplitudes of the different modes are compared as already discussed. When the amplitude is so small that the linear theory is applicable, the acoustic power is proportional to the squared amplitude. Since the perturbation employed in this chapter is proportional to the Legendre polynomial $\mathcal{P}_\ell(\mu)$, the acoustic power is proportional to the angular integrals of the Legendre polynomial $\int_{-1}^{1} \mathcal{P}_\ell(\mu)\mathrm{d}\mu = 2$ for $\ell = 0$ (1D) and 2/3 for $\ell = 1$ (2D). The acoustic power is hence larger for the 1D models than the 2D models even if the dimensionless amplitude δ is the same.

In order to investigate the energetics in more detail, the total heating rates for both the 1D and 2D models on the critical surfaces (see figure 4.6) and the neutrino heating rates are illustrated in figure 4.18. Again the energy required for the shock revival for the

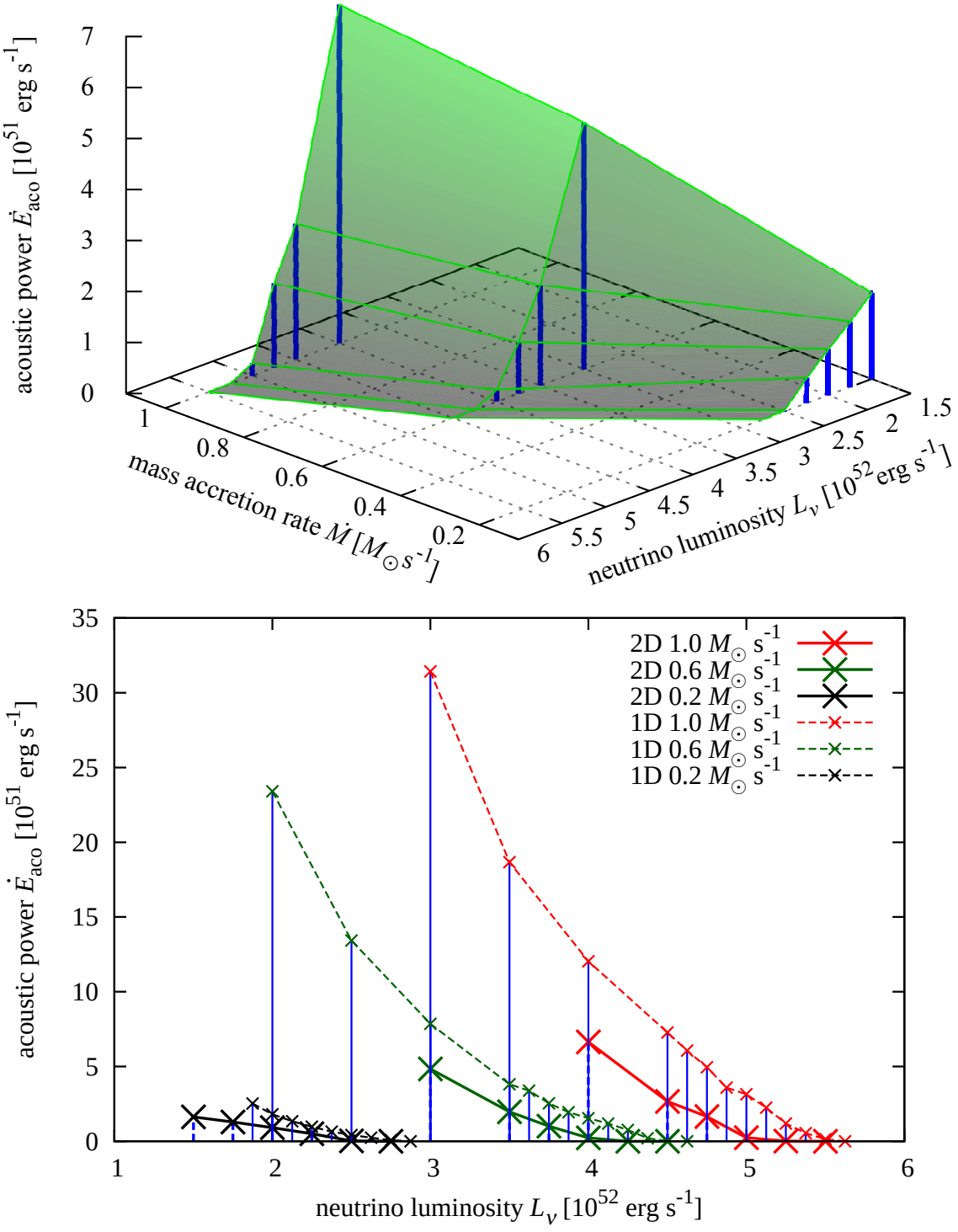

Figure 4.17. The same as figure 4.14 except that acoustic power is used instead of the amplitude. This figure is reproduced from Harada et al. (2017) by permission of the AAS.

2D models are lower than those for the 1D models. For the circled models in the figure, the critical acoustic power is negligibly small, and the shock revives essentially only by the neutrino heating. The acoustic wave is the driver of hydrodynamic instability, which supports the neutrino heating, rather than the energy source of the shock revival. As indicators of the turbulent effects induced by the instability, the turbulent kinetic energy, the gain mass (the mass in the gain layer), and the neutrino heating rate are shown in figure 4.19. The turbulent kinetic energy $E_{\rm turb}$ shown in the top panel of the figure is defined as

$$E_{\rm turb} = \frac{1}{2}\int_{\rm gain} {\rm d}V\rho\left(v_\theta^2 + (v_r - \langle v_r\rangle)^2\right), \tag{4.19}$$

where $\langle v_r\rangle$ is the spherically averaged radial velocity. The domain of integration is the gain layer. The immediate increase in the turbulent kinetic energy $E_{\rm turb}$ indicates the development of the turbulence owing to the injected acoustic waves. The developed turbulence induces the increase in the gain mass as seen in the middle panel of the figure, indicating the increase in the dwell time as discussed in section 2.2.1. The longer the dwell time is, the higher the neutrino heating rate in the gain region is, as shown in the bottom panel of the figure. This enhancement in the neutrino heating rate does not appear in the model without the acoustic wave injection, and hence the acoustic waves are still indispensable for the shock revival even if the amplitudes are small. The shock revivals in these models are, however, essentially not by the acoustic mechanism but by the neutrino heating mechanism.

For the models with small L_ν, the injection of the acoustic power plays a crucial role, i.e., the shocks of these models revive by the acoustic mechanism. The required total heating rates of the 2D models are again smaller than those of the 1D models as expected from figure 4.17. A probable reason for the lower total heating rate of the 2D models on the critical surface is the enhancement of the neutrino heating by the fluid instability again. The neutrino heating, however, plays only a minor role in these models. Similar to figure 4.6, the total heating rate increases with decreasing neutrino heating rate for the 2D models, implying that the acoustic heating is inefficient. The through analysis like what is conducted for the 1D models in section 4.2 cannot be performed for the 2D models since the 2D flows are complicated. It is probable, however, that the reason is the same as the 1D cases: the enhancement of the neutrino cooling by secondary shocks and the partial reflection of acoustic waves are the origins of the reduction of the efficiency of the acoustic heating.

4.4 discussion and conclusion

The shock revival in the supernova core by the acoustic wave injection from the central PNS is simulated under 1D spherical and 2D axial symmetry in a phenomenological way. Although the original acoustic mechanism only works in multi-dimensions, the 1D simulations are first performed in order to understand the energy transport and deposition by the acoustic waves. By performing simulations with various mass accretion rates $\dot{M}$, neutrino luminosities L_ν, and the amplitudes of the injected acoustic waves δ, I draw

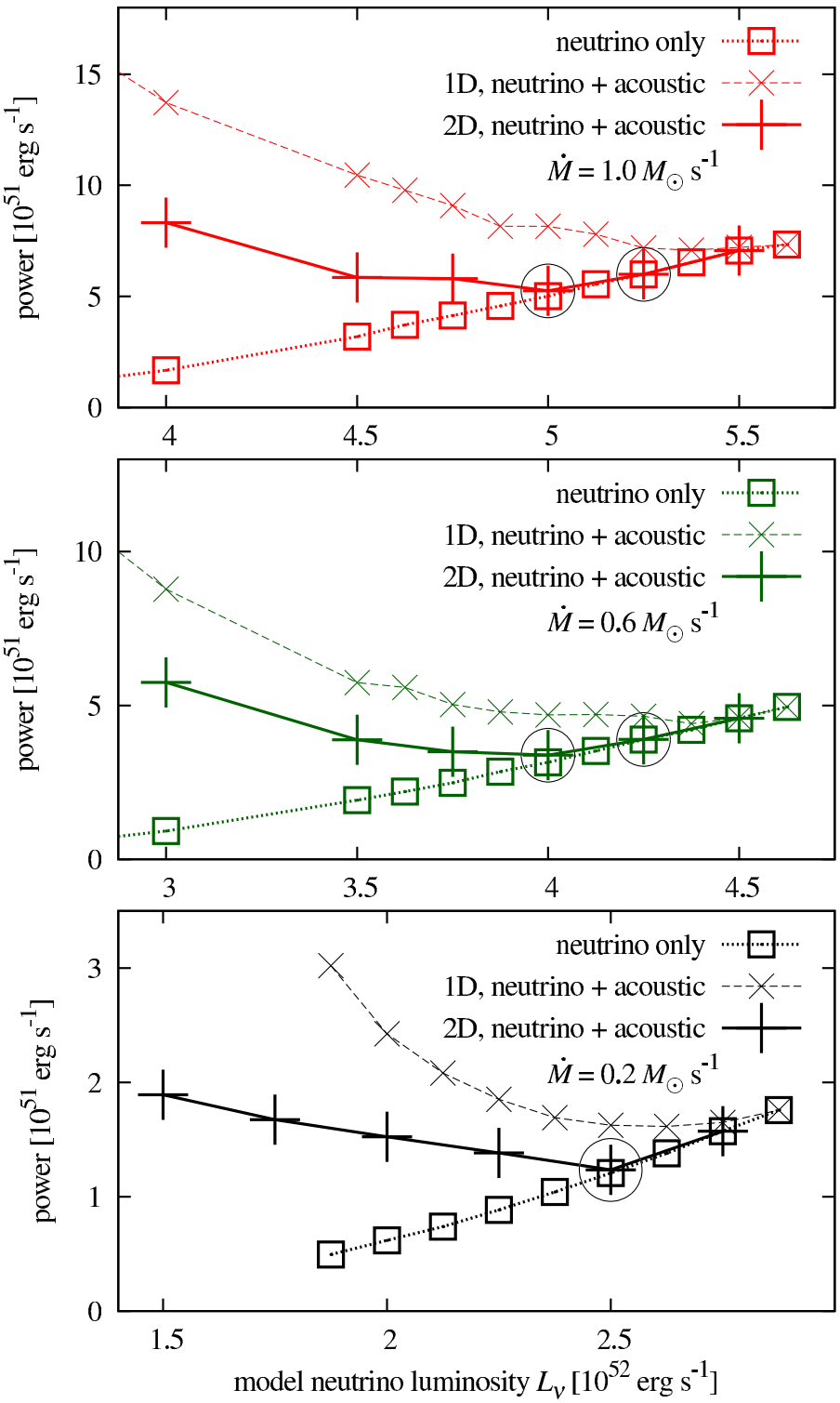

Figure 4.18. The neutrino heating rates (dotted lines) and the total heating rate (the sum of the acoustic power and the neutrino heating rate) for the 1D (dashed lines) and 2D (solid lines) models on the critical surfaces. The top, middle, and bottom panels represent the models with $\dot{M} = 1.0\,M_\odot\,\mathrm{s}^{-1}$, $0.6\,M_\odot\,\mathrm{s}^{-1}$, and $0.2\,M_\odot\,\mathrm{s}^{-1}$, respectively. The models whose critical acoustic powers are negligible compared to the neutrino heating rates are marked with circles. This figure is reproduced from Harada et al. (2017) by permission of the AAS.

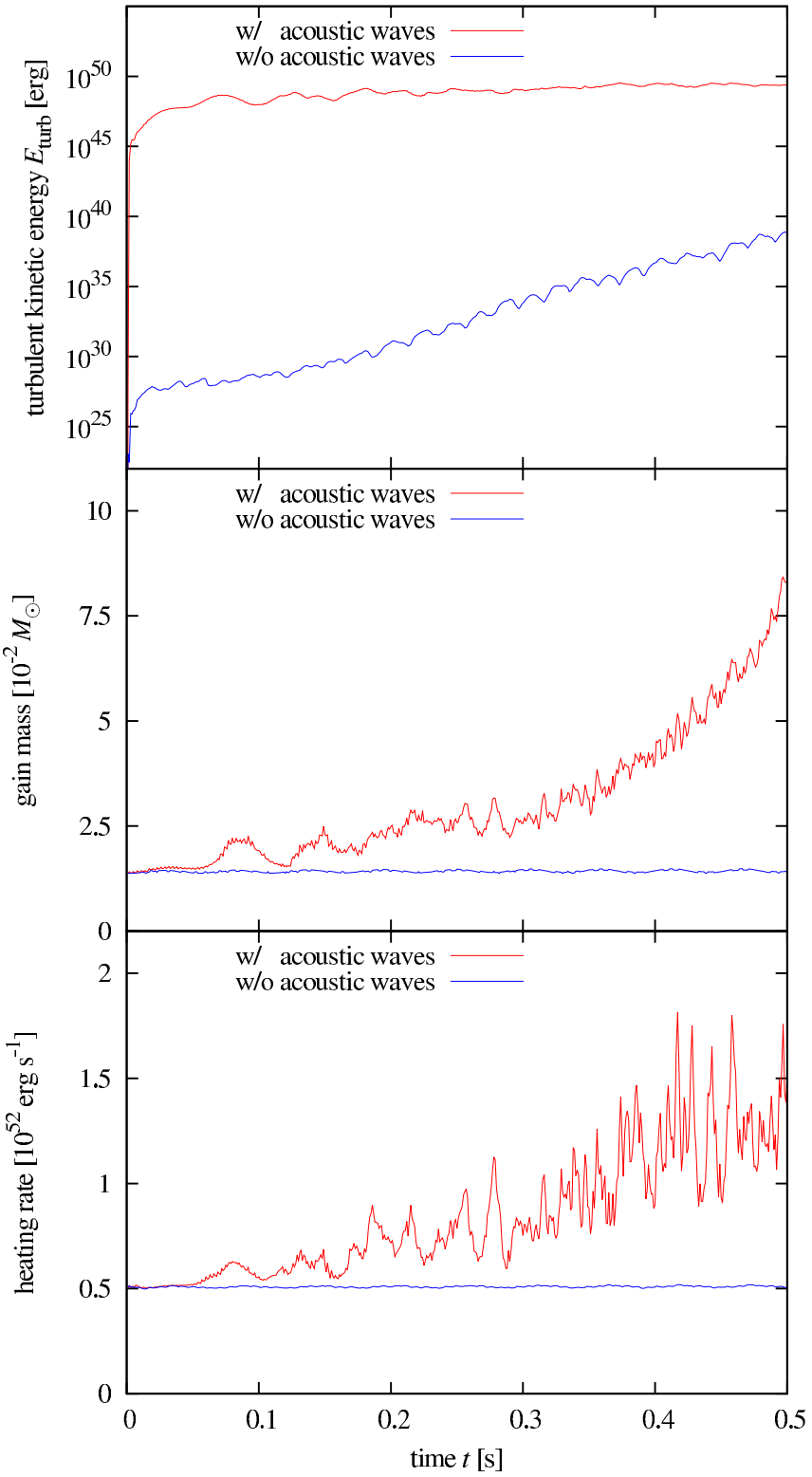

Figure 4.19. Comparisons of the turbulent effects on the models with (red) and without (blue) acoustic waves. The top, middle, and bottom panels display the turbulent kinetic energy, the gain mass, and the neutrino heating rate, respectively. The mass accretion rate and the neutrino luminosity for both models are $1.0\,M_\odot\,\mathrm{s}^{-1}$ and $5.0\times10^{52}\,\mathrm{erg\,s}^{-1}$, respectively. The model with acoustic waves employed here is one of the models with circles in figure 4.18. This figure is reproduced from Harada et al. (2017) by permission of the AAS.

the critical surface which divides the successful and failed model parameters in the space spanned by $\dot{M}$, L_ν, and δ. The secondary shocks, into which the acoustic waves steepen, repeatedly collides with the primary shock. As a consequence, the primary shock oscillates with growing amplitude, and eventually shows the runaway expansion for the successful models. The shock revival in this chapter occurs due to a combination of the neutrino and acoustic heating, however, and the mechanism considered in this chapter might be called the hybrid mechanism.

The Myers corollary of the energy conservation theorem is extended in order to consider the energy flux of the finite-amplitude acoustic waves with the neutrino reactions. Thanks to this extension, the acoustic power $\dot{E}_{\rm aco}$ instead of the amplitude is estimated, and the critical surface is re-drawn in the space spanned by $\dot{M}$, L_ν, and $\dot{E}_{\rm aco}$. With this critical surface, the energetics is discussed. For the models on the critical surface with large L_ν, the total heating rates of the acoustic power and the neutrino heating almost only depend on the mass accretion rate. The decrease in the neutrino heating rate is nearly compensated for by the increase in the acoustic power, and hence there may be a threshold value of the total heating rate for the shock revival. For the models with small L_ν, however, the total heating rates increase with the decreasing L_ν. This is because the acoustic waves with large amplitude form the strong secondary shocks. It results in the higher temperatures, and the neutrino cooling is enhanced. Due to this enhancement, more energy than the threshold in the total heating rate should be injected, and hence the more acoustic power is required. In addition, the timescale ratio and the antesonic condition are applied in order to check whether these diagnostics for the shock revival by the neutrino heating mechanism are also useful in the present mechanism or not. Both of them cannot distinguish the successful models from the failed models.

Next, the 2D axisymmetric simulations are conducted. First, the critical surface for the 2D simulations is drawn in the space spanned by $\dot{M}$, L_ν, and δ. Subsequently, the acoustic power is estimated by using the extended Myers' theory again, and the critical surface with $\dot{M}$, L_ν, and $\dot{E}_{\rm aco}$ is drawn. The comparison between the 1D and 2D models demonstrates that the critical acoustic powers for the 2D models are always smaller than those for the 1D models. The reason is that the acoustic waves induce fluid instability and hence the turbulence, which then enhance the neutrino heating.

From the viewpoint of the energy, let me discuss the results reported in Burrows et al. (2006) with the critical surface obtained in figure 4.17. Burrows et al. (2006) conducted the numerical simulation in a self-consistent manner, and hence the mass accretion rate and the neutrino luminosity depend on time. A representative combination of parameters is needed for the comparison with the critical surface, and I detected that $\dot{M} \sim 0.1\,M_\odot\,{\rm s}^{-1}$ and $L_\nu \sim 2.0 \times 10^{52}\,{\rm erg\,s}^{-1}$ are the representative values from their simulation. The acoustic power estimated in Burrows et al. (2006) is $\sim 4 \times 10^{51}\,{\rm erg\,s}^{-1}$. It is likely that this power is much larger than the critical acoustic power obtained. The critical acoustic power for the shock revival of the model with $\dot{M} \sim 0.2\,M_\odot\,{\rm s}^{-1}$ and $L_\nu \sim 2.0 \times 10^{52}\,{\rm erg\,s}^{-1}$ is $\dot{E}_{\rm aco} \sim 9 \times 10^{50}\,{\rm erg\,s}^{-1}$ in this chapter. Because the critical acoustic power decreases with the mass accretion rate according to figure 4.17, the critical acoustic power for the model

with $(\dot{M},\ L_\nu) = (0.1\,M_\odot\,\mathrm{s}^{-1},\ 2.0\times10^{52}\,\mathrm{erg\,s}^{-1})$ is likely smaller than $\sim 9\times10^{50}\,\mathrm{erg\,s}^{-1}$. Therefore the estimated acoustic power by Burrows et al. (2006) is large enough for the shock to revive via the acoustic mechanism. Incidentally, the acoustic power suggested by Yoshida et al. (2007) is slightly above the critical surface, and the shock can revive via the acoustic mechanism. The acoustic power estimated by Weinberg & Quataert (2008) is, on the other hand, much smaller than the critical value, and the shock revival likely fails.

There may be another interesting constraint for the acoustic mechanism. The maximum possible value for the acoustic amplitude δ is unity since $\delta > 1$ results in the negative density at the PNS surface. With a linear extrapolation of the critical surface in figure 4.14 to $\delta = 1$, the section of the critical surface by the plane with $\delta = 1$ passes through the points $(\dot{M}, L_\nu) = (1.0\,M_\odot\,\mathrm{s}^{-1}, \sim 2\times10^{52}\,\mathrm{erg\,s}^{-1})$, $(0.6\,M_\odot\,\mathrm{s}^{-1}, \sim 1\times10^{52}\,\mathrm{erg\,s}^{-1})$, and $(0.2\,M_\odot\,\mathrm{s}^{-1}, \sim 1\times10^{52}\,\mathrm{erg\,s}^{-1})$. This section is a kind of the critical curve: for given mass accretion rates, the models with neutrino luminosities lower than these values do not explode whatever intense acoustic waves are injected. It is worth noting that only sinusoidal perturbations with the period of 3 ms are imposed at the inner boundary in this chapter, and hence other types of perturbations (different angular modes, oscillation periods, and so on) may result in other estimations of the critical values. The resultant critical values probably do not change by the order of magnitude since the condition that the density is positive limits the maximum fluctuation amplitude whatever types of disturbances are considered.

With the critical surface obtained in this chapter, now the acoustic power required to the shock revival can be estimated, and it seems to be consistent with the realistic simulations. It is hence evident that the shock can certainly revive by the acoustic mechanism, though it depends on the emission of the acoustic waves. There are some caveats, however. First, the turbulence should have existed in the postshock flows before the acoustic wave emission from the PNS since the g-mode oscillation is excited originally by the turbulence. The turbulence hence affects not only the heating processes by the acoustic waves but also the generation of acoustic waves itself. Although these effects are also important, it is beyond the scope of this dissertation. Second, the 2D simulations are considered in this chapter and the original works by Burrows et al. (2006, 2007a,b). In the 3D, however, the properties of turbulence are different due to the inverse cascade as discussed in section 2.2.1. The turbulent eddy is small in 3D (e.g., Couch, 2013; Takiwaki et al., 2014; Melson et al., 2015) and may reduce the neutrino heating rate shown in figure 4.19, and hence the more acoustic power may be required, i.e., the critical surface may rise. On the other hand, smaller turbulent eddies may produce the weaker g-mode oscillation on the PNS, and hence the emitted acoustic waves may also be weaker. These issues should be addressed somewhere, but it is not in the scope of this dissertation.

Chapter 5

Summary and Conclusions

In this dissertation, I investigate the explosion mechanisms of the CCSNe with numerical simulations. The explosion mechanism is still unclear despite much effort paid by numerous supernova modelers. It is determined by the complex interplay among the hydrodynamics, neutrino transport and reactions, nuclear EOS, and strong gravity. Therefore only the numerical simulations can elucidate the explosion mechanism. Several hypotheses of the explosion mechanism have been proposed so far, and which hypothesis is the most realistic is addressed by careful examinations on each hypothesis. In this dissertation, the neutrino heating mechanism and the acoustic mechanism are investigated by the numerical simulations with different levels of sophistication. I give the summary of what is done, what is found, and what is the consequence, and subsequently, conclude this dissertation with some future prospects.

First, the neutrino heating mechanism is investigated. Since the neutrino transport plays a vital role in this mechanism, the Boltzmann-radiation-hydrodynamics code, which solves the Boltzmann equation for the neutrino transport directly, is employed. The preceding simulation demonstrated that a non-rotating progenitor fails to show the shock revival (Nagakura et al., 2018), and hence whether the effects of rotation lead to the successful shock revival or not is investigated in chapter 3. The rotation certainly affects the morphology of the shock. Entropy distributions affected by the centrifugal force are observed. The mean shock radius, the neutrino luminosity, and the mean energy of the neutrinos for the rotating model are, however, very similar to those for the non-rotating counterpart which does not explode. Besides, the timescale ratio, the commonly used diagnostic for the shock revival, exceeds unity for only a limited period. These results imply that the rotation employed in this chapter does not affect the explodability, although it is almost the fastest end expected from the stellar evolution theory.

Incidentally, the distributions of neutrinos in the momentum space is examined, although it does not directly measure the explodability. This is motivated by the fact that the distribution function in the phase space is directly accessible thanks to the Boltzmann-radiation-hydrodynamics code. The effects of rotation on the $Y_{\rm e}$ prescription (Liebendörfer, 2005), the energy dependence of the angular distribution in the momentum space, and the angular moments of the distribution function are investigated. Especially, the careful attention is paid for the second angular moment, or the Eddington tensor.

It is found that the Eddington tensor is determined by the complex combination of the neutrino flux, the neutrino reactions, and the matter velocity. Besides, the accuracy of one of the approximate methods for neutrino transport, the M1-closure method, is examined. The estimated error is $\sim 20\%$ at most. Finally, the angular momentum transport by neutrinos is evaluated. According to the results, the analytic prescription proposed in Epstein (1978) is accurate enough to estimate the order of magnitude of the angular momentum loss.

Since the rotation does not lead the successful shock revival, other physical processes should be considered. There are several possibilities including the updated microphysics, general relativistic gravity, and so on. Besides, the acoustic mechanism is also a possible scenario. In this dissertation, the acoustic mechanism is investigated next.

The acoustic mechanism works after the neutrino heating mechanism fails, and hence it requires long-term simulations exceeding $\mathcal{O}(1)\,\mathrm{s}$ after the core bounce. The significant computational cost needed by the Boltzmann-radiation-hydrodynamics code prohibits such long-term simulations. Instead, I resort to another phenomenological approach in chapter 4: the critical surface drawn in the parameter space spanned by the mass accretion rate, neutrino luminosity, and acoustic power. In order to estimate the acoustic power with large amplitude waves and neutrino reactions, I extend the Myers' corollary of the energy conservation theorem. First, the critical surface for the 1D spherically symmetric simulations is drawn, although the acoustic mechanism intrinsically works in multi-dimensions. This is because the 1D simulations are simple and easy to understand the physical picture. Indeed, by investigating the energy injection of the acoustic waves in the 1D simulations, it is found that there exists threshold value of the total heating rate (the sum of the acoustic power and the neutrino heating rate) depending on the mass accretion rate. It is also detected that the acoustic wave with large amplitude enhances the neutrino cooling by rising the postshock temperature, and hence not all of the acoustic power is used for the shock revival.

The shock revival in 2D by the acoustic mechanism is examined subsequently. By exploiting the extended Myers' corollary again, the critical surface in the space of the mass accretion rate, neutrino luminosity, and acoustic power is drawn. The critical acoustic powers are smaller for 2D than those for 1D because the turbulent effects help the neutrino heating. According to the critical surface for the 2D simulations, the acoustic mechanism is certainly a possible mechanism since the critical surface suggests that the acoustic power estimated in Burrows et al. (2006) is enough for the shock to revive, although the emission process of the acoustic waves is not fully understood yet.

As a consequence of the investigations conducted in this dissertation, the rotation alone is not enough to revive the shock among many possible missing physics of the neutrino heating mechanism. The heating by the acoustic waves in the late phase, i.e., the acoustic mechanism, is one of the promising possibilities. There still are many things to be investigated. In this dissertation, the acoustic mechanism is investigated not in a self-consistent but in a phenomenological way. In order to fully understand the acoustic mechanism, the emission of and heating by the acoustic waves should be simulated coherently with

the time-dependent mass accretion rate and neutrino luminosity. One possible way is to continue the simulation which fails in the shock revival by the neutrino heating mechanism such as what is presented in chapter 3 by an approximate but self-consistent code. Since the neutrino heating is less critical in the late phase than the early phase, the approximate neutrino transport may be sufficient. Although this dissertation relies on the acoustic mechanism to revive the shock, other possible missing physics is also worth investigating. Updating the microphysics is one of the main streams of the exploration of the neutrino heating mechanism as discussed in section 2.2.1. The neutrino reaction rates continue to be updated both theoretically and numerically, and hence implementing it in the Boltzmann-radiation-hydrodynamics code is urgent. As for the microphysics, the EOSs are also continuously updated. For example, the EOS based on the variational method to model the nuclear force is proposed by Furusawa et al. (2017), and applying it to the CCSNe simulations is also required. Incorporating the general relativistic gravity is also important since it not only affects the dynamics in the supernova core but also is indispensable in calculating the gravitational waves. The implementation of the numerical relativity in the code is hence also urgent. Indeed, I have already developed the numerical relativity module in the spherical coordinates proposed by Baumgarte et al. (2013), and it is now ready to implement in the Boltzmann-radiation-hydrodynamics code. Implementing the updated microphysics and the numerical relativity results in the accurate prediction of the multi-messenger (neutrinos and gravitational waves) signal. The resultant code is hence pivotal to not only the exploration of the CCSN explosion mechanism but also the development of the multi-messenger astronomy. Besides, the dimensionality should not be forgotten. Due to the inverse cascade, the properties of turbulence in 2D is different from that in 3D. Although it is impossible to extend the dimensionality of the current Boltzmann-radiation-hydrodynamics code immediately owing to the limited computational resources, such an extension is necessary. By accumulating the improvements in the understanding of the missing physics, the whole picture of the explosion mechanism of the CCSNe will be unveiled.

Acknowledgments

First I acknowledge my supervisor, Naoki Yoshida. Although he is not a specialist in CCSNe, he kindly discusses the direction of my research and so on. Next, I acknowledge the Boltzmann-CCSNe research group, whose member is Shoichi Yamada, Kohsuke Sumiyoshi, Hideo Matsufuru, Hiroki Nagakura, Wakana Iwakami, Hirotada Okawa, and Shun Furusawa. The code used in this dissertation is offered from the group. Shoichi Yamada has excellent ideas, deep insights, and careful attention on CCSNe, and the discussion with him is the most indispensable part in writing this dissertation, and hence I very sincerely acknowledge him. Hiroki Nagakura is a prudent person, and discussion with him provides me a lot of points I missed but necessary to discuss. He is also the leading developer of the code, and he told me a lot of things about the code which is indispensable to analyze the simulation results. I also acknowledge Wakana Iwakami, who mainly teach me how to use the code. Every member of the Boltzmann-CCSNe group provides me with useful insights and encourage me, I sincerely appreciate it. The table of the EOS used in chapter 3 is provided by Shun Furusawa, and the leptonic part of EOS used in figure 3.5 is provided by Yu Yamamoto, and I also thank them. Further, I thank Masataka Ogane and Bernhard Müller for fruitful discussions. I also appreciate the UTAP members for discussions and encouragement. Kazumi Kashiyama gives me fruitful advice about the content and structure of this dissertation and so on, and without his help, this dissertation could not be completed. Through the coursework of Advanced Leading Graduate Course for Photon Science (ALPS) in the University of Tokyo, my sub-supervisor, Kaoru Yamanouchi, provided me useful suggestions from the viewpoint of non-specialist in physics. Numerical simulations presented in chapter 3 were performed in the high performance computing resources of the K computer and the FX10 of the HPCI system provided by the AICS and the University of Tokyo through the HPCI System Research Project (Project ID: hp160071), Computing Research Center in KEK, JLDG on SINET4 of NII, Research Center for Nuclear Physics in Osaka University, Yukawa Institute of Theoretical Physics in Kyoto University, and Information Technology Center in University of Tokyo. The simulations shown in chapter 4 were conducted on Cray XC30 at Center for Computational Astrophysics, National Astronomical Observatory of Japan, and the supercomputer system A at KEK (support by the Large Scale Simulation Program No. 14/15-17 (FY2014-2015), No. 15/16-08 (FY2015-2016), and No. 16/17-11 (FY2016-2017)). I was supported by ALPS in the University of Tokyo and Grant-in-Aid for JSPS Research Fellow (JP17J04422). Finally, I sincerely appreciate my family endlessly supporting and encouraging my life.

Appendix A

Code validation

Although the numerical techniques utilized in chapters 3 and 4 are explained in chapter 2, how they work well is not shown so far. In this appendix, the validation of the code is presented. The Boltzmann-radiation-hydrodynamics code is used in chapter 3 while the hydrodynamics code with neutrino heating terms by light-bulb method is employed in chapter 4. Actually, the hydrodynamics parts of both codes are essentially the same except for the treatment of the neutrino heating and reaction terms, the gravitational potential, and the acceleration terms. Therefore, the common hydrodynamics part is validated first in section A.1. Next, the Boltzmann solver implemented in the Boltzmann-radiation-hydrodynamics code is tested in section A.2. Not only the Boltzmann solver but also it integrated with the hydrodynamics and gravity parts, namely, the Boltzmann-radiation-hydrodynamics code, is validated in the section. Finally, the code employed in chapter 4, the hydrodynamics code with the light-bulb-neutrino-heating is validated in section A.3. Throughout this appendix, the radial, zenith, azimuthal grid numbers are denoted as N_r, N_θ, and N_ϕ, respectively. For the momentum space, the grid numbers of neutrino energy and flight direction are written as N_ϵ, N_{θ_ν}, and N_{ϕ_ν}, respectively.

A.1 Hydrodynamics part

The basic tests for the hydrodynamics part are presented in Nagakura et al. (2011). In this section, they are described to show the validity of the code employed throughout in this dissertation.

The standard test of the hydrodynamics code is the 1D shock tube problem. Two different and uniform fluid states are connected discontinuously initially. Then, three so-called simple waves are generated: the rarefaction wave, the shock wave, and the contact discontinuity. The solution of the shock tube problem is obtained analytically by using simple waves. This analytic solution is compared to the numerical solution.

In figure A.1, the results are presented. Here, two cases are tested. The initial conditions are $(\rho_{\rm L}, v_{\rm L}, p_{\rm L}, \rho_{\rm R}, v_{\rm R}, p_{\rm R}) = (10, 0, 13.3, 1, 0, 10^{-6})$ and $(1, 0, 10^3, 1, 0, 10^{-2})$, where ρ, v, and p are the density, velocity, and pressure, respectively, and the subscripts L and R indicate the left and right states, respectively. Let me call the cases with the former and latter initial conditions case A and case B, respectively. The spatial grid number is 400,

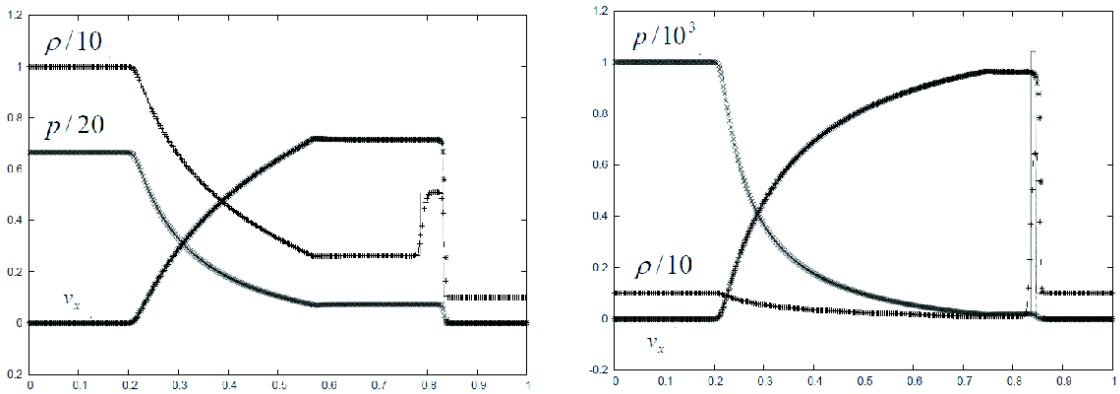

Figure A.1. The shock tube test for cases A (left, at $t = 0.4$) and B (right, at $t = 0.35$). The horizontal axis is the x-coordinate. The solid lines represent the analytic solutions. The plus, cross, and asterisk symbols indicate the density, pressure, and velocity, respectively. Note that the spike of the analytic solution around $x \sim 0.85$ in the right panel is a density spike. This figure is reproduced from Nagakura et al. (2011) by permission of the AAS.

and so-called γ-law EOS with $\gamma = 5/3$ is employed. Figure A.1 demonstrates that the shock tube problems are correctly solved.

For the 2D flow test, the steady-state is evolved by the dynamical code, and it is checked that the solution remains the steady-state. Here, the rotational equilibrium of the stellar matter is considered as the steady-state solution. The computational domain is $10^8\,\mathrm{cm} < r < 2 \times 10^{10}\,\mathrm{cm}$ and $0^\circ < \theta < 90^\circ$, and the grid numbers are $(N_r, N_\theta) = (230, 60)$ and $(460, 60)$. The initial condition is constructed by applying the Hachisu self-consistent field scheme (Hachisu, 1986; Kiuchi et al., 2010), and then it is evolved with the hydrodynamical and Poisson equations. Figure A.2 shows the resultant density profile along the rotational axis at $t = 100\,\mathrm{s}$ and the initial condition for both resolutions. This demonstrates that the hydrodynamics code employed here can correctly describe the 2D steady-state solution with sufficiently high resolution.

A.2 Boltzmann solver

The hydrodynamical part of the code is validated in the previous section. In this section, the Boltzmann solver employed in chapter 3 is validated. They are described in Sumiyoshi & Yamada (2012), Nagakura et al. (2014), and Nagakura et al. (2017).

A.2.1 Validations with the static background

The basic tests for the Boltzmann solver implemented in the Boltzmann-radiation-hydrodynamics code with the static background are reported in Sumiyoshi & Yamada (2012). In the following, code validations in the paper are described in order to convince the reader that the code successfully works. The tests conducted in the following are the

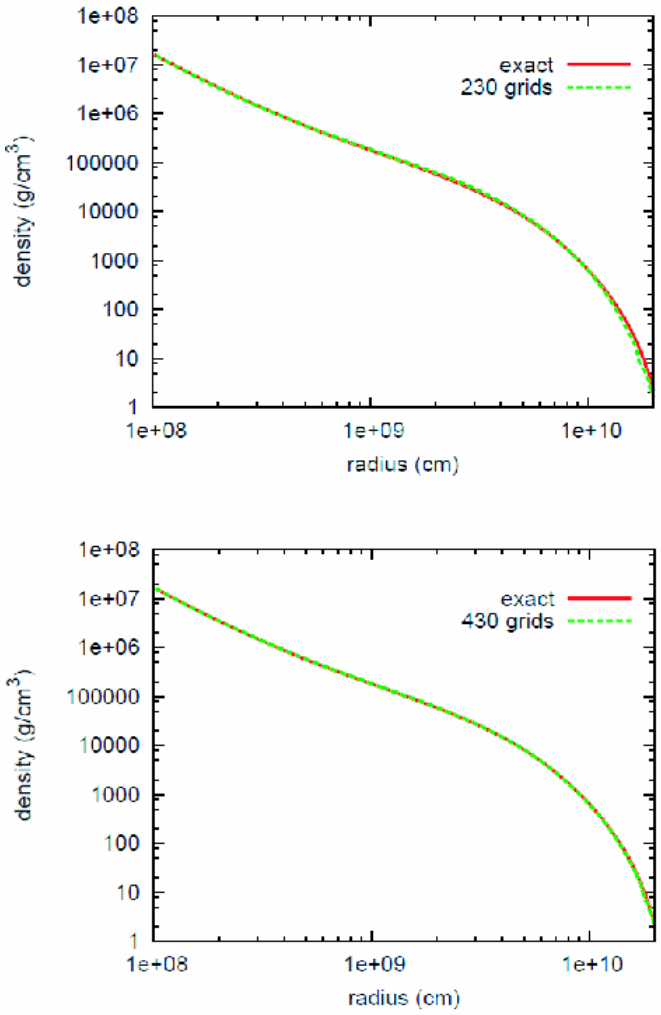

Figure A.2. The steady-state solution of the rotational equilibrium of the stellar matter. The density profiles of the initial condition (exact, red solid lines) and at $t = 100\,\mathrm{s}$ from the beginning of calculation (N_r grids, green dashed lines) along the rotational axis are shown. The employed radial grid numbers are $N_r = 230$ (upper panel) and $N_r = 460$ (lower panel). This figure is reproduced from Nagakura et al. (2011) by permission of the AAS.

spatial diffusion of neutrinos in the optically thick regime, the free-streaming of neutrinos in the optically thin regime, the energy spectrum of the steady-state neutrinos, the time evolution to the equilibrium state, the absorptivity and emissivity of neutrinos, and the steady-state neutrino distributions with realistic background of the CCSN in 1D and 2D.

First, the diffusion of neutrinos is tested. In the optically thick limit, the neutrinos behave diffusively. Therefore the analytic solution of the diffusing Gaussian packet is useful. It is expressed as

$$f(\boldsymbol{r}, t) = f_0 \left(\frac{t_0}{t_0 + t} \right)^{\alpha} \exp \left\{ - \frac{|\boldsymbol{r} - \boldsymbol{r}_0|^2}{4D(t_0 + t)} \right\}, \tag{A.1}$$

where $\boldsymbol{r}_0$, f_0, t_0, $D = c\lambda/3$, c, and λ are the central position of the packet, the initial central value of the distribution, the initial time, the diffusion coefficient, the light speed, and the mean free path of the isotropic scattering, respectively. The index $\alpha = N_\mathrm{d}/2$ is related to the spatial dimension, N_d. Note that the time t is measured from the initial time t_0.

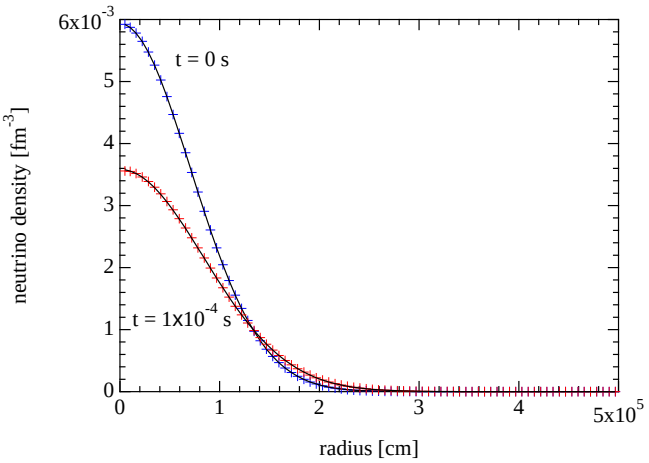

Figure A.3. The spherical diffusion of the Gaussian packet of neutrinos. The radial profiles of the numerical solutions of the neutrino densities at $t = 0\,\mathrm{s}$ (blue crosses) and $t = 10^{-4}\,\mathrm{s}$ (red crosses) are compared to the analytic solution (black solid lines). This figure is reproduced from Sumiyoshi & Yamada (2012) by permission of the AAS.

First, in figure A.3, the diffusion of the packet at the coordinate center is shown. Since $\boldsymbol{r}_0 = \boldsymbol{0}$, the solution is spherically symmetric although the calculation is done in 3D. The computational domain is $0 \le r \le 5\,\mathrm{km}$, $0 \le \theta \le \pi$, and $0 \le \phi \le 2\pi$, respectively, and the grid numbers are $(N_r, N_\theta, N_\phi, N_\epsilon, N_{\theta_\nu}, N_{\phi_\nu}) = (80, 18, 36, 2, 12, 12)$. The mean free path is set to $\lambda = 10^3\,\mathrm{cm}$ and the initial time is set to $t_0 = 2.5 \times 10^{-4}\,\mathrm{s}$ so that the initial width of the packet is 1 km. Figure A.3 implies that the spherical diffusion of the Gaussian packet is correctly solved by the Boltzmann solver since the numerical and analytic solutions coincide.

Next, the diffusion of the 2D Gaussian packet is shown in figure A.4. The center of the packet $\boldsymbol{r}_0$ is located at $1,000\,\mathrm{km}$ on the equator. The computational domain is a square with a side of 10 km whose center is the same as the packet. Since the domain is located far from the center, the coordinates are almost the Cartesian coordinates. It is useful to employ the coordinates spanned by $Z = r\cos\theta$ and $R = r\sin\theta$ instead of r and θ for the presentation in figure A.4. The grid numbers are $(N_r, N_\theta, N_\epsilon, N_{\theta_\nu}, N_{\phi_\nu}) = (100, 96, 4, 12, 12)$. Again, $\lambda = 10^3\,\mathrm{cm}$ and $t_0 = 2.5 \times 10^{-4}\,\mathrm{s}$. From figure A.4, it is proven that the Boltzmann solver correctly treats the 2D diffusion.

Then, the Boltzmann solver in the optically thin limit is tested. In the optically thin region, the neutrinos freely stream with the light speed c. In order to realize the free-streaming, the neutrino reactions are switched off. In figure A.5, the 1D

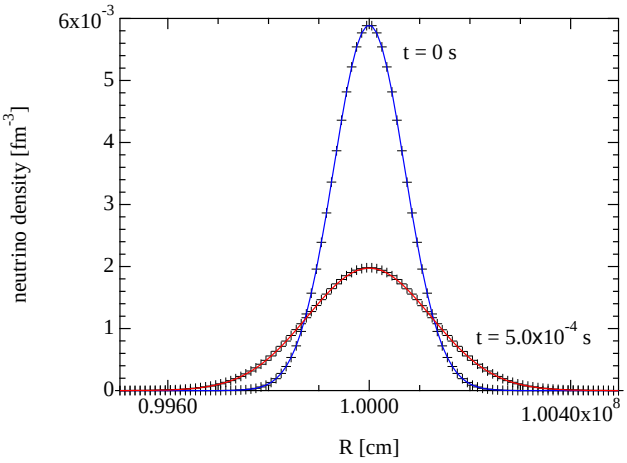

Figure A.4. The 2D diffusion of the Gaussian packet of neutrinos. The numerical solutions (crosses) of the neutrino densities at $t = 0\,\mathrm{s}$ and $t = 10^{-4}\,\mathrm{s}$ are compared to the analytic solution (red and blue solid lines). The profile is along $Z = -8.1\,\mathrm{km}$. This figure is reproduced from Sumiyoshi & Yamada (2012) by permission of the AAS.

advection of the step-like-distributed neutrinos is shown. The grid numbers are $(N_r, N_\theta, N_\phi, N_\epsilon, N_{\theta_\nu}, N_{\phi_\nu}) = (100, 3, 3, 4, 6, 6)$. The initial condition is a step-like distribution as shown in the top panel of figure A.5. Here, only neutrinos with $\cos\theta_\nu = 0.93247$, which correspond to the most forward grid point in the momentum space, have the distribution shown in the figure. The azimuthal distribution is uniform. The middle and bottom panels indicate that the neutrinos freely stream with the light velocity projected onto the radial direction, $c\cos\theta_\nu$. The smearing of the step-like distribution is also seen, but it is not so problematic since the neutrino distributions inside the shock of the CCSN is not forward-peaked. The smearing is reduced when the spatial and temporal resolutions are improved though it is not shown.

The collision term is validated under the spherical symmetry subsequently. For the test, a snapshot of the CCSN whose progenitor mass is $15\,M_\odot$ at 100 ms after the core bounce simulated by the spherically symmetric code (Sumiyoshi et al., 2005) is taken as a background flow. The radial profiles of the density, temperature, and neutrino chemical potential of this snapshot are shown in figure A.6. In the following, this background is fixed and the neutrino distribution only is evolved. Firstly, the steady-state solution of the Boltzmann equation with the collision term is tested, and secondly, the time evolution toward the equilibrium state is examined. For these calculations, the computational domain is $0 \le r \le 1.4 \times 10^3\,\mathrm{km}$, $0 \le \theta \le \pi/2$, and $0 \le \phi \le \pi/2$. The neutrino energy ranges up to 300 MeV, and the grid number is $N_\epsilon = 14$.

For the steady-state solution, the numerically obtained energy spectrum of neutrinos is compared to the spectrum obtained from the formal solution. The well-known radiative

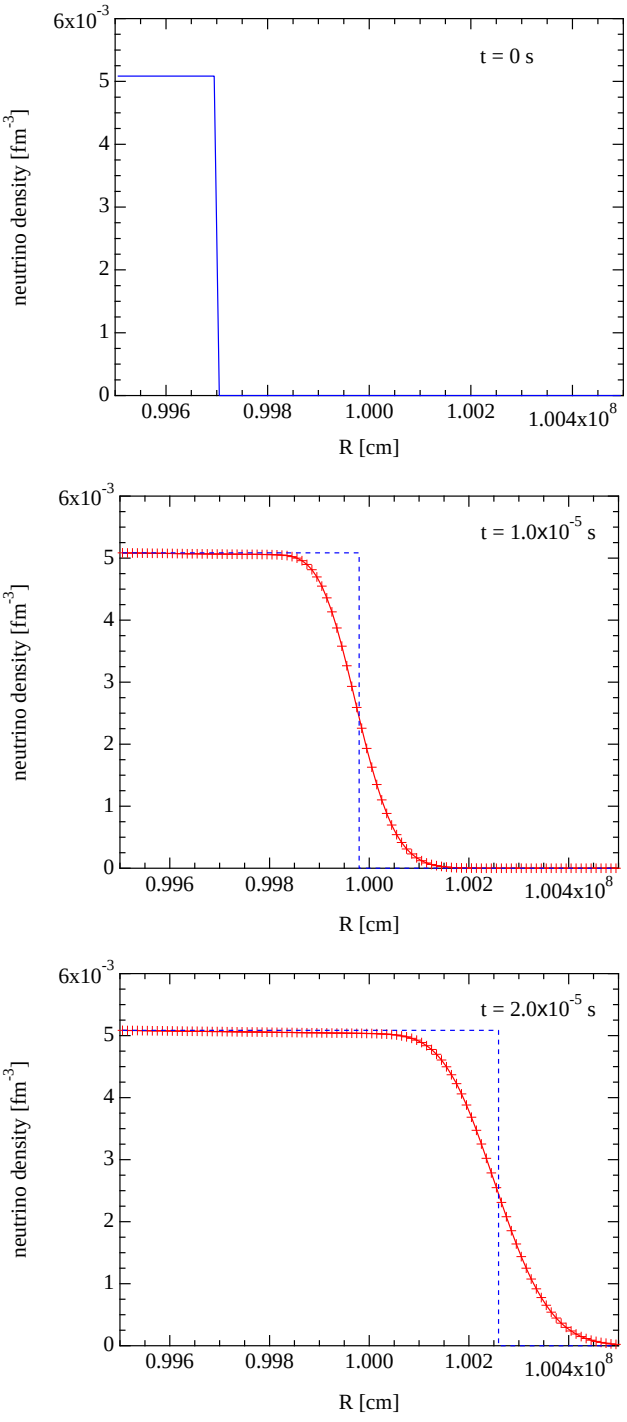

Figure A.5. The free-streaming of neutrinos. The top panel shows the initial condition. The red lines in the middle ($t = 1.0 \times 10^{-5}$ s) and bottom ($t = 2.0 \times 10^{-5}$ s) panels show the subsequent evolutions. The blue dashed lines in the two panels represent the wavefronts analytically obtained. This figure is reproduced from Sumiyoshi & Yamada (2012) by permission of the AAS.

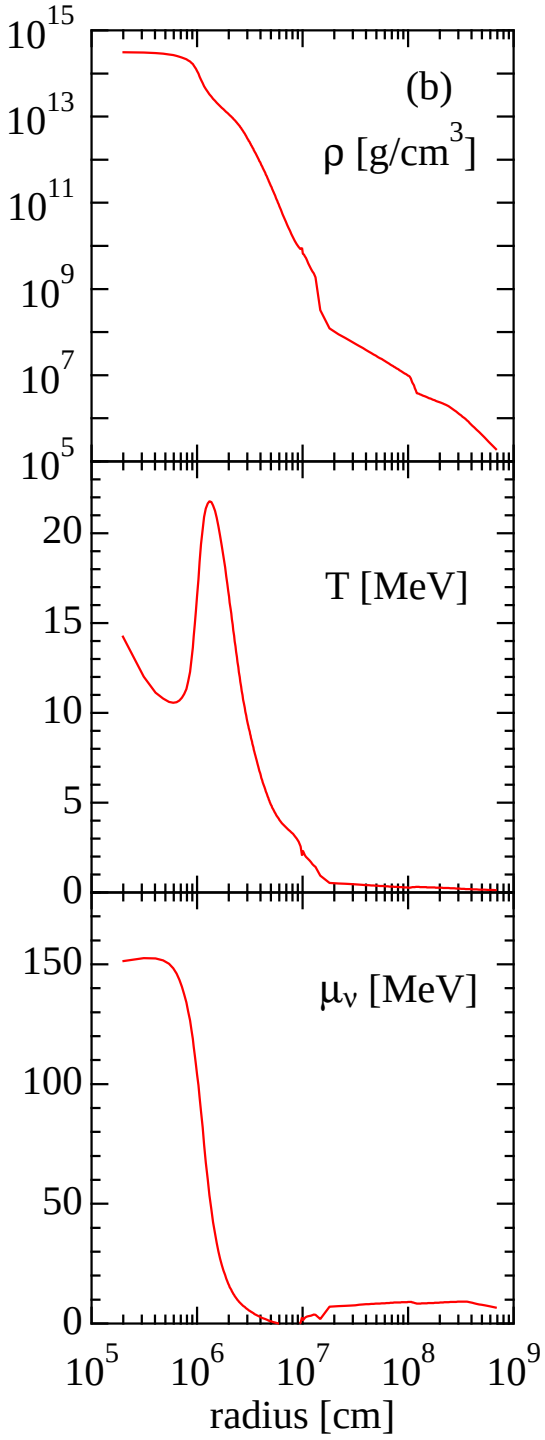

Figure A.6. The radial profiles of the density (top), temperature (middle), and neutrino chemical potential (bottom) at 100 ms after the core bounce taken from Sumiyoshi et al. (2005). This figure is reproduced from Sumiyoshi & Yamada (2012) by permission of the AAS.

transfer equation is[*1]

$$-\frac{\mathrm{d}}{\mathrm{d}s}f(s) = \eta(s) - \chi(s)f(s), \tag{A.2}$$

where s, η, and χ are the path length, the opacity, and the emissivity of neutrinos, respectively. Note that the path length s is along the ray of neutrinos and measured backward from the considered point ($s = 0$) to the boundary ($s = s_\mathrm{b}$). The formal solution of this equation is

$$f(0) = \int_0^{s_\mathrm{b}} \mathrm{e}^{-\tau(s')}\eta(s')\mathrm{d}s', \tag{A.3}$$

with

$$\tau(s) = \int_0^{s} \chi(s')\mathrm{d}s' \tag{A.4}$$

being the optical depth. The incoming neutrinos at the boundary are neglected.

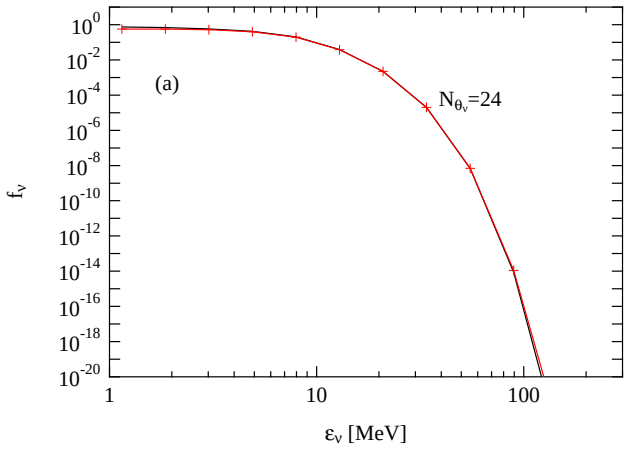

Figure A.7. Energy spectra of neutrinos at $r = 98.4\,\mathrm{km}$ obtained from the formal (equation (A.3), the black line) and numerical (the red line) solutions. This figure is reproduced from Sumiyoshi & Yamada (2012) by permission of the AAS.

In figure A.7, the numerical and formal spectra are compared. The steady-state solution of the Boltzmann equation is obtained by running the Boltzmann solver for a sufficiently long time. The grid numbers here are $(N_r, N_\theta, N_\phi, N_\epsilon, N_{\theta_\nu}, N_{\phi_\nu}) = (200, 3, 3, 14, 24, 6)$. The absorption and emission of neutrinos are considered, and the scattering is neglected. Then, the spectrum numerically obtained as a result of the time evolution of the Boltzmann equation and the spectrum obtained from equation (A.3) are compared. The neutrino angle is $\cos\theta_\nu = 0.99519$, the most forward grid point, and the spatial point is $r = 98.4\,\mathrm{km}$. These two spectra agree well.

It is proven that the Boltzmann solver can successfully reproduce the steady-state solution. Next, the time evolution to the steady, equilibrium state is investigated. With the

[*1] Not the distribution function f but the specific intencity $\mathcal{I} = \epsilon^3 cf/(hc)^3$, where h is the Planck constant, is usually considered in the radiative transfer equation. Since the neutrino energy does not change in this equation, which quantity is used does not matter.

absorption and emission reactions, the time evolution of the distribution function $f(t)$ to the steady-state is given by

$$f(t) = (f_0 - f_{\rm eq})\mathrm{e}^{-t/\tau} + f_{\rm eq}, \tag{A.5}$$

where f_0, $f_{\rm eq}$, and τ are the initial distribution function, the equilibrium distribution nothing but the Fermi-Dirac distribution, and the relaxation timescale. The relaxation timescale is defined as $\tau = \lambda/c$, with λ and c being the effective mean free path and the light speed. Here, the effective mean free path is defined as the reciprocal of the sum of absorptivity of considered reactions. In this test, the electron capture on nuclei and the pair annihilation reactions, and the isotropic scattering are considered.

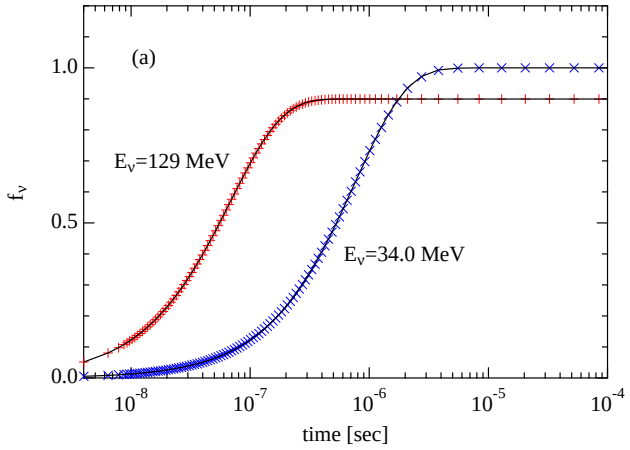

Figure A.8. The numerical evolution of the distribution functions at $\epsilon = 34.0\,\mathrm{MeV}$ (blue crosses) and 129 MeV (red crosses) to the equilibrium values are compared to the analytic solution (black solid lines). This figure is reproduced from Sumiyoshi & Yamada (2012) by permission of the AAS.

In figure A.8, the time evolution to the equilibrium state is shown. The distributions at the neutrino energies of $\epsilon = 34.0\,\mathrm{MeV}$ and 129 MeV are shown. Since the isotropic scattering is switched on, the distributions are isotropic, independent of the neutrino flight direction. The spatial point considered here is the center, whose density, temperature, and chemical potential of neutrinos are $3.15 \times 10^{14}\,\mathrm{g\,cm^{-3}}$, 13.4 MeV, and 158 MeV, respectively, of the CCSN. Initially, the distribution function is set to 10^{-5} times the equilibrium value. This figure indicates that the analytical solution is successfully reproduced by the numerical Boltzmann solver.

Next, the reaction rates considered in the collision terms are tested. The neutrino reaction rates at the chosen snapshot are also given by the 1D code in Sumiyoshi et al. (2005). Here, the neutrino reaction rates for the given snapshot is calculated by the Boltzmann solver and compared to those by the 1D code. This comparison is displayed in figure A.9 in terms of the radial profiles of the effective mean free paths and the emissivities. The reactions considered here and their abbreviations are as follows: the electron capture on nucleon (ecp), the anti-electron capture on nucleon (aecp), the electron

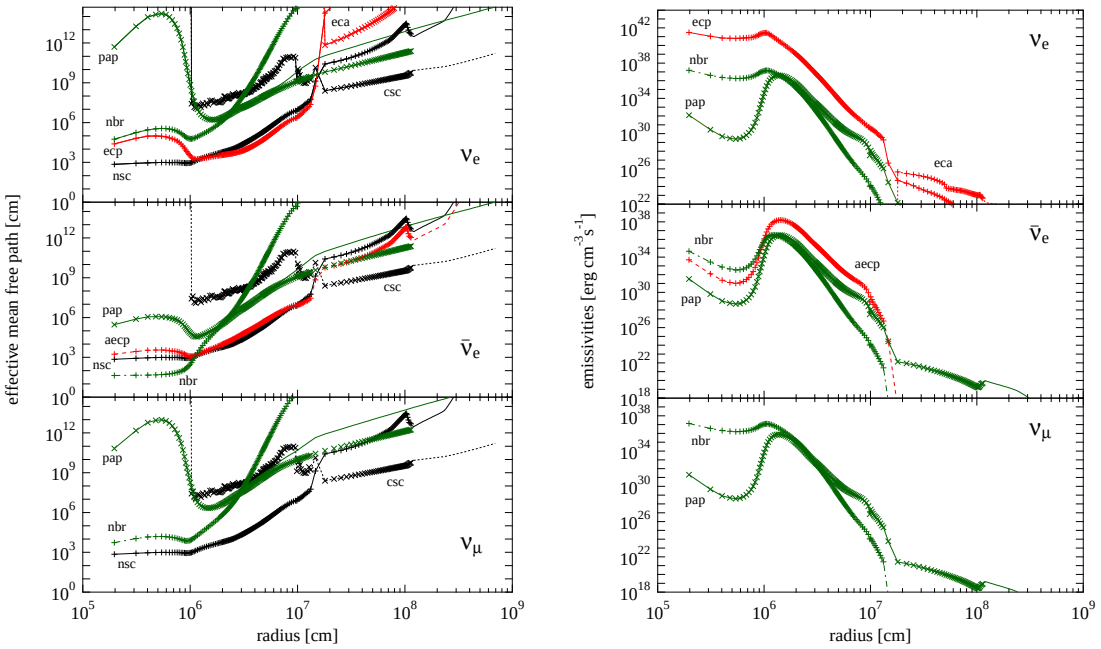

Figure A.9. The radial profiles of effective mean free paths (left panels) and the emissivities (right panels) of each reaction calculated by the Boltzmann solver are compared to those by the spherically symmetric code (Sumiyoshi et al., 2005). The former and the latter are indicated by the symbols and the lines, respectively. Top, middle, and bottom panels show the effective mean free paths and emissivities for the electron-type, the anti-electron-type, and the heavy-lepton-type neutrinos, respectively. The neutrino energy is set to 34.0 MeV. The names of reactions indicated near the lines are described in the text. This figure is reproduced from Sumiyoshi & Yamada (2012) by permission of the AAS.

capture on nuclei (eca), the nucleon scattering (nsc), the coherent scattering (csc), the pair production (pap), and the nucleon-nucleon bremsstrahlung (nbr). Note that the electron capture on nuclei obeys not the updated version in chapter 3 but the prescription suggested in Bruenn (1985). The neutrino energy considered here is 34.0 MeV. This figure indicates that the evaluations from the two different codes coincide, and hence the neutrino reactions are correctly implemented.

For the final 1D test with the snapshot at 100 ms after the core bounce, the neutrino number densities and flux of the steady-state solution is compared with the solution by Sumiyoshi et al. (2005) in figure A.10. The grid numbers to obtain the steady-state solution are $(N_r, N_\theta, N_\phi, N_\epsilon, N_{\theta_\nu}, N_{\phi_\nu}) = (200, 5, 5, 14, 6, 12)$. The profiles obtained by the Boltzmann solver are in good agreement with those by Sumiyoshi et al. (2005), indicating that the Boltzmann solver employed in this dissertation correctly solves the Boltzmann equation.

In addition to the test using the postbounce snapshot shown in figure A.10, the same test with the prebounce fluid profile is conducted. The chosen snapshot here is taken at

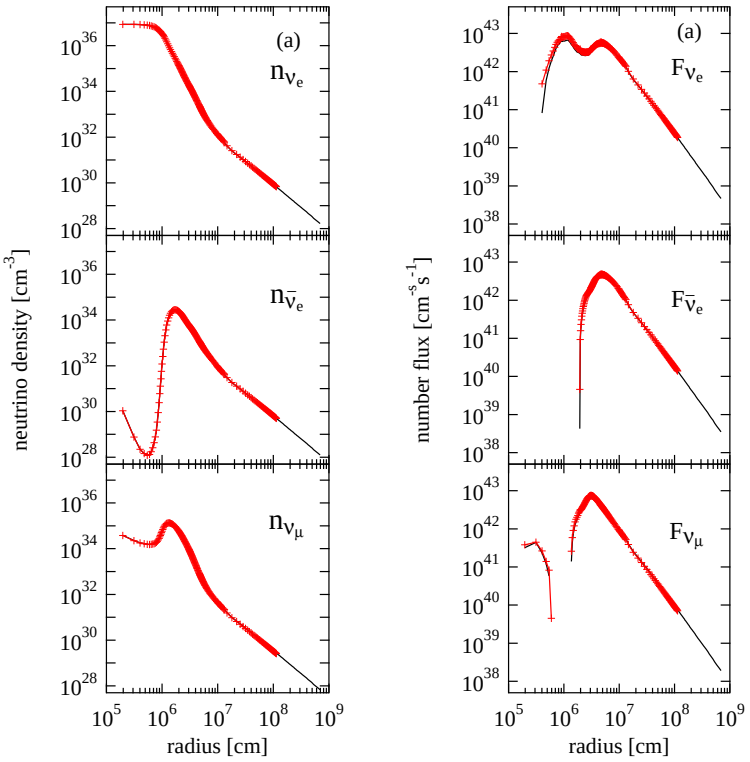

Figure A.10. The neutrino number densities (left panels) and fluxes (right panels) of the steady-state solution with the snapshot at 100 ms after the core bounce. Top, middle, and bottom panels show the effective mean free paths and emissivities for the electron-type, the anti-electron-type, and the heavy-lepton-type neutrinos, respectively. The solution obtained by the Boltzmann solver and that by the 1D code (Sumiyoshi et al., 2005) are indicated by the symbols and the black solid lines, respectively. This figure is reproduced from Sumiyoshi & Yamada (2012) by permission of the AAS.

the time when the central density reaches $10^{12}\,\mathrm{g\,cm^{-3}}$. The radial profiles of the density, temperature, and neutrino chemical potential are indicated in the left column of figure A.11. The neutrino number densities and fluxes obtained by the Boltzmann solver and the 1D code (Sumiyoshi et al., 2005) are compared in the middle and right columns of the figure. Again, the results of both codes coincide, indicating the reliability of the Boltzmann solver.

So far the 1D CCSN profile is employed to test the Boltzmann solver. Finally, the 2D behavior is tested. In order to obtain a 2D background flow, the snapshot at 100 ms after the core bounce, which is employed in previous tests, is deformed by scaling the radius r as

$$\tilde{r} = r(1 - 0.4 \sin\theta), \tag{A.6}$$

depending on the zenith angle θ. The density contours of the deformed background are shown in figure A.12.

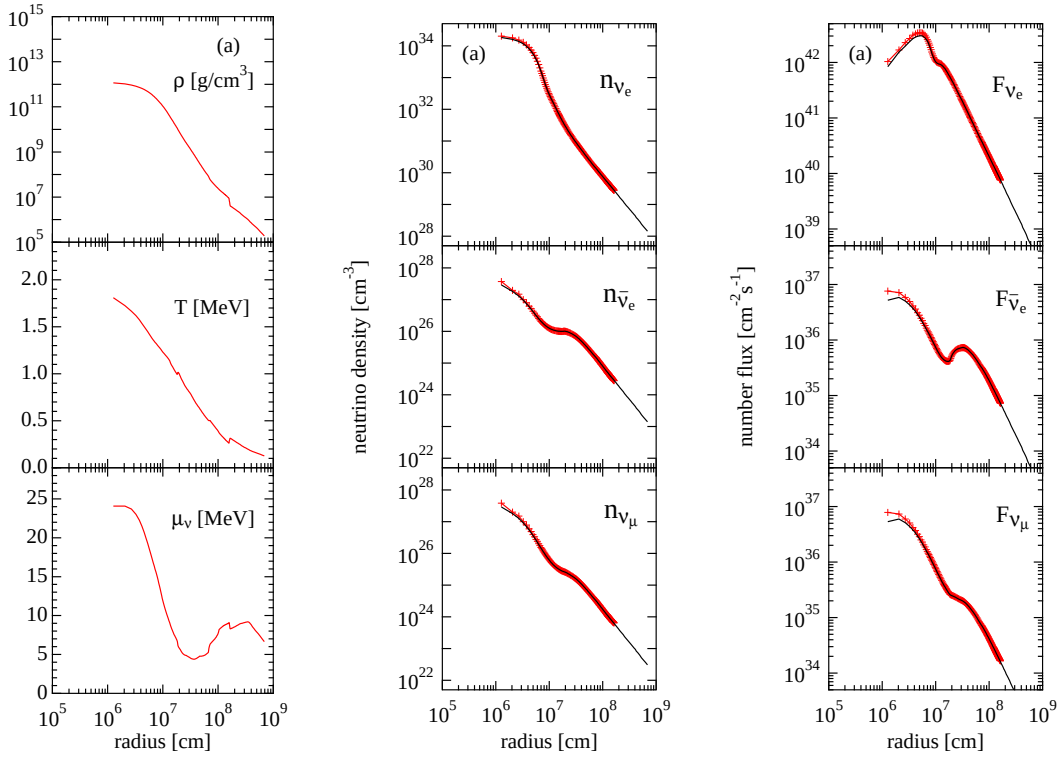

Figure A.11. The radial profiles of several quantities before the core bounce, where the central density reaches $10^{12}\,\mathrm{g\,cm^{-3}}$. The left column shows the density (top), temperature (middle), and neutrino chemical potential (bottom). The middle and right columns display the neutrino number densities and fluxes of the steady-state solution, respectively. They are the same as figure A.10 except for the background fluid profiles. This figure is reproduced from Sumiyoshi & Yamada (2012) by permission of the AAS.

With this background flow fixed, the Boltzmann solver is run for a sufficiently long period to obtain the steady-state solution. Here, only the electron-type neutrinos and the emission/absorption reactions are considered. Again, the first octant, i.e., $0 \le \theta \le \pi/2$, and $0 \le \phi \le \pi/2$ is considered and the grid numbers are $(N_r, N_\theta, N_\phi, N_\epsilon) = (200, 9, 9, 14)$. For the angular coordinates in the momentum space, four sets of grid numbers are employed: $(N_{\theta_\nu}, N_{\phi_\nu}) = (6, 6)$, $(12, 6)$, $(24, 6)$, and $(12, 12)$. Similarly to figure A.7, the formal solution of the spectrum is constructed from equation (A.3) and compared to the numerically obtained spectrum. Here, four spatial points are chosen to examine the spectrum: $(r, \cos\theta) = (98, 4\,\mathrm{km}, 0.082)$, $(198\,\mathrm{km}, 0.082)$, $(98, 4\,\mathrm{km}, 0.98)$, and $(198\,\mathrm{km}, 0.98)$. These points are indicated by the triangles and rectangles in figure A.12. For the simulation with $(N_{\theta_\nu}, N_{\phi_\nu}) = (24, 6)$, the distribution with $\cos\theta_\nu = 0.99515$, the most forward grid point, is considered and the formal solution is obtained by the integral along the black solid lines in figure A.12. For the coarser grid simulations, the most forward grid points are again considered, but the directional cosine of the grid points itself are different from that in the highest-resolution simulation: $\cos\theta_\nu = 0.98156$ for $N_{\theta_\nu} = 12$ and $\cos\theta_\nu = 0.93247$

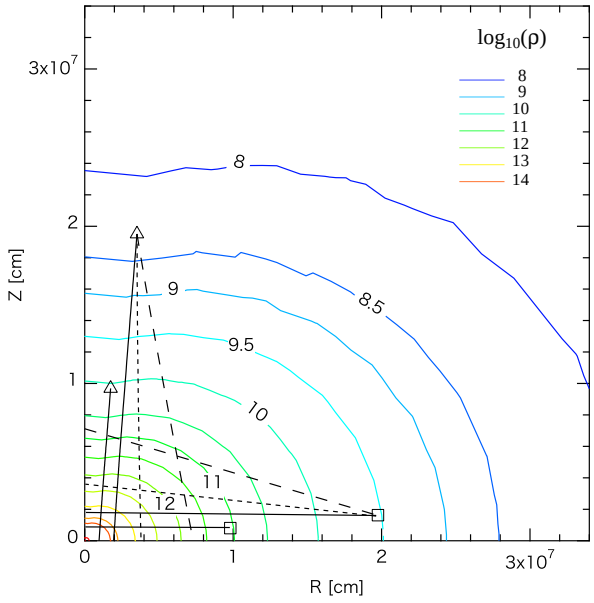

Figure A.12. The density contour obtained by deforming the CCSN profile. The original snapshot is taken at 100 ms after the core bounce by Sumiyoshi et al. (2005). The small triangles and rectangles are the points where the neutrino distributions are examined. Black solid, short-, and long-dashed lines are the paths to obtain the formal solutions in figure A.13. This figure is reproduced from Sumiyoshi & Yamada (2012) by permission of the AAS.

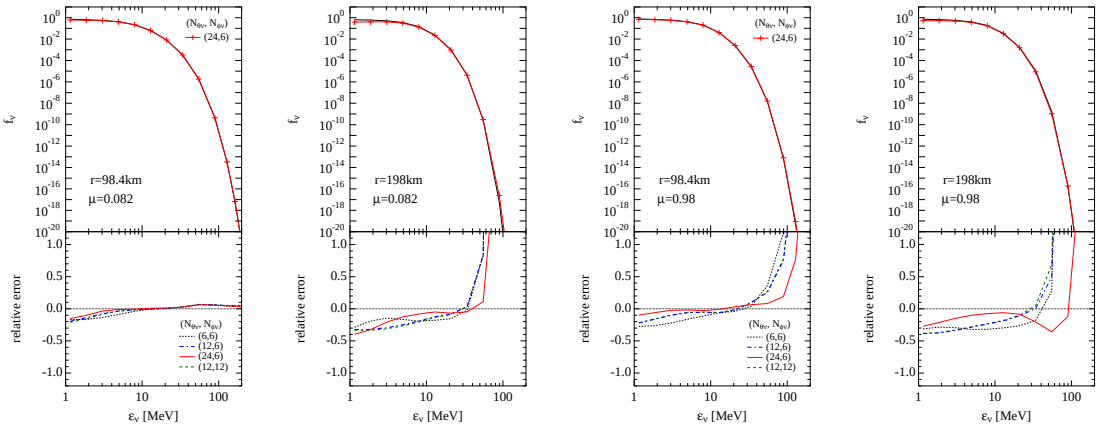

Figure A.13. The spectra obtained from the numerical and formal solutions of the steady-state with the fixed 2D background shown in figure A.12. The spatial points are indicated in each panel, with μ being $\cos\theta$. The top panels show the spectra itself with the highest-resolution simulations and formal solutions. The bottom panels indicate the relative errors of spectra with different resolutions. For all models, the most forward grid points in the momentum space are considered. This figure is reproduced from Sumiyoshi & Yamada (2012) by permission of the AAS.

for $N_{\theta_\nu} = 6$. For these simulations, the paths for the formal solution are the black short- and long-dashed lines in figure A.12. In figure A.13, the comparisons between numerical and formal solutions are indicated. For the spectra themselves, only the results of the highest-resolution simulations are shown. All these panels demonstrate that they are in good agreement. For the relative errors, the results of not only the highest-resolution simulations but also the lower-resolution simulations are indicated. The errors between the numerical and formal solutions reduce with increasing the resolution. One may think that the relative errors at high neutrino energies are large. The distribution function itself, however, is small there, and hence it is not so problematic. From these results, it is proven that the Boltzmann solver can correctly treat the multi-dimensional neutrino transport in the CCSN simulations.

A.2.2 Validations of the special relativistic effects

The tests investigated above consider the static background of fluid. On the other hand, the fluid velocity cannot be neglected for the actual CCSN. The velocity reaches $\sim 10\%$ of the light speed at most, and hence the special relativistic effect should not be forgotten. This is implemented in Nagakura et al. (2014). Here, the code validations reported in the paper are described.

In order to see the neutrino trapping in moving matter, the relaxation of the neutrinos to the isotropic distribution in the fluid rest-frame is tested. This test only concerns the collision term, and hence the spatially one-zone calculation is conducted, and the advection terms are neglected. The density, temperature, and electron fraction are set to $\rho = 10^{12}\,\mathrm{g\,cm^{-3}}$, $T = 2\,\mathrm{MeV}$, and $Y_\mathrm{e} = 0.4$. The velocity is set to $(v^r, v^\theta, v^\phi) = (\sqrt{2}, 1, 1) \times 10^{10}\,\mathrm{cm\,s^{-1}}$, approximately 2/3 of the light speed. Note that this is much larger than the typical velocity of the CCSNe. The grid numbers in the momentum space are $(N_\epsilon, N_{\theta_\nu}, N_{\phi_\nu}) = (20, 6, 6)$. The isoenergetic scattering reactions, namely, the nucleon scattering and coherent scattering are considered for the collision term. For the initial condition, the neutrinos are isotropically distributed in the laboratory frame. Since the isoenergetic scattering is considered, the initial distribution relaxes to the isotropic distribution in the fluid-rest frame.

In figure A.14, the time evolution of the distribution function in the fluid-rest frame at $\epsilon_\mathrm{fr} = 60\,\mathrm{MeV}$ are shown for several directions, where ϵ_fr is the neutrino energy measured in the fluid-rest frame. Initially, the distribution is anisotropic in the fluid-rest frame due to the Lorentz transformation from the laboratory frame. The distributions in any direction relax to the isotropic analytical value denoted as "ana". Relaxation of the spectra in the fluid-rest and laboratory frames is shown in figures A.15 and A.16, respectively. Initially, the distributions of the most forward and backward directions are the same in the laboratory frame and different in the fluid-rest frame due to the Lorentz transformation. Here, "forward" and "backward" mean the first and last grid point of the θ_ν coordinate. Owing to the isoenergetic scattering, the distributions of the most forward and backward directions in the fluid-rest frame become the same while those in the laboratory frame are different. This behavior is common for the all neutrino energy bins. This result indicates

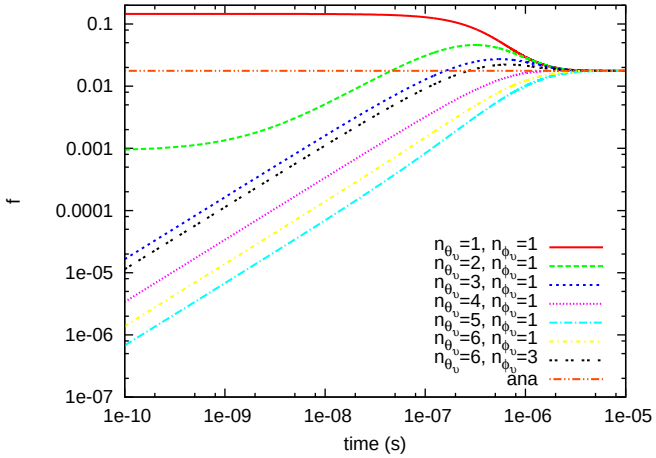

Figure A.14. The time evolution of the distribution function in the fluid-rest frame. Lines other than orange dash-two-dotted line represent the distribution functions in each angular bin indicated in the legend. Symbols n_{θ_ν} and n_{ϕ_ν} indicate the n_{θ_ν}-th and n_{ϕ_ν}-th grid point. The orange dash-two-dotted line is the analytically estimated isotropic distribution. This figure is reproduced from Nagakura et al. (2014) by permission of the AAS.

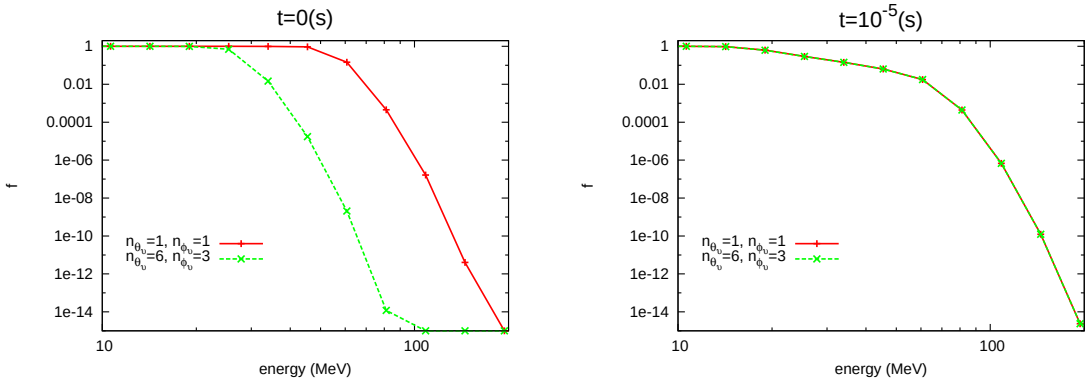

Figure A.15. Relaxation of the spectra of the forward- (the first grid of the θ_ν coordinate, red) and backward- (the last grid of the θ_ν coordinate, green) directed neutrinos in the fluid-rest frame. The left and right panels show the initial condition and the steady-state solution, respectively. Symbols n_{θ_ν} and n_{ϕ_ν} indicate the n_{θ_ν}-th and n_{ϕ_ν}-th grid point. This figure is reproduced from Nagakura et al. (2014) by permission of the AAS.

that the neutrino trapping in moving matter discussed in section 2.2.1 is correctly realized.

One of the difficulties in the radiative transfer is the radiation field with a discontinuous background. It is convenient to measure the neutrino energy in the fluid-rest frame since the matter-neutrino interaction is formulated in that frame. It poses a difficulty if there is a shock wave in the background matter since the neutrino energy in the fluid-rest frame suddenly changes even if it does not change in the laboratory frame. The Boltzmann solver in this dissertation mainly employs the fluid-rest frame although the laboratory

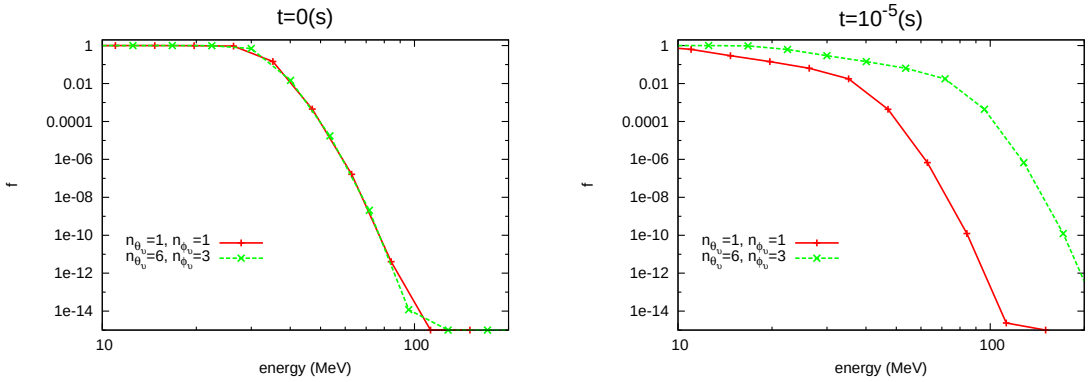

Figure A.16. The same as figure A.15 except that the laboratory frame is employed. This figure is reproduced from Nagakura et al. (2014) by permission of the AAS.

frame is utilized subsidiary, and hence this may be problematic.

In order to check whether the Boltzmann solver correctly treats this situation, the steady-state solution with the discontinuous background is constructed. The computational domain is $10^8\,\mathrm{cm} < r < (10^8 + 10^5)\,\mathrm{cm}$ and the spherical symmetry is imposed. Since distant point from the origin of the coordinate center is employed, the plane-parallel flow is realized virtually. The grid numbers are $(N_r, N_\epsilon, N_{\theta_\nu}) = (6, 20, 6)$. The matter velocity is set to zero for the first three grid points, while it is set to $-2 \times 10^{10}\,\mathrm{cm\,s^{-1}}$ for the last three points. The collision terms are switched off, and hence the optically thin regime is considered. Outgoing neutrinos with the Fermi-Dirac distribution is injected from the inner boundary.

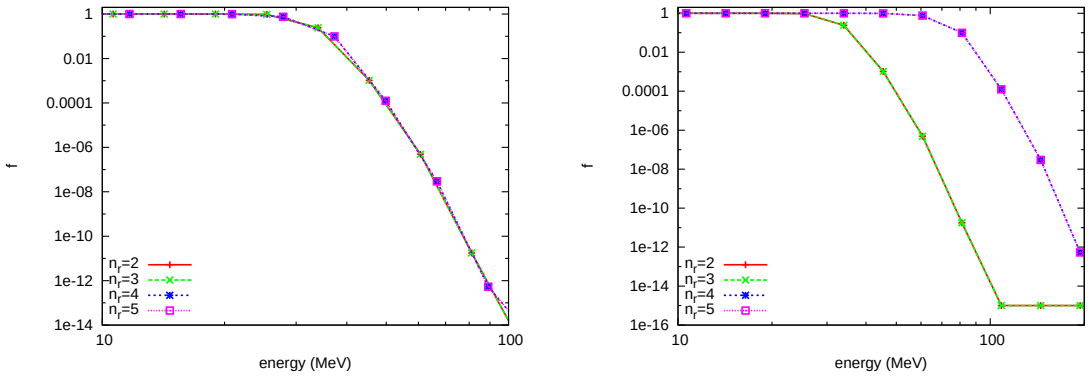

Figure A.17. The spectra of neutrinos with the discontinuous background in the laboratory frame (left) and the fluid-rest frame (right). The symbol n_r indicates the n_r-th radial grid point and the discontinuity lies between $n_r = 3$ and $n_r = 4$. This figure is reproduced from Nagakura et al. (2014) by permission of the AAS.

Figure A.17 shows the resultant spectra in the laboratory and fluid-rest frames. Since the optically thin regime is considered, the injected spectrum is not affected as shown in the left panel of the figure. On the other hand, the spectrum in the fluid-rest frame

suddenly changes due to the discontinuous background as shown in the right panel of the figure. The figure demonstrates that the radiative transfer with the discontinuous background is correctly solved by the Boltzmann solver.

The tests of special relativistic effects presented above consider ideal situations. Here, a test with a more realistic situation is conducted: the dynamical core-collapse of a massive star. The computational domain is $0 < r < 4,000\,\mathrm{km}$ and spherical symmetry is imposed. The grid numbers are $(N_r, N_\epsilon, N_{\theta_\nu}) = (300, 20, 8)$. The progenitor is $15\,M_\odot$ model in Woosley et al. (2002), and the STOS EOS is employed. Not only a special relativistic simulation but also a non-relativistic simulation is performed.

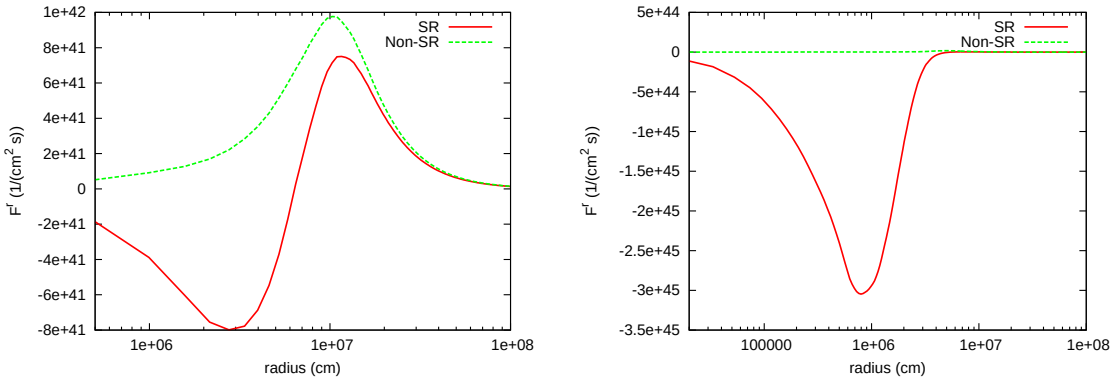

Figure A.18. The radial profiles of the neutrino number fluxes when the central density reaches $10^{12}\,\mathrm{g\,cm^{-3}}$ (left) and $10^{14}\,\mathrm{g\,cm^{-3}}$ (right). The red solid lines represent the result of the special relativistic simulation, whereas the green dashed lines indicate that of the non-relativistic simulation. This figure is reproduced from Nagakura et al. (2014) by permission of the AAS.

In figure A.18, the neutrino number fluxes in the laboratory frame when the central density reaches $10^{12}\,\mathrm{g\,cm^{-3}}$ and $10^{14}\,\mathrm{g\,cm^{-3}}$ are indicated for both the special relativistic and non-relativistic simulations. For the non-relativistic simulation, the neutrino flux is always positive. This indicates that the neutrinos always escape away from the core and not trapped. On the other hand, the flux in the special relativistic simulation is negative for the inner region. Considering that the velocity is negative in this prebounce phase, the neutrinos are correctly trapped by matter and flow inward in unison. This demonstrates that the neutrino trapping in the realistic CCSN is correctly reproduced by the Boltzmann solver.

A.2.3 Validations of the Boltzmann-radiation-hydrodynamics code

The Boltzmann-radiation-hydrodynamics code employed in chapter 3 is implemented and tested in Nagakura et al. (2017). The tests reported in the paper are described in the following.

A core-collapse simulation of the $15\,M_\odot$ model in Woosley et al. (2002) is conducted under spherical symmetry. The input physics is the same as that in chapter 3. The

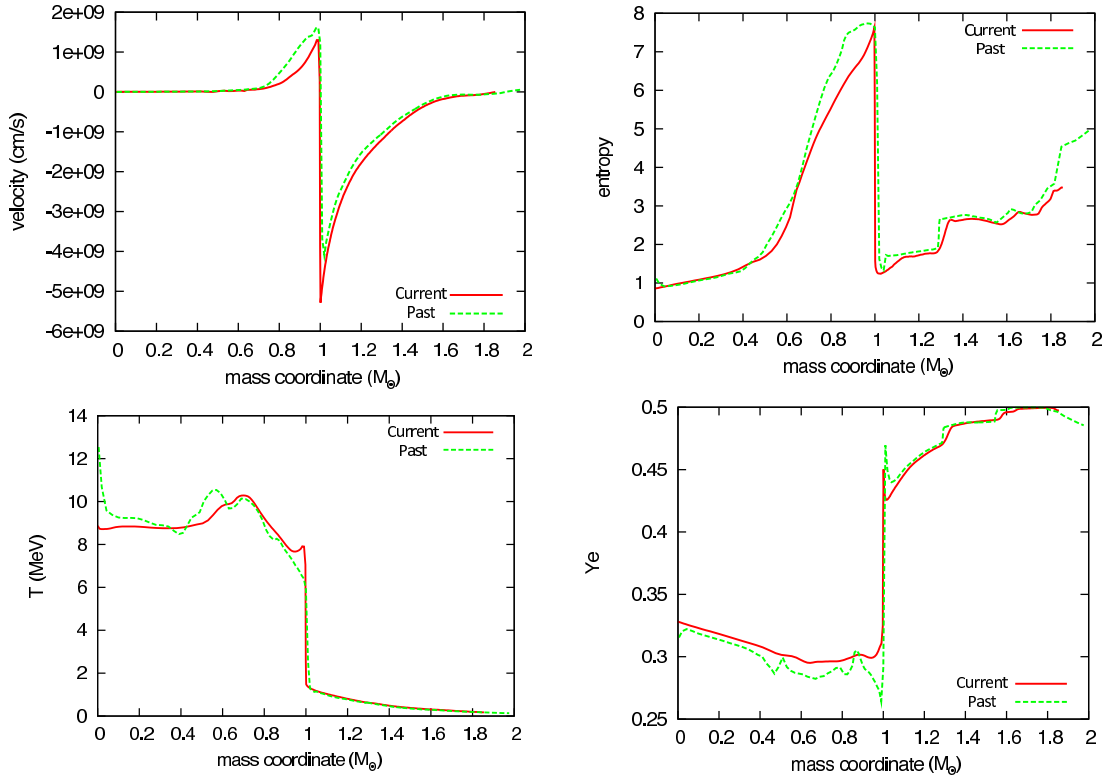

Figure A.19. The radial profiles of the radial velocity, entropy, temperature, and electron fraction at the core bounce. The red solid lines named "current" represent the result by the Boltzmann-radiation-hydrodynamics code, while the green dashed lines named "past" indicate those by the 1D code in Sumiyoshi et al. (2005). Note that the horizontal axis is not the radial but the mass coordinate. This figure is reproduced from Nagakura et al. (2017) by permission of the AAS.

resultant radial profiles of the velocity, entropy, temperature, and electron fraction at the core bounce are shown in figure A.19. It is compared to the result of the 1D code described in Sumiyoshi et al. (2005) with the same input physics except for the inclusion of the general relativistic effects. Although a perfect agreement is not achieved, they agree reasonably well. The slight differences seen in the figure probably come from the general relativistic effects, which is not considered in the Boltzmann-radiation-hydrodynamics code.

In addition, the moving-mesh technique is tested. For the validation, the gravitational collapse of the $11.2\,M_\odot$ model taken from Woosley et al. (2002) is simulated. Since the non-rotating model is considered, spherically symmetric simulation is run from the onset of the collapse to the core bounce. After that, the fluid distribution is mapped to the 2D grids, and axially symmetric simulation is run. At this mapping, the velocity of $100\,\mathrm{km\,s^{-1}}$ is added along the symmetric axis in the region of $r < 30\,\mathrm{km}$ in order to mimic the oscil-

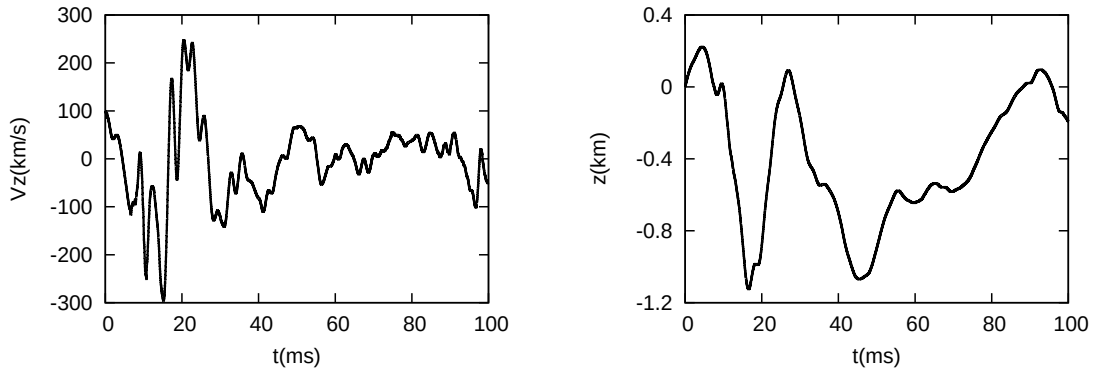

Figure A.20. The time evolutions of velocity (left) and offset (right) of the coordinate center for the PNS oscillation test. This figure is reproduced from Nagakura et al. (2017) by permission of the AAS.

lation of the PNS. The grid numbers are $(N_r, N_\theta, N_\epsilon, N_{\theta_\nu}, N_{\phi_\nu}) = (192, 32, 20, 4, 4)$. The resolution is rather coarse, but it is enough for the current purpose. The resultant velocity evolution and trajectory of the origin of the spherical coordinates are shown in figure A.20. Owing to the non-spherical accretion with respect to the PNS, the oscillation of the PNS is seen. This motion cannot be reproduced by other codes which fix the PNS center artificially. It is also checked that the central physical quantities take unphysical values artificially without moving-mesh though it is not shown. The moving mesh technique successfully captures the proper motion of the PNS without numerical problems.

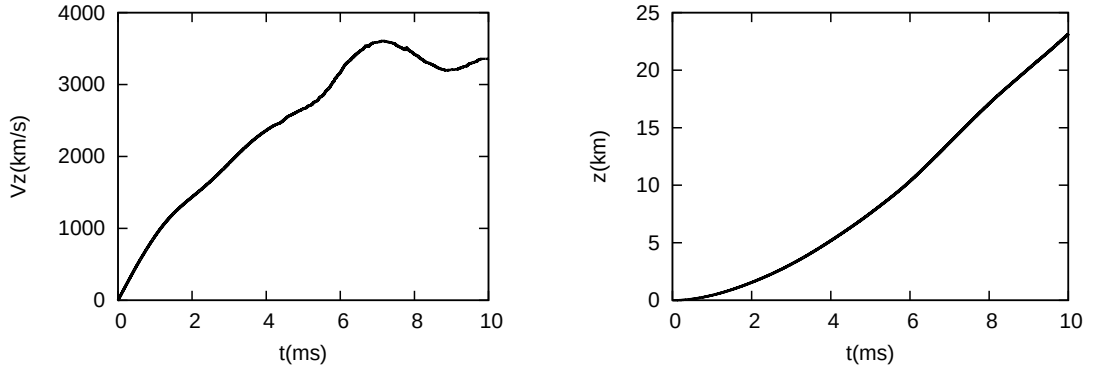

Figure A.21. The time evolutions of velocity (left) and offset (right) of the coordinate center for the PNS kick test. This figure is reproduced from Nagakura et al. (2017) by permission of the AAS.

On the other hand, the runaway motion of the PNS, or the PNS kick, is tested in figure A.21. The setup is the same as those in the PNS oscillation test except that not the velocity but the acceleration of $10^{11}\,\mathrm{cm\,s^{-1}}$ is permanently imposed along the axis in the region of $r < 30\,\mathrm{km}$. Due to the imposed acceleration, the velocity increases to reach several thousands of $\mathrm{km\,s^{-1}}$, and the trajectory indicates the extremely fast kick of the PNS. Note that the PNS kick velocity is $\mathcal{O}(100)\,\mathrm{km\,s^{-1}}$ typically. Figure

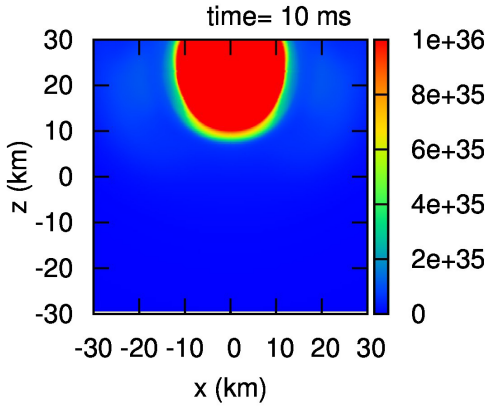

Figure A.22. The electron-type neutrino number density in the laboratory frame at 10 ms. This figure is reproduced from Nagakura et al. (2017) by permission of the AAS.

A.22 indicates the electron-type neutrino number densities in the laboratory frame at 10 ms and demonstrates that the trapped neutrinos successfully follow the PNS located at $z \sim 20$ km at that time as indicated in figure A.21. These results prove that the moving-mesh technique implemented in the Boltzmann-radiation-hydrodynamics code can treat the neutrino transfer in the acceleration frame.

A.3 Light-bulb method

Finally, the light-bulb method employed in chapter 4 is tested. Here, the steady-state solution is considered like the test in section A.1. The steady-state solution constructed for the initial condition of the simulations in chapter 4 should remain the steady-state with fixed inner boundary. Since the code to generate the initial condition and the dynamical code are independent of each other, this test simultaneously validates these two codes. Contrary to the results presented so far in this appendix, this test is not reported in other papers.

Figure A.23 indicates the dynamically evolved steady-state solutions under spherical symmetry. The axisymmetric simulation is also performed, and the same results in figure A.23 for each radial ray are obtained. Thus showing only the 1D results suffices here. The set up is the same with that in chapter 4 with vanishing acoustic amplitude, i.e., fixed inner boundary. According to the obtained numerical solution, the steady-state flow indeed remains steady. This hence demonstrates that not only the initial conditions are correctly generated but also the neutrino heating by the light-bulb method is correctly implemented in the dynamical code in chapter 4.

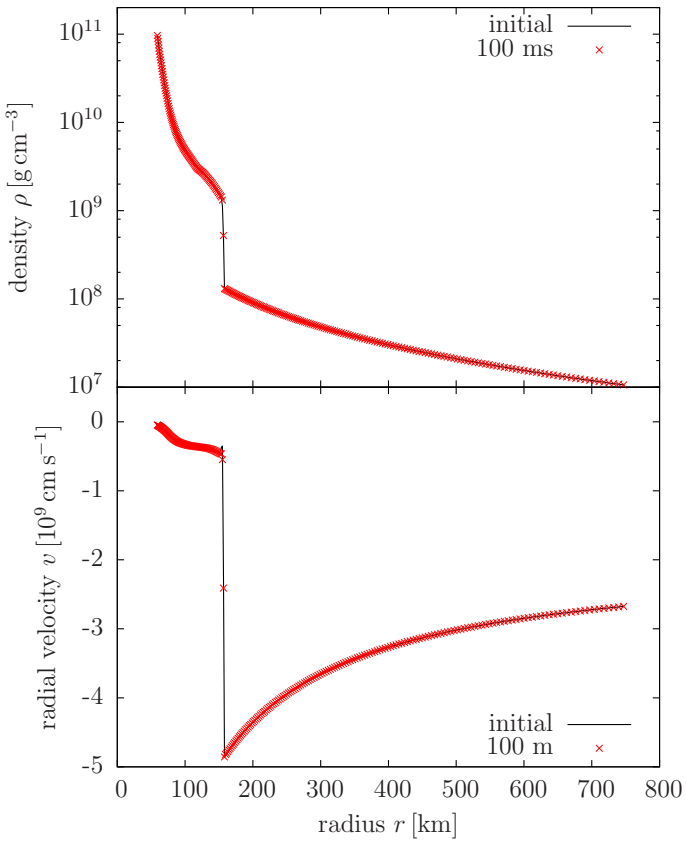

Figure A.23. The steady-state solution of the stalled shock with neutrino heating. The density (upper panel) and radial velocity (lower panel) profiles at the initial condition (black solid lines) and $t = 100\,\mathrm{ms}$ (red crosses) are shown.

Appendix B

Myers' corollary

In this appendix, I extend the Myers' corollary of the energy conservation theorem for perturbations with not-necessarily-small-amplitude (Myers, 1986, 1991) and derive equations (4.6–4.9). Here I refer to the energy conservation law as the theorem because it is derived from the continuity, Euler, and heat (entropy) equations. The discussion in this appendix is almost a review of (Myers, 1991), except that the effects of neutrino reactions are included. I believe, however, that it is worth summarizing.

The basic equations here are

$$\frac{\partial \rho}{\partial t} + \boldsymbol{\nabla}\cdot\boldsymbol{m} = 0 \Leftrightarrow C = 0, \tag{B.1}$$

$$\frac{\partial \boldsymbol{v}}{\partial t} + \boldsymbol{\zeta} + \boldsymbol{\nabla} H - T\boldsymbol{\nabla} s - \frac{\mu}{m_{\rm u}}\boldsymbol{\nabla} Y_{\rm e} = -\boldsymbol{\nabla}\Phi + \frac{1}{\rho}\boldsymbol{M} \Leftrightarrow \boldsymbol{L} = \boldsymbol{\lambda}, \tag{B.2}$$

$$\frac{\partial \rho s}{\partial t} + \boldsymbol{\nabla}\cdot(\boldsymbol{m}s) = \frac{Q - \frac{\mu}{m_{\rm u}}\Gamma - \boldsymbol{v}\cdot\boldsymbol{M}}{T} \Leftrightarrow S = \sigma, \tag{B.3}$$

$$\frac{\partial \rho Y_{\rm e}}{\partial t} + \boldsymbol{\nabla}\cdot(\boldsymbol{m}Y_{\rm e}) = \rho\Gamma \Leftrightarrow G = \gamma, \tag{B.4}$$

$$\Phi = -\frac{G_{\rm c} M_{\rm PNS}}{r}. \tag{B.5}$$

Here, ρ, $\boldsymbol{v}$, T, s, $m_{\rm u}$, $Y_{\rm e}$, Φ, $\boldsymbol{M}$, Q, Γ, $G_{\rm c}$ and $M_{\rm PNS}$ are the density, fluid velocity, temperature, specific entropy, atomic mass unit, electron fraction, gravitational potential, momentum transfer from neutrinos, neutrino heating rate per unit volume, change rate in the electron fraction, gravitational constant, and PNS mass, respectively; $\boldsymbol{m} = \rho\boldsymbol{v}$ and $H = e + P/\rho + \frac{1}{2}\boldsymbol{v}^2$ are the mass flux and specific stagnation entropy, or Bernoulli function; by defining the vorticity by $\boldsymbol{\omega} := \boldsymbol{\nabla}\times\boldsymbol{v}$, the shorthand notation of the outer product of the vorticity and velocity is $\boldsymbol{\zeta} := \boldsymbol{\omega}\times\boldsymbol{v}$; by letting $\mu_{\rm e,p,n}$ be the chemical potentials of electrons, protons, and neutrons, $\mu := \mu_{\rm e} + \mu_{\rm p} - \mu_{\rm n}$ is the chemical potential of neutrinos. These basic equations are equivalent to equations (4.1–4.4) in chapter 4 except for the inclusion of the term $\boldsymbol{M}$. Thanks to this term the following discussion is as general as possible, though it finally vanishes. It is also worth noting that the heat equation (B.3) is presented instead of the energy equation (4.3) since it is easy to consider the homentropic or isentropic flow with the heat equation. The symbols C, $\boldsymbol{L}$, S, and G are the left-hand sides of the continuity, Euler, heat, and electron fraction equations in

the expressions of equations (B.1–B.4), respectively[*1]. The symbols $\boldsymbol{\lambda}$, σ, and γ are the corresponding right-hand side terms. The thermodynamic relations which is useful for the following discussions are

$$\mathrm{d}e = T\mathrm{d}s + \frac{P}{\rho^2}\mathrm{d}\rho + \frac{\mu}{m_\mathrm{u}}\mathrm{d}Y_\mathrm{e}, \tag{B.6}$$

$$\mathrm{d}h = T\mathrm{d}s + \frac{1}{\rho}\mathrm{d}P + \frac{\mu}{m_\mathrm{u}}\mathrm{d}Y_\mathrm{e}, \tag{B.7}$$

where e, P, and h are the specific energy, pressure, and specific enthalpy, respectively. As I stated, the energy conservation theorem cast in the following form,

$$\frac{\partial}{\partial t}(\rho H - P) + \boldsymbol{\nabla}\cdot(H\boldsymbol{m}) + \boldsymbol{m}\cdot\boldsymbol{\nabla}\Phi - Q = 0, \tag{B.8}$$

is derived from equations (B.1–B.4) with the identity $\boldsymbol{v}\cdot\boldsymbol{\zeta} = \boldsymbol{v}\cdot(\boldsymbol{\omega}\times\boldsymbol{v}) = 0$.

Let me express perturbative expansion of a quantity q as $q(\boldsymbol{r},t) = q_0(\boldsymbol{r}) + \sum_{n=1}^{\infty}\delta^n q_n(\boldsymbol{r},t)$, where δ is a dimensionless parameter of the perturbation. The subscript n indicates the order of the perturbation, and especially q_0 represent the unperturbed state. Since the point mass gravity with constant central mass is considered in this appendix and chapter 4, the gravitational potential is not perturbed. By applying this perturbative expansion to the basic equations and collecting terms of the same order, the equations at each order are obtained:

$$C_i = 0,\ \boldsymbol{L}_i = \boldsymbol{\lambda}_i,\ S_i = \sigma_i,\ \text{and}\ G_i = \gamma_i, \tag{B.9}$$

where the symbols with subscript i corresponds to the i-th order perturbations of each shorthand expressions. Similarly, the energy conservation equation (B.8) is expanded as

$$\boldsymbol{\nabla}\cdot(\boldsymbol{m}_0 H_0) + \boldsymbol{m}_0\cdot\boldsymbol{\nabla}\Phi - Q_0 = 0\ \text{(zero-th-order)}, \tag{B.10}$$

$$\frac{\partial}{\partial t}(\rho H - P)_1 + \boldsymbol{\nabla}\cdot(\boldsymbol{m}_0 H_1 + \boldsymbol{m}_1 H_0) + \boldsymbol{m}_1\cdot\boldsymbol{\nabla}\Phi - Q_1 = 0\ \text{(first-order)}, \tag{B.11}$$

and

$$\frac{\partial}{\partial t}(\rho H - P)_2 + \boldsymbol{\nabla}\cdot(\boldsymbol{m}_0 H_2 + \boldsymbol{m}_1 H_1 + \boldsymbol{m}_2 H_0) + \boldsymbol{m}_2\cdot\boldsymbol{\nabla}\Phi - Q_2 = 0\ \text{(second-order)}. \tag{B.12}$$

Subsequently, these expressions for the energy conservation is cast in the following form:

$$\left(H - Ts - \frac{\mu}{m_\mathrm{u}}Y_\mathrm{e}\right)_0 C_0 + \boldsymbol{m}_0\cdot(\boldsymbol{L}_0 - \boldsymbol{\lambda}_0) + T_0(S_0 - \sigma_0) + \frac{\mu_0}{m_\mathrm{u}}(G_0 - \gamma_0) = 0\ \text{(zero-th-order)}, \tag{B.13}$$

$$\left(H - Ts - \frac{\mu}{m_\mathrm{u}}Y_\mathrm{e}\right)_0 C_1 + \boldsymbol{m}_0\cdot(\boldsymbol{L}_1 - \boldsymbol{\lambda}_1) + T_0(S_1 - \sigma_1) + \frac{\mu_0}{m_\mathrm{u}}(G_1 - \gamma_1) + \left(H - Ts - \frac{\mu}{m_\mathrm{u}}Y_\mathrm{e}\right)_1 C_0 + \boldsymbol{m}_1\cdot(\boldsymbol{L}_0 - \boldsymbol{\lambda}_0) + T_1(S_0 - \sigma_0) + \frac{\mu_1}{m_\mathrm{u}}(G_0 - \gamma_0) = 0\ \text{(first-order)}, \tag{B.14}$$

[*1] The symbol G represents the shorthand notation of the equation in this appendix and the gravitational constant in the main body. Only the former is applied in this appendix, and the gravitational constant is denoted as G_c instead of G.

and

$$\left(H - Ts - \frac{\mu}{m_{\rm u}}Y_{\rm e}\right)_0 C_2 + \boldsymbol{m}_0{\cdot}(\boldsymbol{L}_2 - \boldsymbol{\lambda}_2) + T_0(S_2 - \sigma_2) + \frac{\mu_0}{m_{\rm u}}(G_2 - \gamma_2)$$
$$+ \left(H - Ts - \frac{\mu}{m_{\rm u}}Y_{\rm e}\right)_2 C_0 + \boldsymbol{m}_2{\cdot}(\boldsymbol{L}_0 - \boldsymbol{\lambda}_0) + T_2(S_0 - \sigma_0) + \frac{\mu_2}{m_{\rm u}}(G_0 - \gamma_0)$$
$$+ \frac{\partial E_2}{\partial t} + \boldsymbol{\nabla}{\cdot}\boldsymbol{F}_2 + D_2 = 0 \ \text{(second-order)}, \tag{B.15}$$

where E_2, $\boldsymbol{F}_2$, and D_2 are

$$E_2 = \frac{P_1^2}{2\rho_0 a_0^2} + \frac{\rho_0 u_1^2}{2} + \rho_1 \boldsymbol{u}_0{\cdot}\boldsymbol{u}_1 + \frac{\rho_0}{2}\left\{\left(\frac{\partial T}{\partial s}\right)_{P,Y_{\rm e}} s_1 + \left(\frac{\partial T}{\partial Y_{\rm e}}\right)_{s,P} Y_{\rm e1}\right\} s_1$$
$$+ \frac{\rho_0}{2m_{\rm u}}\left\{\left(\frac{\partial \mu}{\partial Y_{\rm e}}\right)_{s,P} Y_{\rm e1} + \left(\frac{\partial \mu}{\partial s}\right)_{P,Y_{\rm e}} s_1\right\} Y_{\rm e1}, \tag{B.16}$$

$$\boldsymbol{F}_2 = (P_1 + \rho_0 \boldsymbol{u}_1{\cdot}\boldsymbol{u}_0)\left(\boldsymbol{u}_1 + \frac{\rho_1}{\rho_0}\boldsymbol{u}_0\right) + \rho_0 \boldsymbol{u}_0\left(s_1 T_1 + Y_{\rm e1}\frac{\mu_1}{m_{\rm u}}\right), \tag{B.17}$$

and

$$D_2 = \boldsymbol{m}_1{\cdot}\left(\boldsymbol{\zeta}_1 + s_1\boldsymbol{\nabla}T_0 + Y_{\rm e1}\boldsymbol{\nabla}\frac{\mu_0}{m_{\rm u}}\right) - s_1\boldsymbol{m}_0{\cdot}\boldsymbol{\nabla}T_1 - Y_{\rm e1}\boldsymbol{m}_0{\cdot}\boldsymbol{\nabla}\frac{\mu_1}{m_{\rm u}}$$
$$- T_1\sigma_1 - \frac{\mu_1}{m_{\rm u}}\gamma_1 - \boldsymbol{u}_1{\cdot}\boldsymbol{M}_1 - \frac{\rho_1}{\rho_0}(\boldsymbol{u}_0{\cdot}\boldsymbol{M}_1 - \boldsymbol{u}_1{\cdot}\boldsymbol{M}_0). \tag{B.18}$$

In the derivation, the thermodynamic relations (B.6–B.7) and Maxwell's relations are utilized. It should be noted that the zeroth- and first-order equations (B.13–B.14) are trivially satisfied thanks to equations (B.9). The first and second lines of the second-order equation (B.15) also vanish trivially with equations (B.9), whereas the last line does not vanish trivially. For the following reasons, the last line is regarded as the energy conservation theorem for the first-order perturbation. It is worth noting that up to first-order terms are contained in the expressions for E_2, $\boldsymbol{F}_2$ and D_2.

The well-known expression for the acoustic energy density in the homentropic flow appears as the first three terms in the right-hand side of equation (B.16). The fourth term in the equation represents the contribution from the non-uniform entropy and is originated from the term $T\mathrm{d}s$ in equations (B.6–B.7). The disturbance energy should not vanish by the periodic average of the oscillation, and hence the product of the first-order perturbations in temperature and entropy should be included in these terms. Indeed, $(\partial T/\partial s)_{P,Y_{\rm e}} s_1$ and $(\partial T/\partial Y_{\rm e})_{s,P} Y_{\rm e1}$ represents the variation in temperature induced by the perturbation in entropy and electron fraction, respectively, and these terms are the product of the entropy and temperature perturbations. Similarly, the contribution from the non-uniform composition originated from the term $\frac{\mu}{m_{\rm u}}\mathrm{d}Y_{\rm e}$ is represented by the fifth term in equation (B.16). The flux $\boldsymbol{F}_2$ is similarly interpreted: the acoustic energy flux in the homentropic flow with inhomogenous velocity field appears in the first term on the right-hand side in equation (B.17), and the contributions from the terms $T\mathrm{d}s$ and $\frac{\mu}{m_{\rm u}}\mathrm{d}Y_{\rm e}$ are expressed in the second term. On the contrary to E_2 and $\boldsymbol{F}_2$, the term D_2 is difficult

to interpret. This is because it is a collection of the remaining terms other than E_2, and $\boldsymbol{F}_2$, and well-known counterpart in homentropic flow does not appear. Considering that E_2 and $\boldsymbol{F}_2$ can be interpreted as the energy density and flux of the perturbation, however, the form of equation (B.15) can be regarded as a conservative form of the disturbance energy and D_2 can be interpreted as a dissipation term. Indeed, the neutrino cooling term, which is expressed as the fourth term $-T_1\sigma_1$, dissipate the energy. The positive (negative) T_1 leads the enhanced (suppressed) neutrino emission, and hence the term $\sigma_1 = \{(Q - \mu\gamma/m_\mathrm{u} - \boldsymbol{v}\cdot\boldsymbol{M})/T\}_1$ takes negative (positive) values, resulting in the positive values of $-T_1\sigma_1$ for both cases. As a consequence, the neutrino cooling reduces the perturbation energy. Although other terms are still difficult to interpret, the term D_2 is regarded as the dissipation term in this appendix and chapter 4.

The perturbative expansion up to the second order of the basic equations and energy conservation theorem is conducted so far. Myers focused on the structure of the perturbed equation systems. First, the energy conservation equations (B.13–B.15) commonly have the same structure: expression of

$$\left(H - Ts - \frac{\mu}{m_\mathrm{u}}Y_\mathrm{e}\right)(C - 0) + \boldsymbol{m}\cdot(\boldsymbol{L} - \boldsymbol{\lambda}) + T(S - \sigma) + \frac{\mu}{m_\mathrm{u}}(G - \gamma) \tag{B.19}$$

at each order, which is trivially zero, presents in each equation, and remaining terms other than this expression construct the non-trivial parts of the energy conservation equation. Myers guessed that this structure is common for all orders. Based on this notion, he recast the exact energy conservation equation including all orders by separating the trivial contributions from equation (B.8):

$$\begin{aligned}
&\left(H - Ts - \frac{\mu}{m_\mathrm{u}}Y_\mathrm{e}\right)_0 C + \boldsymbol{m}_0\cdot(\boldsymbol{L} - \boldsymbol{\lambda}) + T_0(S - \sigma) + \frac{\mu_0}{m_\mathrm{u}}(G - \gamma) + \\
&\left(H - Ts - \frac{\mu}{m_\mathrm{u}}Y_\mathrm{e}\right) C_0 + \boldsymbol{m}\cdot(\boldsymbol{L}_0 - \boldsymbol{\lambda}_0) + T(S_0 - \sigma_0) + \frac{\mu}{m_\mathrm{u}}(G_0 - \gamma_0) \\
-&\left(H - Ts - \frac{\mu}{m_\mathrm{u}}Y_\mathrm{e}\right)_0 C_0 - \boldsymbol{m}_0\cdot(\boldsymbol{L}_0 - \boldsymbol{\lambda}_0) - T_0(S_0 - \sigma_0) - \frac{\mu_0}{m_\mathrm{u}}(G_0 - \gamma_0) \\
&\qquad + \frac{\partial E_\mathrm{dis}}{\partial t} + \boldsymbol{\nabla}\cdot\boldsymbol{F}_\mathrm{dis} + D_\mathrm{dis} = 0.
\end{aligned} \tag{B.20}$$

The terms $E_{\rm dis}$, $\boldsymbol{F}_{\rm dis}$, and $D_{\rm dis}$ appearing in this form are given as

$$E_{\rm dis} = \rho\left(H - H_0 - T_0(s-s_0) - \frac{\mu_0}{m_{\rm u}}(Y_{\rm e} - Y_{\rm e0})\right) - \boldsymbol{m}_0\cdot(\boldsymbol{u}-\boldsymbol{u}_0) - (P - P_0), \tag{B.21}$$

$$\begin{aligned}\boldsymbol{F}_{\rm dis} = {} & (\boldsymbol{m}-\boldsymbol{m}_0)\left(H - H_0 - T_0(s-s_0) - \frac{\mu_0}{m_{\rm u}}(Y_{\rm e} - Y_{\rm e0})\right) \\ & + \boldsymbol{m}_0\left((T-T_0)(s-s_0) + \frac{\mu-\mu_0}{m_{\rm u}}(Y_{\rm e} - Y_{\rm e0})\right),\end{aligned} \tag{B.22}$$

$$\begin{aligned}D_{\rm dis} = {} & -(s-s_0)\boldsymbol{m}_0\cdot\boldsymbol{\nabla}(T-T_0) - (Y_{\rm e} - Y_{\rm e0})\boldsymbol{m}_0\cdot\boldsymbol{\nabla}\frac{\mu-\mu_0}{m_{\rm u}} \\ & + (\boldsymbol{m}-\boldsymbol{m}_0)\cdot\left(\boldsymbol{\zeta} - \boldsymbol{\zeta}_0 + (s-s_0)\boldsymbol{\nabla}T_0 + (Y_{\rm e} - Y_{\rm e0})\boldsymbol{\nabla}\frac{\mu_0}{m_{\rm u}}\right) \\ & - (T-T_0)\left(\frac{Q}{T} - \frac{Q_0}{T_0}\right) + \frac{\mu\mu_0}{m_{\rm u}}\left(\frac{T}{\mu} - \frac{T_0}{\mu_0}\right)\left(\frac{\gamma}{T} - \frac{\gamma_0}{T_0}\right) \\ & - TT_0\left(\frac{\boldsymbol{m}}{T} - \frac{\boldsymbol{m}_0}{T_0}\right)\cdot\left(\frac{\boldsymbol{M}}{\rho T} - \frac{\boldsymbol{M}_0}{\rho_0 T_0}\right).\end{aligned} \tag{B.23}$$

Because the non-trivial part of equation (B.20) takes the conservative form, he regarded these terms as the energy density, energy flux, and dissipation of the energy for the general disturbances. Note that although the procedure is the same as Myers' theory, the terms related to the neutrino reactions are also included. Whether his interpretation is appropriate or not is difficult to judge, however, there is supporting evidence: by taking the limit of small perturbations, the expressions of $E_{\rm dis}$, $\boldsymbol{F}_{\rm dis}$, and $D_{\rm dis}$ are reduced to those of E_2, $\boldsymbol{F}_2$, and D_2, respectively. By setting the momentum transfer $\boldsymbol{M}$ ($\boldsymbol{M}_0$) zero, equations (B.20–B.23) become equations (4.6–4.9). As discussed in section 4.2.2, the term $-(T-T_0)(Q/T - Q_0/T_0)$ in equation (B.23) represents the energy dissipation by the neutrino heating/cooling.

Bibliography

Abbott, B. P., Abbott, R., Abbott, T. D., et al. 2016, GW151226: Observation of Gravitational Waves from a 22-Solar-Mass Binary Black Hole Coalescence. Physical Review Letters, 116, 241103

—. 2017a, GW170817: Observation of Gravitational Waves from a Binary Neutron Star Inspiral. Physical Review Letters, 119, 161101

—. 2017b, Multi-messenger Observations of a Binary Neutron Star Merger. The Astrophysical Journal, Letters, , 848, L12

Abdikamalov, E., Gossan, S., DeMaio, A. M., & Ott, C. D. 2014, Measuring the angular momentum distribution in core-collapse supernova progenitors with gravitational waves. Physical Review D, , 90, 044001

Arnett, W. D., & Meakin, C. 2011, Toward Realistic Progenitors of Core-collapse Supernovae. The Astrophysical Journal, , 733, 78

Baade, W., & Zwicky, F. 1934, On Super-novae. Proceedings of the National Academy of Science, 20, 254

Baumgarte, T. W., Montero, P. J., Cordero-Carrión, I., & Müller, E. 2013, Numerical relativity in spherical polar coordinates: Evolution calculations with the BSSN formulation. Physical Review D, , 87, 044026

Baumgarte, T. W., Montero, P. J., & Müller, E. 2015, Numerical relativity in spherical polar coordinates: Off-center simulations. Physical Review D, , 91, 064035

Baumgarte, T. W., & Shapiro, S. L. 1999, Numerical integration of Einstein's field equations. Physical Review D, , 59, 024007

Bethe, H. A. 1990, Supernova mechanisms. Reviews of Modern Physics, 62, 801

Bethe, H. A., Brown, G. E., Applegate, J., & Lattimer, J. M. 1979, Equation of state in the gravitational collapse of stars. Nuclear Physics A, 324, 487

Bionta, R. M., Blewitt, G., Bratton, C. B., Casper, D., & Ciocio, A. 1987, Observation of a neutrino burst in coincidence with supernova 1987A in the Large Magellanic Cloud. Physical Review Letters, 58, 1494

Blondin, J. M., Mezzacappa, A., & DeMarino, C. 2003, Stability of Standing Accretion Shocks, with an Eye toward Core-Collapse Supernovae. The Astrophysical Journal, , 584, 971

Bollig, R., Janka, H.-T., Lohs, A., et al. 2017, Muon Creation in Supernova Matter Facilitates Neutrino-Driven Explosions. Physical Review Letters, 119, 242702

Bray, J. C., & Eldridge, J. J. 2016, Neutron Star Kicks and their Relationship to Supernovae Ejecta Mass. Monthly Notices of the Royal Astronomical Society, ,

arXiv:1605.09529

Brown, G. E., Bethe, H. A., & Baym, G. 1982, Supernova theory. Nuclear Physics A, 375, 481

Bruenn, S. W. 1985, Stellar core collapse - Numerical model and infall epoch. The Astrophysical Journal, Supplement, , 58, 771

Bruenn, S. W., & Mezzacappa, A. 1994, Prompt convection in core collapse supernovae. The Astrophysical Journal, Letters, , 433, L45

Bruenn, S. W., Mezzacappa, A., Hix, W. R., et al. 2013, Axisymmetric Ab Initio Core-collapse Supernova Simulations of 12-25 M $_{\rm sun}$ Stars. The Astrophysical Journal, Letters, , 767, L6

Bruenn, S. W., Lentz, E. J., Hix, W. R., et al. 2016, The Development of Explosions in Axisymmetric Ab Initio Core-collapse Supernova Simulations of 12-25 M Stars. The Astrophysical Journal, , 818, 123

Buras, R., Janka, H.-T., Keil, M. T., Raffelt, G. G., & Rampp, M. 2003a, Electron Neutrino Pair Annihilation: A New Source for Muon and Tau Neutrinos in Supernovae. The Astrophysical Journal, , 587, 320

Buras, R., Rampp, M., Janka, H.-T., & Kifonidis, K. 2003b, Improved Models of Stellar Core Collapse and Still No Explosions: What Is Missing? Physical Review Letters, 90, 241101

—. 2006, Two-dimensional hydrodynamic core-collapse supernova simulations with spectral neutrino transport. I. Numerical method and results for a 15 $M_{\odot}$ star. Astronomy & Astrophysics, , 447, 1049

Burrows, A., Dessart, L., Ott, C. D., & Livne, E. 2007a, Multi-dimensional explorations in supernova theory. Physics Reports , 442, 23

Burrows, A., & Goshy, J. 1993, A Theory of Supernova Explosions. The Astrophysical Journal, Letters, , 416, L75

Burrows, A., Hayes, J., & Fryxell, B. A. 1995, On the Nature of Core-Collapse Supernova Explosions. The Astrophysical Journal, , 450, 830

Burrows, A., Livne, E., Dessart, L., Ott, C. D., & Murphy, J. 2006, A New Mechanism for Core-Collapse Supernova Explosions. The Astrophysical Journal, , 640, 878

—. 2007b, Features of the Acoustic Mechanism of Core-Collapse Supernova Explosions. The Astrophysical Journal, , 655, 416

Cabezón, R. M., Pan, K.-C., Liebendörfer, M., et al. 2018, Core-collapse supernovae in the hall of mirrors. A three-dimensional code-comparison project. Astronomy & Astrophysics, , 619, A118

Cercignani, C., & Kremer, G. M. 2002, The relativistic Boltzmann equation: theory and applications

Colella, P., & Woodward, P. R. 1984, The Piecewise Parabolic Method (PPM) for gas-dynamical simulations. Journal of Computational Physics, 54, 174

Colgate, S. A., Grasberger, W. H., & White, R. H. 1961, The Dynamics of Supernova Explosions. The Astronomical Journal, , 66, 280

Colgate, S. A., & Johnson, M. H. 1960, Hydrodynamic Origin of Cosmic Rays. Physical

Review Letters, 5, 235

Colgate, S. A., & White, R. H. 1966, The Hydrodynamic Behavior of Supernovae Explosions. The Astrophysical Journal, , 143, 626

Couch, S. M. 2013, On the Impact of Three Dimensions in Simulations of Neutrino-driven Core-collapse Supernova Explosions. The Astrophysical Journal, , 775, 35

Couch, S. M., & Ott, C. D. 2015, The Role of Turbulence in Neutrino-driven Core-collapse Supernova Explosions. The Astrophysical Journal, , 799, 5

Demorest, P. B., Pennucci, T., Ransom, S. M., Roberts, M. S. E., & Hessels, J. W. T. 2010, A two-solar-mass neutron star measured using Shapiro delay. Nature, , 467, 1081

Dimmelmeier, H., Novak, J., Font, J. A., Ibáñez, J. M., & Müller, E. 2005, Combining spectral and shock-capturing methods: A new numerical approach for 3D relativistic core collapse simulations. Physical Review D, , 71, 064023

Dolence, J. C., Burrows, A., & Zhang, W. 2015, Two-dimensional Core-collapse Supernova Models with Multi-dimensional Transport. The Astrophysical Journal, , 800, 10

Epstein, R. 1978, Neutrino angular momentum loss in rotating stars. The Astrophysical Journal, Letters, , 219, L39

Eriguchi, Y., & Müller, E. 1984, Equilibrium models of differentially rotating polytropes and the collapse of rotating stellar cores. Max Planck Institut fur Astrophysik Report, 168

Fernández, R. 2012, Hydrodynamics of Core-collapse Supernovae at the Transition to Explosion. I. Spherical Symmetry. The Astrophysical Journal, , 749, 142

Fischer, T., Martínez-Pinedo, G., Hempel, M., et al. 2016, in European Physical Journal Web of Conferences, Vol. 109, European Physical Journal Web of Conferences, 06002

Foglizzo, T. 2002, Non-radial instabilities of isothermal Bondi accretion with a shock: Vortical-acoustic cycle vs. post-shock acceleration. Astronomy & Astrophysics, , 392, 353

Foglizzo, T., Galletti, P., Scheck, L., & Janka, H.-T. 2007, Instability of a Stalled Accretion Shock: Evidence for the Advective-Acoustic Cycle. The Astrophysical Journal, , 654, 1006

Foglizzo, T., Scheck, L., & Janka, H.-T. 2006, Neutrino-driven Convection versus Advection in Core-Collapse Supernovae. The Astrophysical Journal, , 652, 1436

Freedman, D. Z. 1974, Coherent effects of a weak neutral current. Physical Review D, , 9, 1389

Friman, B. L., & Maxwell, O. V. 1979, Neutrino emissivities of neutron stars. The Astrophysical Journal, , 232, 541

Fryer, C. L., & Warren, M. S. 2002, Modeling Core-Collapse Supernovae in Three Dimensions. The Astrophysical Journal, Letters, , 574, L65

Furusawa, S., Sumiyoshi, K., Yamada, S., & Suzuki, H. 2013, New Equations of State Based on the Liquid Drop Model of Heavy Nuclei and Quantum Approach to Light Nuclei for Core-collapse Supernova Simulations. The Astrophysical Journal, , 772, 95

Furusawa, S., Togashi, H., Nagakura, H., et al. 2017, A new equation of state for core-collapse supernovae based on realistic nuclear forces and including a full nuclear ensem-

ble. Journal of Physics G Nuclear Physics, 44, 094001

Furusawa, S., Yamada, S., Sumiyoshi, K., & Suzuki, H. 2011, A New Baryonic Equation of State at Sub-nuclear Densities for Core-collapse Simulations. The Astrophysical Journal, , 738, 178

Glas, R., Just, O., Janka, H.-T., & Obergaulinger, M. 2018, Three-Dimensional Core-Collapse Supernova Simulations with Multi-Dimensional Neutrino Transport Compared to the Ray-by-Ray-plus Approximation. ArXiv e-prints, arXiv:1809.10146

Hachisu, I. 1986, A versatile method for obtaining structures of rapidly rotating stars. The Astrophysical Journal, Supplement, , 61, 479

Hanke, F., Marek, A., Müller, B., & Janka, H.-T. 2012, Is Strong SASI Activity the Key to Successful Neutrino-driven Supernova Explosions? The Astrophysical Journal, , 755, 138

Hanke, F., Müller, B., Wongwathanarat, A., Marek, A., & Janka, H.-T. 2013, SASI Activity in Three-dimensional Neutrino-hydrodynamics Simulations of Supernova Cores. The Astrophysical Journal, , 770, 66

Harada, A., Nagakura, H., Iwakami, W., & Yamada, S. 2017, A Parametric Study of the Acoustic Mechanism for Core-collapse Supernovae. The Astrophysical Journal, , 839, 28

Harten, A., Lax, P. D., & van Leer, B. 1983, On Upstream Differencing and Godunov-Type Schemes for Hyperbolic Conservation Laws. SIAM Review, 25, 35

Heger, A., Langer, N., & Woosley, S. E. 2000, Presupernova Evolution of Rotating Massive Stars. I. Numerical Method and Evolution of the Internal Stellar Structure. The Astrophysical Journal, , 528, 368

Heger, A., Woosley, S. E., & Spruit, H. C. 2005, Presupernova Evolution of Differentially Rotating Massive Stars Including Magnetic Fields. The Astrophysical Journal, , 626, 350

Herant, M., Benz, W., Hix, W. R., Fryer, C. L., & Colgate, S. A. 1994, Inside the supernova: A powerful convective engine. The Astrophysical Journal, , 435, 339

Hirata, K., Kajita, T., Koshiba, M., Nakahata, M., & Oyama, Y. 1987, Observation of a neutrino burst from the supernova SN1987A. Physical Review Letters, 58, 1490

Horowitz, C. J. 2002, Weak magnetism for antineutrinos in supernovae. Physical Review D, , 65, 043001

Horowitz, C. J., Caballero, O. L., Lin, Z., O'Connor, E., & Schwenk, A. 2016, Neutrino-nucleon scattering in supernova matter from the virial expansion. ArXiv e-prints, arXiv:1611.05140

Isenberg, J. A. 2008, Waveless Approximation Theories of Gravity. International Journal of Modern Physics D, 17, 265

Iwakami, W., Nagakura, H., & Yamada, S. 2014, Critical Surface for Explosions of Rotational Core-collapse Supernovae. The Astrophysical Journal, , 793, 5

Janka, H.-T. 2001, Conditions for shock revival by neutrino heating in core-collapse supernovae. Astronomy & Astrophysics, , 368, 527

—. 2012, Explosion Mechanisms of Core-Collapse Supernovae. Annual Review of Nuclear

and Particle Science, 62, 407

Juodagalvis, A., Langanke, K., Hix, W. R., Martínez-Pinedo, G., & Sampaio, J. M. 2010, Improved estimate of electron capture rates on nuclei during stellar core collapse. Nuclear Physics A, 848, 454

Just, O., Bollig, R., Janka, H.-T., et al. 2018, Core-collapse supernova simulations in one and two dimensions: comparison of codes and approximations. Monthly Notices of the Royal Astronomical Society, , 481, 4786

Just, O., Obergaulinger, M., & Janka, H.-T. 2015, A new multidimensional, energy-dependent two-moment transport code for neutrino-hydrodynamics. Monthly Notices of the Royal Astronomical Society, , 453, 3386

Keil, W., Janka, H.-T., & Mueller, E. 1996, Ledoux Convection in Protoneutron Stars—A Clue to Supernova Nucleosynthesis? The Astrophysical Journal, Letters, , 473, L111

Kitaura, F. S., Janka, H.-T., & Hillebrandt, W. 2006, Explosions of O-Ne-Mg cores, the Crab supernova, and subluminous type II-P supernovae. Astronomy & Astrophysics, , 450, 345

Kiuchi, K., Nagakura, H., & Yamada, S. 2010, Multi-layered Configurations in Differentially Rotational Equilibrium. The Astrophysical Journal, , 717, 666

Kolmogorov, A. 1941a, The Local Structure of Turbulence in Incompressible Viscous Fluid for Very Large Reynolds' Numbers. Akademiia Nauk SSSR Doklady, 30, 301

Kolmogorov, A. N. 1941b, Dissipation of Energy in Locally Isotropic Turbulence. Akademiia Nauk SSSR Doklady, 32, 16

Kotake, K., Sato, K., & Takahashi, K. 2006, Explosion mechanism, neutrino burst and gravitational wave in core-collapse supernovae. Reports on Progress in Physics, 69, 971

Kotake, K., Takiwaki, T., Fischer, T., Nakamura, K., & Martínez-Pinedo, G. 2018, Impact of Neutrino Opacities on Core-collapse Supernova Simulations. The Astrophysical Journal, , 853, 170

Kotake, K., Yamada, S., & Sato, K. 2003, Anisotropic Neutrino Radiation in Rotational Core Collapse. The Astrophysical Journal, , 595, 304

Kraichnan, R. H. 1967, Inertial Ranges in Two-Dimensional Turbulence. Physics of Fluids, 10, 1417

Kuroda, T., Kotake, K., & Takiwaki, T. 2012, Fully General Relativistic Simulations of Core-collapse Supernovae with an Approximate Neutrino Transport. The Astrophysical Journal, , 755, 11

—. 2016a, A New Gravitational-wave Signature from Standing Accretion Shock Instability in Supernovae. The Astrophysical Journal, Letters, , 829, L14

Kuroda, T., Takiwaki, T., & Kotake, K. 2014, Gravitational wave signatures from low-mode spiral instabilities in rapidly rotating supernova cores. Physical Review D, , 89, 044011

—. 2016b, A New Multi-energy Neutrino Radiation-Hydrodynamics Code in Full General Relativity and Its Application to the Gravitational Collapse of Massive Stars. The Astrophysical Journal, Supplement, , 222, 20

Langanke, K., & Martínez-Pinedo, G. 2000, Shell-model calculations of stellar weak in-

teraction rates: II. Weak rates for nuclei in the mass range /A=45-65 in supernovae environments. Nuclear Physics A, 673, 481

Langanke, K., Martínez-Pinedo, G., Sampaio, J. M., et al. 2003, Electron Capture Rates on Nuclei and Implications for Stellar Core Collapse. Physical Review Letters, 90, 241102

Lattimer, J. M., & Swesty, F. D. 1991, A generalized equation of state for hot, dense matter. Nuclear Physics A, 535, 331

Lentz, E. J., Bruenn, S. W., Hix, W. R., et al. 2015, Three-dimensional Core-collapse Supernova Simulated Using a 15 $M_{\odot}$ Progenitor. The Astrophysical Journal, Letters, , 807, L31

Levermore, C. D. 1984, Relating Eddington factors to flux limiters. Journal of Quantitative Spectroscopy and Radiative Transfer, , 31, 149

Liebendörfer, M. 2005, A Simple Parameterization of the Consequences of Deleptonization for Simulations of Stellar Core Collapse. The Astrophysical Journal, , 633, 1042

Liebendörfer, M., Mezzacappa, A., Thielemann, F.-K., et al. 2001, Probing the gravitational well: No supernova explosion in spherical symmetry with general relativistic Boltzmann neutrino transport. Physical Review D, , 63, 103004

Liebendörfer, M., Whitehouse, S. C., & Fischer, T. 2009, The Isotropic Diffusion Source Approximation for Supernova Neutrino Transport. The Astrophysical Journal, , 698, 1174

Lindquist, R. W. 1966, Relativistic transport theory. Annals of Physics, 37, 487

Maeder, A., & Meynet, G. 2012, Rotating massive stars: From first stars to gamma ray bursts. Reviews of Modern Physics, 84, 25

Marek, A., Dimmelmeier, H., Janka, H.-T., Müller, E., & Buras, R. 2006, Exploring the relativistic regime with Newtonian hydrodynamics: an improved effective gravitational potential for supernova simulations. Astronomy & Astrophysics, , 445, 273

Marek, A., & Janka, H.-T. 2009, Delayed Neutrino-Driven Supernova Explosions Aided by the Standing Accretion-Shock Instability. The Astrophysical Journal, , 694, 664

Martínez-Pinedo, G., Fischer, T., Lohs, A., & Huther, L. 2012, Charged-Current Weak Interaction Processes in Hot and Dense Matter and its Impact on the Spectra of Neutrinos Emitted from Protoneutron Star Cooling. Physical Review Letters, 109, 251104

Maxwell, O. V. 1987, Neutrino emission processes in hyperon-populated neutron stars. The Astrophysical Journal, , 316, 691

Mazurek, T. J. 1982, The energetics of adiabatic shocks in stellar collapse. The Astrophysical Journal, Letters, , 259, L13

Melson, T., Janka, H.-T., & Marek, A. 2015, Neutrino-driven Supernova of a Low-mass Iron-core Progenitor Boosted by Three-dimensional Turbulent Convection. The Astrophysical Journal, Letters, , 801, L24

Mewes, V., Zlochower, Y., Campanelli, M., et al. 2018, Numerical relativity in spherical coordinates with the Einstein Toolkit. Physical Review D, , 97, 084059

Montero, P. J., Baumgarte, T. W., & Müller, E. 2014, General relativistic hydrodynamics in curvilinear coordinates. Physical Review D, , 89, 084043

Müller, B. 2015, The dynamics of neutrino-driven supernova explosions after shock revival in 2D and 3D. Monthly Notices of the Royal Astronomical Society, , 453, 287

Müller, B., & Janka, H.-T. 2015, Non-radial instabilities and progenitor asphericities in core-collapse supernovae. Monthly Notices of the Royal Astronomical Society, , 448, 2141

Müller, B., Janka, H.-T., & Dimmelmeier, H. 2010, A New Multi-dimensional General Relativistic Neutrino Hydrodynamic Code for Core-collapse Supernovae. I. Method and Code Tests in Spherical Symmetry. The Astrophysical Journal, Supplement, , 189, 104

Müller, B., Janka, H.-T., & Marek, A. 2012, A New Multi-dimensional General Relativistic Neutrino Hydrodynamics Code for Core-collapse Supernovae. II. Relativistic Explosion Models of Core-collapse Supernovae. The Astrophysical Journal, , 756, 84

Murphy, J. W., & Dolence, J. C. 2017, An Integral Condition for Core-collapse Supernova Explosions. The Astrophysical Journal, , 834, 183

Murphy, J. W., Dolence, J. C., & Burrows, A. 2013, The Dominance of Neutrino-driven Convection in Core-collapse Supernovae. The Astrophysical Journal, , 771, 52

Murphy, J. W., & Meakin, C. 2011, A Global Turbulence Model for Neutrino-driven Convection in Core-collapse Supernovae. The Astrophysical Journal, , 742, 74

Myers, M. 1986, An exact energy corollary for homentropic flow. Journal of Sound and Vibration, 109, 277

Myers, M. K. 1991, Transport of energy by disturbances in arbitrary steady flows. Journal of Fluid Mechanics, 226, 383

Nagakura, H., Ito, H., Kiuchi, K., & Yamada, S. 2011, Jet Propagations, Breakouts, and Photospheric Emissions in Collapsing Massive Progenitors of Long-duration Gamma-ray Bursts. The Astrophysical Journal, , 731, 80

Nagakura, H., Iwakami, W., Furusawa, S., et al. 2017, Three-dimensional Boltzmann-Hydro Code for Core-collapse in Massive Stars. II. The Implementation of Moving-mesh for Neutron Star Kicks. The Astrophysical Journal, Supplement, , 229, 42

Nagakura, H., Sumiyoshi, K., & Yamada, S. 2014, Three-dimensional Boltzmann Hydro Code for Core Collapse in Massive Stars. I. Special Relativistic Treatments. The Astrophysical Journal, Supplement, , 214, 16

Nagakura, H., Iwakami, W., Furusawa, S., et al. 2018, Simulations of Core-collapse Supernovae in Spatial Axisymmetry with Full Boltzmann Neutrino Transport. The Astrophysical Journal, , 854, 136

Nordhaus, J., Burrows, A., Almgren, A., & Bell, J. 2010, Dimension as a Key to the Neutrino Mechanism of Core-collapse Supernova Explosions. The Astrophysical Journal, , 720, 694

O'Connor, E., & Ott, C. D. 2011, Black Hole Formation in Failing Core-Collapse Supernovae. The Astrophysical Journal, , 730, 70

O'Connor, E., Bollig, R., Burrows, A., et al. 2018, Global comparison of core-collapse supernova simulations in spherical symmetry. Journal of Physics G Nuclear Physics, 45, 104001

O'Connor, E. P., & Couch, S. M. 2018, Two-dimensional Core-collapse Supernova Ex-

plosions Aided by General Relativity with Multidimensional Neutrino Transport. The Astrophysical Journal, , 854, 63

Ohnishi, N., Kotake, K., & Yamada, S. 2006, Numerical Analysis of Standing Accretion Shock Instability with Neutrino Heating in Supernova Cores. The Astrophysical Journal, , 641, 1018

Ott, C. D., Burrows, A., Dessart, L., & Livne, E. 2008, Two-Dimensional Multiangle, Multigroup Neutrino Radiation-Hydrodynamic Simulations of Postbounce Supernova Cores. The Astrophysical Journal, , 685, 1069

Ott, C. D., Burrows, A., Livne, E., & Walder, R. 2004, Gravitational Waves from Axisymmetric, Rotating Stellar Core Collapse. The Astrophysical Journal, , 600, 834

Ott, C. D., Roberts, L. F., da Silva Schneider, A., et al. 2017, The Progenitor Dependence of Three-Dimensional Core-Collapse Supernovae. ArXiv e-prints, arXiv:1712.01304

Pan, K.-C., Mattes, C., O'Connor, E. P., et al. 2019, The impact of different neutrino transport methods on multidimensional core-collapse supernova simulations. Journal of Physics G Nuclear Physics, 46, 014001

Pejcha, O., & Thompson, T. A. 2012, The Physics of the Neutrino Mechanism of Core-collapse Supernovae. The Astrophysical Journal, , 746, 106

Rampp, M., & Janka, H.-T. 2002, Radiation hydrodynamics with neutrinos. Variable Eddington factor method for core-collapse supernova simulations. Astronomy & Astrophysics, , 396, 361

Richers, S., Nagakura, H., Ott, C. D., et al. 2017, A Detailed Comparison of Multidimensional Boltzmann Neutrino Transport Methods in Core-collapse Supernovae. The Astrophysical Journal, , 847, 133

Ruchlin, I., Etienne, Z. B., & Baumgarte, T. W. 2018, SENR /NRPy + : Numerical relativity in singular curvilinear coordinate systems. Physical Review D, , 97, 064036

Saad, Y. 2003, Iterative Methods for Sparce Linear Systems, 2nd edn. (Philadelphia, PA: SIAM)

Sato, K. 1975, Supernova explosion and neutral currents of weak interaction. Progress of Theoretical Physics, 54, 1325

Shapiro, S. L., & Teukolsky, S. A. 1983, Black holes, white dwarfs, and neutron stars: The physics of compact objects

Shen, H., Toki, H., Oyamatsu, K., & Sumiyoshi, K. 1998, Relativistic equation of state of nuclear matter for supernova and neutron star. Nuclear Physics A, 637, 435

Shibata, M., Karino, S., & Eriguchi, Y. 2002, Dynamical instability of differentially rotating stars. Monthly Notices of the Royal Astronomical Society, , 334, L27

—. 2003, Dynamical bar-mode instability of differentially rotating stars: effects of equations of state and velocity profiles. Monthly Notices of the Royal Astronomical Society, , 343, 619

Shibata, M., Kiuchi, K., Sekiguchi, Y., & Suwa, Y. 2011, Truncated Moment Formalism for Radiation Hydrodynamics in Numerical Relativity. Progress of Theoretical Physics, 125, 1255

Shibata, M., Nagakura, H., Sekiguchi, Y., & Yamada, S. 2014, Conservative form of

Boltzmann's equation in general relativity. Phys. Rev. D, 89, 084073

Shibata, M., & Nakamura, T. 1995, Evolution of three-dimensional gravitational waves: Harmonic slicing case. Physical Review D, , 52, 5428

Shibata, M., & Taniguchi, K. 2006, Merger of binary neutron stars to a black hole: Disk mass, short gamma-ray bursts, and quasinormal mode ringing. Physical Review D, , 73, 064027

Sugahara, Y., & Toki, H. 1994, Relativistic mean-field theory for unstable nuclei with non-linear σ and ω terms. Nuclear Physics A, 579, 557

Sumiyoshi, K., & Yamada, S. 2012, Neutrino Transfer in Three Dimensions for Core-collapse Supernovae. I. Static Configurations. The Astrophysical Journal, Supplement, , 199, 17

Sumiyoshi, K., Yamada, S., Suzuki, H., et al. 2005, Postbounce Evolution of Core-Collapse Supernovae: Long-Term Effects of the Equation of State. The Astrophysical Journal, , 629, 922

Summa, A., Hanke, F., Janka, H.-T., et al. 2016, Progenitor-dependent Explosion Dynamics in Self-consistent, Axisymmetric Simulations of Neutrino-driven Core-collapse Supernovae. The Astrophysical Journal, , 825, 6

Summa, A., Janka, H.-T., Melson, T., & Marek, A. 2018, Rotation-supported Neutrino-driven Supernova Explosions in Three Dimensions and the Critical Luminosity Condition. The Astrophysical Journal, , 852, 28

Suwa, Y., Tominaga, N., & Maeda, K. 2017, Importance of ^{56}Ni production on diagnosing explosion mechanism of core-collapse supernova. ArXiv e-prints, arXiv:1704.04780

Takiwaki, T., Kotake, K., & Suwa, Y. 2012, Three-dimensional Hydrodynamic Core-collapse Supernova Simulations for an 11.2 $M_\odot$ Star with Spectral Neutrino Transport. The Astrophysical Journal, , 749, 98

—. 2014, A Comparison of Two- and Three-dimensional Neutrino-hydrodynamics Simulations of Core-collapse Supernovae. The Astrophysical Journal, , 786, 83

—. 2016, Three-dimensional simulations of rapidly rotating core-collapse supernovae: finding a neutrino-powered explosion aided by non-axisymmetric flows. Monthly Notices of the Royal Astronomical Society, , 461, L112

Tamborra, I., Raffelt, G., Hanke, F., Janka, H.-T., & Müller, B. 2014, Neutrino emission characteristics and detection opportunities based on three-dimensional supernova simulations. Physical Review D, , 90, 045032

Thompson, T. A., Quataert, E., & Burrows, A. 2005, Viscosity and Rotation in Core-Collapse Supernovae. The Astrophysical Journal, , 620, 861

Vartanyan, D., Burrows, A., Radice, D., Skinner, M. A., & Dolence, J. 2019, A successful 3D core-collapse supernova explosion model. Monthly Notices of the Royal Astronomical Society, , 482, 351

Walder, R., Burrows, A., Ott, C. D., et al. 2005, Anisotropies in the Neutrino Fluxes and Heating Profiles in Two-dimensional, Time-dependent, Multigroup Radiation Hydrodynamics Simulations of Rotating Core-Collapse Supernovae. The Astrophysical Journal, , 626, 317

Weinberg, N. N., & Quataert, E. 2008, Non-linear saturation of g-modes in proto-neutron stars: quieting the acoustic engine. Monthly Notices of the Royal Astronomical Society, , 387, L64

Wilson, J. R. 1985, in Numerical Astrophysics, ed. J. M. Centrella, J. M. Leblanc, & R. L. Bowers, 422

Wilson, J. R., Mathews, G. J., & Marronetti, P. 1996, Relativistic numerical model for close neutron-star binaries. Physical Review D, , 54, 1317

Woosley, S. E., Heger, A., & Weaver, T. A. 2002, The evolution and explosion of massive stars. Reviews of Modern Physics, 74, 1015

Yahil, A. 1983, Self-similar stellar collapse. The Astrophysical Journal, , 265, 1047

Yamada, S., & Sato, K. 1994, Numerical study of rotating core collapse in supernova explosions. The Astrophysical Journal, , 434, 268

Yamasaki, T., & Yamada, S. 2005, Effects of Rotation on the Revival of a Stalled Shock in Supernova Explosions. The Astrophysical Journal, , 623, 1000

—. 2006, Standing Accretion Shocks in the Supernova Core: Effects of Convection and Realistic Equations of State. The Astrophysical Journal, , 650, 291

—. 2007, Stability of Accretion Flows with Stalled Shocks in Core-Collapse Supernovae. The Astrophysical Journal, , 656, 1019

Yoshida, S., Ohnishi, N., & Yamada, S. 2007, Excitation of g-Modes in a Proto-Neutron Star by the Standing Accretion Shock Instability. The Astrophysical Journal, , 665, 1268

Zwerger, T., & Mueller, E. 1997, Dynamics and gravitational wave signature of axisymmetric rotational core collapse. Astronomy & Astrophysics, , 320, 209